LIST OF CORRIGENDA IN
THESIS SUBMITTED FOR THE DEGREE OF
DOCTOR OF PHILOSOPHY
IN THE UNIVERSITY OF LONDON
ENTITLED

CONFINED ISOTHERMAL AND COMBUSTING FLOWS BEHIND AXISYMMETRIC BAFFLES

by

A. M. K. P. TAYLOR

SUBMITTED AUGUST, 1981

--ooOoo--

LIST OF CORRIGENDA CORRECT
AS OF FEBRUARY, 1984

CORRIGENDA

LOCATION	READS	CORRECT TO
ABSTRACT, page (iii), line 4	... (in pipe radii) ...	... (in baffle radii) ...
EQUATION 2.17, page 48	$\dot{m} = \frac{\dot{m}_o}{1 - \alpha}$	$\frac{\dot{m}}{\dot{m}_o} = \frac{\alpha}{1 - \alpha}$
SECTION 2.3, page 52, second paragraph, final line	... is substantially larger than that of either of the other two baffles	... is about 0.8 that of the smaller disc and is due to the narrower width of the recirculation bubb
SUMMARY, page 69, item 2(b)	-	(b) decrease (by 16 per cent) the dimensionless recirculating mass flow rate
TABLE 2.7, page 60	-	(see attached version)
FIGURE 2.10, page 83	-	(see attached version)
FIGURE 4.5, page 278	PINHOLE MASK (ϕ 0.033 mm)	PINHOLE MASK (ϕ 0.33 mm)
FIGURE 3.5, page 157	-	(see attached version)

TABLE 2.7

SIZE OF THE RECIRCULATION ZONE AND RECIRCULATING MASS FLOW RATE

AUTHORS	FLOW TYPE	LENGTH[a]	WIDTH[a]	$\frac{\dot{m}_r}{\dot{m}_o}$[b]	$\frac{\dot{m}_r}{\dot{m}}$[c]
This thesis	Confined disc, 25% blockage	1.75	0.62	~~0.11~~ 0.10	~~0.08~~ 0.31
	Confined cone, 25% blockage	1.55	0.55	~~0.07~~ 0.06	~~0.05~~ 0.19
	Confined disc, 50% blockage	2.20	0.55	~~0.24~~ 0.26	~~0.12~~ 0.26
Winterfeld (1965)	Confined disc, 25% blockage	2.0	0.74	-	-
	Confined 90° cone, 25% blockage	1.9	0.64	-	-
	Confined 45° cone, 25% blockage	1.7	0.58	-	-
	Confined disc, 4% blockage	2.0	0.84	-	-
	Confined 90° cone, 4% blockage	1.9	0.72	-	-
	Confined 45° cone, 4% blockage	1.7	0.60	-	-
Fujii et al (1978)	Confined 60° wedge, 50% blockage	1.88	0.59	0.10	~~0.05~~ 0.10
Bradbury (1976)	Confined flat plate, 10% blockage	1.98	0.80	~~0.27~~ 0.028	~~0.24~~ 0.25
Davies and Beér (1971)	Annular jet, disc, 25% blockage	1.52	0.60	0.15	~~0.11~~ 0.45
	Annular jet, 45° cone, 25% blockage	1.24	0.50	0.08	~~0.06~~ 0.24
	Annular jet, cylinder, 25% blockage	0.72	0.50	-	-
	Annular jet, disc, 54% blockage	1.16	0.56	0.27	~~0.12~~ 0.23

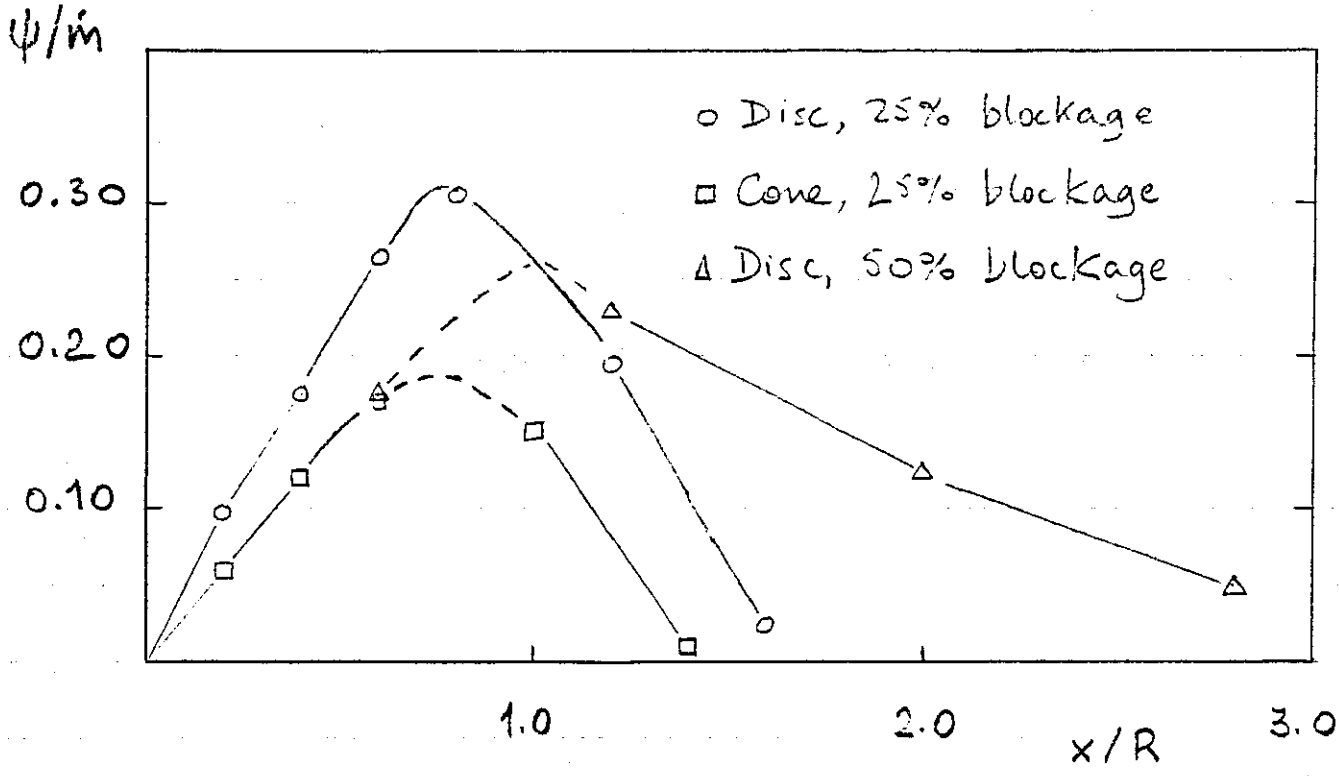

Figure 2.10 (revised)

TABLE 3.5

MEASURED AND CALCULATED DIMENSIONS OF RECIRCULATION BUBBLE AND RECIRCULATING MASS FLOW RATE FOR FLOWS OF CHAPTER II

	x_r/R	W/R	$\dot{m}_r/\dot{m}_o$
Disc, 25% blockage			
measured	1.75	0.63	~~11~~ 10 %
calculated	1.56	0.60	8.2 %
Cone, 25% blockage			
measured	1.55	0.56	~~7~~ 6 %
calculated	1.41	0.54	5.4 %
Disc, 50% blockage			
measured	3.11	0.79	~~24~~ 26 %
calculated	2.78	0.74	14.4 %

CONFINED, ISOTHERMAL AND COMBUSTING FLOWS BEHIND AXISYMMETRIC BAFFLES

ALEXANDER MARINOS KRETON PETER TAYLOR
B.Sc. (Eng.), A.C.G.I.

Thesis submitted for the degree of
Doctor of Philosophy
in the University of London
and for the
Diploma of Membership of the Imperial College

Imperial College of Science and Technology
(Department of Mechanical Engineering)

August, 1981

To those who have taught me
in the Humanities and Sciences
but above all
to my Parents

ABSTRACT

Field measurements of the mean velocity and Reynolds stresses, by laser-Doppler velocimetry, and wall pressure measurements in the isothermal, turbulent near-wake of three baffles in a long pipe are reported. The recirculation lengths (in pipe radii) and maximum values of turbulent kinetic energy (normalised using the bulk velocity in the plane of the baffle) were 1.75 and 19 per cent, 1.55 and 11 per cent and 2.20 and 16 per cent for 25 per cent area blockage disc, cone and 50 per cent blockage disc respectively. The increase in the recirculation length with blockage is opposite to the trend in unconfined, annular jets. For the smaller blockage the maximum value of turbulent kinetic energy lies near the rear stagnation point: in this region normal stress/strain generation is more important than in the larger blockage.

The flows have been calculated by a finite difference technique using the "k-ε" model of turbulence. The local numerical diffusion error in a given solution was derived from the difference between central and upwind differencing of the partial derivatives representing convection and this was made small by selective grid refinement. The recirculation lengths are short by 10 per cent and the turbulent kinetic energies are too low although the qualitative differences between the baffles are present. The results are more accurate than published calculations of a related flow which are shown to have been tainted by numerical diffusion. It is concluded that the influence of streamline curvature on shear stress is inadequately represented and that a Reynolds stress turbulence model should be used.

Similar measurements, together with mean temperature profiles, are presented for premixed, air/natural gas, low Mach number, baffle

stabilised flames at Reynolds numbers of 2.3 and 4.9 x 10^4. Frequency spectra of sound level and temperature show up to two standing acoustic quarter-waves with one driving large pressure oscillations over a wide range of fuel to air ratio: within this range the recirculation length becomes shorter and the variance of velocity larger. In the absence of large oscillations, for an equivalence ratio of 0.69, the recirculation lengths were 2.20, 2.20 and 3.15 for the 25 per cent blockage disc, cone and 50 per cent blockage disc respectively. Combustion increases the variance of velocity as compared with the corresponding isothermal flow because of the occurence of greater shear strain. The results are suitable for the assessment of models of turbulence and combustion.

ACKNOWLEDGEMENTS

I have been fortunate in having received the assistance of a number of people during the preparation of this thesis and it gives me pleasure to acknowledge this.

I am deeply indebted to my supervisor, Prof. J. H. Whitelaw, who provided me with sound advice, valuable criticism and maintained a constant interest in my work.

I am obliged to Prof. F. Durst, for his supervision during my stay at the University of Karlsruhe, and Prof. P. Bradshaw, for helpful discussions on chapter II.

Dr. Jim McGuirk, Prof. Margarido Ribeiro and Dr. Nick Vlachos gave generously of their time and knowledge: I gratefully acknowledge their contributions to this work. I have also benefitted from my association with all my colleagues, particularly Dr. Apostolos Goulas, Dr. Pepé Humphrey, Dr. Hany Moneib and Mr. Mihalis Yianneskis.

My thanks go to Messrs. R. Church, J. Laker and O. Vis for their execution of, and help with, the experimental apparatus. Mr. R. Potter, Mr. G. Tindall, Mr. A. Tipple and Miss E. Archer have also been most helpful.

I thank Mrs. Helen Bastin for her excellent, and speedy, typing.

I welcome the opportunity to record my thanks to the Science Research Council for the financial support provided for this work.

TABLE OF CONTENTS

LIST OF TABLES

LIST OF FIGURES

GLOSSARY OF SYMBOLS

Roman characters

A	Subscripted (N, S, E, W) influence coefficient, equations (3.12), (3.31), (3.36).
A_P	$A_P \equiv A_N + A_S + A_E + A_W$
b, b_o	Diameters of laser beams at e^{-2} intensity level, equation (2.3)
b_x, b_y	Measuring volume dimensions, equations (2.1), (2.2), figure 2.3
b_{ij}	Anisotropy of Reynolds stress, in tensor notation, equation (3.52)
C_p	Borda-Carnot pressure rise, equation (2.19)
$C_{\varepsilon_1, \varepsilon_2, \varepsilon_3}$	Constants used in transport equation for ε, equations (3.9, (3.8) and (3.48) respectively
C_μ	Constant used in equation (3.6)
c	Velocity of sound
c''	Fluctuations of a scalar about a Favre (mass-averaged) mean, equation (4.15)
d	Diameter of a baffle
E	Constant in the 'law of the wall', equation (3.21)
E_T	Tracker output voltage, equation (2.12)
f_i	Centre-frequencies of intervals forming histogram describing Doppler signal probability distribution, equations (4.2), (4.3)
f_p	Doppler frequency observed by photomultiplier tube, equation (2.7)
f_s	Imposed Doppler shift frequency, equation (2.7)

f_v	Instantaneous Doppler frequency caused by particle motion
$f_{1,2,3}$	Focal lengths of lenses L_1, L_2, L_3 (figure 2.3)
G	Tracker transfer constant (volts/Hz), equation (2.12)
g	Acceleration of gravity
h	Manometer fluid height, table 2.5
K	Velocimeter transfer constant (ms^{-1}/Hz), equation (2.6)
k	Turbulent kinetic energy $\equiv \frac{1}{2}\{\langle u^2\rangle + \langle v^2\rangle + \langle w^2\rangle\}$
$\tilde{k}$	Favre-averaged turbulent kinetic energy, equation (4.16)
ℓ	Size of large scale eddies, equations (3.19), (4.13)
$\dot{m}$	Mass flow rate $\equiv \rho U_o \frac{\pi d^2}{4}$
$\dot{m}_o$	Mass flow rate through pipe
$\dot{m}_r$	Recirculating mass flow rate
N	Number of line pairs on radial diffraction grating, equation (2.8), table 2.2
Nu	Nusselt number, equation (4.5)
N_i	Number of Doppler signals with a frequency in the range $f_i \pm \frac{1}{2}(\delta f)$
n	Refractive index of medium (chapter II)
Pe	Computational Péclet number, equation (3.35)
p	Mean pressure
p(t)	Instantaneous pressure
p'	Pressure-correction variable (chapter III)
	Pressure fluctuations about p (chapter IV)
p_d	Pressure recovery downstream of baffle, equation (2.20)
R	Radius of confining pipe.
R_ϕ	Residual due to non-convergence, equation (3.27)

$\dot{R}$	Rate of arrival of scattering particles in measuring volume, equation (4.4)
r	Distance along radial co-ordinate
S_L	Laminar flame speed
T	Magnitude of numerical diffusion; chapter III, equation (3.47)
$T(t)$	Instantaneous temperature } equations (4.7),
T_b	Temperature of (burnt) products } (4.8)
T_g	Instantaneous gas temperature, equation (4.5)
$T_{g,m}$	Gas temperature measured by thermocouple, equation (4.5)
T_u	Temperature of (unburnt) reactants
T_+	Dimensionless temperature
T_+'	Fluctuations of T_+ about the time mean
$U(t)$	Instantaneous axial velocity
U	Time-mean axial velocity
U_c	Convecting velocity, equation (2.5)
$\tilde{U}_j$	Favre-averaged velocity component
U_o	Annular bulk velocity
$\hat{U}_o$	Maximum annular velocity
$\langle u^2 \rangle$	Variance of axial velocity fluctuations
u_i''	Fluctuation of velocity about a Favre-averaged mean
$\langle uv \rangle$	Time mean of cross-correlation
V	Radial velocity
$\langle v^2 \rangle$	Variance of radial velocity fluctuations
$\langle w^2 \rangle$	Variance of azimuthal velocity fluctuations
x	Axial distance
x_r	Length of recirculation bubble

y	Distance from wall
y_a	Distance to grid node adjacent to wall, equation (3.24)
y^+	Variable in law of the wall, equation (3.21)

Greek characters

α	Area blockage ratio of baffle ($d^2/4R^2$)
δ	Large-structure length scale, equation (2.5)
δ_{ij}	Kronecker's delta
δ_L	Laminar flame thickness
δf	Width of frequency interval centred at f_i
δr	Radial spacing of finite differance grid
δx	Axial spacing of finite difference grid, figure (3.1)
δx	Fringe spacing, chapter II
$\delta\Omega$	r.m.s. fluctuation of Ω, table 2.2
ε	Isotropic rate of dissipation of turbulent kinetic energy
η	Kolmogorov microscale, equations (4.13), (4.14)
θ	Half-angle of beam intersection (figure 2.3)
κ	von Kármán's constant, equation (3.21)
λ	Wavelength of laser light
μ	Instantaneous scattering particle density (m^{-3}), equation (4.4)
μ_t	Scalar turbulent viscosity, equation (3.4)
μ_{num}	Estimate of coefficient of numerical viscosity, equation (3.44)
ν	Kinematic viscosity
ρ	Density of fluid
σ_ϕ	Effective turbulent Prandtl number for variable ϕ, equation (3.10)

τ_a	Value of wall shear stress, equation (3.21)
τ_p	Time-scale of scattering particle arrival rate
τ_s	Mean time between valid Doppler signals, equation (2.5)
τ_t	Time-scale of turbulence
ϕ	. Equivalence ratio, equation (4.6) . Power spectral density of velocity fluctuations (chapter II) . Surrogate variable for U, V, p´, k and ε in chapter III
Φ^*	Iteratively converged solution to equation (3.12), sub-section 3.3.2
χ	Tensor-invariant measure of vortex stretching, equation (3.48)
ψ	Stream function, equation (2.17)
Ω	Angular velocity of rotating grating, equation (2.18)

Operators

P(...)	Production of Reynolds stress component
<...>	Time-averaged value
$\tilde{...}$	Instantaneous value (chapter II)
	Favre-averaged value (chapter IV)

Subscripts

i	Chapter III: surrogate variable for N, S, E, W
N, S, E, W, P	Values appropriate to nodes marked in figure 3.1
n, s, e, w	Values appropriate to control volume faces shown in figure 3.1
n, s	Distance normal to, and along, streamline (figure 3.34)

Superscripts

*	Guessed value of variable, sub-section 3.2.3
$\ldots''$	Fluctuation about a Favre-averaged mean

CHAPTER I

INTRODUCTION TO THE THESIS

1.1 The flows considered

The flow about a bluff body involves a region of separated, recirculating flow in its near-wake and is characterised by a large loss in total pressure head and an intense generation of turbulence, and therefore mixing, in the recirculating flow. Bluff bodies are found in a wide variety of situations in both nature and industrial plant, and an understanding of the resulting flows is important for design. For example, the pressure loss in the flow over land vehicles or tall buildings is undesirable and its magnitude is an important quantity. In contrast, the turbulent mixing in the recirculation bubble, whether generated by a bluff body or in some other way, is crucial to the successful stabilisation of the flame in many high performance combustors and furnaces. In this thesis bluff body flows are considered in the context of flame stabilisers ("baffles") with particular reference to premixed fuel-air combustion. An important reason for studying premixed combustion is that, at least in some circumstances, premix can result in smaller levels of fuel consumption and emissions of particulates, unburnt hydrocarbons, carbon monoxide and nitrogen oxides (NO_x) as compared to diffusion flames (Ferri, 1973; Weinberg, 1974; Ganji and Sawyer, 1979).

In the study of flames stabilised by recirculating flow, knowledge of the aerodynamics is fundamental. According to one view, the mechanism of stabilisation results from turbulent heat and mass transfer between the lee of the baffle, which contains the hot products of combustion, and the unburnt reactants outside this zone. The recirculation zone is regarded as a 'well-stirred reactor', and flame

extinction, for example as a function of the fuel-to-air ratio, is interpreted as the result of excessive chemical loading of this reactor; whence the importance of the volume of the recirculation bubble. Both the turbulent transport and the recirculation bubble are aerodynamic quantities. The temperature profile, whose magnitude and shape is important in determining levels of emission and the creep life of components, is another example of a variable which is influenced by the flow pattern and consequent turbulent transport.

Because of the importance of the aerodynamics, a large part of this thesis involves the measurement, and subsequent comparison with numerical analysis, of the mean and fluctuating velocity in the near wake of several baffles. Experiments are reported not only for combusting flows, but also for isothermal models because much can be usefully learnt about the recirculation bubble, and parameters affecting it, in such experimentally, and conceptually, simpler flows.

1.2 Previous work

This section reviews relevant literature and is included to provide the background necessary for formulating and assessing the aims and purposes of the present contribution, which are the subjects of the following section. The reasons for interest in isothermal flows have already been established in the previous section and the review begins by considering experimental, and then computational, work on isothermal flow. Previous experimental work on combusting flows, stabilised by recirculation, is then considered and the section finishes by briefly considering the calculation of combusting flows.

Isothermal flow: experiments

Recirculating flows which can be used for flame stabilisation

may be established in a number of ways such as the application of swirl (El Banhawy and Whitelaw, 1979) or by opposed jets (Arcoumanis, 1980; Schefer and Sawyer, 1976; Peck and Samuelsen, 1976). In bluff body flows separation originates at a solid surface and the following review is restricted to separation which initiates at a surface discontinuity, such as a corner. The references that have been selected consider high Reynolds number, low Mach number flows so that there is no influence of laminar-to-turbulent transition or compressibility. Table 1.1 summarises the experiments and findings.

The lee of a baffle is a region of low pressure which is generated by the streamline curvature of the flow. Measurements of the pressure, and also of the length of the recirculation bubble, are available for a wide variety of cross-sectional and forebody shapes (e.g. Fail et al, 1957; Calvert, 1967; Humphries and Vincent, 1976a, 1976b; Chigier and Gilbert, 1968; Winterfeld, 1965; Sullerey et al, 1975). These show that bluffer bodies, which give rise to large streamline deflections at their trailing edge, result in larger negative pressures and longer, wider recirculation zones. An important observation for the application to flame stabilisation is that the length of recirculation is reduced by confinement. Annular jets (e.g. Davies and Beér, 1971) are found to be somewhat shorter than confined flows (e.g. Winterfeld, 1965), although the latter reference suggests that the length is influenced more by bluffness (forebody shape) than by blockage, at least for isothermal flows of less than 25% blockage.

Vortex shedding, similar to that occuring in flows around circular cylinders, has been observed in unconfined flows, particularly for plane, two-dimensional baffles (Fail et al, 1957; Calvert, 1967). Neither extensive shedding nor bimodal velocity probability density distributions have been observed in annular jets (Durão and Whitelaw,

1978) and it is likely that the same holds true for confined flows. A further difference between plane and axisymmetric baffles concerns the behaviour of the scales of the recirculation bubble. The maximum negative pressure on the centreline behind a baffle, and its location, have been used as characteristic scales of recirculation bubbles (e.g. Calvert, 1967). In plane flows, increases in the maximum negative pressures are associated with decreasing length scales: the opposite is true for axisymmetric geometries (Sullerey et al, 1975).

Profiles of the mean flow are interesting because, for example, the mean streamline pattern can be deduced and thus so can the mean bubble length, width and recirculating mass flow rate. The latter is a useful measure of both the size and turbulent transport in the recirculation bubble, both quantities being influential in determining the flame extinction limits. It is found that larger, bluffer, baffles result in an increased recirculating flow, in agreement with the measured trends in stability limits (Davies and Beér, 1971).

The magnitude of the turbulent transport across the mean separation streamline has been examined either by measurements of the mean concentration of a "passive scalar" (Schofield and Keeble, 1975; Fujii et al, 1978) or by estimation of the residence time of such a scalar when injected into the recirculation region (Winterfeld, 1965; Humphries and Vincent, 1976a and 1976b). The residence time is found to scale well with the mean flow time scale and comparative measurements suggest that bluffer bodies give rise to higher turbulent transport.

The precise measurement of the instantaneous velocity in the near wake has, until recently, been restricted by the unsuitability of hot-wire anemometry for highly turbulent, reversed flows. Although much early work relied on this instrument (e.g. Carmody, 1964), work by Bradbury (1976) shows that results can be qualitatively incorrect.

The development of the pulsed-wire anemometer and laser-Doppler velocimeter has provided the means to make reliable observations, with references available on plane baffles (Bradbury, 1976; Fujii et al, 1978) and axisymmetric and three-dimensional annular jets (Durão and Whitelaw, 1978; Durão, Founti and Whitelaw, 1979). The particular advantages of laser-Doppler velocimetry are that there are effectively no limits to the turbulence intensities which can be measured and, being an optical technique, it does not disturb the recirculating flow.

The data show that turbulence increases as the shear layers develop, reaching a maximum value of Reynolds stress of about 6% (normalised by the annular bulk velocity) upstream of the free stagnation point. Equally large values occur on the centreline at the free stagnation point. For the case of a flow over a flat plate, Bradbury (1976) has suggested an explanation for the high centreline values based on the existence of vortex shedding. The absence of this mechanism in annular jets suggests the presence of an alternative source of the turbulence, and one such is discussed in Chapter II. It is also found (Fujii et al, 1978; Durão and Whitelaw, 1978) that there are regions of the shear layer where shear stress is zero but mean strain is not. This implies that the transport of shear stress may be important and that a calculation scheme based on an effective viscosity hypothesis may be inappropriate.

The pulsed-wire anemometer and laser-Doppler velocimeter have been particularly applied to the study of separated flows in which the separation streamline reattaches to a solid surface: the last six references in Table 1.1 are of this type. The flows are similar in principle to those already considered, but the presence of the wall gives rise to generally longer recirculation lengths, smaller streamline curvature and hence smaller negative pressures than for flows with

free stagnation points (Moss, Baker and Bradbury, 1977). The comparatively short lengths measured by Freeman (1975) and Smyth (1979) are due in the case of Freeman to the large pipe expansion ratio and in that of Smyth to the small influence of the boundary condition near the centreline in an axisymmetric flow. Part of the relevance of this literature is that it establishes the distribution and magnitudes of Reynolds stress which are expected in turbulent, separated flows.

Two aspects of separated flows can be examined using the information gathered in flows with reattachment. The first is to examine to what extent the shear layer emanating from a corner resembles a plane, two-dimensional mixing layer such as that of Wygnanski and Fielder (1970). The comparisons made by Moss et al (1977) suggest that only the 'high-speed' side exhibits similarity, thereby implying that the process of reattachment and the convection of turbulent fluid from the rear stagnation point is important. The second aspect is concerned with the behaviour of the turbulent length scale at, and downstream of, the rear stagnation point. Bradshaw and Wong (1972), in an investigation downstream of a reattaching turbulent shear layer, suggested that there was a sudden decrease in length scale as the reattachment took place. In contrast, the work of Etheridge and Kemp (1978), who investigated a similar flow using laser-Doppler velocimetry, concluded that there was only slight evidence in support of this observation, probably because only a small fraction of the shear layer was deflected back towards the step.

Isothermal flow: calculation

Calculation of the flow about baffles can be made by the numerical solution of the partial differential equations for the conservation of mass and momentum, together with the necessary boundary

conditions. Some of the details of such a calculation are given in Chapter III. Here it is noted that the momentum equations are solved in the Reynolds-averaged form, with various phenomenological ("turbulence") models replacing the velocity-fluctuation correlations which appear.

Table 1.2 summarises a number of papers which present calculations and compare these with experimental data. Although the compilation is by no means exhaustive, representative conclusions regarding the performance of the calculations can be drawn.

The calculation of the unconfined flow about a baffle, measured by Carmody (1964), was reported by Pope and Whitelaw (1976) and showed that the calculated length of the recirculation bubble was too small (by about 1/3), as was the spreading rate of the downstream wake. For reasons of economy the calculation scheme started at the trailing edge of the disc, but the results of the calculation were shown to be particularly sensitive to the assumed distribution of radial velocity at this station, for which there were no measurements. Two turbulence model types were used, the "k-ε" model (Jones and Launder, 1972) and the more advanced "Reynolds stress model" (Launder, Reece and Rodi, 1975). The latter conferred no improvement in the agreement between calculation and experiment, and it was concluded that both uncertainties in the boundary conditions for radial velocity and deficiencies in the modelled form of the equation for the rate of dissipation of turbulent kinetic energy were to blame. The same authors presented calculations for the annular jet flow of Durão and Whitelaw (1974), with similar results. Other authors (e.g. Leschziner and Rodi, 1980) have sought improvements in the "k-ε" model's performance in annular jet flows by accounting for the effect of streamline curvature on turbulence. It has been found, however, (e.g. Leonard, Leschziner and McGuirk, 1978; Leschziner and Rodi, 1980) that care is required to avoid truncation errors ("numerical

diffusion") in the solution as well as changes in the mathematical model of turbulence. The use of the modified turbulence model still results in discrepancies between the measurements and calculation. The subject of truncation errors and the question of whether the calculations of Pope and Whitelaw (1976) and Leschziner and Rodi (1980) are "grid independent" are examined in detail in Chapter III and not considered further here.

An arrangement corresponding closely to that of a confined flow about a baffle has been calculated by Gosman et al (1979). The data relevant to this thesis concern an annular jet flow behind a stationary valve, which modelled the cylinder head of a reciprocating engine. The flow was driven by the reciprocating motion of a piston. In common with the study of Pope and Whitelaw (1976), the results of the analysis using the k-ε model were found to be strongly influenced by the radial velocity assumed to exist in the annular orifice. The flowfield was found to spread and decay too rapidly, with associated poor predictions of the turbulence structure.

Separated flows with reattachment have been considered by a number of authors in a wide variety of experimental configurations. For example, the work of Nielsen, Restivo and Whitelaw (1978) was concerned with modelling the velocity characteristics of ventilated rooms, using the k-ε model of turbulence. Comparison with measurements, using laser-Doppler velocimetry, suggested that the precision of the calculated mean velocity was adequate for design purposes. In contrast, the recirculation region in an axisymmetric sudden expansion, measured and calculated by Habib and Whitelaw (1978), gave rise to substantial errors. They suggested that the disagreement was due to the inapplicability of the effective viscosity hypothesis used in the k-ε model because of the large anisotropy in the turbulence.

The last flow to be reviewed involves the flow over a plane rib in a channel (Durst and Rastogi, 1977). In this case, the solution domain extended far enough upstream of the rib for the flow to be uninfluenced by the presence of the rib, and thus removed any uncertainty in the boundary conditions. The solution was obtained using the k-ε model and, in certain regions, a simplified version of the Reynolds stress model (Hanjalić and Launder, 1972). Agreement was good only for profiles upstream of the rib, where the flow is dominated by pressure gradients. The flow over and behind the rib was poorly represented, with an underprediction in the axial velocity of 20 - 30% at ten rib heights downstream. Numerical experiments suggested that the discrepancies in the far-wake were due to the poor calculation of the recirculation bubble, and that in common with the findings of Pope and Whitelaw (1976), the more advanced turbulence model did not offer substantial improvements in the calculation.

Combusting flow: experiments

This subsection reviews references which are relevant to flames stabilised by baffles and on which the separation streamline may originate at either a corner (e.g. a disc) or a smooth surface (e.g. a circular cylinder). Most of the references available consider flows with free stagnation points and almost all are totally enclosed, so that the degree of blockage is important. With few exceptions, the reactants are supplied as a premixed stream.

Table 1.3 presents a summary of the references which are relevant to this flow category. It is convenient to distinguish the references under three headings: those which quantify the flame extinction limits for a variety of operating conditions, those which report the corresponding changes in, for example, the recirculation

length and those which present field measurements of some quantity in the near or far wake of the baffle.

Because of their obvious practical importance, particular attention has been paid to determining the flame extinction limits (that is, the equivalence ratios) as a function of the flow velocity, temperature and pressure or the baffle shape and size (Longwell, Chenevey, Clark and Frost, 1949; Barrère and Mestre, 1954; Williams et al, 1949; DeZubay, 1950). Flame extinction can be supposed to occur (e.g. Spalding, 1979) when the supply of reactants, by turbulent exchange, to the reaction zone does not balance the rate of consumption, by the chemical reaction, for whatever reason. Thus, for example, increasing the flow velocity increases the supply of reactants, because of the increased turbulent exchange, until the reaction "blows-out" when the rate of reaction can no longer keep pace. Increasing the pressure increases the reaction rate (proportional to pressure squared for a bi-molecular reaction) but also increases the density (proportional to pressure) so that the "p-D" scaling rule (Spalding, 1979), established experimentally by DeZubay (1950), comes about. The bluffness ("shape") of the baffle gives rise to two partly compensatory effects. Increasing bluffness gives rise to increased turbulence, and hence turbulent exchange, but also to a larger (wider and longer) recirculation region and hence a larger region of reaction and hence increased rate of consumption. The net result seems to be that increasing bluffness results in slightly increased stability limits.

Gross aerodynamic quantities, such as the size of the recirculation zone, the rate of flame spread from the baffle and the residence time of a passive scalar within the recirculation bubble, are estimates of the volume of the reaction zone and the rate of turbulent exchange. Measurements of these quantities have been made

as a function of the free stream velocity, turbulence intensity, Mach number, equivalence ratio and baffle blockage and shape (Wright, 1959; Wright and Zukoski, 1962; Bovina, 1958; Winterfeld, 1965). The principal differences compared with the equivalent isothermal flow are that blockage ratio is a more important parameter, that the recirculation length is longer (by a factor of up to two) and that turbulent transport across the separation streamline is smaller (by between two to three times). The latter two results are a direct outcome of the decrease in density, due to the combustion, within the recirculation zone.

A further effect of heat release on the flow is to increase the Reynolds number of transition and to delay the establishment of flow independent of the Reynolds number. The data of Winterfeld (1965) indicate that although the recirculation length is independent of the Reynolds number above about 2×10^3 for isothermal flow, in combusting flow the length continues to increase, albeit slowly, at the highest Reynolds numbers measured ($\simeq 2.2 \times 10^5$). Wright and Zukoski (1962) set the critical value at about 5×10^4 on the basis that above this value the flame width was constant. According to Spalding (1979), however, the existence of the maximum blow-off velocity on the fuel-rich side of stoichiometric in the data of Barrère and Mestre (1954) suggests that laminar transport is still important at values of 5×10^5.

Field measurements in the wake of bluff body stabilised flames are rare in comparison to the more extensive work in swirl-stabilised diffusion flames. Early work by Howe, Shipman and Vranos (1963) reported mean velocity profiles at stations downstream of the recirculation zone. Mean velocity profiles in the near-wake of a confined, premixed flame, stabilised on an annular "vee-gutter" (Harrison, 1973 and 1974; cited by Pope, 1976) and detailed measurements of a confined, bluff body stabilised diffusion flame (Elliman, Fussey

and Hay, 1978) have been reported recently. In both cases the measurement technique is restricted to values of mean velocity only, although the merit of the work of Harrison (1973) and (1974) is that the Reynolds number is probably high enough for laminar transport effects to be unimportant.

The measurement of any quantity in the near wake of stabilised, premixed flames is particularly difficult because of the high temperatures. In this region probe interference is particularly undesirable because the probe itself can act as a flame stabiliser and thus completely change the flow. The laser-Doppler velocimeter is thus particularly well-suited for making measurements of mean and fluctuating velocity, although there are very few references available which report such measurements. The work of Clare et al (1976) reports velocity characteristics for "smooth" combustion and also in the presence of combustion induced oscillations ("buzz"). Although confined, premixed flames are prone to such oscillations both in the laboratory and in industry, it is desirable that they be absent. Their violence may be such as to destroy the combustor and their presence is unwanted in data taken to evaluate combustion and turbulence models. This aspect of the flow is considered in greater detail in Chapter IV. The data of Durão and Whitelaw (1977) were also obtained using a laser-Doppler velocimeter in an annular jet configuration for both premixed and diffusion flames. Their measurements show similarity in the length of the recirculation, although not in the magnitude of the maximum reversed velocity.

Combusting flow: calculations

Although calculations of combusting flow are not presented in this thesis, the ability to make such calculations forms an important background to the rationale of this work. This subsection presents a

brief summary of how such calculations can be carried out.

The calculation of a turbulent, premixed combusting flow can proceed by the solution of the (modelled) conservation equations for mass, momentum and species in a way analagous to the calculation of isothermal turbulent flow. The "combustion model" embodies assumptions concerning both the mean rate of reaction and the representation of the fluxes owing to turbulent transport. A number of proposals have been made for the representation of the mean rate of reaction (e.g. Spalding, 1971 and 1976; Bray and Moss, 1974; Borghi, 1975; Borghi, Moreau, Bonniot, 1978) and several reviews of these proposals have been published (Jones and Whitelaw, 1978; Pope, 1976). Turbulent transport can then be represented by "turbulence models", with the influence of density fluctuations being avoided by the use of density weighted variables (Favre et al, 1976). However, the validity of the "gradient transport" concept has recently been questioned in combusting flows (Borghi and Dutoya, 1978; Libby and Bray, 1980). Discrepancies which may result between calculations and experiment can stem from either the combustion or the turbulence model, or both. Comparison between the errors in calculating a combusting and similar isothermal flow may lead to an assessment of the weakness of the combustion model; this provides a further reason for studying isothermal flow. Calculations of premixed flames have been performed (e.g. Mason and Spalding, 1973; Gosman et al, 1978; Borghi, Moreau and Bonniot, 1978; Pope, 1976), but lack of suitably detailed measurements, particularly in recirculating flows, has precluded detailed evaluation of the models.

1.3 The present contribution

The review presented in the previous section showed that there is no detailed experimental information on the velocity characteristics

in the near wake of confined flows behind bluff bodies for either isothermal or premixed combusting flow: that the use of laser-Doppler velocimetry results in accurate measurements of these characteristics: and that parameters of interest include the forebody shape and blockage ratio of the baffle.

As a result of the lack of data, the evaluation of current prediction procedures has yet to be made in such flows. Related work, however, indicates that the k-ε model, rather than any more advanced model, is indicated for use: and that, if the boundary of the solution domain includes the trailing edge of the baffle, measurements of the magnitude and direction of velocity at this station are desirable for use as boundary conditions.

The contributions of this thesis can be separated into two categories. The first consists of an experimental and computational investigation into the isothermal, turbulent flow behind bluff bodies. There are two related purposes in undertaking the experimental work. The first is to quantify the influence of the blockage ratio and baffle forebody shape on the features of the flow, particularly the re-circulation bubble, and so provide a basis for understanding the flows' development. The second purpose is to evaluate the performance of the k-ε model of turbulence in these flows and thereby make suggestions for the improvement of the computational procedure.

The second contribution consists of an experimental investigation into premixed, combusting flows which are, as far as possible, geometrically similar to the isothermal flow. The purpose, again, is to quantify the influence of forebody shape and the blockage ratio on the flow. A further purpose is to provide experimental data for the evaluation of the performance of computational techniques. An important objective in performing isothermal and combusting

experiments in geometrically similar configurations is to be able to apportion errors in calculations separately to the models of turbulence and combustion.

The dissertation provides measurements of mean velocities, Reynolds stresses, wall static pressures and, in the case of combusting flow, mean temperature in sufficient detail to fulfil the purposes listed in the previous two paragraphs.

1.4 Thesis content

The remainder of the thesis is presented in four chapters. Chapter II describes experimental work conducted on turbulent flow in a water tunnel. The experimental method is described and includes a detailed estimate of the errors incurred in the measurements. The results are then presented and discussed with particular reference to the influence of the baffle forebody shape and blockage ratio.

Chapter III is devoted to numerical computation of the experiments of Chapter II. The analysis proceeds by presenting the partial differential equations to be solved and includes a brief description of the turbulence model used. The method of numerical solution of the corresponding finite difference equations is outlined and there follows a careful consideration of the accuracy of the numerical solution. The results of the computations are presented and the shortcomings of the turbulence model are discussed.

Chapter IV is concerned with experiments in combusting flow. The experimental method, which includes the measurement of mean temperature, is described; particular attention is given to the importance of combustion-induced oscillations. The results are compared to some isothermal air flows and, again, the influence of the forebody shape and blockage of the baffles is discussed.

Chapter V presents the concluding remarks to the dissertation. Its purpose is to summarise the achievements of the thesis and to suggest the directions in which further work may be required.

TABLE 1.1

SUMMARY OF CITED ISOTHERMAL FLOW EXPERIMENTS

Authors	Experiment	Findings
Fail et al (1957)	Unconfined flow over plates of various shapes and aspect ratios. $Re^* \simeq 6 \times 10^4$. Measurements by pitot-static tubes and hot-wire anemometry.	Effect of aspect ratio on drag, base pressure and flow pattern small for aspect ratio < 10. Recirculation length for disc: 2.6 diameters.
Calvert (1967)	Unconfined flow over cones between 0^0 and 180^0 apex angle. Measurements of static pressure and by hot-wire anemometry. $Re \simeq 5 \times 10^4$.	Strouhal frequencies measured. Base, minimum and maximum pressures rise as apex angle decreases. Bubble length (3.0 diameters for a disc) increases with apex angle.
Humphries and Vincent (1976a) and (1976b)	Unconfined flow over various axisymmetric baffles for smooth and turbulent airflow. $2 \times 10^3 < Re < 4 \times 10^4$. Principal measurements by smoke probe.	Increasing airflow turbulence decreases smoke residence time, shape factor and bubble length (1.9 - 2.6 diameters for disc).
Carmody (1964)	Unconfined flow over a disc. Re = 3.2 and 7×10^4. Field measurements of total and static pressure, mean velocity, turbulence intensity and shear stress (hot-wire anemometry).	Similarity profiles established 15 diameters downstream of disc. Bubble length: 2.6 diameters.

* Re signifies Reynolds number

TABLE 1.1 (CONTINUED)

Authors	Experiment	Findings
Bradbury (1976)	Flow over a flat plate. 0.10 blockage ratio, $Re = 3.8 \times 10^5$. Field measurements of mean and fluctuating velocities and probability density distributions.	Comparative measurements between hot-wire and pulsed-wire anemometry. Bubble length: 2 plate widths.
Chigier and Gilbert (1968)	Disc in 24^o divergent quarl. Blockage ratio: 0.43. Measurements of mean velocity and static pressure by impact probe. $Re \simeq 1.3 \times 10^6$.	Separation streamline trajectory and re-circulating mass flow rate. Bubble length: 1.26 diameters.
Davies and Beér (1971)	Annular jet flow over cylinder, 45^o cone and disc. Blockage from 0.11 to 0.54. Measurements by pressure probe and hot-wire anemometry.	Increasing baffle bluffness and blockage increases recirculating mass flow rate. Increasing blockage decreases bubble length from 2.2 (0.11 blockage) to 1.16 (0.54 blockage) diameters for disc.
Durão and Whitelaw (1978)	Annular jet flow over disc baffles with blockage from 0.2 to 0.5. Field measurements of mean velocity and turbulence intensity by laser-Doppler velocimetry. $Re = 8.6$ to 36.2×10^3.	Large anisotropy of centreline Reynolds stresses. Increasing blockage decreases recirculation length from 1.45 (0.2 blockage) to 1.00 (0.50 blockage) diameters.

TABLE 1.1 (CONTINUED)

Authors	Experiment	Findings
Durão, Founti and Whitelaw (1979)	Annular jet flow over disc baffles with 90^0 sector removed. Blockage: 0.50. Re = 7.5 to 17.3 x 10^3. Field measurements of mean velocity and turbulence intensity by laser-Doppler velocimetry.	Flow field skewed towards notch, and bubble length reduced relative to axisymmetric flow (1.1 versus 1.2 diameters). Anisotropy increased by notch.
Winterfeld (1965)	Confined flow over axisymmetric baffles (disc, 45^0 and 90^0 apex cone) for blockage up to 0.25. Measurements of bubble length and width and residence time by passive tracer. Re = 2 x 10^3 - 2.2 x 10^5.	Influence of blockage small (isothermal flow only), Increasing bluffness increases bubble length (2 diameters for 0.25 blockage disc) and decreases residence time.
Sullerey, Gupta and Moorthy (1975)	Confined flow over plane and axisymmetric baffles for blockage up to 0.25. Measurements of pressure and velocity by shielded hot-wire anemometer. Re = 1.1 - 5.0 x 10^4.	Location of minimum pressure suggested as characteristic length scale. For plane baffles, length decreases with minimum pressure (1.92 wedge heights for 0.25 blockage), opposite trend for axisymmetric baffles.
Schofield and Keeble (1975)	Confined flow over axisymmetric baffle in converging duct. Re ≃ 5 x 10^4. Field measurements of pressure and mean velocity and passive scalar concentration.	Mass and momentum exchange in shear layer are similar. Qualitative features similar to plane, non-ducted mixing layer flows.

TABLE 1.1 (CONTINUED)

Authors	Experiment	Findings
Fujii, Gomi and Eguchi (1978)	Confined flow over plane 60^{o} baffle with upstream nozzle. Blockage: 0.50, Re = 2.5×10^{5}. Field measurements of pressure and tracer gas concentration. Velocity measured by laser-Doppler velocimeter.	Nozzle blowing decreases bubble length from 1.9 to 1.5 baffle widths, and increases mixing of tracer gas with surrounding flow.
Etheridge and Kemp (1978)	Flow over a rearward facing step. Measurements of mean velocities, turbulence intensities and structural variables by laser-Doppler anemometry.	Length scale at reattachment increases at twice rate of a normal boundary layer. Recirculation length: approximately 5 step heights.
Moss, Baker and Bradbury (1977)	Flow over a rearward facing step. Re = 5×10^{4}. Measurements of mean flow (pulsed-wire), Reynolds stress (hot-wire) and surface pressure.	Strength of recirculation less than that behind flat plate. Maximum Reynolds stress occurs upstream of reattachment (approx. 5 step heights). High speed side of mixing layer resembles a plane, two-dimensional mixing layer.
Freeman (1975)	Flow in a sudden pipe expansion (2.1 : 1). Re = 3×10^{4}. Field measurements by laser-Doppler velocimetry.	Recirculation length: 2.3 pipe diameters.

TABLE 1.1 (CONCLUDED)

Authors	Experiment	Findings
Smyth (1979)	Unconfined flow over a disc mounted on a downstream sting. Re = 1.3×10^5. Field measurements by laser-Doppler velocimetry.	Recirculation length: 1.4 diameters. Maximum turbulence occurs around separation streamline.
Castro and Robbins (1977)	Flow over a surface-mounted cube for both uniform and sheared approach flow. Re = 2 to 10×10^4. Velocity measured by pulsed-wire anemometry.	Recirculation length smallest for turbulent, sheared approach stream. For flow approaching at 45^0, near wake dominated by vortices shed from top edges.
Crabb, Durão and Whitelaw (1978)	Flow over a surface-mounted, two-dimensional rib. Wall pressure distribution, field measurements of axial mean velocity and Reynolds stress by laser- Doppler velocimetry. Re = 2.7×10^4.	Length of rib (1 rib height) influences trajectory of separation streamline. Bubble length: 12 rib heights. Presence of significant turbulent fluctuation energy at discrete frequency.

TABLE 1.2

SUMMARY OF CITED CALCULATIONS OF ISOTHERMAL FLOW

Authors	Experimental Data	Findings
Pope and Whitelaw (1976)	Unconfined flow over a disc (Carmody, 1964) and annular jet flow of Durão and Whitelaw (1974).	Significant discrepancies between measurement and calculation (e.g. recirculation zone 30% too short and rate of wake decay too slow). Turbulence model type (k-ε or Reynolds stress) is less important than assumed radial velocity profile at trailing edge of baffle.
Leonard, Leschziner and McGuirk (1978)	Annular jet flow of Durão and Whitelaw (1978)	Third-order finite difference method proposed and applied to a step profile of a scalar. Comparison with 'upstream-differencing' shows reduced numerical diffusion. Use of third-order differencing in experiment results in increased sensitivity to changes in k-ε turbulence model as compared with upstream-differencing.
Leschziner and Rodi (1980)	Annular jet flow of Durão and Whitelaw (1978)	Skew-upwind and quadratic-upstream differencing schemes shown to result in improved solution over upwind-differencing. k-ε turbulence model modified to take account of the effect of streamline curvature on constant relating shear stress to shear strain. Discrepancy between experiment and calculations reduced.

TABLE 1.2 (CONCLUDED)

Authors	Experimental Data	Findings
Gosman et al (1979)	Flow in a (motored) reciprocating engine with an annular orifice inlet (Morse, Whitelaw and Yianneskis, 1978)	Calculations of annular jet trajectory, using k-ε model, particularly sensitive to assumed inlet flow angle. Rate of jet spread and decay too rapid.
Nielsen, Restivo and Whitelaw (1978)	Model of a ventilated room. Velocity measured by laser-Doppler velocimeter.	Precision of calculation is adequate for design purposes for ventilation slots which do not produce significant three-dimensional effects. k-ε model used.
Habib and Whitelaw (1978)	Confined coaxial jets in a sudden expansion. Velocity measured by laser-Doppler velocimeter.	Calculation provides close representation of measurements except in vicinity of recirculation in corner of sudden expansion. k-ε model used. Discrepancies in mean velocity do not exceed 15% of maximum value: velocity maximum, minimum and length of recirculation too small.
Durst and Rastogi (1977)	Flow over a plane, two-dimensional, confined, surface-mounted rib. Measurements by laser-Doppler velocimetry.	Calculation domain extended far upstream of rib. k-ε model used in separated flow, and both k-ε and k-$\langle uv \rangle$-ε models used downstream of reattachment. Flow development in region after reattachment poorly predicted because of errors in separated region. More advanced model does not offer worthwhile advantages over k-ε model.

TABLE 1.3

SUMMARY OF CITED COMBUSTING FLOW EXPERIMENTS

Authors	Experiment	Findings
Longwell et al (1949)	Flame extinction data as a function of mixture velocity, temperature and pressure and baffle shape and blockage (4% to 23%). Axisymmetric geometry; Re = 1.1 to 22 x 10^6.	Increasing mixture velocity and decreasing temperature narrows stability limits. Influence of pressure small. Streamlined trailing edges and smaller baffles narrow stability limits.
Barrère and Mestre (1954)	Flame extinction data as a function of mixture velocity and temperature for a number of baffle shapes. Plane, two-dimensional geometry; Re $\simeq$ 5 x 10^5.	Increasing mixture velocity and decreasing temperature narrows stability limits. Increasing bluffness and blockage increases limits. Drag of flameholder is less during combustion.
Williams et al (1949)	Flame extinction data as a function of mixture velocity and approach-stream turbulence for rod, multiple rod and gutter baffles. Blockage from 0.5% to 17%. Plane, two-dimensional geometry; Re from 150 to 10^5.	Increasing mixture velocity and increasing approach-stream turbulence narrows stability limits. Baffle shape unimportant; smaller blockage decreases limits.
DeZubay (1950)	Flame extinction data as a function of mixture velocity and pressure for blockage between 0.8% and 13%. Axisymmetric discs; Re = 90 to 680 x 10^3.	Increasing mixture velocity and decreasing size and pressure narrows stability limits.

TABLE 1.3 (CONTINUED)

Authors	Experiment	Findings
Wright (1959)	Recirculation bubble length and width as a function of blockage ratio (< 25%), subsonic Mach number and equivalence ratio. Plane baffles; Re = 8 to 37 x 10^4.	Length decreases with increasing blockage (7 baffle heights at 25% blockage), weakly dependent on Mach number and is shortest at stoichiometric conditions. At blow-off, 'characteristic mechanical time' is independent of blockage. Recirculation length longer for plane than axisymmetric baffles.
Wright and Zukoski (1962)	Flame width as a function of equivalence ratio, approach stream temperature, velocity and fuel type. Circular cylinders used for blockage up to 33%; Re = 3.8 to 12.7 x 10^5.	Rate of spreading from baffle is independent of equivalence ratio, etc., as long as flame is turbulent and flow is subsonic. Spreading also independent of blockage.
Bovina (1958)	Residence time as a function of approach stream velocity, turbulence and equivalence ratio. Baffles were 30^0 apex plane wedges with blockage from 0.22 to 0.66. Re = 1.2 to 9.6 x 10^6.	Residence time is inversely proportional to velocity, increases with turbulence and is independent of equivalence ratio. Time is proportional to baffle blockage.
Winterfeld (1965)	(See also Table 1.1). Recirculation length and residence time as a function of approach stream velocity, equivalence ratio, blockage ratio and baffle shape.	Recirculation length increases with velocity, minimum at stoichiometric conditions, decreases with blockage and increases with bluffness (length between 2½ and 3 diameters for 25% blockage). Residence time increases in presence of combustion, decreases with velocity and is independent of blockage.

TABLE 1.3 (CONTINUED)

Authors	Experiment	Findings
Howe, Shipman and Vranos (1963)	Density, velocity and mass fraction profiles for 3 approach velocities in far-wake. Cylindrical baffle in rectangular duct. Re = 5 to 30 x 10^4; blockage 3.5 and 7%.	Profiles of turbulent mass transfer coefficients and reaction rates. Reaction controlled by flow than by chemical kinetics.
Lewis and Moss (1978)	Power spectral density and probability density function of density gradient, temperature and positive ion current in far-wake. Cylindrical baffle in rectangular duct (blockage 7%). Re = 1 to 3 x 10^4.	Measurements of large scale ordered structures. Findings compatible with description of turbulent flame zone as comprising narrow burning regions embedded in extensive regions of burnt and unburnt gas.
Harrison (1973, 1974)	Measurements of velocity and chemical composition. Annular, 30^0 vee-gutter mounted in circular duct (28% blockage). Re = 8.3 to 25 x 10^6.	(Cited by Pope, 1976).
Elliman et al (1978)	Measurements of mean velocity, temperature and local equivalence ratio. Diffusion flame stabilised on an axisymmetric baffle in a duct of 67% blockage. Re = 5 to 8 x 10^4.	Comparison with numerical analysis shows that models of turbulence and mixing give results of use in design. Recirculation length: one baffle diameter.

TABLE 1.3 (CONCLUDED)

Authors	Experiment	Findings
Clare et al (1976)	Laser-Doppler velocimetry used and measurements of fluctuating wall pressure and high speed Schlieren photography. Plane, 45^0 gutter used as baffle: 25% blockage. Re = 7.2×10^4.	Recirculation length four gutter heights. Velocity probability density function measured in presence and absence of combustion-induced oscillations. No bi-modal distributions found.
Durão and Whitelaw (1977)	Measurements of centreline axial velocity, Reynolds stress and probability density distributions by laser-Doppler velocimetry. Unconfined, disc stabilised premixed and diffusion flames attached to a 50% blockage baffle. Re = 2.9 to 5.3×10^3.	Recirculation lengths for isothermal, premixed and diffusion flames are similar at about one baffle diameter. Reynolds stress in flames is smaller than for isothermal flow: diffusion flames result in larger values than pre-mixed flames.

CHAPTER II

EXPERIMENTS IN ISOTHERMAL FLOWS

2.1 Introduction

This chapter describes experiments made in isothermal flows to obtain detailed field measurements of the mean velocity and corresponding Reynolds stresses in axisymmetric, confined, turbulent flows. The flow examined is that of water flow past a baffle in a pipe, with three separate baffles being investigated: a disc presenting an area blockage of 25 per cent, a cone of 25 per cent blockage and a disc of 50 per cent blockage. In this way a comparative study can be undertaken on the influence of the forebody shape of the baffle and the area blockage on, for example, the size of the recirculation zone and the intensity of the turbulence which is generated.

The following section gives details of the experimental method and considers, in turn, the flow configuration, the laser-Doppler velocimeter and the errors incurred in the measurements. The subsequent section, 2.3, presents the mean flow velocities and Reynolds stresses for each baffle and is followed by a discussion, in section 2.4, of the influence of the baffle forebody shape, blockage and the effect of confinement downstream of the baffle. The final section, 2.5, presents a summary of the main findings and conclusions of the experimental programme.

2.2 Experimental method

2.2.1 Flow configuration

The baffles, which are described below, were inserted in a water tunnel, which is shown schematically in figure 2.1, whose working

section was formed by a Perspex pipe (50.27 ± 0.5 mm diameter, 5 mm thickness). The use of water, rather than air, as the working fluid has two advantages when using laser-Doppler velocimetry. Water is naturally laden with particles which are suitable for use as scattering centres, so that seeding of the flow is unnecessary. Secondly, the required Reynolds numbers can be achieved at bulk velocities of about 1 m/s, which corresponds to Doppler frequencies, together with light frequency shifting (see 2.2.2 below), of a few megahertz which can be conveniently demodulated by a frequency tracker. The use of air would result in frequencies larger by one order of magnitude which are too great for use with a frequency tracker (see, for example, Chapter IV). The length of pipe upstream of the baffle (22 hydraulic diameters) was sufficiently long to establish a turbulent flow, while the downstream length (22 hydraulic diameters) was sufficiently long to remove any influence of the discharge tank on the flow immediately behind the baffle. The flow rate through the tunnel was established by the pressure difference between the constant head and discharge tanks. The flow conditions and the Reynolds numbers for each baffle are summarised in table 2.1.

Optical access to the working section was primarily limited by refraction at the curved wall of the pipe. The subject is considered at greater length in subsection 2.2.2 below, but for the moment it is noted that the working section of the pipe was immersed in a plane-walled water trough which improved the access.

The two forebody shapes of the baffle were those of a disc and a cone of 45 degrees included angle, both of 25 per cent area blockage. The details of the three baffles are illustrated in figure 2.2(a), and figure 2.2(b) shows the co-ordinate system adopted in this chapter. The factors determining the choice of shape included the

TABLE 2.1

BLOCKAGE, BULK VELOCITY AND REYNOLDS NUMBER FOR ISOTHERMAL EXPERIMENTS

SHAPE	AREA BLOCKAGE RATIO (%)	ANNULAR BULK VELOCITY (m/s)	REYNOLDS NUMBER
Disc	25	1.37	34 700
Cone	25	1.53	38 700
Disc	50	1.62	57 400

NB (i) annular bulk velocity refers to bulk velocity at the trailing edge of the baffle.

(ii) the Reynolds number is based on the annular bulk velocity and the diameter of the baffle.

provision of a single, well-defined surface discontinuity from which the separation streamline would originate. This requirement leads to the use of a leading-edge chamfer on the disc (see figure 2.2(a)). A further restriction was the ease of description of the flow field boundaries for the numerical method, presented in Chapter III, which precluded the use of, for example, a 'vee-gutter' shape. The influence of blockage was examined by the use of a disc baffle that resulted in a 50 per cent blockage.

Each baffle was positioned by four radial pylons abutting against the sting which was attached to the upstream face of each baffle, as shown in figure 2.2(a). The pylons were streamlined plates, 76 mm long and 2 mm thick, and could be moved radially by fine screw threads. The accuracy with which each baffle could be centred was better than 0.3 mm.

2.2.2 Velocimeter configuration, Doppler signal processing and measurement technique

Velocimeter configuration

The optical arrangement of the laser-Doppler velocimeter, which was designed and constructed for the measurements of this chapter, is shown in figure 2.3. It operated in a symmetric heterodyne, forward-scatter mode with light 'frequency shifting' provided by the rotation of a radial diffraction grating. The principles and practice of laser-Doppler velocimetry are well documented in a number of texts (e.g. Durst, Melling and Whitelaw, 1976) and so only the features and advantages of the present design are indicated here.

The provision of direction sensitivity in the velocimeter is essential in flows with regions of recirculation. It is allowed for by arranging a frequency difference, or shift, between the two beams which form the symmetric heterodyne velocimeter: a comprehensive review of frequency shifting techniques is available in the literature (Durst and Zaré, 1974). For the magnitude of the Doppler frequencies encountered in these experiments (several hundred kilohertz), the frequency shift is conveniently derived from the frequency difference between the first order maxima of a rotating radial diffraction grating. The grating acts both to provide the frequency shift and as a beam splitter to create the two 'channels' of the velocimeter (see figure 2.3). Frequency shifting confers two further advantages concerning the demodulation of the Doppler signal. Frequency shifting increases the separation, in frequency space, between the Doppler-shift frequency and the 'pedestal' frequency (the frequency component associated with the time of flight of a scattering centre across the light beams): this is important in regions where the flow lies at large angles to the sensitivity vector of the velocimeter (Durst and Zaré, 1974). The second advantage has

to do with being able to select a range of the Doppler frequency demodulator which can accommodate the spread (due to turbulence) of the velocity probability density distribution at every point in the flow. The selection of a suitable range is made possible by varying the magnitude of the frequency shift which is applied (see also below under "Doppler signal processing").

The transmission phase diffraction grating used was manufactured by the Technische Physische Dienst tno-th, Holland, designated 'type H'. The principal characteristics are summarised in the following table: further information is given by Oldengarm, van Krieken and Raternik (1976).

TABLE 2.2

PRINCIPAL CHARACTERISTICS OF THE RADIAL DIFFRACTION (TRANSMISSION PHASE) GRATING

Number of line pairs (N)		16384
Spacing	(μm)	6.08 (± 0.14)
Diffraction angle for first order maxima for wavelength of 632.8 nm	(degrees)	5.98 (± 0.14)
Disc diameter	(mm)	35
Efficiency of diffraction for first order maxima	(each)	25 - 30 %
Nominal speed of rotation (Ω)	(r.p.m.)	3360
Long term stability		0.1 %
Short term stability (δΩ)	(r.m.s.)	0.2 %
Shift frequency	(MHz)	1.8

The velocimeter incorporates three lenses which are shown in figure 2.3. The position of the measuring volume, which is formed by

lens L_3, is determined by geometrical optics and so is independent of the position of lens L_1. In contrast, diffraction phenomena determine the uniformity of the 'fringe spacing' within the ellipsoidal measuring volume (Hansen, 1973) and the latter's size, which is of great importance in estimating the "Doppler broadening" (see subsection 2.2.3). The greatest uniformity of the fringe spacing and smallest size of the measuring volume occur when the beam waist (Kogelnik and Li, 1966) coincides with the measuring volume and lens L_1 is placed so as to achieve this condition. The measuring volume then has the form of an ellipsoid with major (b_y) and minor (b_x) axes, defined at the e^{-2} level of intensity, of length:-

$$b_x = \frac{b}{\cos \theta} \tag{2.1}$$

$$b_y = \frac{nb}{\sin \theta} \tag{2.2}$$

with:-

$$b = \frac{4\lambda f_1 f_3}{\pi b_o f_2} \tag{2.3}$$

(The dimensions b_x and b_y are defined in the insert on figure 2.3). The fringe spacing (δx) is:-

$$\delta x = \frac{\lambda}{2 \sin \theta} \tag{2.4}$$

The table on the following page summarises the principal characteristics of the laser-Doppler velocimeter.

TABLE 2.3

PRINCIPAL CHARACTERISTICS OF
THE LASER-DOPPLER VELOCIMETER

5 mW, He-Ne laser	λ = 632.8 nm
Focal length of lenses:	
L_1 (nominal)	f_1 = 150 mm
L_2 (nominal)	f_2 = 300 mm
L_3 (nominal)	f_3 = 200 mm
Beam diameter, b_0, at e^{-2} intensity, of laser	0.65 mm
Measured half-angle of intersection, θ, (in air)	9.09 degrees
Calculated half-angle of intersection (in water)	6.82 degrees
Fringe separation (line pair spacing)	2.003 μm
Calculated dimensions of measuring volume (in water):	
b_x	0.13 mm
b_y	1.34 mm
b_z	0.12 mm
Calculated number of fringes within e^{-2} intensity level	63
Velocimeter transfer constant, K^{-1}	0.499 MHz/ms^{-1}

Doppler signal processing

The Doppler signals were detected by a photomultiplier tube (E.M.I. 9558) and demodulated by a frequency tracker (Cambridge Consultants CC01). The mode of operation of this tracker is outlined below in sufficient detail to describe the precautions taken for correct signal demodulation.

The tracker is based on the autodyne tracking filter

described by Durrani, Greated and Wilmshurst (1972). The tracker consists of the tracking filter, a direct frequency discriminator and a voltage-controlled oscillator connected to form a feedback loop. The centre frequency of the tracking filter is the same as the frequency of the voltage-controlled oscillator, which is used to tune the filter. The type of discriminator employed acts so as to drive the oscillator frequency to the first moment of the input-signal power spectrum. The output of the tracker is the voltage level of the oscillator. The advantage of using a direct frequency discriminator, rather than phase comparison used in offset heterodyne systems, is that a single lag feedback-loop can be used. This confers greater stability than higher-order loops and allows the tracking of rapid velocity changes (i.e. high frequency slew rate).

The concentration of the naturally-occurring scattering centres, which give rise to Doppler signals, in water is such that the probability of finding more than one particle in the measuring volume of the velocimeter is negligibly small: hence the occurrence of Doppler signals is a discrete, rather than a continuous, process and the correct operation of the tracker depends on being able to distinguish the presence of a suitable signal from the noise base line and to accommodate both the magnitude ('capture range') and the rate of change ('slew rate') in Doppler frequency from one scattering centre to the next. The following paragraph briefly considers each of these three points.

The criterion of a suitable signal is based on comparing the amplitude of the signal at the input with that of a variable-level comparator. The level of the comparator is set so that this is larger than the noise level at the input. In the absence of a suitable signal the feedback loop is broken and the oscillator output is held constant

at the level of the last valid signal. The capture range of the tracker was very large, owing to the design of the frequency discriminator, and was not a limiting factor. A related restriction is that of 'tracking range' (in this case 0.7 to 15.0 MHz) which requires that the Doppler frequency to be demodulated lies within the selected tracking range at all times. This can be expressed as a maximum permissible turbulence intensity, which is a function of the mean Doppler frequency (as quantified by Durst, Melling and Whitelaw, 1976, page 228). This maximum is a potentially important limitation for the flows of this chapter which are highly turbulent. The use of frequency shifting, as described above, resulted in turbulence intensities (expressed as a r.m.s. Doppler frequency fluctuation divided by the mean Doppler frequency) which were sufficiently low ($\lesssim$ 15 per cent) to be within the maximum permissible turbulence intensity. In principle, the slew rate of the instrument can limit the temporal rate of change in Doppler frequency which can be tracked. The design of the feedback loop, referred to above, results in a high value of the slew rate (0.5 MHz/μs) for the range (1 - 10 MHz) used. This corresponds to tracking turbulent frequencies up to about 100 KHz, which is much larger than the highest energy containing motion expected in the flows of this chapter.

The analogue output of the tracker has a noise component associated with it, so that even if a continuous sine wave of constant frequency is applied to the tracker input, the output has a small root mean square component, referred to as 'instrument noise' in subsection 2.2.3. Further noise is introduced during the capture of discontinuous input signals and it is advantageous to operate away from the lower end of each frequency range of the tracker.

The output of the tracker was processed to give the mean

velocity, Reynolds stresses and the power spectral density of the turbulent fluctuations as shown in figure 2.4, the implication being that the output of the tracker is a good representation of the instantaneous velocity at the measuring volume. The previous paragraph has shown, however, that the output level of the tracker changes as a discrete process. The condition under which the output is a good analogue of a continuous signal (for the purposes of evaluating the time mean and variance of velocity) have been discussed by, for example, Dimotakis (1976) and Owen and Rogers (1975). The requirement that must be met is:-

$$\tau_s \, |U_c| < \delta \qquad (2.5)$$

where:-

τ_s is the mean time between valid signals.

$|U_c|$ is the magnitude of the mean convecting velocity.

δ is the large-structure length scale.

For the experiments reported in this chapter, $\tau_s \simeq 2.5$ ms, $|U_c| \simeq 0.5$ ms^{-1}, suggesting that structures of the order of 1 mm and above can be resolved. This is about an order of magnitude less than the largest length scales in the pipe, which implies that the energy containing motions are resolved by the tracker. The frequency response of the velocimeter is limited by the mean arrival frequency ($1/\tau_s$ Hz) of the scattering particles. If this frequency is considered as a sampling frequency, then the power spectral density can be reconstructed up to $1/2\ \tau_s$ Hz, or about 200 Hz.

Measurement technique

The optical orientation of the velocimeter is shown in figure 2.5 for the measurement of axial, radial and azimuthal velocities. The difference in the refractive indices of the working fluid (n = 1.33) and the pipe material (n = 1.49) gives rise to the refraction of the laser beams on passing from one medium to the other, resulting in the displacement of the measuring volume and, with the exception of the arrangement for axial velocities downstream of the baffles, changes in the transfer function (see equation (2.6) below). The effects of refraction at the external surface of the pipe were reduced by immersing the pipe in a water trough. Thus, the change in refractive index, and hence also the degree of refraction, on passing from the surrounding water (n = 1.33) to the Perspex (n = 1.49) is smaller than it would have been in the absence of the trough. The position of the measuring volume and the associated changes in the transfer function were calculated by an extension of the analysis of Kirmse (1974), and was typically found to be about 1 per cent of the undisturbed value.

A limitation lay in the measurement of radial velocity, which became progressively more difficult as the measuring volume approached the pipe wall because of the increasing refraction and dispersion at solid-liquid interfaces. The furthest position at which values could be reliably obtained corresponded to about 0.8 (r/R). The deterioration in the signal quality of radial velocity as the measuring volume lies further off axis impairs the reliability of demodulation. As a consequence some values far from the pipe axis have been deleted in the presentation of section 2.3 on the grounds that they were unreliable. A further restriction imposed by the curved pipe surface was that quantification of the cross correlation,

<uv>, was unfeasible. When using a single-channel velocimeter, this correlation is obtained by measuring the mean-square fluctuations in three directions; say the axial, radial and one at 45 degrees to the pipe's axis. For circular pipes, skew-symmetric refraction of each beam of the velocimeter occurs in planes outside those whose normal is not parallel or perpendicular to the pipe's axis, and hence a measuring volume is no longer formed. Without measurements in such planes, it is not possible to determine <uv> and this represents a limitation of the laser-Doppler velocimeter in such flows. In contrast, the measurements of axial velocity (downstream of the baffle) and azimuthal Reynolds stress were virtually unaffected by these considerations and values could be obtained throughout the width of the pipe.

2.2.3 Data reduction and error estimates

This section begins by presenting the equations relating the mean velocity and Reynolds stress to the Doppler frequency. The sources of broadening of the velocity probability density are then introduced and quantified. Estimates of the systematic and random errors of measurement conclude the sub-section.

Velocity∿Doppler frequency relation

The instantaneous relation between the velocity of a scattering centre (assumed to be identical with that of the associated fluid particle) and its Doppler frequency is:

$$\tilde{U} = \tilde{f}_v \frac{\lambda/n}{2 \sin \theta} \equiv K\tilde{f}_v \qquad (2.6)$$

Tap water contains scattering centres of a sufficiently small size for the above assumption to be a good one (see Durst, Melling and Whitelaw, 1976, Chapter 10). Equation (2.6) indicates that the transfer function of the velocimeter within the pipe is different from that in air because of the change in refractive index, n, and the change in the intersection angle, θ. The exception to this general result is the arrangement shown in figure 2.5(a), where the change in the velocity of light is exactly balanced by the change in the intersection angle. The frequency observed by the photomultiplier is:-

$$\tilde{f}_p = |f_s \pm \tilde{f}_v| \tag{2.7}$$

where the modulus sign indicates that only positive frequencies exist and the value of the sign is determined by the direction of the frequency shift, known a priori. The frequency shift applied by the grating is, for the first order maxima:-

$$f_s = 2N\Omega \tag{2.8}$$

where Ω is the angular velocity of the rotating grating, in hertz. The time-mean velocity is thus:-

$$U = \langle\tilde{U}\rangle = K \cdot \langle\tilde{f}_v\rangle \tag{2.9}$$

and the corresponding variance (Reynolds stress/density) is:-

$$\langle u^2\rangle = K^2 \cdot \langle\{\tilde{f}_v - \langle\tilde{f}_v\rangle\}^2\rangle \tag{2.10}$$

Doppler broadening

The Doppler-frequency probability density is affected by sources other than true velocity fluctuations at a point. These sources include the influence of mean velocity gradients across the measuring volume, finite transit time broadening, turbulent velocity fluctuations within the measurement volume, instrument noise (see 2.2.2; Doppler signal processing) and short-term fluctuations in the rotation of the grating; these are generally referred to as non-turbulent Doppler broadening. Full accounts of these sources are to be found in the literature, such as Durst et al (1976), and are not given here. The net effect is that the distribution is broader than that of the velocity. The sources of broadening are summarised in table 2.4, together with formulae for their magnitude and estimates of the contribution in the flows of this chapter. In principle, these estimates should be used to correct the measured values; in practice the values in table 2.4 are sufficiently small for their effect to be neglected.

Measurement errors

Apart from non-turbulent Doppler broadening, errors arise in the evaluation of the mean velocity and variance (Reynolds stress) through the averaging of voltages corresponding to Doppler frequencies (voltage output of mean and r.m.s. meters), in the conversion of these voltages to Doppler frequencies (tracker output transfer function) and from Doppler frequencies to velocities (equation (2.6)). The accuracy (systematic error) of the voltage output of the tracker (which affects the mean voltage) is quoted by the manufacturer as 1 per cent of full scale deflection, which corresponds to about 0.15 U_o. This error can, however, be removed by calibration to the level of the random error

TABLE 2.4

SOURCES AND MAGNITUDE OF NON-TURBULENT DOPPLER BROADENING

SOURCE	EFFECT ON	FORMULA	REFERENCE	MAGNITUDE
Gradient of mean velocity	mean (m/s)	$\langle U_v \rangle - U \approx \frac{1}{2}\left(\frac{b_y}{4}\right)^2 \left(\frac{\partial^2 U}{\partial r^2}\right) + \frac{1}{8}\left(\frac{b_y}{4}\right)^4 \left(\frac{\partial^4 U}{\partial r^4}\right) + \ldots$ where $\langle U_v \rangle$ is the velocity averaged over the measuring volume	Melling (1975)	$\approx 10^{-4}\ U_o$
	variance ($m^2 s^{-2}$)	$\approx \left(\frac{b_y}{4}\right)^2 \left(\frac{\partial U}{\partial r}\right)^2 + \frac{1}{2}\left(\frac{b_y}{4}\right)^4 \left(\frac{\partial^2 U}{\partial r^2}\right)^2 + \ldots$	Melling (1975)	$\approx 10^{-3}\ U_o^2$
Finite transit time	variance ($m^2 s^{-2}$)	$\left[\frac{U/2\pi}{2\ (b_x/4)} \cdot \frac{\lambda}{2 \sin \theta}\right]^2$	George and Lumley (1973)	$\approx 2 \times 10^{-5}\ U_o^2$
Velocity fluctuations within measuring volume	variance ($m^2 s^{-2}$)	Taken as comparable to magnitude of mean velocity gradient or transit time broadening	Melling (1975)	
Tracker instrument noise	variance ($m^2 s^{-2}$)	From direct measurement	Durão and Whitelaw (1974)	$(1.2 \times 10^{-2})^2$ ($m^2 s^{-2}$)
Grating jitter (short term stability, table 2.2)	variance ($m^2 s^{-2}$)	$= \left[\delta\Omega\ f_s \frac{\lambda}{2 \sin \theta}\right]^2$	Manufacturer's specification	$(7.2 \times 10^{-3})^2$ ($m^2 s^{-2}$)

in the measurement of mean velocity. It is assumed that the systematic error originates as an offset in the calibration curve of the tracker output. The voltage output of the tracker is:-

$$\tilde{E}_T = (\tilde{f}_v + f_s)\, G + \varepsilon_o \qquad (2.11)$$

where:-

$\tilde{E}_T$ is the tracker voltage output.

G is the transfer function from hertz to volts.

ε_o is the offset voltage giving rise to systematic errors.

If the direction of the frequency shift is reversed (and providing that the passband of the demodulator is not exceeded) then, assuming $f_s > f_v$:-

$$\tilde{E}_T' = (f_s - \tilde{f}_v)\, G + \varepsilon_o \qquad (2.12)$$

Hence:-

$$\varepsilon_o = \frac{\tilde{E}_T + \tilde{E}_T'}{2} + Gf_s \qquad (2.13)$$

and thus the systematic error is reduced to the precision (random error) of measuring $\tilde{E}_T$ and $\tilde{E}_T'$, which results in the systematic error for U and V quoted in table 2.5. The value of the mean voltage is further limited by the random error of the mean meter which was ± 1 per cent of the value. Other sources of systematic errors include the measurement of the beam intersection angle and the departure from linearity of the tracker transfer function (G, equation (2.11)); these

are, however, small in comparison to those already considered. The calculation of the variance of velocity was made by squaring the measured r.m.s. velocity fluctuation. The random error in the output of the r.m.s. unit (figure 2.4) was 1 per cent of full scale deflection, corresponding to a maximum of 3 per cent of the smallest value measured on any one range. The largest and smallest errors in the variance of velocity, and hence turbulent kinetic energy, are given in table 2.5. The errors associated with the location of the measuring volume (x and r) and the measurement of the manometer fluid height, for wall static pressure, are also given.

TABLE 2.5

SYSTEMATIC AND RANDOM ERRORS IN MEASURED QUANTITIES

QUANTITY	SYSTEMATIC ERROR	RANDOM ERROR
U, V	0.04 U_o	± 2%
$\langle u^2 \rangle$, $\langle v^2 \rangle$, $\langle w^2 \rangle$	nil	± 2% to ± 6%
k, turbulent kinetic energy	nil	± 3% to ± 9%
x	0.25 mm	± 0.02 mm
r	0.03 mm	± 0.03 mm
θ	0.05 degrees	nil
h, manometer fluid height	0.5 mm	± 0.5 mm $\left(\equiv \pm 0.003 \left(\frac{1}{2} \rho U_o^2 \right) \right)$

The r.m.s. error in values of the power spectral density of turbulent fluctuations, presented in sub-section 2.3.2, is given by

(Anon., 1972):-

$$\frac{1}{\sqrt{BT}} \qquad (2.14)$$

where:-

B is the spectrum analyzer bandwidth in hertz.

T is the averaging time in seconds.

The experiment was made using a 1/10 octave filter for which:-

$$B = 0.069 \times \{\text{centre-frequency}\} \qquad (2.15)$$

The largest errors occur at the smallest centre-frequencies; for example at 25 hertz, with an averaging time of 100 seconds, the r.m.s. error is 7.5 per cent.

2.3 Results

The results are considered under two headings; the first presents profiles of mean velocity and wall pressure and the second considered profiles of Reynolds stress and the spectra of turbulent fluctuations. Each baffle is considered separately under each heading, while a detailed discussion of the results is reserved for section 2.4.

2.3.1 Profiles of mean velocity and wall pressures

Disc, 25 per cent blockage

Fig. 2.6 presents radial profiles of axial velocity

for stations upstream and downstream of the trailing edge of the baffle. The profiles upstream, at x/R = - 0.84 and - 0.20, show a rapid deceleration of fluid closest to the sting as the baffle is approached accompanied by a corresponding acceleration towards the annular region formed by the space between the baffle and the confining pipe wall. The profile at x/R = 0.02, which was the closest to the trailing edge that measurements could be made, indicates that the maximum velocity lies close ($\simeq$ 0.14 r/R) to the baffle tip, which is at r/R = 0.50. This is reminiscent of the inviscid solution for the flow over a sphere and suggests that the upstream flow is dominated by pressure gradients.

Downstream of the baffle, profiles could be obtained over the whole width of the pipe: asymmetries in the profile are within the systematic error of positioning the measuring volume (see table 2.5). A further check on the consistency of the profiles was made by evaluating the mass flow rate on either side of the axis of symmetry of the pipe. The mass flow rate shows a scatter of about 5 per cent about the mean, with the exception of the profile for x/R = 0.02 which was 10 per cent smaller than the mean. The increased error is associated with the greater curvature of the profile, giving rise to larger errors in numerical integration.

The development downstream of the baffle can be conveniently summarised by inspection of the profile of centreline axial velocity and the streamline pattern. Fig. 2.7 shows the centreline axial velocity and indicates the region of reversed velocity in the lee of the baffle, which extends for 1.75 x/R, and the subsequent development as the wake profile reforms towards that of a pipe flow. Figure 2.8 shows the streamline pattern corresponding to the profiles of figure 2.6. The plots were constructed by evaluating the stream function:-

$$\psi\ (x,\ r) \equiv \int_0^r \rho U\ (x,\ r)\ r\ dr \qquad (2.16)$$

with $\psi\ (x,\ r = 0) \equiv 0$, for each side of the pipe axis, obtaining the position of a given stream function value by linear interpolation and drawing the contour levels. These plots were made using a procedure described by Vlachos (1977). For reasons concerned with this procedure, the profiles of figure 2.6 were (linearly) interpolated onto a uniformly spaced radial grid; other than this, no data manipulation has been applied. Only minor irregularities are evident, such as the shape of the streamlines closest to the pipe wall. The maximum width of the recirculation bubble is 0.62 R, indicating that the mean blockage presented by the recirculation bubble is greater than that of the baffle. Hence fluid accelerates up to the maximum blockage presented by the bubble, for reasons of continuity of mass, and this can be seen in the profiles of figure 2.6.

The mean streamline pattern of figure 2.8 is qualitatively confirmed by figure 2.9 which presents photographs of the result of flow visualization using the hydrogen bubble technique. Figure 2.9(a) shows the streaklines of fluid originating upstream of the trailing edge of the baffle and the trajectory of the separation streamline over the recirculation bubble. Figure 2.9(b) is the result of placing the electrode near the rear stagnation point; the width of the re-circulation bubble estimated from this photograph is close to that obtained from figure 2.8. The final photograph, figure 2.9(c), shows the 're-entrant jet' which was visualized by placing the electrode close to the position of maximum reversed velocity.

The magnitude of the recirculating mass flow rate is an interesting quantity because it conveniently summarises the influence

of the size of the recirculation bubble and the turbulent transport within it. Figure 2.10 plots the magnitude of the maximum negative value of the stream function ψ (x, r), as a function of axial location, x: the value has been normalised by $\dot{m} \equiv \rho U_o \pi d^2/4$, rather than by the mass flow rate through the pipe, because this definition remains useful in the limit of vanishingly small blockage.

If $\dot{m}_o$ is the total mass flow rate through the pipe, then $\dot{m}$ and $\dot{m}_o$ are related by:-

$$\dot{m} = \frac{\dot{m}_o}{1 - \alpha} \tag{2.17}$$

where α is the area blockage presented by the baffle.

Figure 2.11 displays the locus of the separation streamline. As already noted the flow outside the recirculation bubble must accelerate to flow over the maximum bubble width. For qualitative analysis, the drop in pressure due to this acceleration can be estimated by applying Bernoulli's equation to streamlines outside the separation streamline. The assumptions made include being able to assign uniform values of pressure and velocity across the planes containing the trailing edge of the baffle and the maximum width of the recirculation bubble. Hence the magnitude of this fall is approximated by:-

$$\frac{p_m - p_o}{\frac{1}{2}\rho U_o^2} = 1 - \frac{(1 - \alpha)^2}{(1 - W^2/R^2)^2} \tag{2.18}$$

where:-

p_m is the minimum wall pressure.

p_o is the wall pressure in the plane containing the trailing edge of the baffle.

W is the maximum width of the separation bubble, figure 2.2(b).

Figure 2.12 shows measurements of the wall pressure which confirm the expectation expressed in equation (2.18). For the purposes of comparison the fall in pressure predicted by equation (2.18), with the value of W taken from figure 2.11, is also given on the figure. The pressure recovery in the downstream region may be compared to the 'Borda-Carnot' pressure rise coefficient:-

$$C_p \equiv \frac{p_d - p_o}{\frac{1}{2}\rho U_o^2} = 2\alpha \left[1 - \alpha\right] \qquad (2.19)$$

where p_d is the value of the pressure recovered far downstream. Formula (2.19) is derived by applying the conservation of mass and momentum and assuming one-dimensional profiles of velocity and pressure and neglecting friction and fluctuation terms. The effect of friction can be estimated by comparing the Borda-Carnot pressure rise with that estimated from figure 2.12. This shows that about one-third of the expected recovery is lost, a result which is in agreement with other flows with recirculation (Johnston, 1976).

Radial profiles of radial velocity are presented in figure 2.13. Immediately upstream of the baffle (at $x/R \simeq -0.20$) the magnitude of radial velocity is larger than $0.5\ U_o$ because of the large streamline curvature as the flow approaches the baffle. These relatively large values are present at the trailing edge of the baffle but decay very rapidly downstream of this station and this is confirmed by the trajectory of the streaklines in figure 2.9(a).

Comparison between the sign of the radial velocity far downstream of the baffle and the direction of the streamlines in figure 2.8 suggests the presence of a systematic error of the order expected from the error analysis presented in subsection 2.2.3. The random error of the measurements is uninfluenced by the systematic error and this can be seen from the lack of scatter in the data. A further check on the consistency of the data is the comparison between the sign of $\partial U/\partial x$ and $\partial V/\partial r$ on the centreline because there:-

$$\frac{\partial U}{\partial x} = -2\frac{\partial V}{\partial r} \qquad \text{(by continuity)} \qquad (2.20)$$

Thus in figure 2.7, $\partial U/\partial x$ changes sign at $x/R \simeq 1$ which agrees with the change of sign of $\partial V/\partial r$ in figure 2.13 between $x/R = 0.80$ and 1.60. For subsequent comparison, the angle of the streamline to the pipe axis, at the trailing edge of the baffle, is given in figure 2.14. The very steep angle close to the baffle tip ($r/R = 0.5$) is in accordance with the flow visualization of figure 2.9(a).

Cone, 25 per cent blockage

The radial profiles of axial velocity for the cone of 25 per cent blockage are depicted in figure 2.15. The profile upstream of the baffle at $x/R = -0.80$ suggests, in comparison with the corresponding profile in figure 2.6, that the disturbance of the flow is less than for the disc. This result is expected because of the faired forebody shape of the cone. The shape of the profile close to the trailing edge of the baffle, at $x/R = 0.02$, is similar to that of the disc although the maximum velocity lies closer to the baffle tip (at $r/R = 0.50$).

The profiles downstream of the baffle show a similar develop-

ment to that of the disc and the symmetry is of the same quality. Reference to figure 2.7, which shows the centreline velocity profile, indicates that the recirculation length ($x/R \approx 1.55$) is smaller than for the disc, as is the maximum reversed velocity. It is noted that the decrease in length is associated with a decrease in the length to the occurrence of maximum reversed velocity; the latter has been used as a characteristic length scale of the near wake by Calvert (1967) and Sullerey et al (1975). The results shown in figure 2.7 suggest that this similarity is only approximate.

Figure 2.16 presents the mean streamline pattern which was plotted in the same manner as figure 2.8. The maximum negative value of the stream function, which is derived from the stream function data of figure 2.16, is given as a function of axial distance in figure 2.10. The magnitude is smaller at any given axial station than for the disc, which is partly the result of the smaller reversed centreline velocity and partly the result of a narrower recirculation bubble. The locus of the separation streamline is redrawn in figure 2.11 which shows the maximum width of the recirculation bubble to be smaller, at 0.55 R, than that of the disc. A consequence of the smaller width is that the minimum wall static pressure, figure 2.12, is correspondingly smaller. The downstream pressure recovery is faster and suggests that the loss to friction is less than for the disc.

Figure 2.17 shows the radial profiles of radial velocity upstream and downstream of the baffle. The smaller disturbance of the radial profiles of axial velocity, figure 2.15, have their counterpart in the smaller values of radial velocity. This is particularly reflected in the values at $x/R = 0.02$ which are about half those of the disc. The resulting streamline angles at this station, figure 2.13, are thus smaller. The magnitude of the systematic error is similar to

that of the disc and, as before, the signs of $\partial U/\partial x$ and $\partial V/\partial r$ on the centreline are consistent.

Disc, 50 per cent blockage

The radial profiles of axial velocity, and the corresponding streamline pattern, are drawn in figures 2.18 and 2.19 respectively: as before, asymmetries are within experimental error. The centreline velocity profile in figure 2.7 shows that although the magnitude of the minimum centreline velocity is similar to the 25 per cent blockage disc the recirculation length ($x/R = 3.05$) is longer, irrespective of whether this is normalised by the radius of the confining pipe (74 per cent) or the diameter of the baffle (26 per cent), figure 2.38. Figure 2.10 shows the variation of the maximum negative stream function with axial distance. The figure shows that the recirculating mass flow rate is substantially larger than that of either of the other two baffles.

The maximum width, W, of the recirculation zone can be estimated from figure 2.11 to be between 0.76 R and 0.80 R, with the uncertainty arising because of asymmetry in the measured velocity profiles. The resulting pressure drop at the wall, up to the position of maximum blockage, is shown in figure 2.12. Agreement with the calculated minimum pressure, equation (2.18), is fair considering that the sensitivity to even small errors in W is very great.

Figure 2.20 gives the radial profiles of radial velocity. Close to the plane containing the trailing edge of the baffle, $x/R = 0.04$, the magnitude of the maximum velocity is only half that for the 25 per cent blockage disc. Although measurements are restricted to $r/R \lesssim 0.82$, the decay of the radial velocity to the wall must be rapid and extrapolation to the pipe wall should be reliable. The streamline

angles at this station, figure 2.13, are also smaller than for the 25 per cent blockage disc which is consistent with the shallower trajectory of the separation streamline in figure 2.11. This is the result of the comparatively greater confinement. The marked minimum in these profiles of radial velocity close to the baffle tip (for $x/R \leq 1.2$) is present in the measurements of all three baffles and is associated with small values of axial velocity at these locations. The resulting streamline angles are directed at large angles to the pipe axis.

2.3.2 Profiles of Reynolds stress and turbulence spectra

Disc, 25 per cent blockage

Figures 2.21, 2.22 and 2.23 present radial profiles of the axial, radial and azimuthal components of the Reynolds stress tensor respectively. (Measurements of azimuthal mean velocity, made at the same time as $\langle w^2 \rangle$, showed that, within experimental accuracy, there was no swirl component to the flow). It should be emphasized that these are not resolved in streamline co-ordinates. Figures 2.21 and 2.23 show, in particular, that the degree of symmetry achieved is slightly worse than for the mean velocity profiles. For the ease of the subsequent discussion, the same information is presented as contours of equal stress for each component in figure 2.34. In addition, contours of the turbulent kinetic energy have been constructed by adding the individual components of normal stress. The contours were drawn using the same plotting program as for the streamlines and, as before, no other operation other than linear interpolation has been applied. (The centreline value of $\langle v^2 \rangle$ was taken as equal to the centreline value of $\langle w^2 \rangle$; for an axisymmetric flow, the two quantities are identically equal).

The contours of each component indicate that the recirculation bubble is a region of intense generation of turbulence, followed by dissipation downstream. The large increase in $\langle u^2 \rangle$ up to the axial position of the rear stagnation point, which is followed by a rapid decay, accords with the data available in separated flows (e.g. Durão and Whitelaw, 1978; Crabb et al, 1978; Etheridge and Kemp, 1978; Moss et al, 1979). Table 2.6 summarises the maxima of the r.m.s. velocity fluctuations which have been measured in a variety of separated, recirculating flows, either by laser-Doppler velocimetry or hot-wire anemometry. The present results are similar to those reported by other workers, particularly when notice is taken of the different ways in which the normalising velocity has been chosen: see the footnote to table 2.6. The highest measured is the data of Crabb et al (1978) which may be explained by their observation of bimodal probability distributions.

The development of $\langle v^2 \rangle$ and $\langle w^2 \rangle$ is markedly different from that of $\langle u^2 \rangle$, with the maxima occurring very close to the rear stagnation point. As a result the anisotropy of Reynolds stress on the centreline, figure 2.24, is particularly high. Comparison with many of the flows in table 2.6 does not allow useful generalisations to be drawn, because similar behaviour is impossible in flows for which the rear stagnation point lies at a solid surface. Of the flows with free rear stagnation points, the qualitative behaviour of the contours in figure 2.34 is similar to the data of Durão and Whitelaw (1978), although the latter pertain to a higher blockage ratio. The unusually high value for $\sqrt{\langle v^2 \rangle}/U_o$ reported by Bradbury (1976), given in table 2.6, was explained as the result of vortex shedding. Figure 2.25 shows the power spectral density of the turbulent fluctuations at three positions: close to the baffle tip on either side of the separation streamline, and far down-

TABLE 2.6

MAXIMUM r.m.s. VELOCITY FLUCTUATIONS IN SEPARATED, RECIRCULATING FLOWS

AUTHORS	FLOW TYPE	$\frac{\sqrt{\langle u^2 \rangle}}{U_o}$ (a)	$\frac{\sqrt{\langle v^2 \rangle}}{U_o}$ (a)	$\frac{\sqrt{\langle w^2 \rangle}}{U_o}$ (a)
This thesis	Confined disc, 25% blockage	0.35	0.42	0.42
	Confined cone, 25% blockage	0.30	0.28	0.33
	Confined disc, 50% blockage	0.36	0.26	0.36
Fujii et al (1978)	Confined wedge, 50% blockage		$\sqrt{\frac{2}{3}}\, k/U_o \simeq 0.26$	
Durão and Whitelaw (1978)	Annular jet, disc, 50% blockage	0.30	0.30	0.25
Smyth (1979)	Wall-mounted disc	0.30	0.25	-
Bradbury (1976)	Flat plate, 10% blockage	0.35	0.65	0.35
Castro and Robbins (1977)	Surface mounted cube	0.28	-	-
Crabb et al (1978)	Surface mounted rib	0.40	-	-

TABLE 2.6 CONCLUDED

AUTHORS	FLOW TYPE	$\frac{\sqrt{\langle u^2 \rangle}}{U_o}$(a)	$\frac{\sqrt{\langle v^2 \rangle}}{U_o}$(a)	$\frac{\sqrt{\langle w^2 \rangle}}{U_o}$(a)
Etheridge and Kemp (1978)	Backward facing step	0.20	0.15	-
Moss et al (1979)	Backward facing step	0.35	0.20	0.33

(a) Note that normalising velocity U_o is defined as:-

(i) Maximum value at trailing edge of baffle (Fujii et al, 1978; Durão and Whitelaw, 1978).

(ii) Approach velocity (Smyth, 1979; Castro and Robbins, 1977; Crabb et al, 1978).

(iii) Free stream velocity (Bradbury, 1976; Moss et al, 1979).

(iv) Maximum axial velocity at given station (Etheridge and Kemp, 1978).

stream on the centreline. The figure is drawn in the conventional log-log representation, which is appropriate for establishing the existence of the Kolmogorov spectrum law:-

$$\phi\ (k) = A\epsilon^{-2/3}\ .\ k^{-5/3}$$

where ϕ is the spectral density, A is a constant and k a wave number. The straight line superimposed on figure 2.25 represents a decay of '- 5/3' and is included for comparison with the measurements. The measurements indicate that there is no unusually large amount of energy associated with any particular frequency, as would be expected in the case of vortex shedding. It is noted that although the frequency response of the velocimeter extends only to about 200 Hz (see sub-section 2.2.2) this is not expected to be a limitation. The frequency of oscillation of the flow, were it to exist, would be such as to give rise to a Strouhal number of less than unity (e.g. Strouhal number for a cylinder is approximately 0.2). On this basis, the frequency of oscillation would lie below 60 Hz and thus within the velocimeter's response. As a further check, experiments were made using flow visualisation with hydrogen bubbles in conjunction with a stroboscope. Varying the frequency of the stroboscope confirmed the absence of any discernable flow oscillation. Similar results have been found by Durão and Whitelaw (1978) within the recirculation zone of an annular jet flow.

Cone, 25 per cent blockage

Figures 2.26, 2.27 and 2.28 give the profiles of the axial, radial and azimuthal Reynolds stress from which the contours of figure 2.35 have been drawn. The qualitative features of this flow are

similar to those of the 25 per cent blockage disc: $\langle v^2 \rangle$ and $\langle w^2 \rangle$ are largest close to the rear stagnation point, while the highest value of $\langle u^2 \rangle$ lies at $r/R \simeq 0.5$. The maxima of the Reynolds stresses are smaller, as is the centreline anisotropy shown in figure 2.29.

Disc, 50 per cent blockage

The profiles of the axial, radial and azimuthal Reynolds stress are presented in figures 2.30, 2.31 and 2.32 respectively, with figure 2.36 summarising the information in the form of contour levels, together with contours of the turbulent kinetic energy. Attention is drawn to the radial profiles of $\langle v^2 \rangle$, figure 2.31, and the use of linear interpolation between $0.6 < r/R < 0.76$ for estimating contour levels. It is likely that this practice underestimates the value in this region.

Although the position and value of maximum $\langle u^2 \rangle$ is similar to the 25 per cent blockage disc, the present flow results in the maxima of $\langle v^2 \rangle$ and $\langle w^2 \rangle$ being approximately coincident with that of $\langle u^2 \rangle$, rather than on the centreline. Because the development of each component is similar, with the largest values at a given axial station lying close to the separation streamline, the shear layer resembles a simple mixing layer. That this is so is presumably because of the elongated shape of the recirculation bubble caused by confinement, rather than the larger blockage. For this reason little similarity would be expected with the annular jet, measured by Durão and Whitelaw (1978), for a 50 per cent blockage disc which resulted in a shorter recirculation zone than the present flow.

The maximum value of the turbulent kinetic energy is about $0.14\ U_o^2$, as compared with $0.18\ U_o^2$ for the 25 per cent blockage disc. If the underestimation of $\langle v^2 \rangle$ in the present flow is taken into

account it is likely that this difference is even smaller. However, the partitioning of this energy is quite different, as exemplified by the approximate isotropy of the centreline Reynolds stress, figure 2.33.

2.4 Discussion

The aspects of the flowfield that are of interest in this study are the size of the recirculation region, the recirculating mass flow rate and the levels of turbulence which are generated. The following three subsections examine the influence of the forebody shape, the blockage and the effect of confinement on these characteristics. Blockage refers to the area blockage presented by the baffle to the approaching stream. In the experiments of this thesis, the flow downstream of the baffle is always confined by the pipe wall. The flow investigated by Durão and Whitelaw (1978) was, in contrast, unconfined downstream of the baffle, although the baffle still presented a blockage.

2.4.1 Influence of baffle forebody shape

The influence of the forebody on the flowfield is exerted by means of the magnitude and direction of the velocity vector field at the trailing edge of the baffle. Comparison between figures 2.6 and 2.15 shows that the magnitude of the axial component is similar for both the disc and cone. The angle of the streamlines at the trailing edge depicted in figure 2.14 is, however, quite different. This is particularly noticeable close to the baffle, where the angle for the disc is about 80 degrees as compared to about 20 degrees for the cone.

The trajectory of the separation streamline is accordingly shallower for the cone than for the disc, as shown in figure 2.11, giving rise to a narrower recirculation bubble. Table 2.7 compares

TABLE 2.7

SIZE OF THE RECIRCULATION ZONE AND RECIRCULATING MASS FLOW RATE

AUTHORS	FLOW TYPE	LENGTH[a]	WIDTH[a]	$\frac{\dot{m}_r}{\dot{m}_o}$[b]	$\frac{\dot{m}_r}{\dot{m}}$[c]
This thesis	Confined disc, 25% blockage	1.75	0.62	0.11	0.08
	Confined cone, 25% blockage	1.55	0.55	0.07	0.05
	Confined disc, 50% blockage	2.20	0.55	0.24	0.12
Winterfeld (1965)	Confined disc, 25% blockage	2.0	0.74	-	-
	Confined 90^o cone, 25% blockage	1.9	0.64	-	-
	Confined 45^o cone, 25% blockage	1.7	0.58	-	-
	Confined disc, 4% blockage	2.0	0.84	-	-
	Confined 90^o cone, 4% blockage	1.9	0.72	-	-
	Confined 45^o cone, 4% blockage	1.7	0.60	-	-
Fujii et al (1978)	Confined 60^o wedge, 50% blockage	1.88	0.59	0.10	0.05
Bradbury (1976)	Confined flat plate, 10% blockage	1.98	0.80	0.27	0.24
Davies and Beér (1971)	Annular jet, disc, 25% blockage	1.52	0.60	0.15	0.11
	Annular jet, 45^o cone, 25% blockage	1.24	0.50	0.08	0.06
	Annular jet, cylinder, 25% blockage	0.72	0.50	-	-
	Annular jet, disc, 54% blockage	1.16	0.56	0.27	0.12

TABLE 2.7 CONCLUDED

AUTHORS	FLOW TYPE	LENGTH[a]	WIDTH[a]	$\frac{\dot{m}_r}{\dot{m}_o}$[b]	$\frac{\dot{m}_r}{\dot{m}}$[c]
Durão and Whitelaw (1978)	Annular jet, disc, 20% blockage	1.45	-	-	-
	Annular jet, disc, 39% blockage	1.15	-	-	-
	Annular jet, disc, 50% blockage	1.00	-	-	-
Carmody (1964)	Unconfined disc	2.5	0.85	-	0.24

a Lengths and widths expressed in baffle heights, 'd'

b $\dot{m}_r$ is the recirculating mass flow rate

$\dot{m}_o$ is the total flow rate past the trailing edge of the baffle

c $\dot{m}$ is $\left(\rho U_o \frac{d^2\pi}{4}\right)$, where ρ is the density of the fluid
U_o is the bulk velocity at the baffle's trailing edge

the size of the recirculation zones measured in this thesis with those of other workers. Without exception (e.g. Davies and Beér, 1971; Winterfeld, 1965; Calvert, 1967) it is found that decreasing bluffness gives rise to narrower and shorter recirculation bubbles, although the lengths vary from reference to reference. This is not only the result of differences in experimental apparatus but also in measurement technique. Despite the differences in lengths, the decrease in length between a disc and a 45 degree cone is similar ($\simeq$ 15 per cent) in all references.

The magnitude of the maximum negative centreline axial velocity is smaller, figure 2.7, for the cone than for the disc. This velocity is interesting because it is a characteristic velocity of the recirculation zone and also because it influences the magnitude of the recirculating mass flow rate. Table 2.7 compares values of this quantity and shows, for example, that the recirculating mass flow rate behind the 25 per cent blockage cone is only 60 per cent that of the equivalent disc. To explain the reason for the smaller velocity in the wake of the cone, it is necessary to outline how this flow comes about.

The flow, on separating from the baffle tip, undergoes substantial streamline curvature which is evident in, say, the locus of the separation streamline in figure 2.11. The curvature is brought about by pressure gradients normal to the streamlines and a pressure minimum exists at the 'eye' of the recirculation bubble whose magnitude depends on the extent of the curvature. The distribution of pressure on the centreline, and in particular the pressure minimum, is closely associated with the pressure at the eye. Figure 2.40 shows isobars for the three flows taken from the calculations of Chapter III. Although these are calculated, rather than measured, the qualitative

distribution and related change from one flow to another are correct. The maximum reversed velocity is dependent on the centreline pressure gradient and figure 2.40 shows that that for the 25 per cent blockage disc is greater than that for the cone, principally because of the smaller pressure minimum of the flow (disc) with the larger streamline curvature. As a result, the maximum negative centreline velocity is also larger.

Inspection of the contours of Reynolds stress for the disc and the cone, figures 2.34 and 2.35, reveal distributions which are qualitatively similar. This result is unsurprising because the velocity fields, and hence the rates of strain, are also similar. The magnitudes of $\langle v^2 \rangle$ and $\langle w^2 \rangle$ (and less so $\langle u^2 \rangle$) are smaller, by about one half and one third respectively, for the cone with the result that the centreline distribution of turbulent kinetic energy is found to be only 60 per cent that of the disc (figure 2.37). Because the recirculation is a region of intense generation of turbulence, these results can be explained by examination of the exact equations for the transport of the individual components of Reynolds stress (see e.g. Bradshaw, 1971) and in particular those terms which express the generation of each component:-

$$P\ (\langle u^2 \rangle) = -\ 2 \left[\langle u^2 \rangle \frac{\partial U}{\partial x} + \langle uv \rangle \frac{\partial U}{\partial r} \right] \qquad (2.21a)$$

$$P\ (\langle v^2 \rangle) = -\ 2 \left[\langle uv \rangle \frac{\partial V}{\partial x} + \langle v^2 \rangle \frac{\partial V}{\partial r} \right] \qquad (2.21b)$$

$$P\ (\langle w^2 \rangle) = -\ 2 \frac{V}{r} \langle w^2 \rangle \equiv 2 \left[\frac{\partial U}{\partial x} + \frac{\partial V}{\partial r} \right] \langle w^2 \rangle \qquad (2.21c)$$

(although the term referred to as "pressure-strain":-

$$\left\langle \frac{p'}{\rho} \left(\frac{\partial u_i}{\partial x_j} + \frac{\partial u_j}{\partial x_i} \right) \right\rangle$$

see for example Launder, Reece and Rodi (1975), can appear as a source term in equations (2.21), the contraction of the pressure-strain tensor is, however, zero and thus its rôle is only redistributive).

The radial position of maximum $\langle u^2 \rangle$ lies in the region of large $\partial U/\partial r$: this is because in the curved shear layer the production of $\langle u^2 \rangle$ is principally by $\langle uv \rangle \partial U/\partial r$, and the production of $\langle uv \rangle$ is itself dependent on $\partial U/\partial r$. Since the flow behind the disc is associated with larger values of $\partial U/\partial r$ than the cone, larger values of $\langle u^2 \rangle$ are produced.

The maxima of both $\langle v^2 \rangle$ and $\langle w^2 \rangle$ lie close to the rear stagnation point ($x = x_r$) and give rise to the large values of turbulent kinetic energy there. The production of $\langle w^2 \rangle$ is $\langle w^2 \rangle \partial U/\partial x$ on the centreline: examination of the mean strain rate $\partial U/\partial x$ shows that it is of the required sign (positive) and magnitude:-

$$\frac{\partial U}{\partial x} \left(x = x_r \, , \, \frac{r}{R} = 0 \right) \simeq \frac{1}{2} \frac{\partial U}{\partial r} \left(x = x_r \, , \, \frac{r}{R} \simeq 0.5 \right) \quad \text{for the cone}$$

and:-

$$\frac{\partial U}{\partial x} \left(x = x_r \, , \, \frac{r}{R} = 0 \right) \simeq \frac{1}{4} \frac{\partial U}{\partial r} (x_r, \, 0.5) \quad \text{for the disc}$$

The similarity of $\partial U/\partial x$ on the centreline and $\partial U/\partial r$ in the free stream indicates that the concept of a "thin shear layer" (Cebeci and Bradshaw, 1977) is inapplicable in this region and that, therefore, turbulence models based on an effective viscosity hypothesis may be of limited use. The counterpart production term for $\langle u^2 \rangle$ in this region is $- 2 \langle u^2 \rangle \frac{\partial U}{\partial x}$,

which is a sink. The high anisotropy that is observed on the centre-line can thus be interpreted as the result of relatively large values of P ($\langle u^2 \rangle$) and P ($\langle w^2 \rangle$) with opposite signs. The absence of large convective transport near the rear stagnation point is important in allowing the production terms to dominate, giving rise to the centre-line maxima in $\langle u^2 \rangle$ and $\langle w^2 \rangle$ at $x = x_r$ (see figures 2.24 and 2.29). For positions closer to the baffle than the position of maximum negative centreline velocity, the above arguments are reversed because $\partial U/\partial x$ changes sign. This accounts for the local maximum in $\langle u^2 \rangle$ closest to the baffle observed in figures 2.24 and 2.29, and in the experiments of Durão and Whitelaw (1978), produced in figure 2.39(a). Although the smaller anisotropy on the centreline for the cone, as compared with the disc, is probably the result of smaller values of $\partial U/\partial x$, see figure 2.7, the smaller level of centreline kinetic energy, figure 2.37, is due to the generally reduced levels of kinetic energy.

The object of this analysis is to establish that the dominant production of turbulent kinetic energy, at least near the centreline, occurs by normal stress-normal strain interaction. It implies that calculation of the flow using the k-ε turbulence model may be inaccurate, at least for the turbulence near the rear stagnation point, because scalar effective viscosity models do not adequately represent normal stresses. Although the gradients of normal stress (where "normal" now refers to streamline co-ordinates) are not large terms in the transport of mean momentum, the importance of the various production terms in generating turbulent kinetic energy implies that it is necessary to calculate the individual normal stresses adequately (using an appropriate turbulence model) if the correct turbulent kinetic energy is to be obtained. This distribution is crucial to the correct representation of the effective viscosity (see Chapter III)

and the latter quantity is of importance in the mean momentum equations.

The importance of turbulent exchange between the recirculating and surrounding flow in flame stabilisation has been presented in Chapter I. Taking turbulent kinetic energy as a measure of the exchange, the contour levels in figures 2.34 and 2.35 show that this is higher for the disc than the cone. This is in agreement with Winterfeld's (1965) measurements for the residence time of a passive scalar in the recirculation bubble.

2.4.2 Influence of blockage

On increasing the blockage of the disc from 25 per cent to 50 per cent, the angles of the streamlines at the trailing edge of the baffle, figure 2.14, are substantially reduced. This results in a maximum width which is also reduced, see table 2.7, although the length of the recirculation bubble has increased by about one quarter. Table 2.7 shows that all previous measurements have shown the opposite trend with increasing blockage; that is the recirculation length decreases irrespective of whether the flow is confined or not. Observations in confined axisymmetric flows have been, however, restricted to blockage less than 25 per cent.

The increased length and decreased width of the recirculation bubble correspond to decreased streamline curvature, particularly downstream of the maximum bubble width. The reason for this is the greater proximity of the separation streamline to the pipe wall as compared to the 25 per cent blockage disc. As a consequence the generation of large velocities normal to the wall, which would be required for large curvature, is inhibited. The distance of the separation streamline from the wall is closely related to the distance of the baffle tip from the wall. It is noted that on changing from

25 to 50 per cent blockage, in axisymmetric flows, corresponds to the baffle diameter increasing from 0.5 R to 0.71 R, whereas the same change in blockage in a plane geometry results in increasing the width from 0.25 R to 0.50 R. The influence of area blockage on, say, re-circulation length can thus be expected to be substantially weaker in plane geometries, and this is confirmed by comparing the measurements of Fujii et al (1978) with that of Bradbury (1976), given in table 2.7.

The increased length of the recirculation zone results in qualitatively different distribution of the Reynolds stresses as compared with the smaller baffles. Figure 2.7 shows that the centre-line value of $\partial U/\partial x$ is smaller than for the 25 per cent blockage disc and so, using the arguments of subsection 2.4.1, the importance of normal stress-normal strain interactions is reduced, giving rise to the small anisotropy of figure 2.33. A further result of the reduced centreline production of $\langle w^2 \rangle$ is the low value of the centreline turbulent kinetic energy, shown in figure 2.37. Turbulent production is thus principally restricted to the shear layer surrounding the separation streamline, close to the location of the greatest width of the recirculation bubble. This, however, should not be taken to imply that the entire production of kinetic energy is by $\langle uv \rangle \partial U/\partial r$ and that $\langle v^2 \rangle$ and $\langle w^2 \rangle$ receive energy from pressure interaction alone, as they would, for example, in a homogeneous shear flow. This cannot be so because the maximum values of $\langle u^2 \rangle$ and $\langle w^2 \rangle$ (the components most free of measurement error) are similar, excluding pressure interaction as a dominant mechanism (see Tennekes and Lumley, 1972, page 75).

2.4.3 Influence of confinement

The influence of a confining wall on the flow downstream of a baffle, as opposed to one in which the downstream flow is free (such

as an annular jet), can be explained on the basis of the above description of the flow development. Whether confined or not, table 2.7 shows that decreasing forebody bluffness results in narrower, shorter recirculation zones, because the angle of separation becomes smaller in both cases. The dimensionless lengths of the recirculation bubble are, however, consistently larger for confined flows. This is the influence of the confining wall in preventing large streamline curvature towards the axis of symmetry and possibly because of a larger velocity deficit in the case of a confined flow. In other words, an annular jet entrains at its outer edge as well as at its inner, which tends to reduce radial gradients more rapidly than in a confined flow. In the (unconfined) case of Durão and Whitelaw (1978), for example, the maximum axial velocity (for an annular jet behind a disc of 50 per cent blockage) at the end of the recirculation bubble was about 0.7 U_o, whereas here the velocity is about 1.5 U_o for the disc of 50 per cent blockage. The resulting shear stress gradients which act to accelerate fluid in the axial direction, and which scales with the velocity deficit (Durão and Whitelaw, 1978), can also be expected to be larger in confined flows. This results in longer recirculation zones.

Comparison of the results of this work and those of Durão and Whitelaw (1978) reveals the effect of confinement on the Reynolds stresses. Figure 2.37 shows that the annular jet of 50 per cent blockage gives rise to higher centreline turbulent kinetic energy than the equivalent confined flow near the free stagnation point. Examination of the development of the centreline axial velocity, figure 2.38, shows that $\partial U/\partial x$ is larger in this region for the unconfined flow. The arguments presented in subsection 2.4.1 lead to the expectation of low $\langle u^2 \rangle$ and high $\langle w^2 \rangle$ in the annular jet flow as

compared to the confined flow. Figures 2.39(a) and (b) confirm this.

2.5 Summary

The following is a summary of the more important findings and conclusions of this chapter:-

1. The influence of baffle forebody shape, on changing from a disc to a 45 degree cone of 25 per cent blockage is to:-

   (a) shorten and narrow (by 10 per cent) the recirculation bubble;

   (b) decrease (by 40 per cent) the recirculating mass flow rate;

   (c) reduce (by 40 per cent) the largest value of turbulent kinetic energy.

2. The influence of baffle blockage, on changing from a disc of 25 per cent to 50 per cent blockage is to:-

   (a) lengthen (by 30 per cent) the recirculation bubble;

   (b) leave the dimensionless recirculating mass flow rate unchanged;

   (c) reduce (by about 16%) the largest value of turbulent kinetic energy.

3. The decrease in the length and width of the recirculation bubble with diminishing bluffness is the result of decreased streamline angles at the trailing edge of the baffle.

4. The increase in recirculation length with blockage for blockage above 25 per cent is opposite to the trend in unconfined flows. The difference is due to the confining wall preventing the generation of large streamline curvature towards the rear stagnation point.

5. The distribution of the Reynolds stresses changes markedly with increase in blockage: for the 25 per cent blockage disc the maximum turbulent kinetic energy lies near the rear stagnation point, whereas for the 50 per cent blockage disc it is far from the centreline, in the shear layer. Examination of the Reynolds transport equations shows that different terms dominate in each flow, brought about by differences in the length of the recirculation bubble.

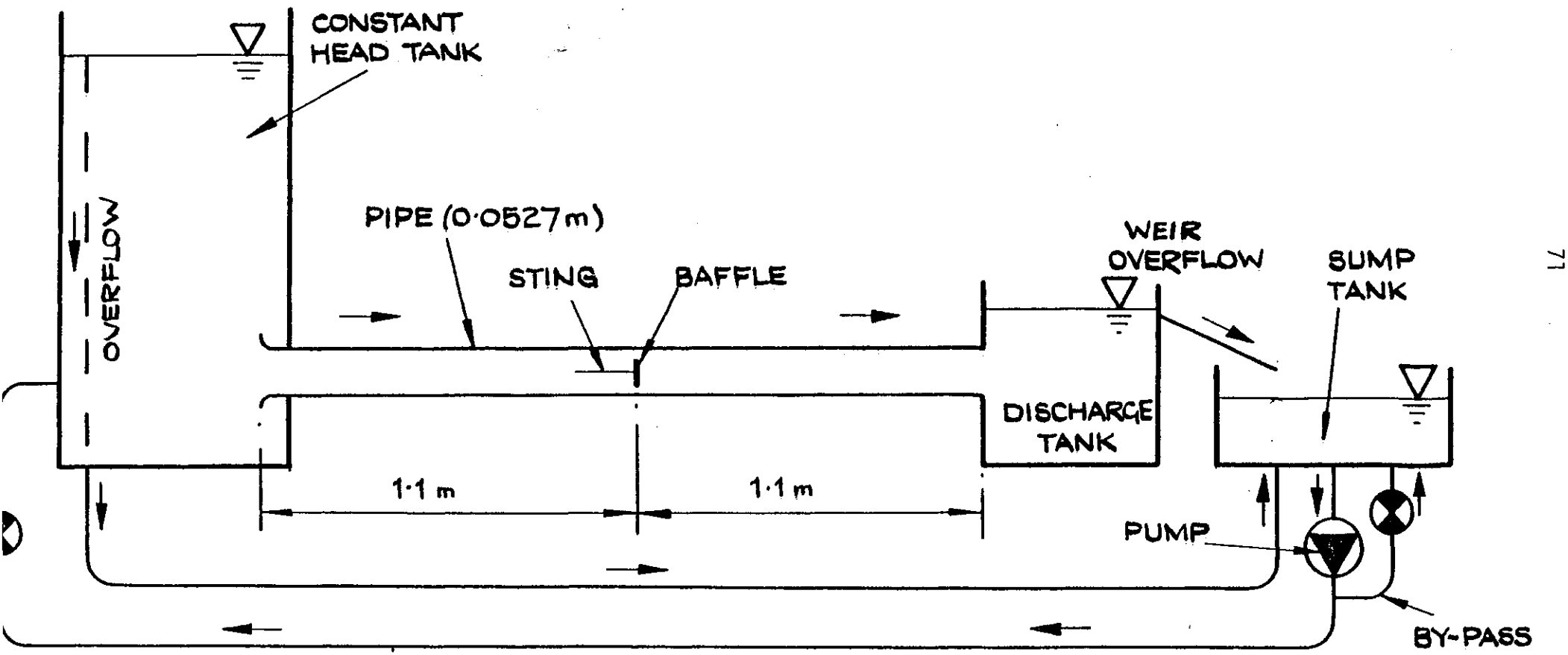

Figure 2.1 Diagram of water-tunnel

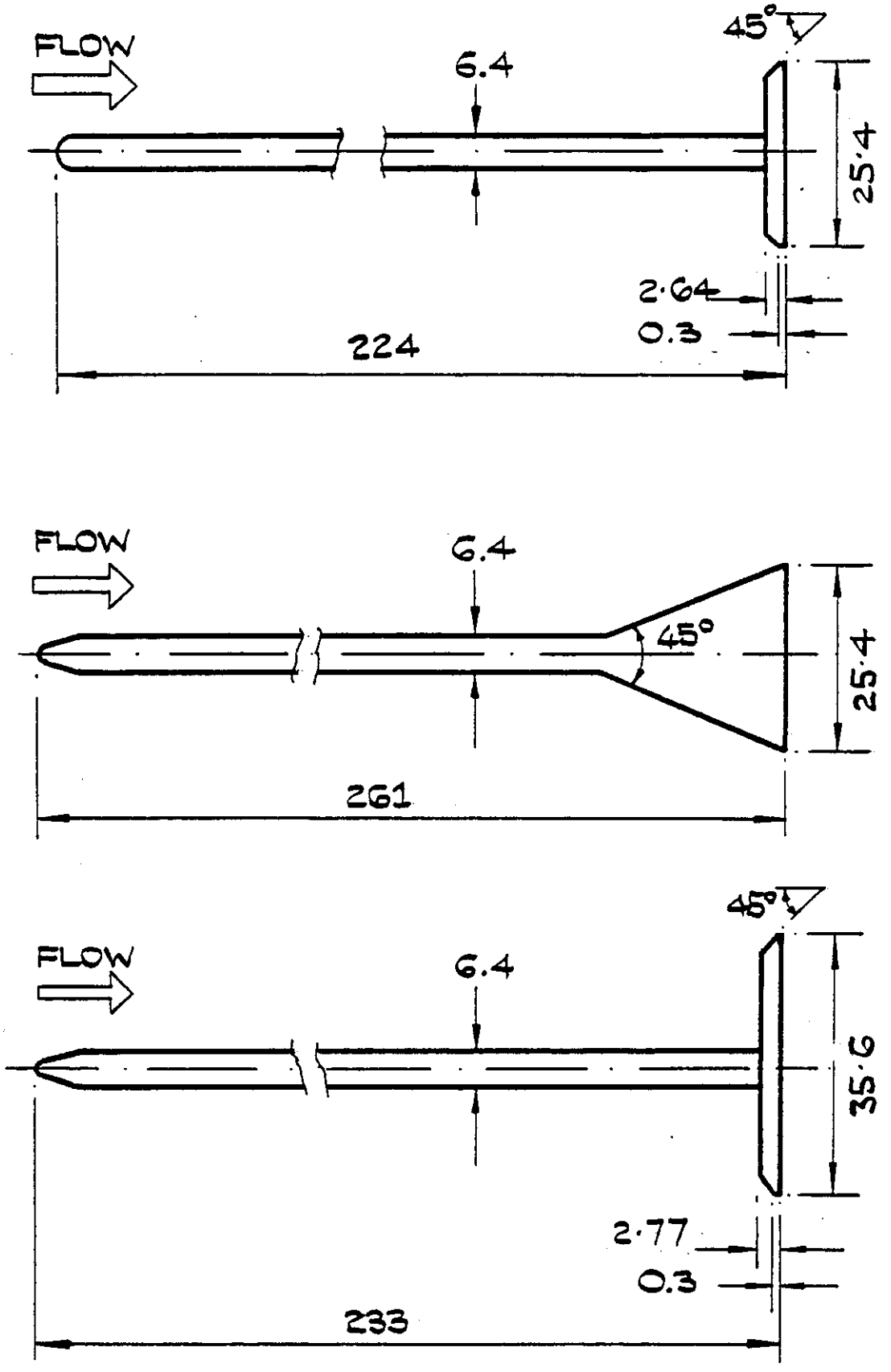

Figure 2.2(a) Shapes and dimensions of baffles

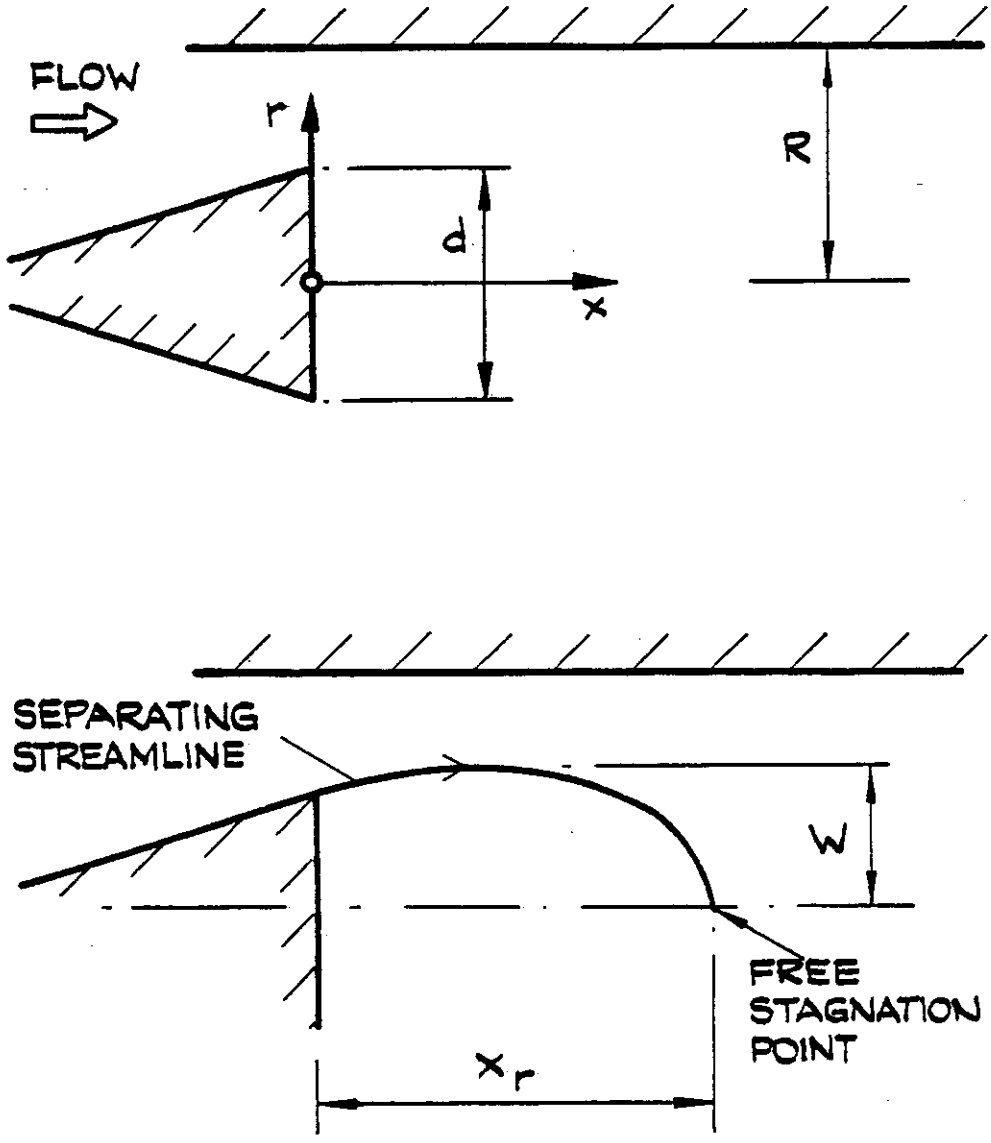

Figure 2.2(b) Definition sketch of co-ordinate system and important dimensions

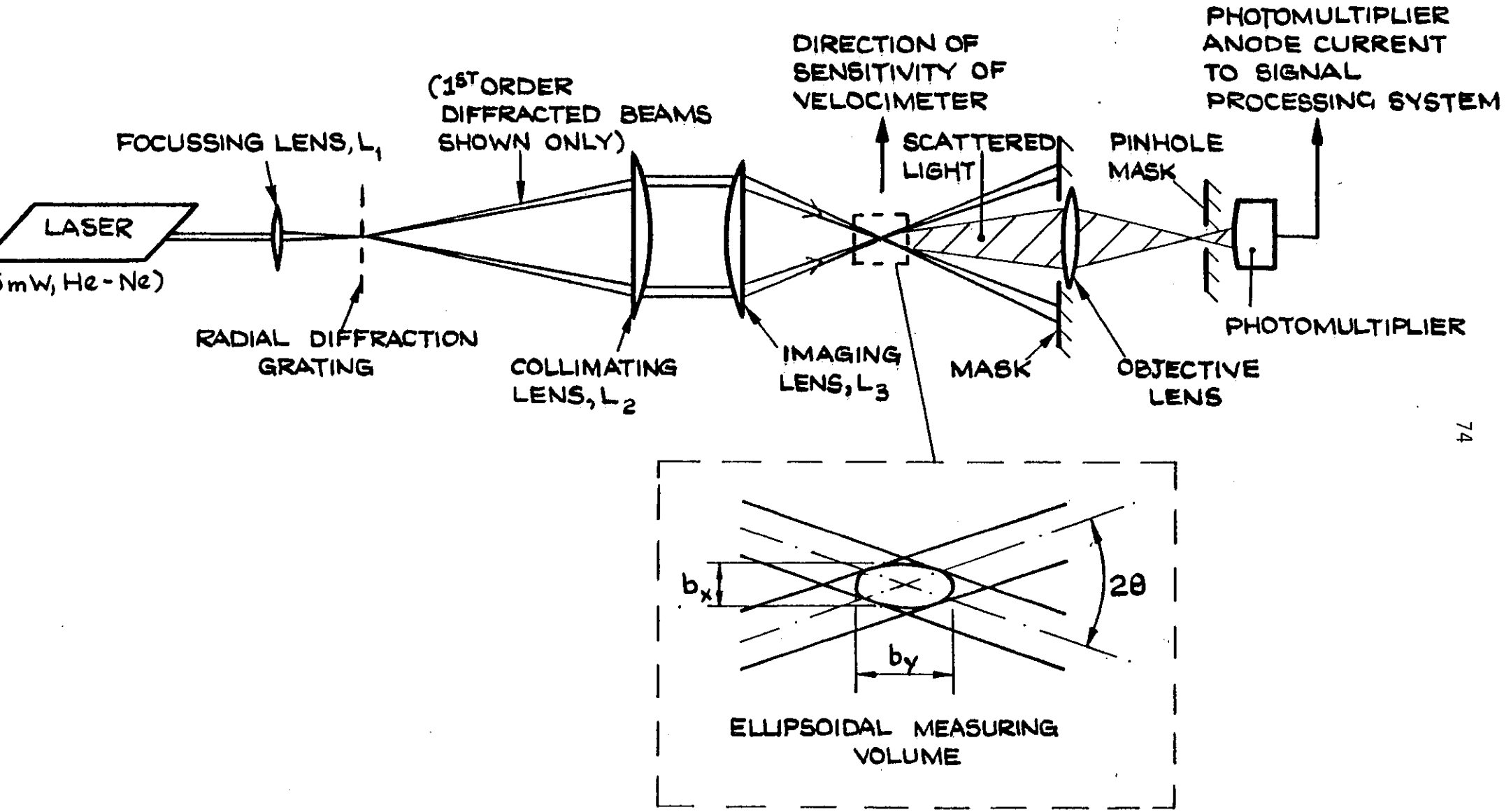

Figure 2.3 Optical arrangement of laser-Doppler velocimeter

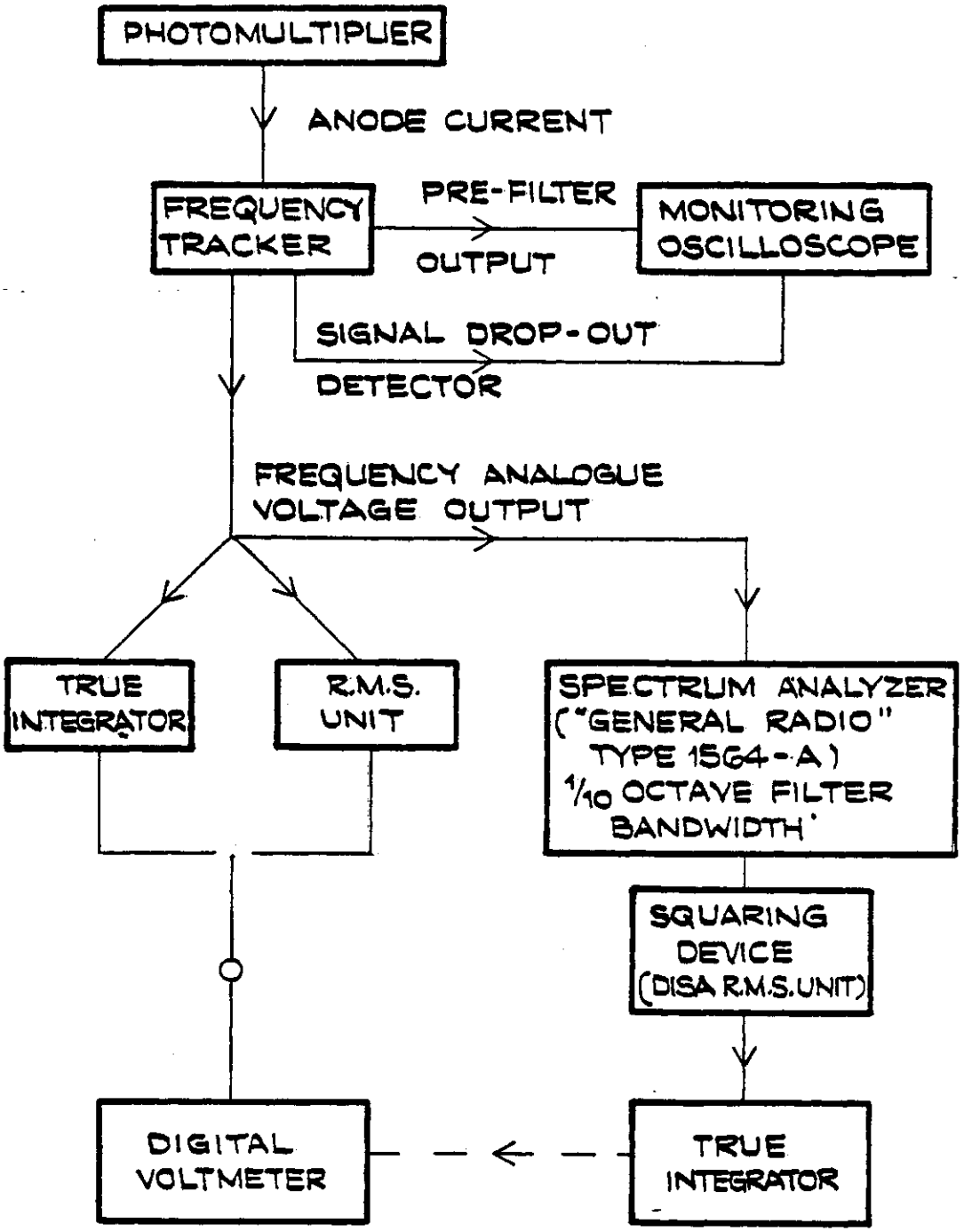

Figure 2.4 Block diagram of Doppler signal processing arrangement

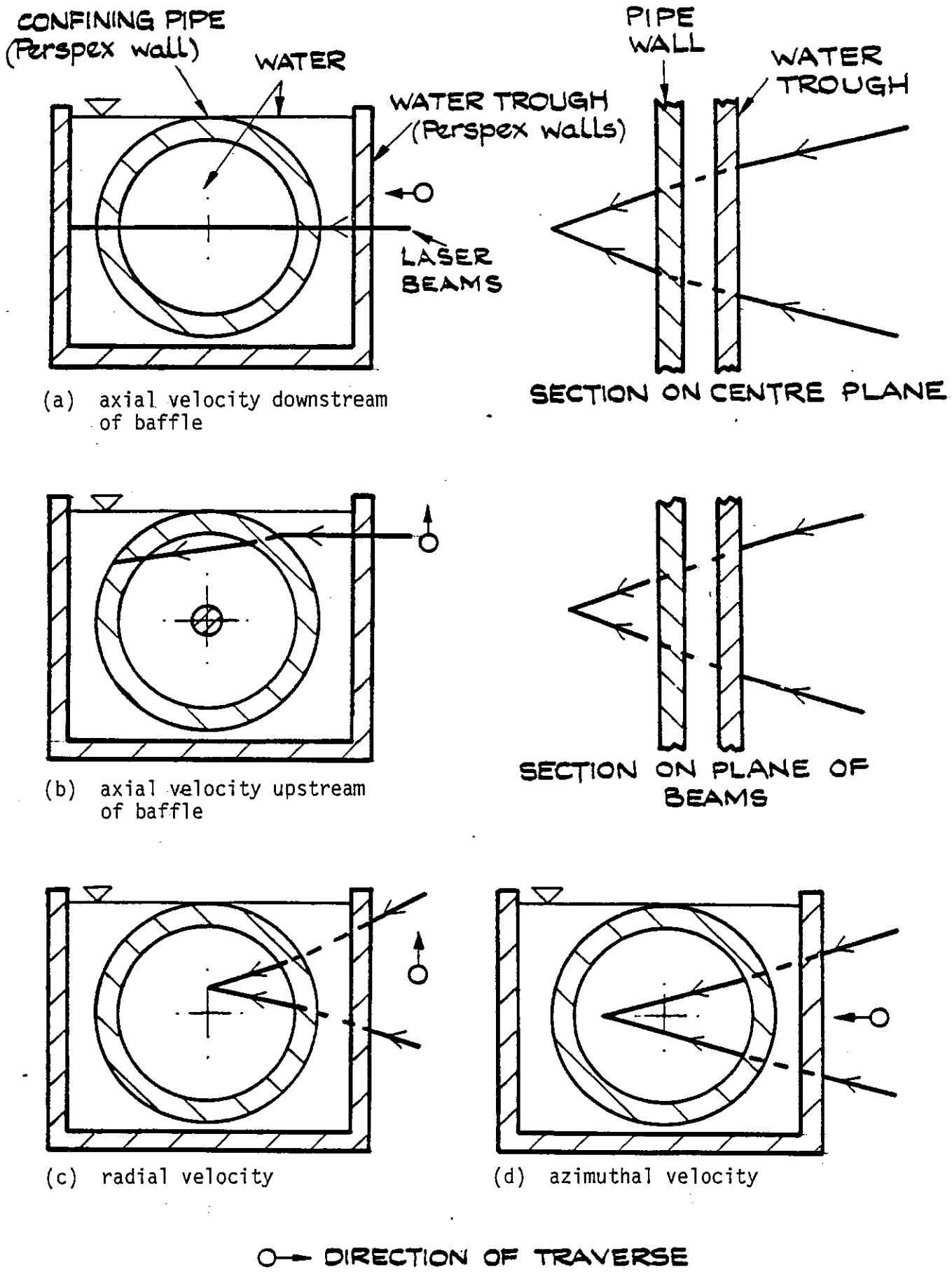

(a) axial velocity downstream of baffle

(b) axial velocity upstream of baffle

(c) radial velocity

(d) azimuthal velocity

Figure 2.5 Beam attitude and direction of traverse for measurement of velocity components

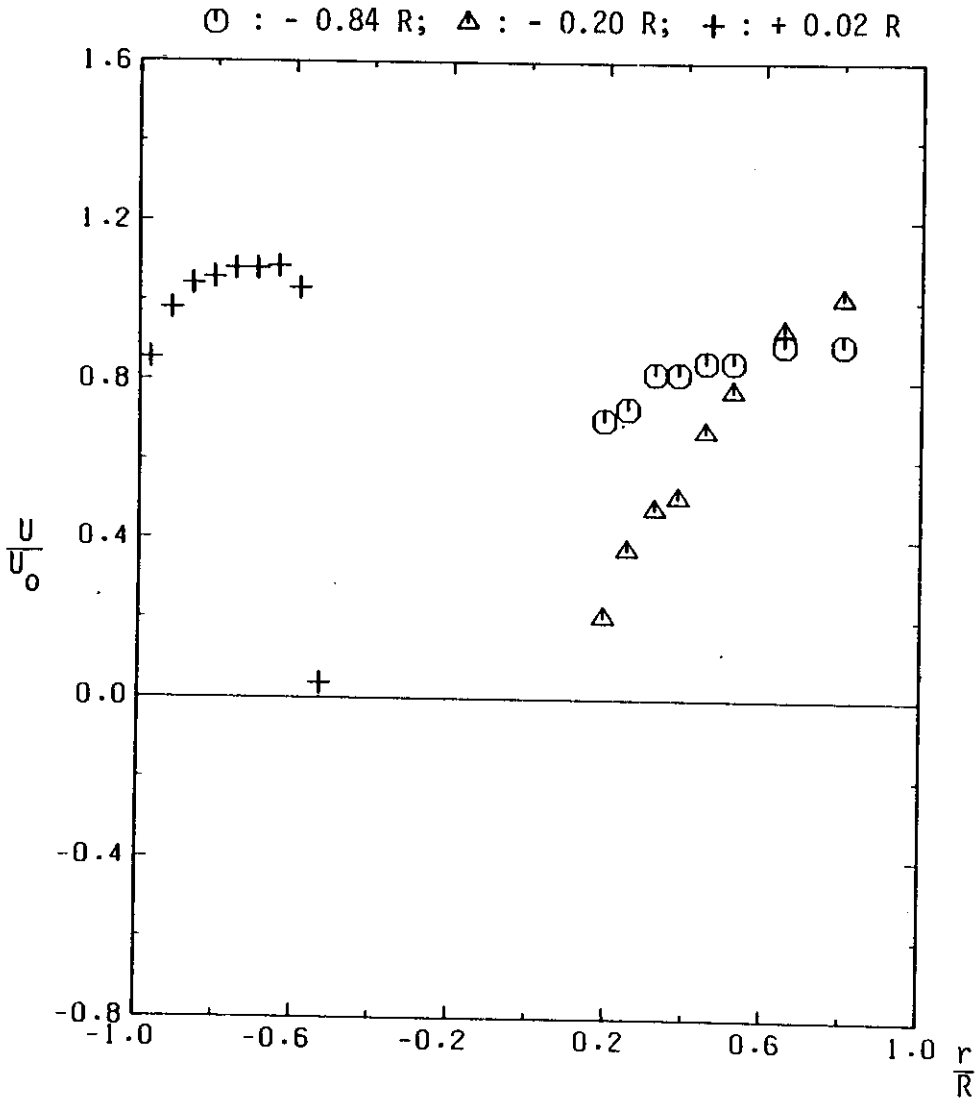

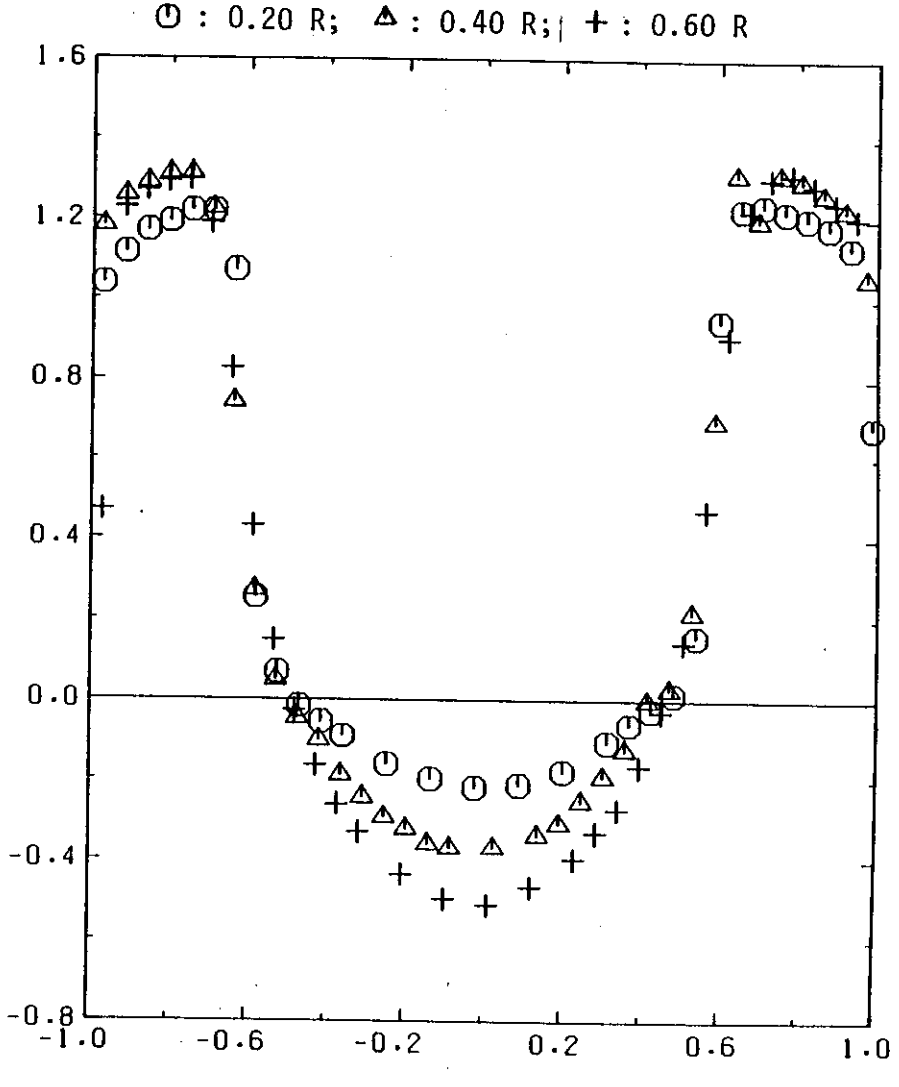

Figure 2.6 Disc, 25% blockage: radial profiles of axial velocity at successive axial stations (U_0 = 1.37 m/s)

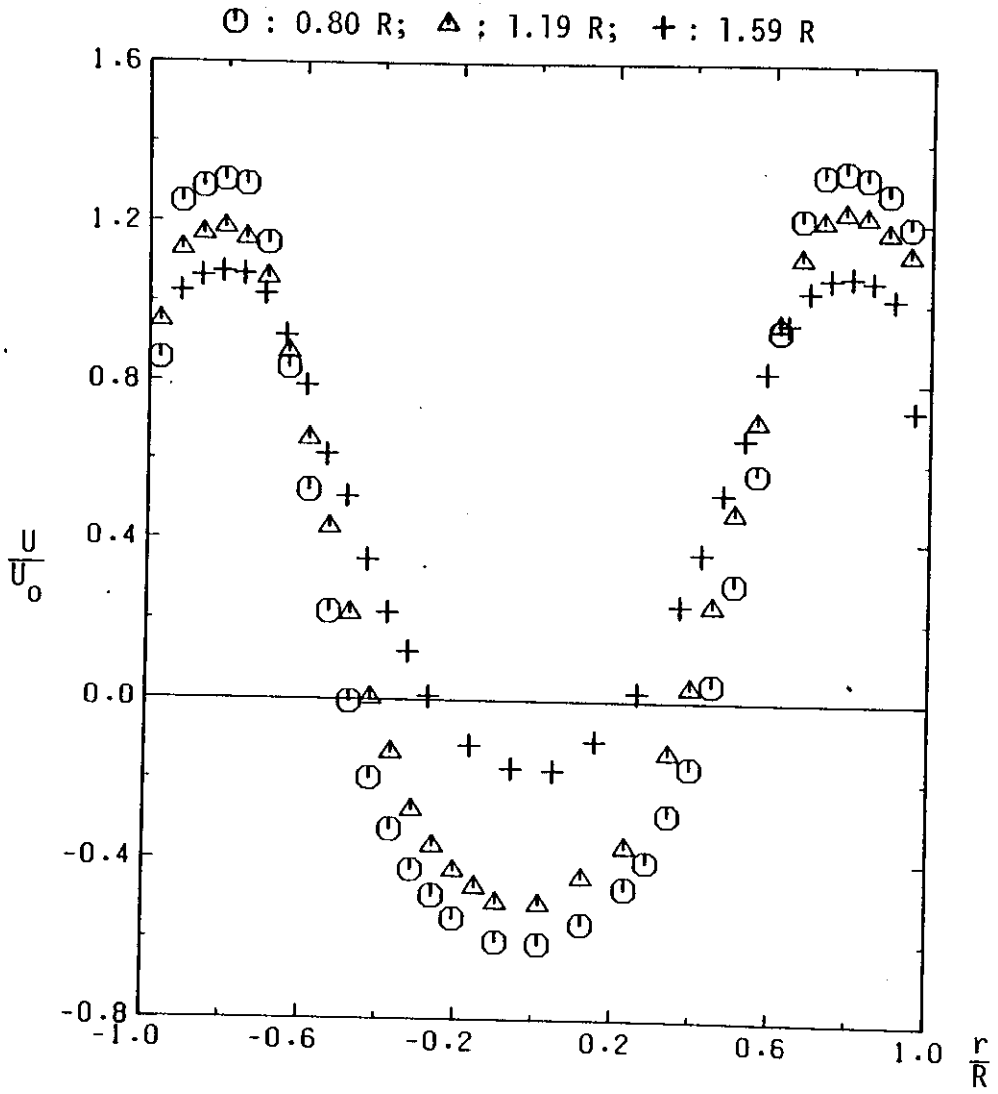

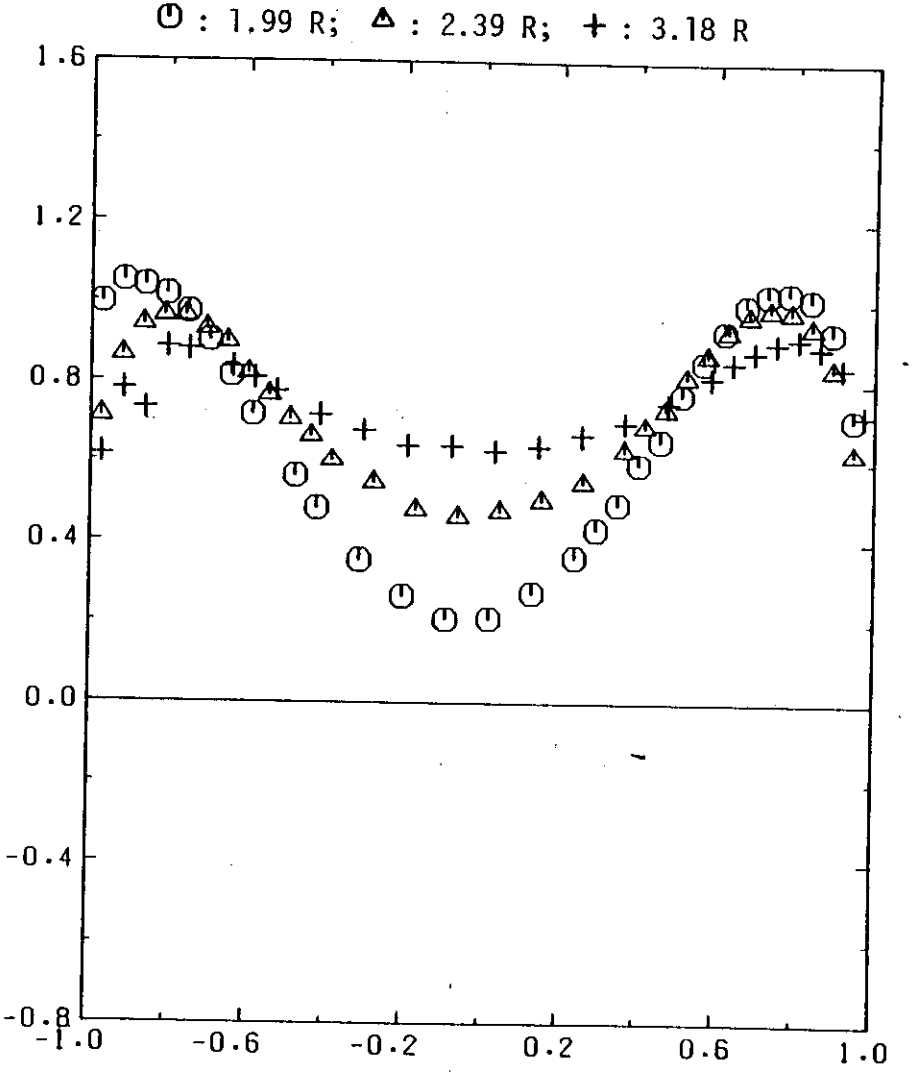

Figure 2.6 (Continued)

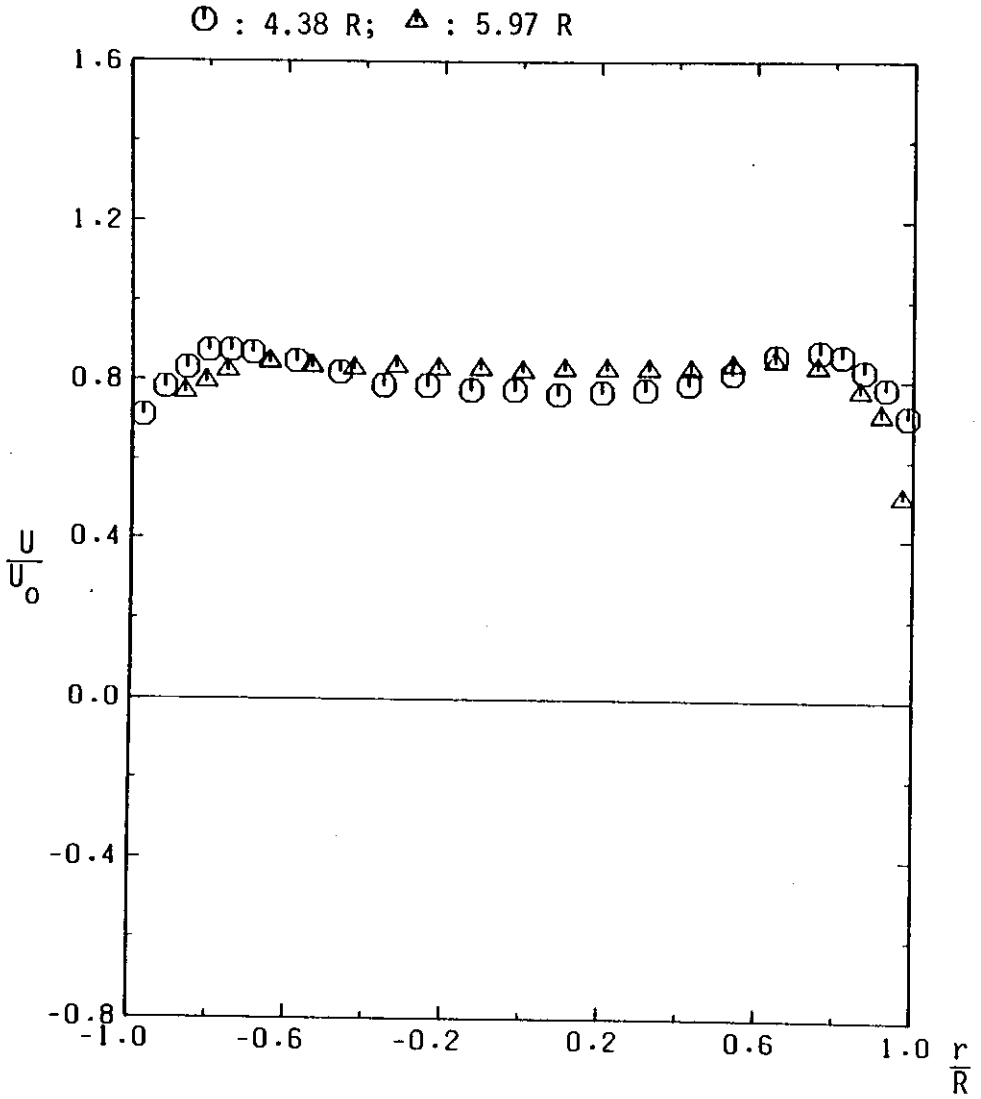

Figure 2.6 (Concluded)

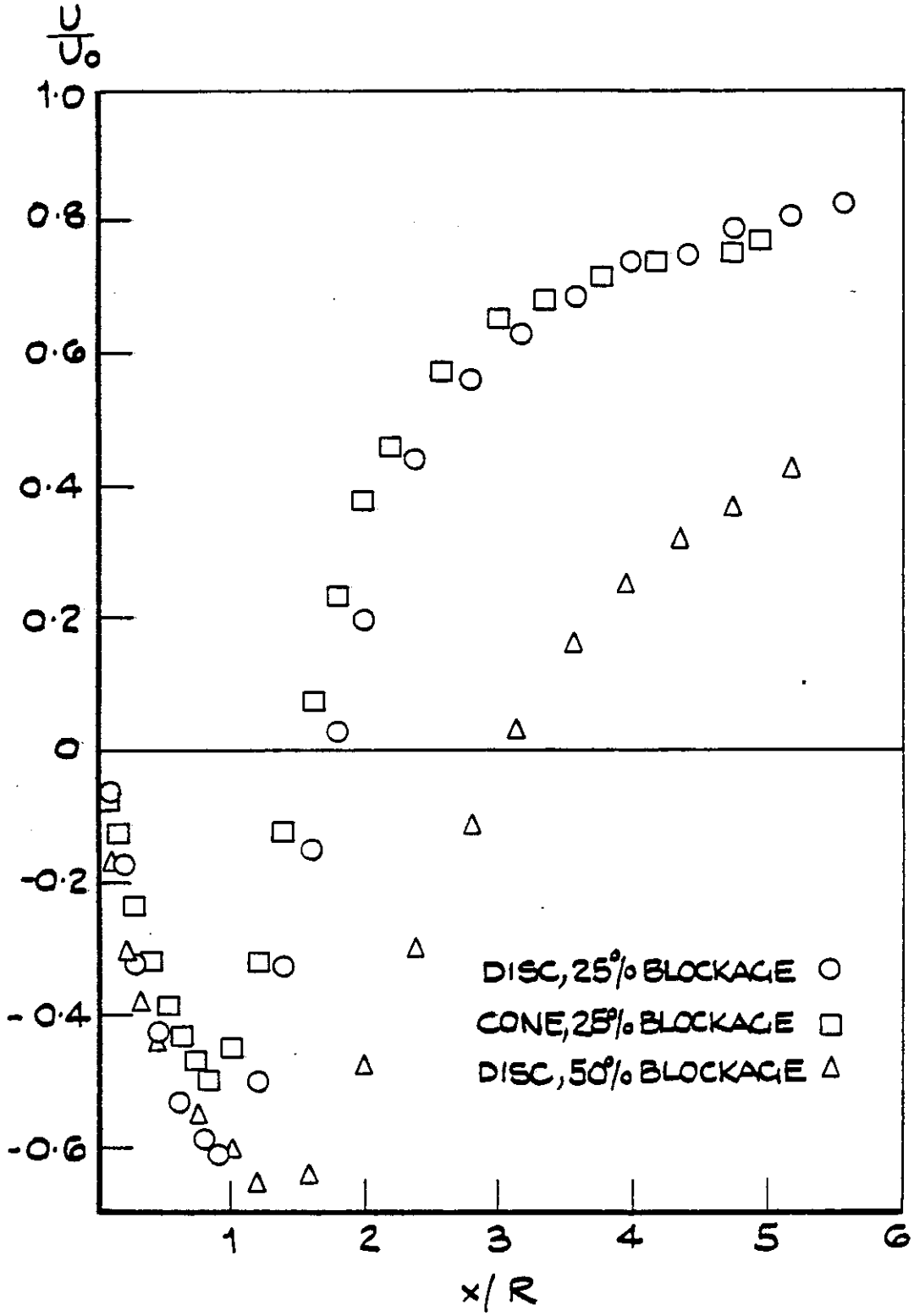

Figure 2.7 Centreline profiles of axial velocity for three baffles

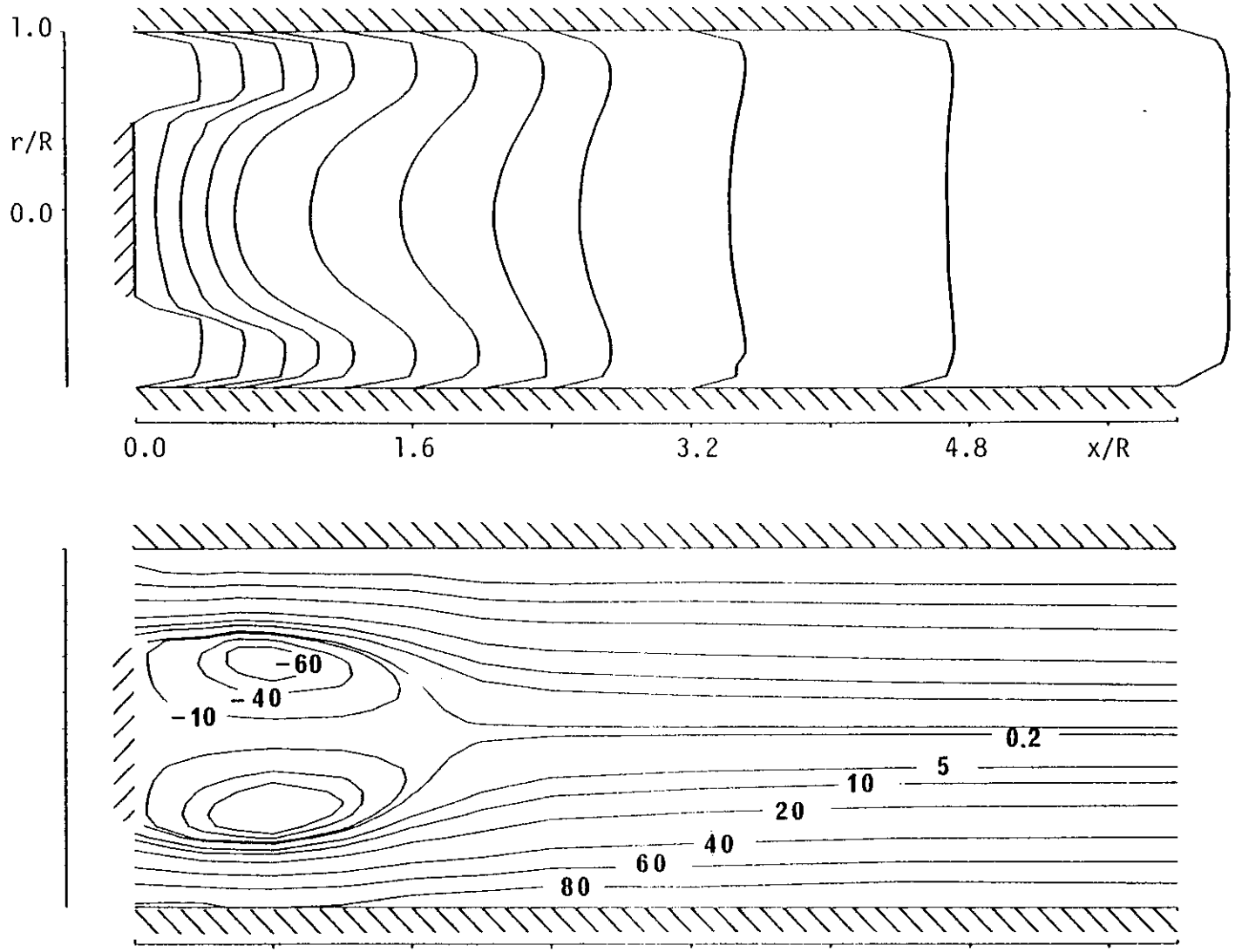

Figure 2.8 Disc, 25% blockage: profiles of axial velocity and corresponding contours of constant stream function (% of maximum positive and negative values)

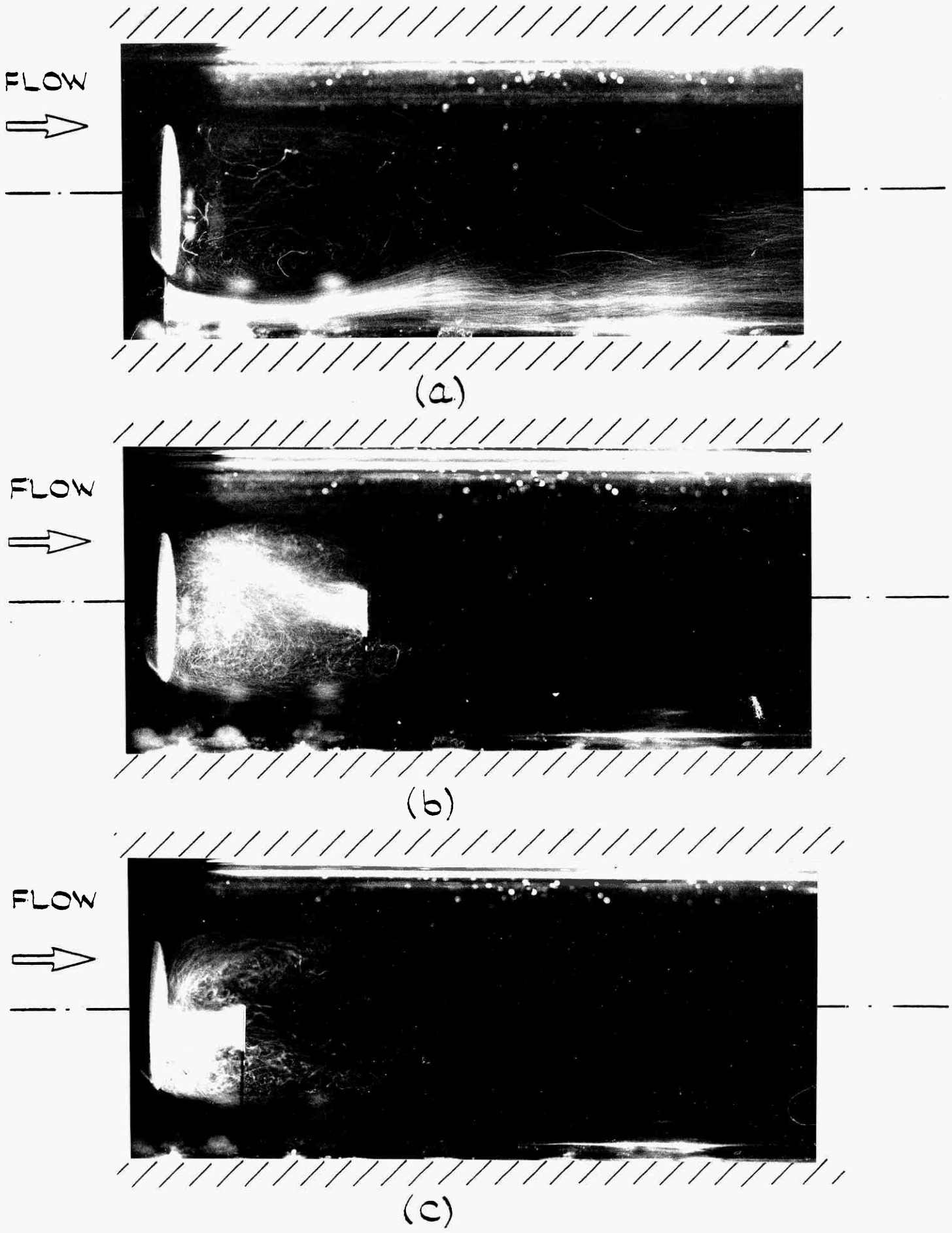

Figure 2.9 Disc, 25 per cent blockage. Visualization of flow in the near-wake by hydrogen bubble technique

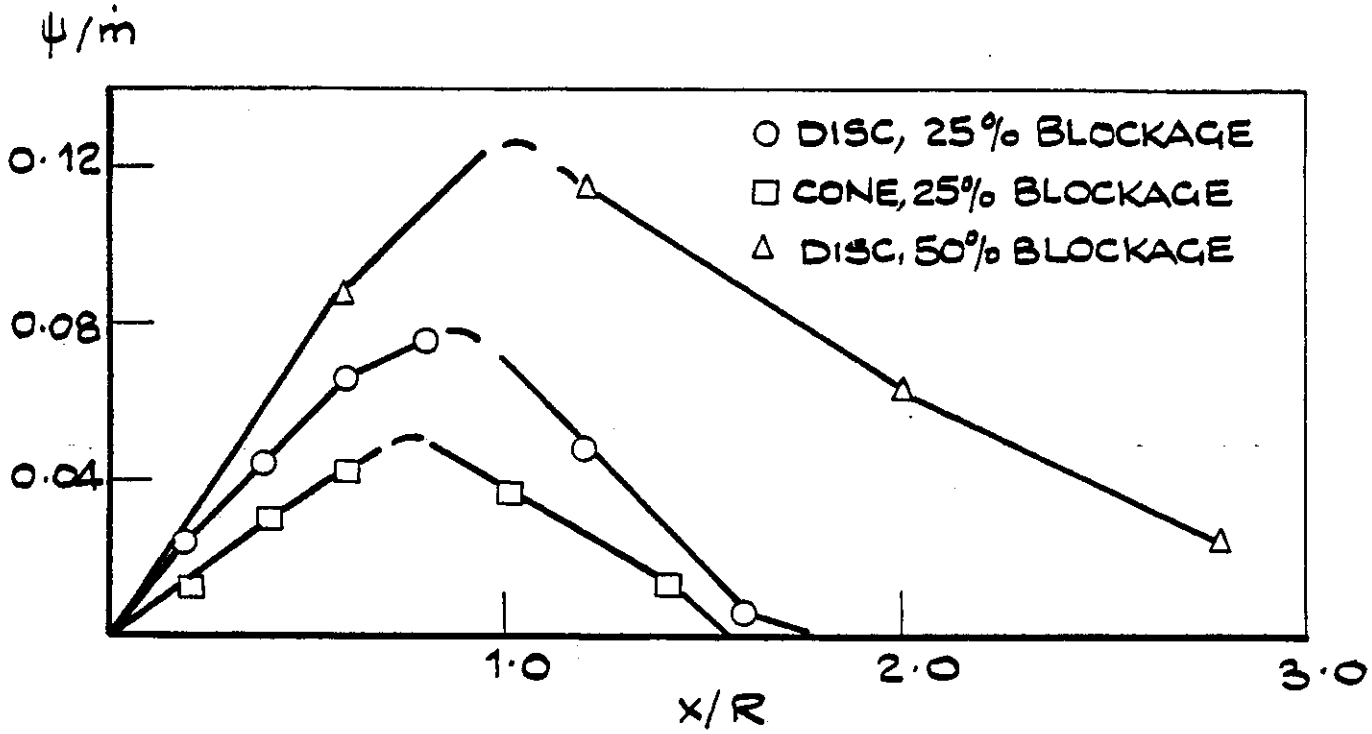

Figure 2.10 Variation of maximum negative stream function with axial distance

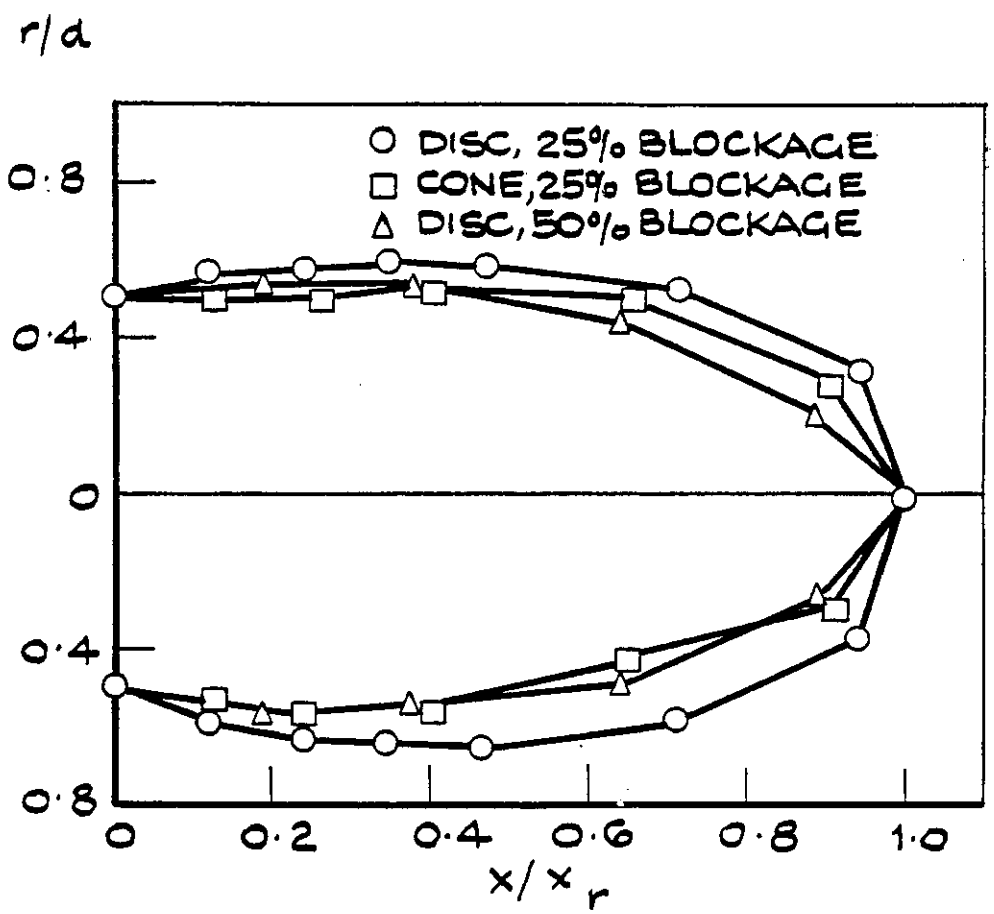

Figure 2.11 Locus of separation streamline for three baffles

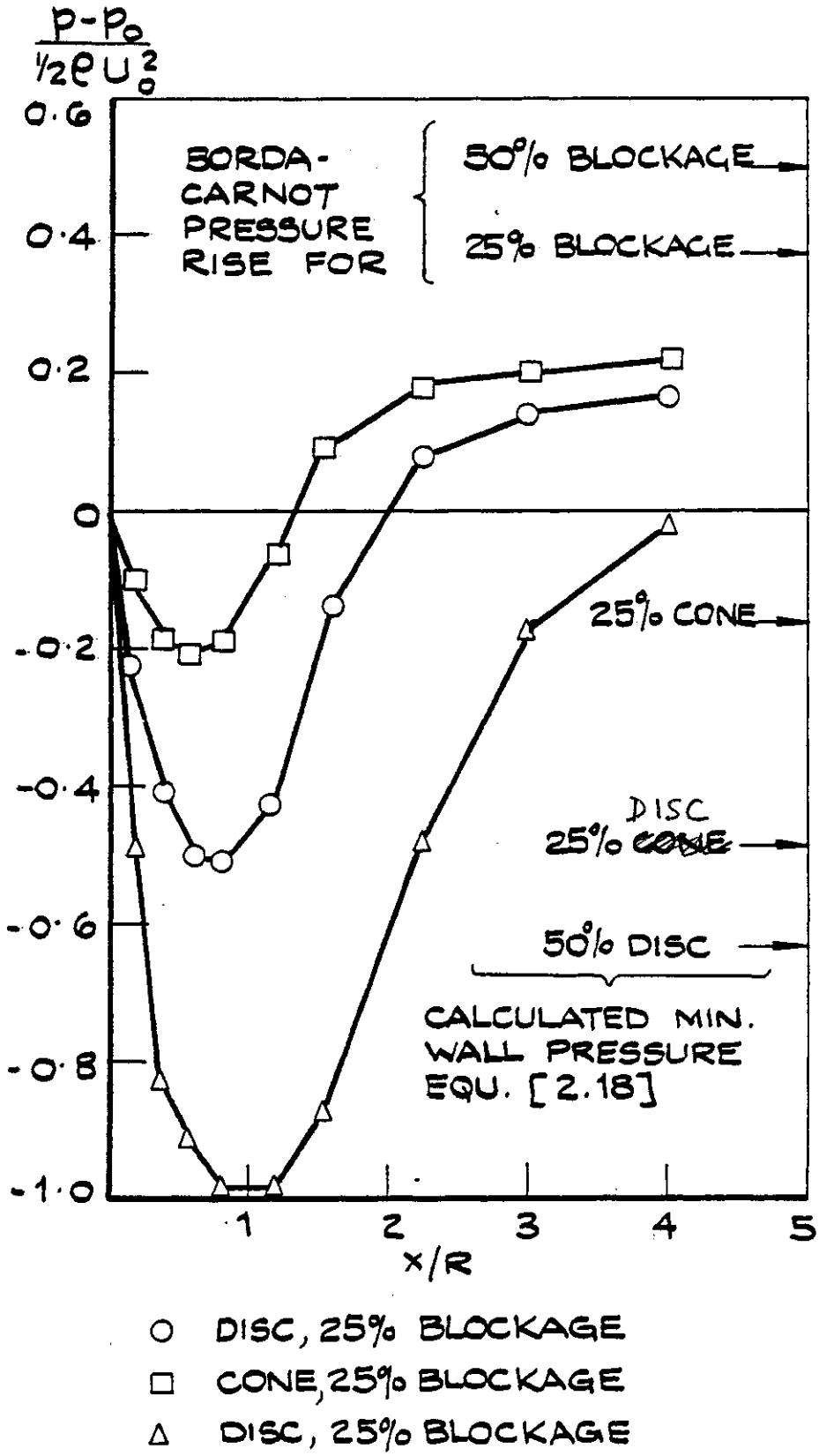

Figure 2.12 Axial variation of wall pressure coefficient

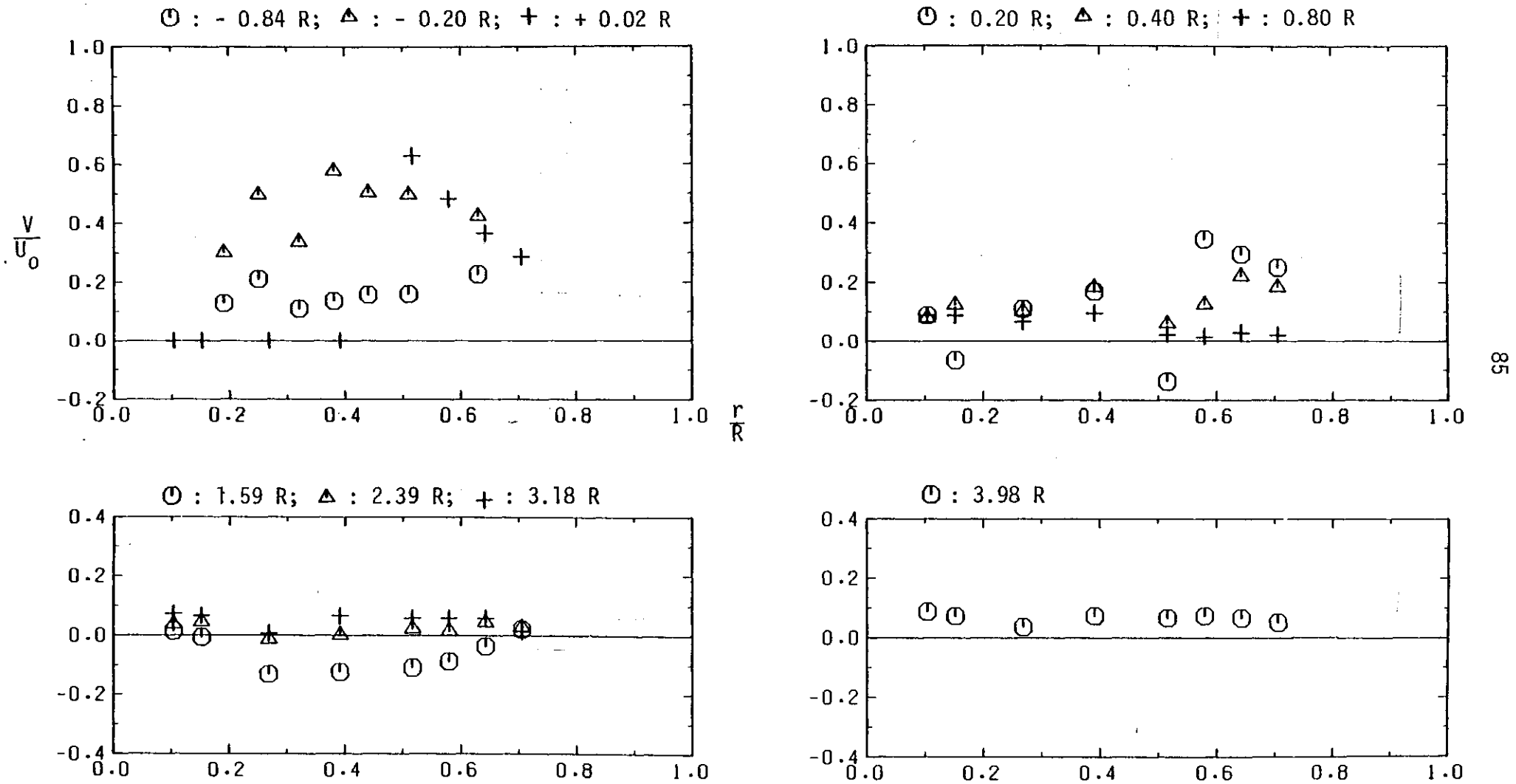

Figure 2.13 Disc, 25% blockage: radial profiles of radial velocity at successive axial stations (U_0 = 1.37 m/s)

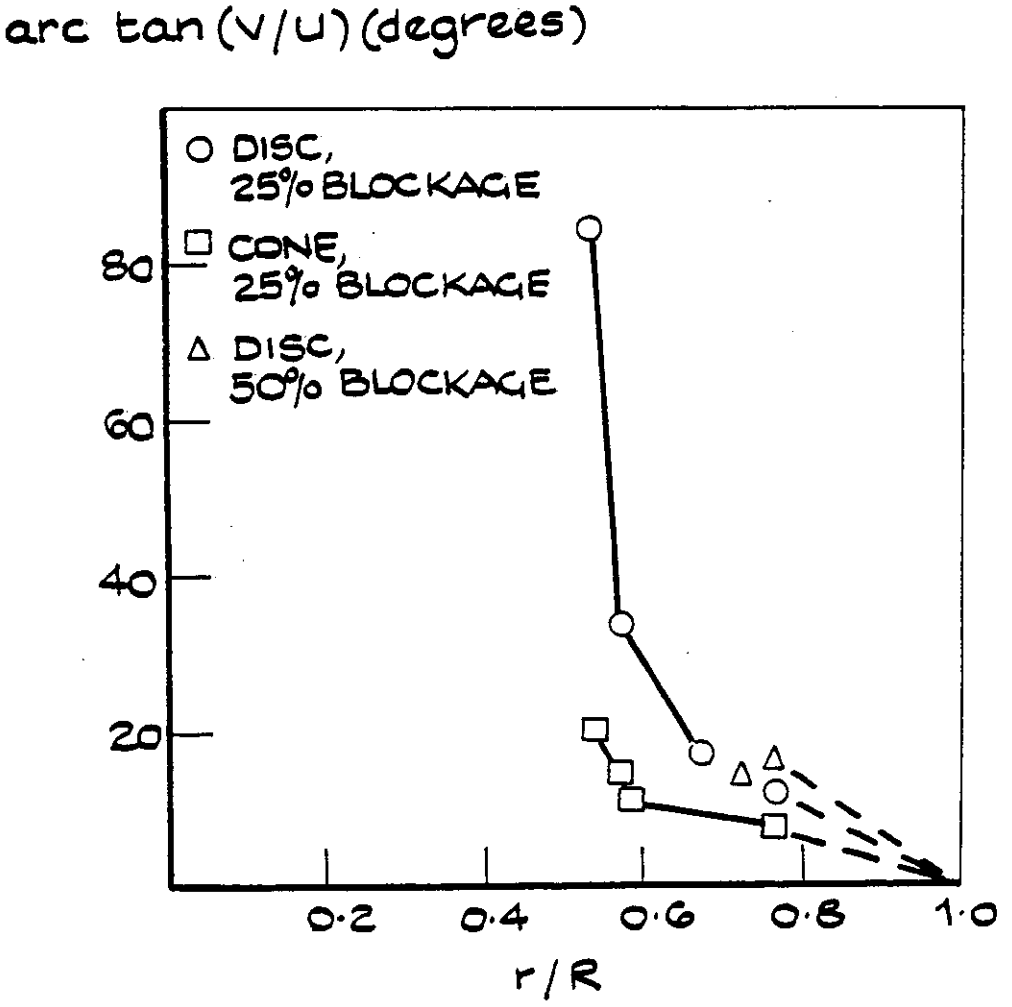

Figure 2.14 Angles of streamlines in plane of trailing edge of baffle

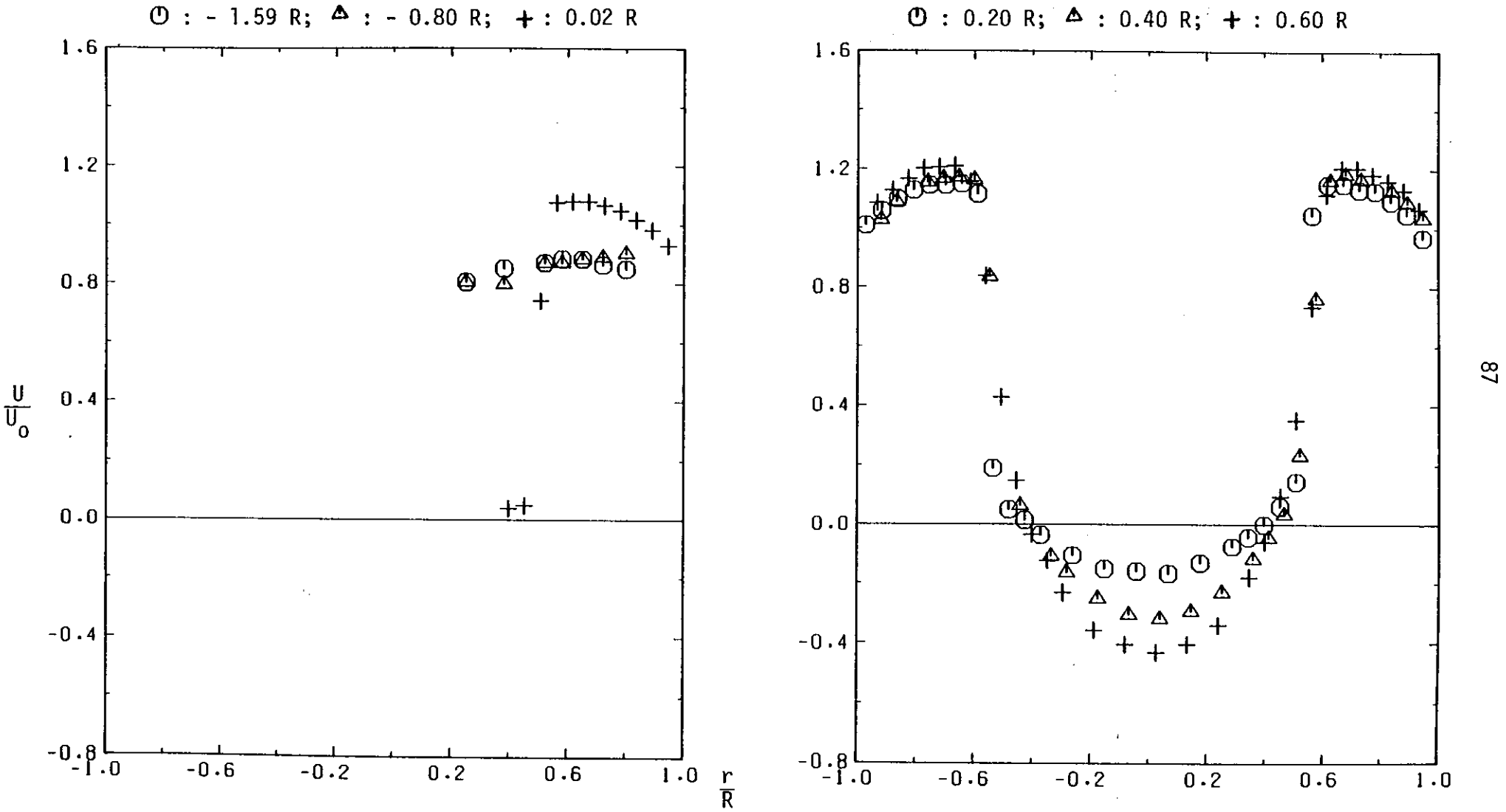

Figure 2.15 Cone, 25% blockage: radial profiles of axial velocity at successive axial stations (U_o = 1.53 m/s)

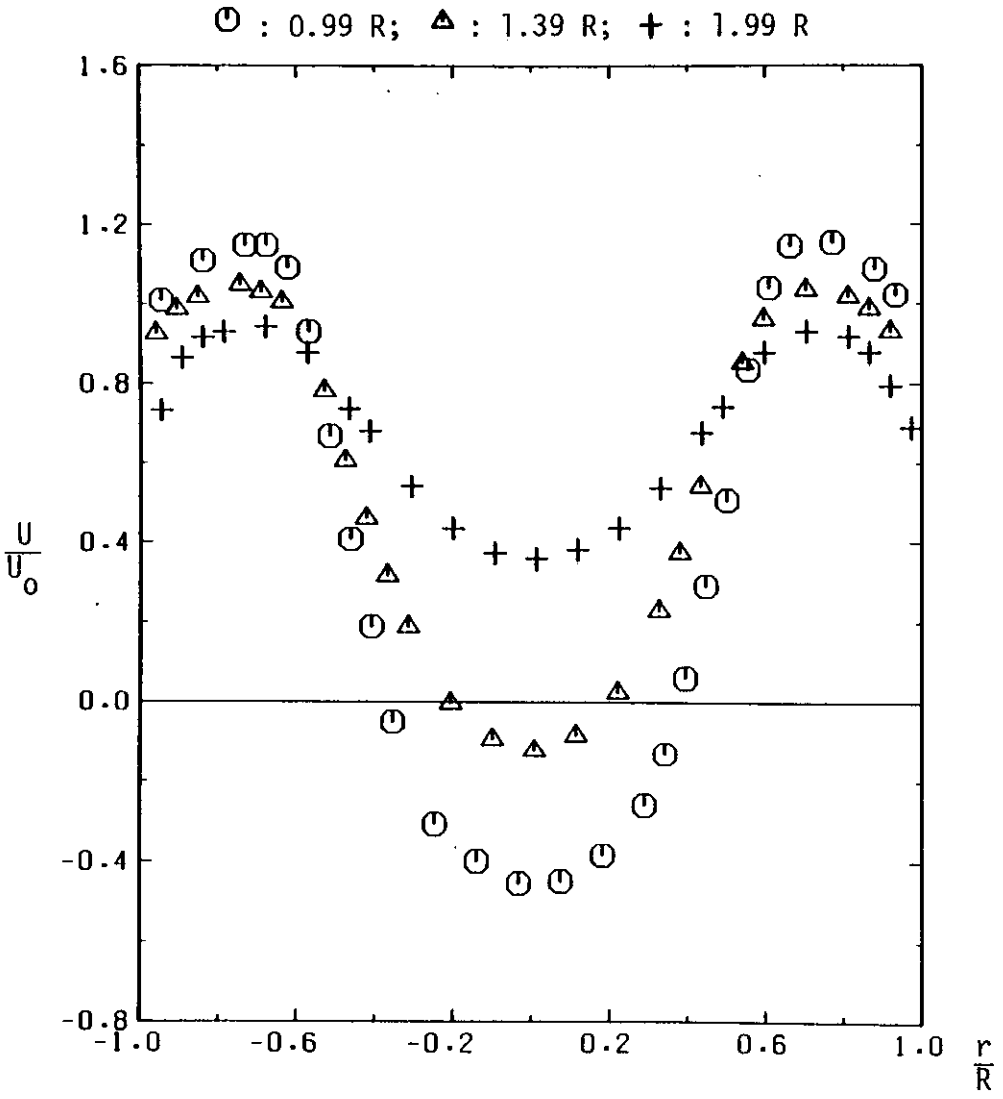

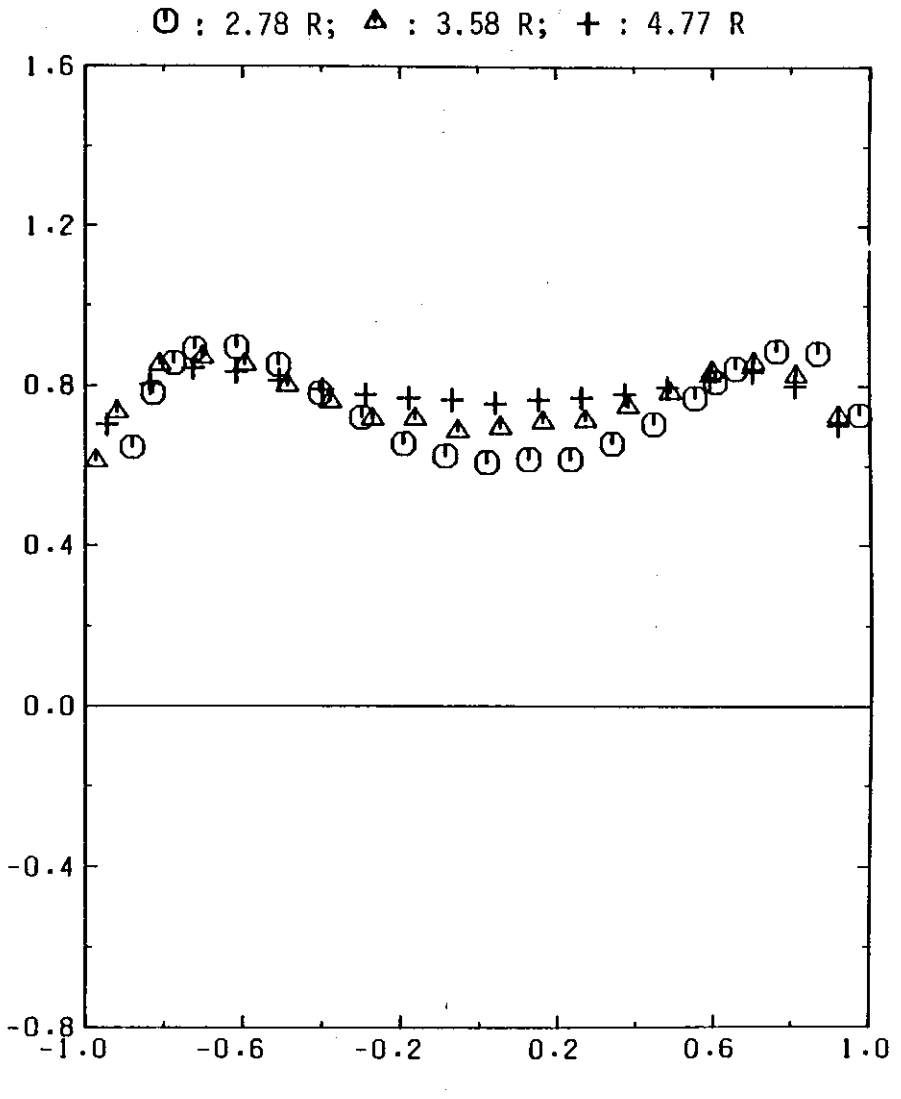

Figure 2.15 (Concluded)

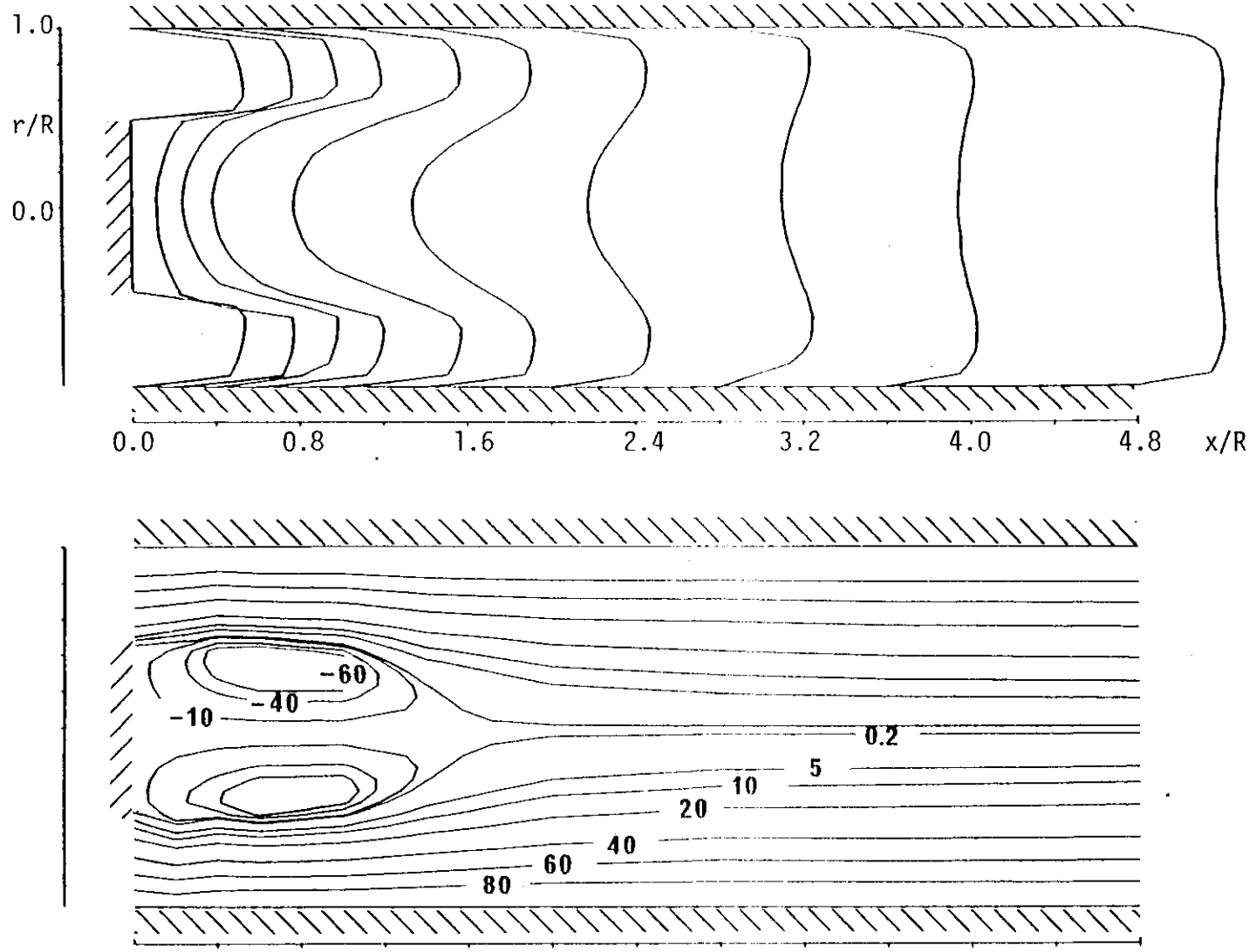

Figure 2.16 Cone, 25% blockage: profiles of axial velocity and corresponding contours of constant stream function (% of maximum positive and negative values)

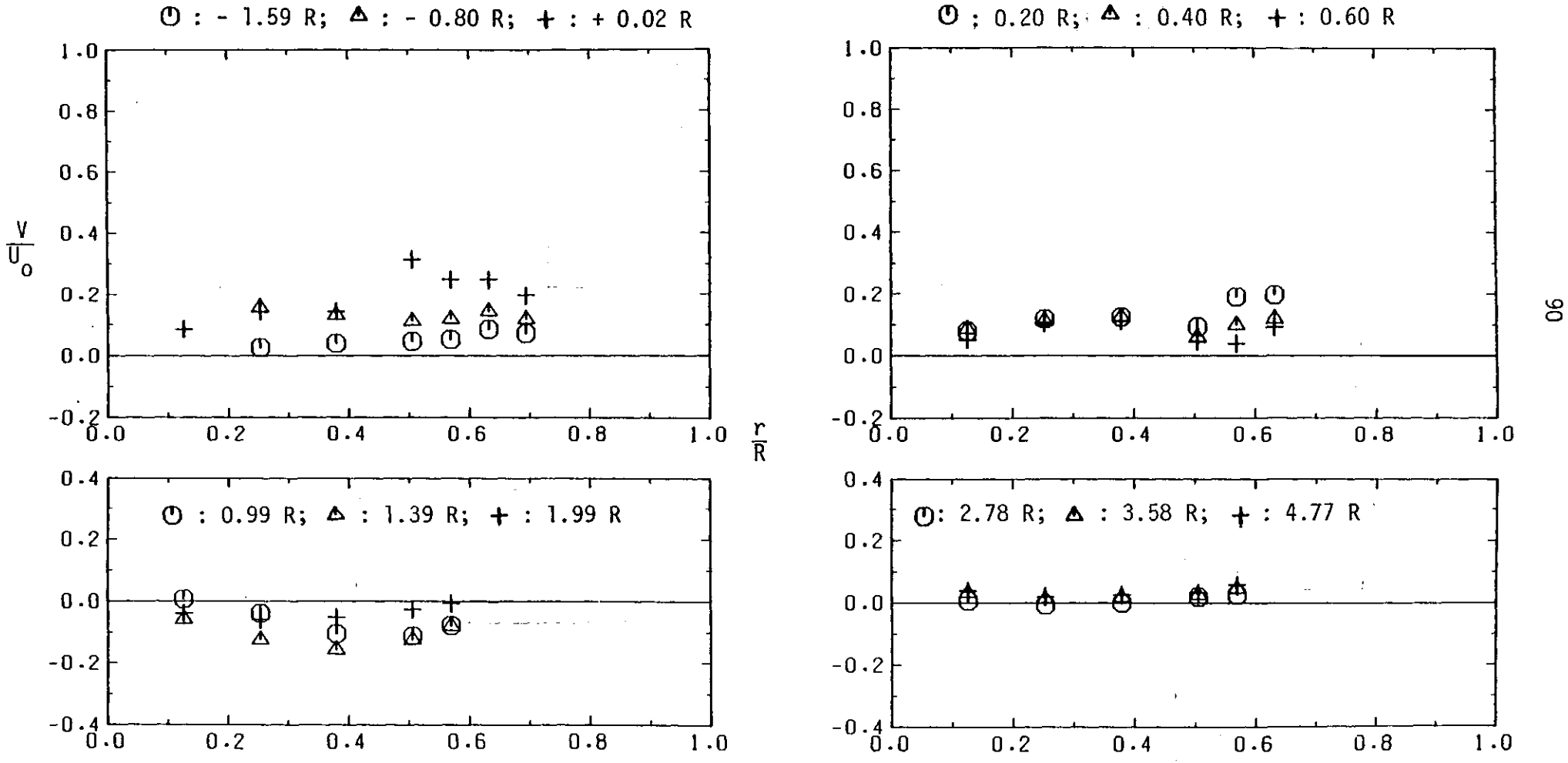

Figure 2.17 Cone, 25% blockage: radial profiles of radial velocity at successive axial stations (U_o = 1.53 m/s)

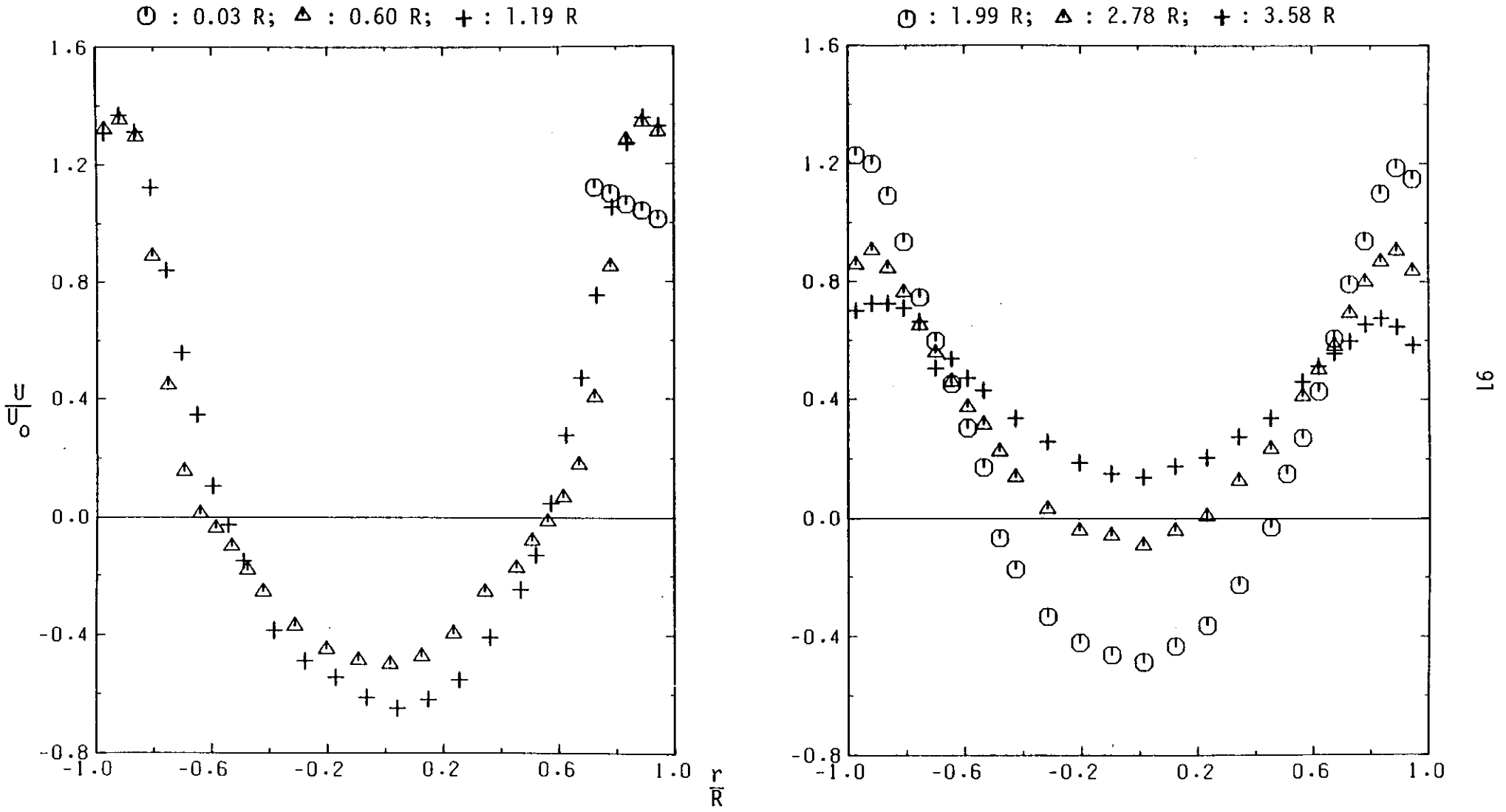

Figure 2.18 Disc, 50% blockage: radial profiles of axial velocity at successive axial stations (U_0 = 1.62 m/s)

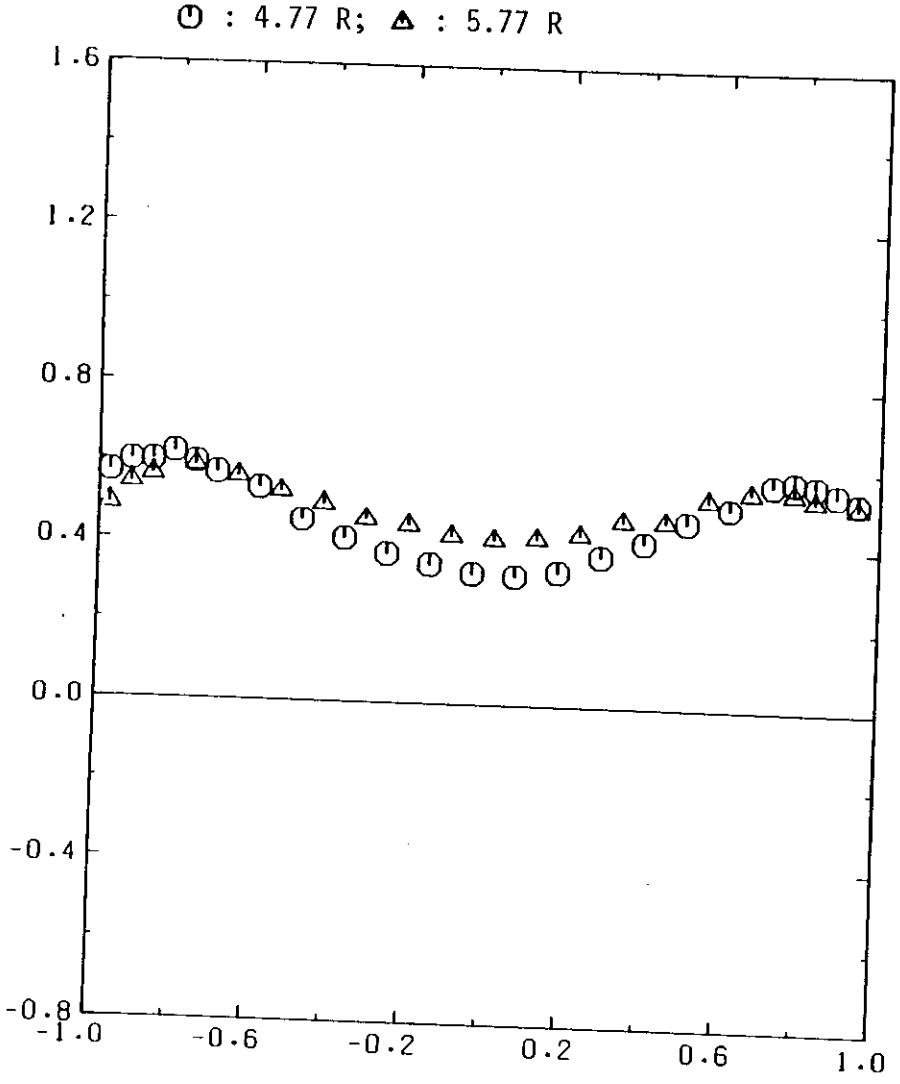

Figure 2.18 (Concluded)

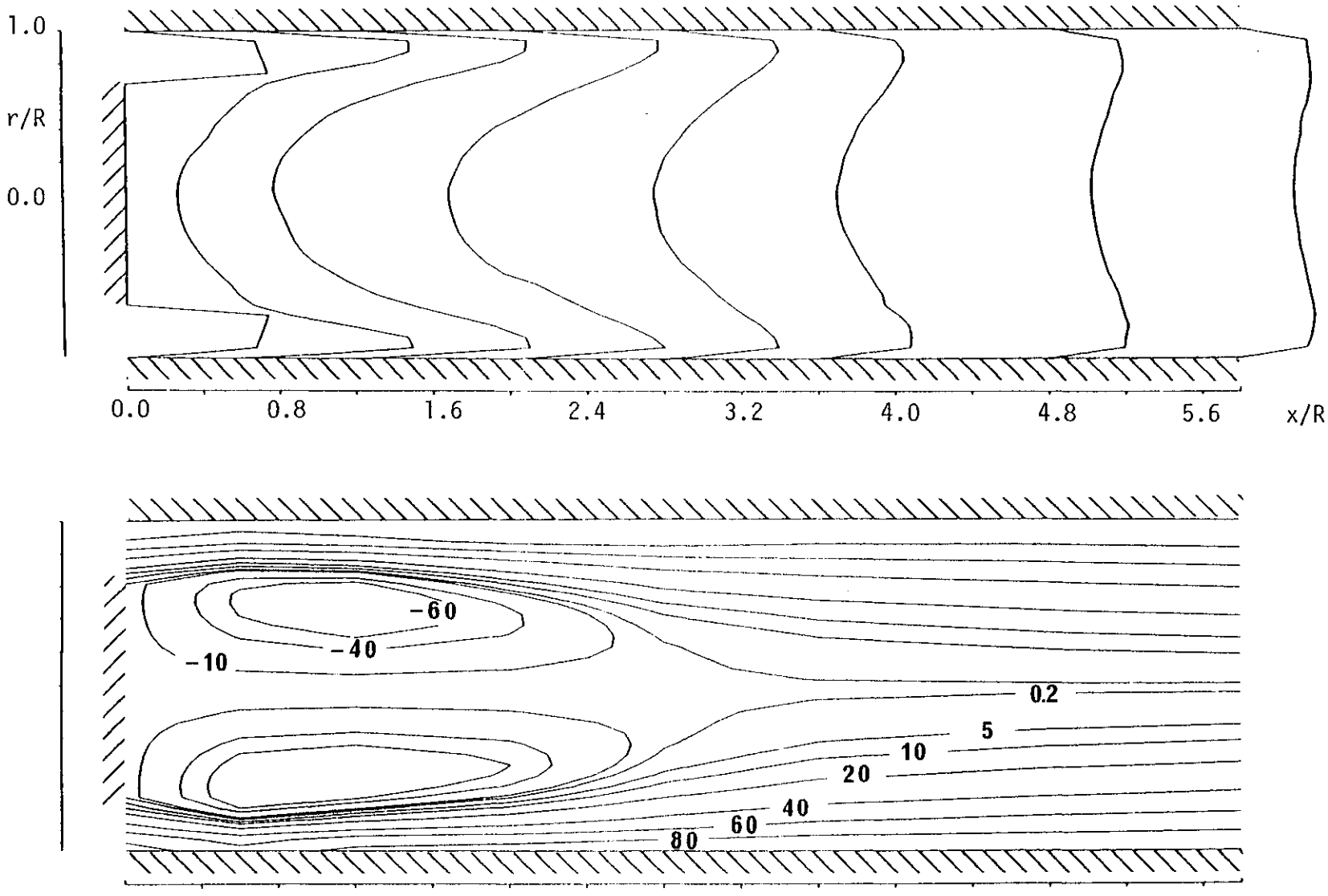

Figure 2.19 Disc, 50% blockage: profiles of axial velocity and corresponding contours of constant stream function (% of maximum positive and negative values)

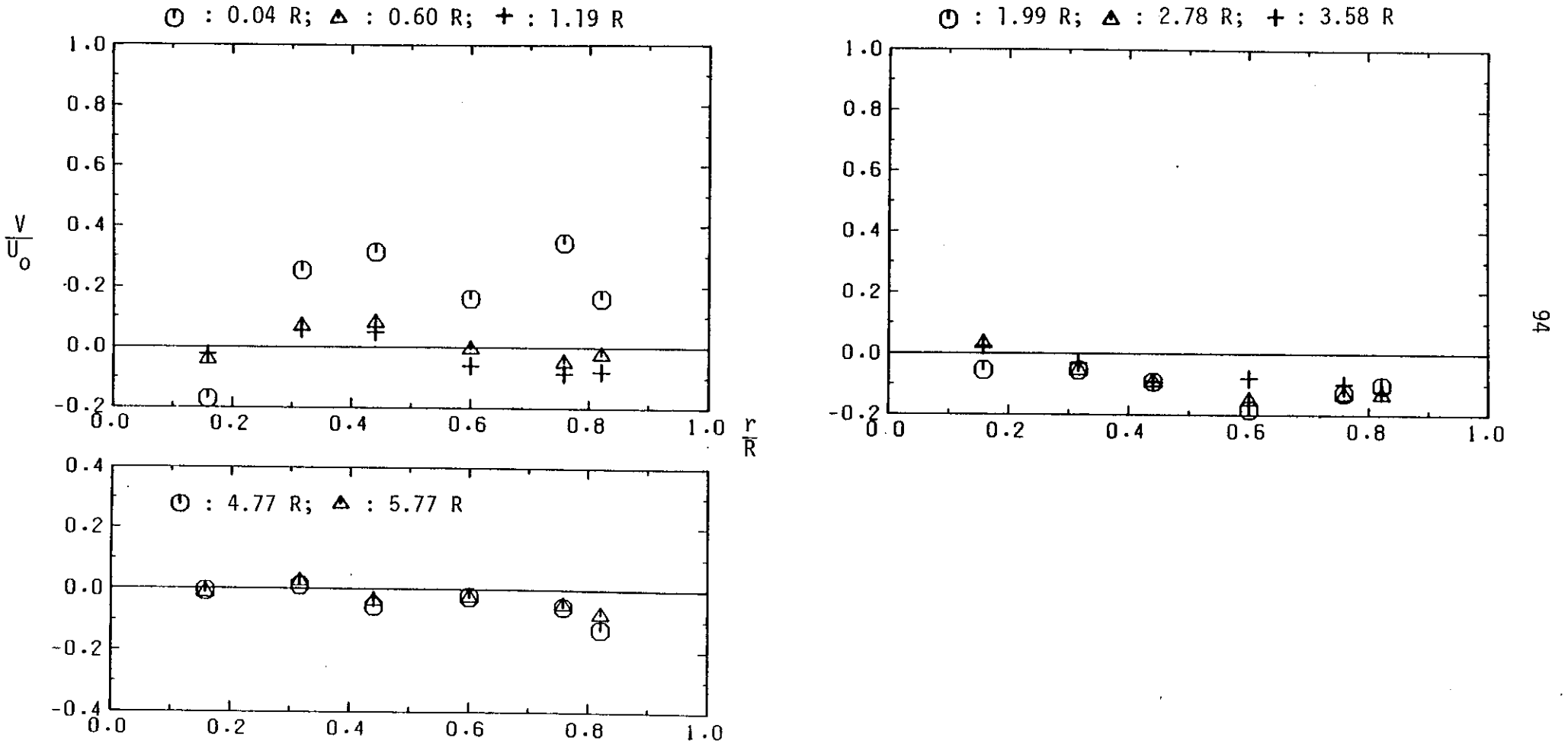

Figure 2.20 Disc, 50% blockage: radial profiles of radial velocity at successive axial stations (U_o = 1.62 m/s)

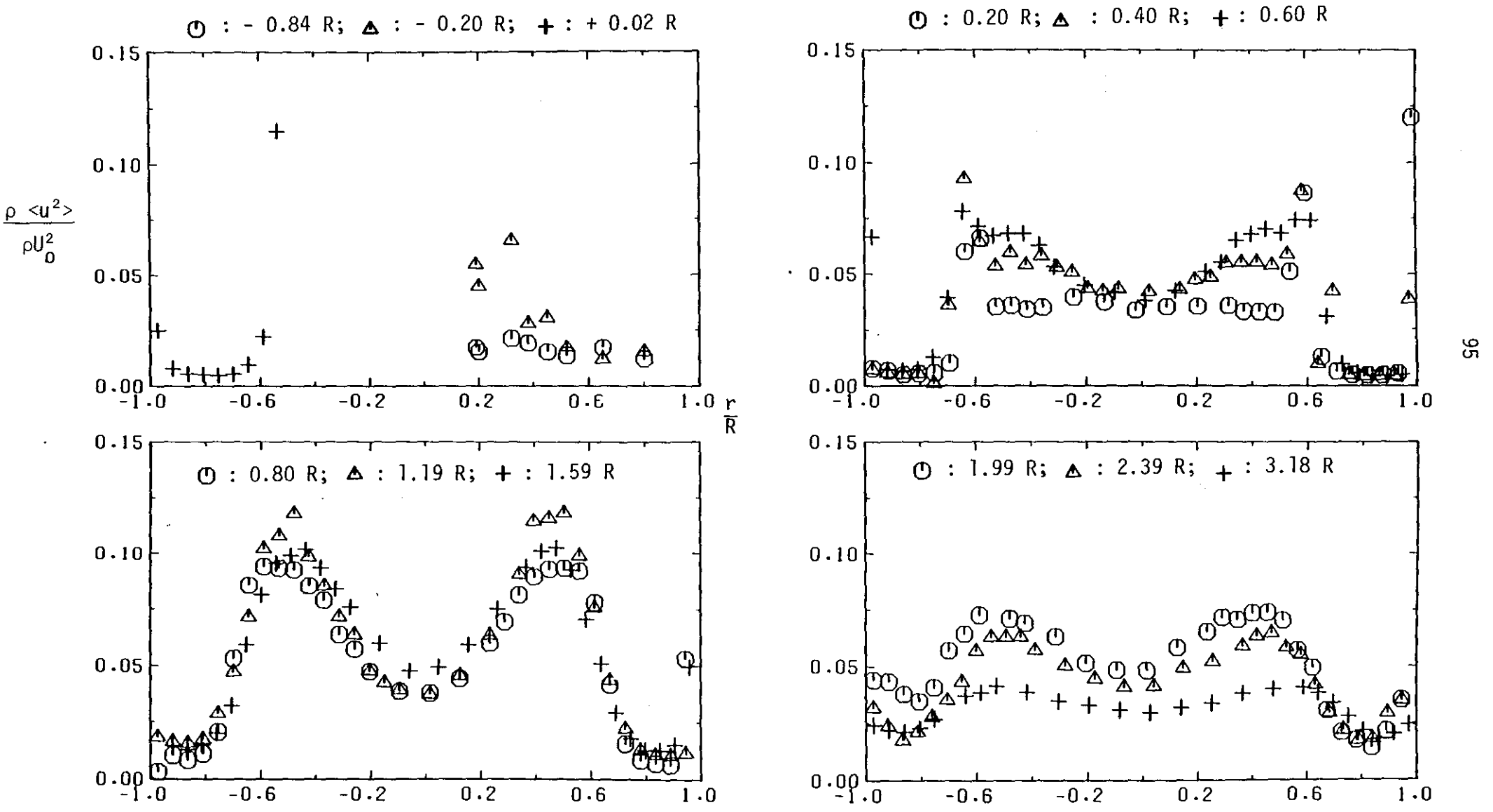

Figure 2.21 Disc, 25% blockage: radial profiles of axial Reynolds stress at successive axial stations (U_o = 1.37 ms^{-1})

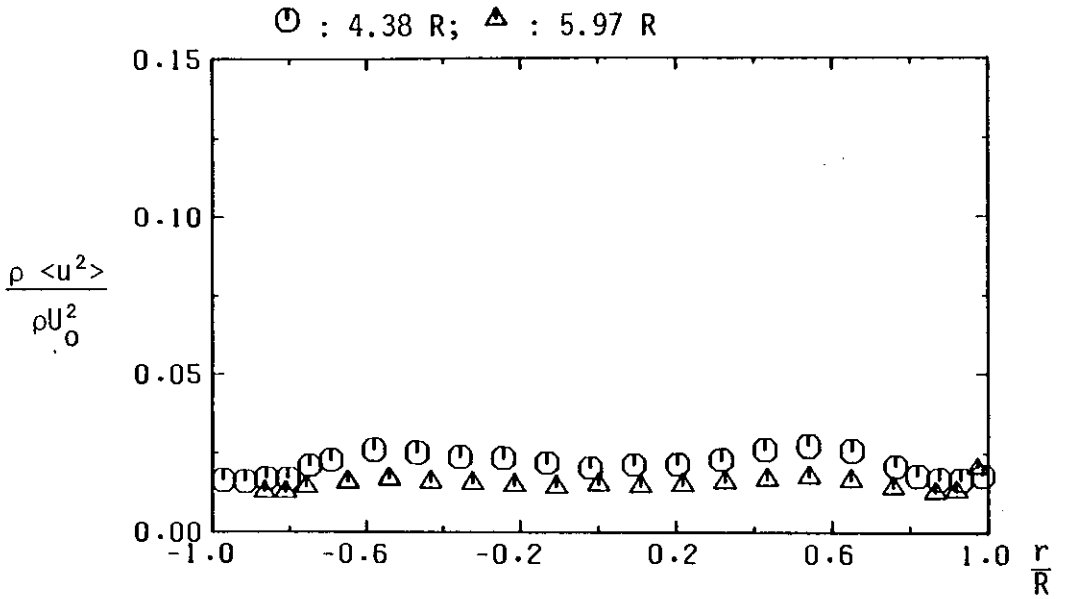

Figure 2.21 (Concluded)

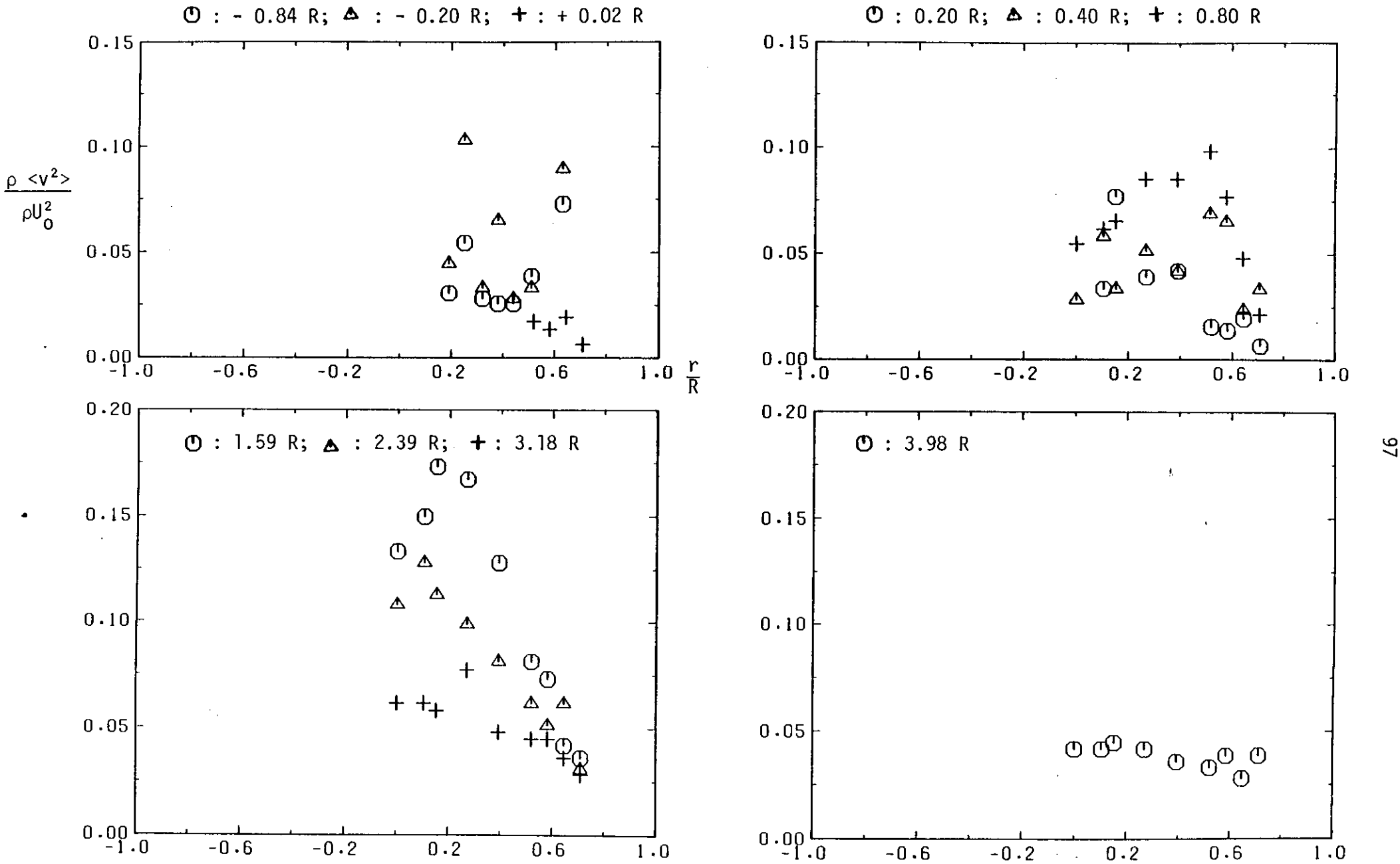

Figure 2.22 Disc, 25% blockage: radial profiles of radial Reynolds stress at successive axial stations (U_0 = 1.37 ms^{-1})

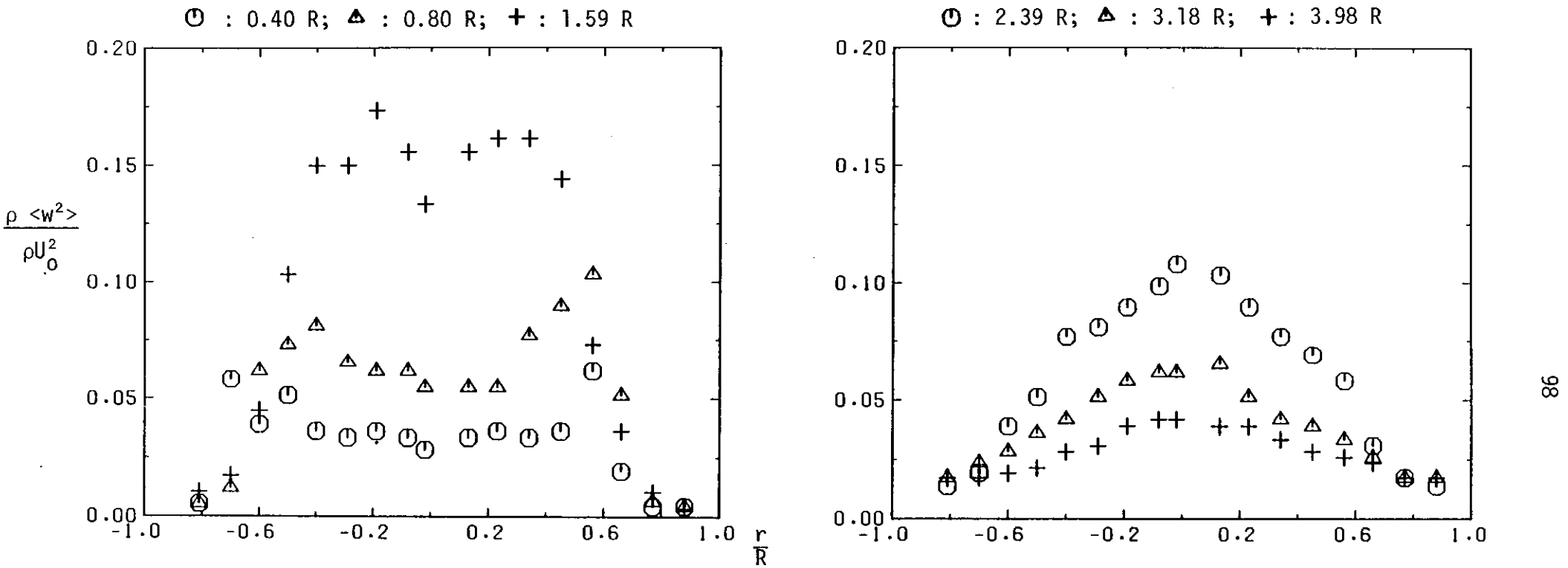

Figure 2.23 Disc, 25% blockage: radial profiles of azimuthal Reynolds stress at successive axial stations (U_0 = 1.37 ms^{-1})

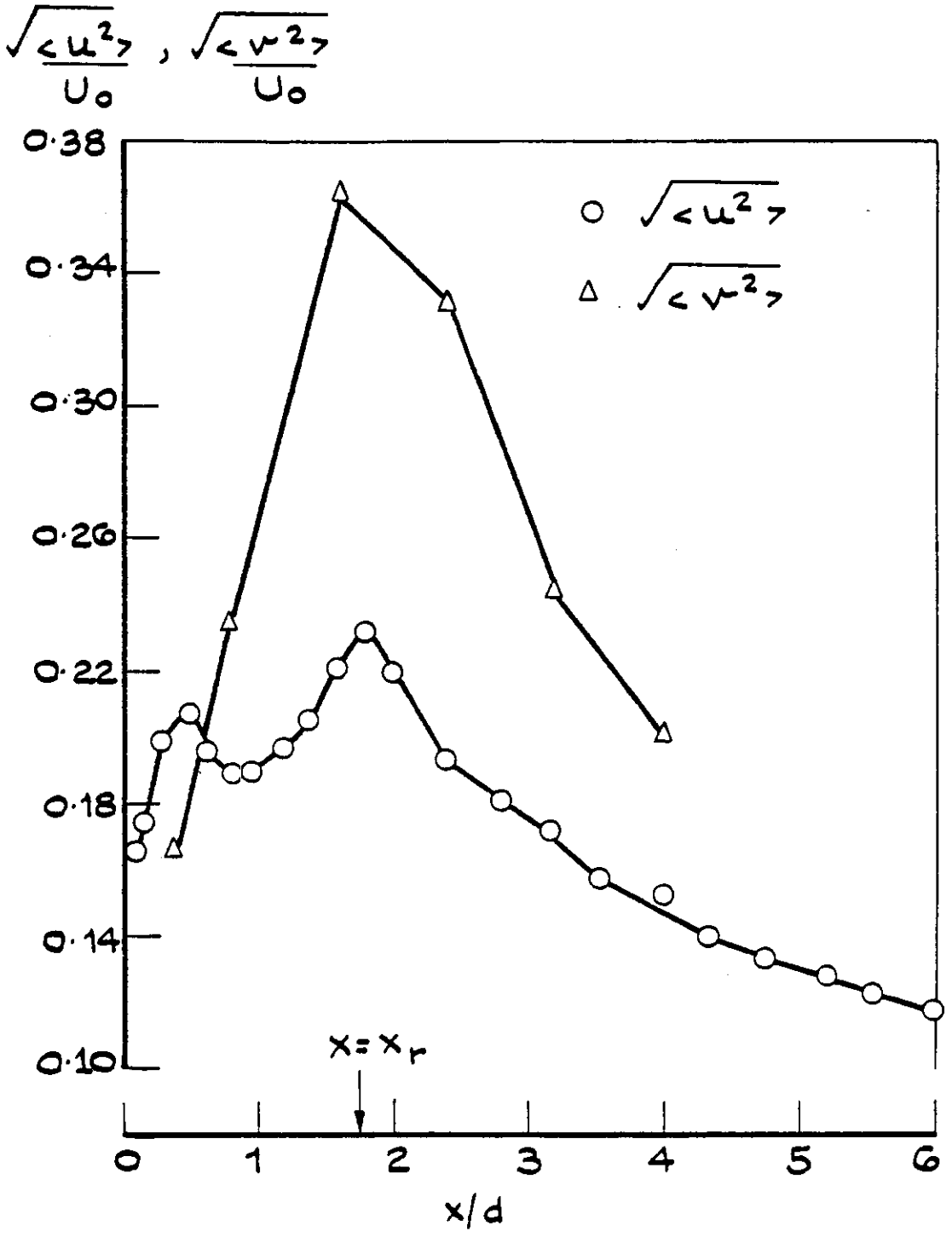

Figure 2.24 Disc, 25% blockage: centreline values of turbulence intensity

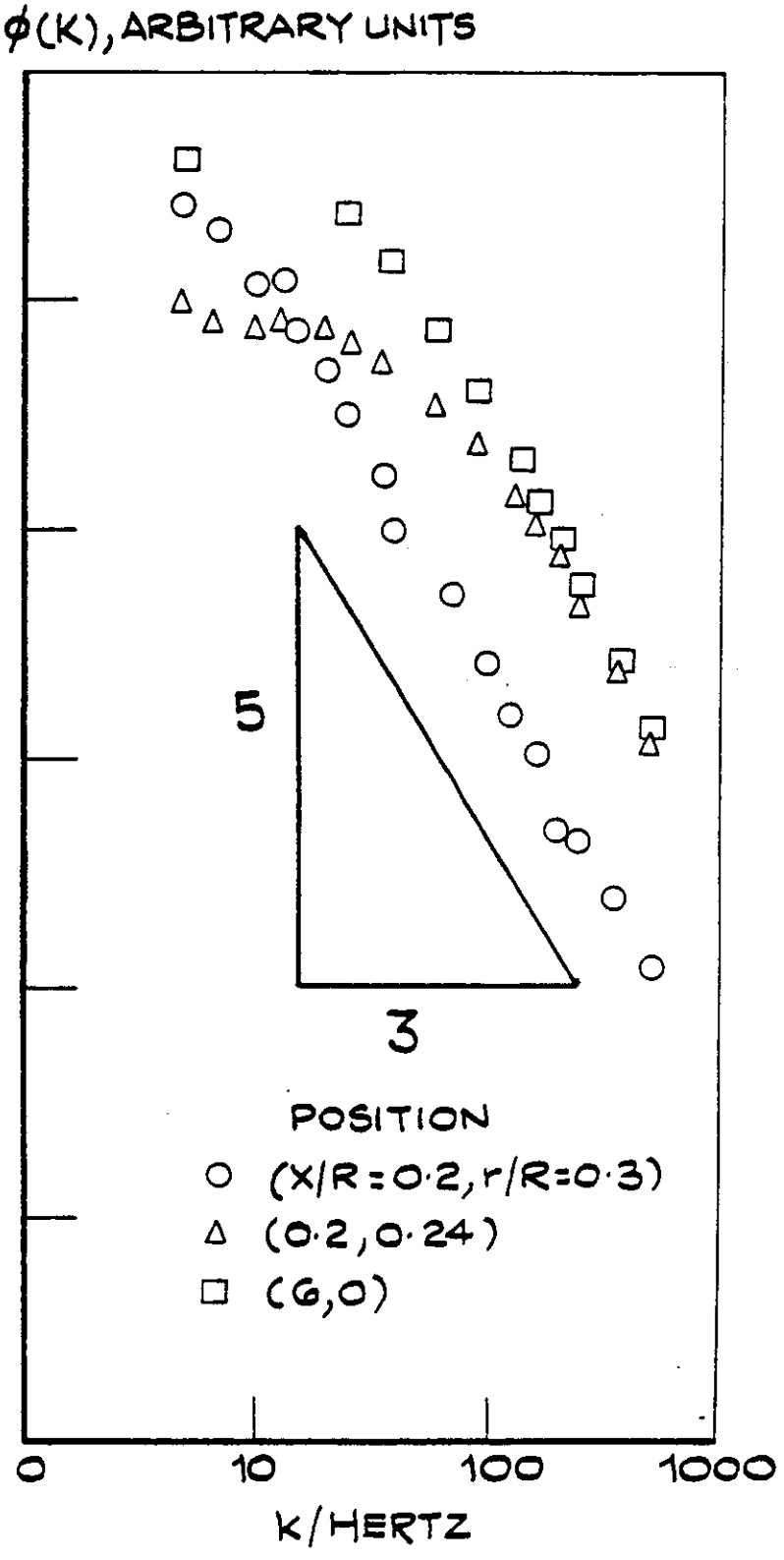

Figure 2.25 Disc, 25% blockage: turbulent power spectral densities

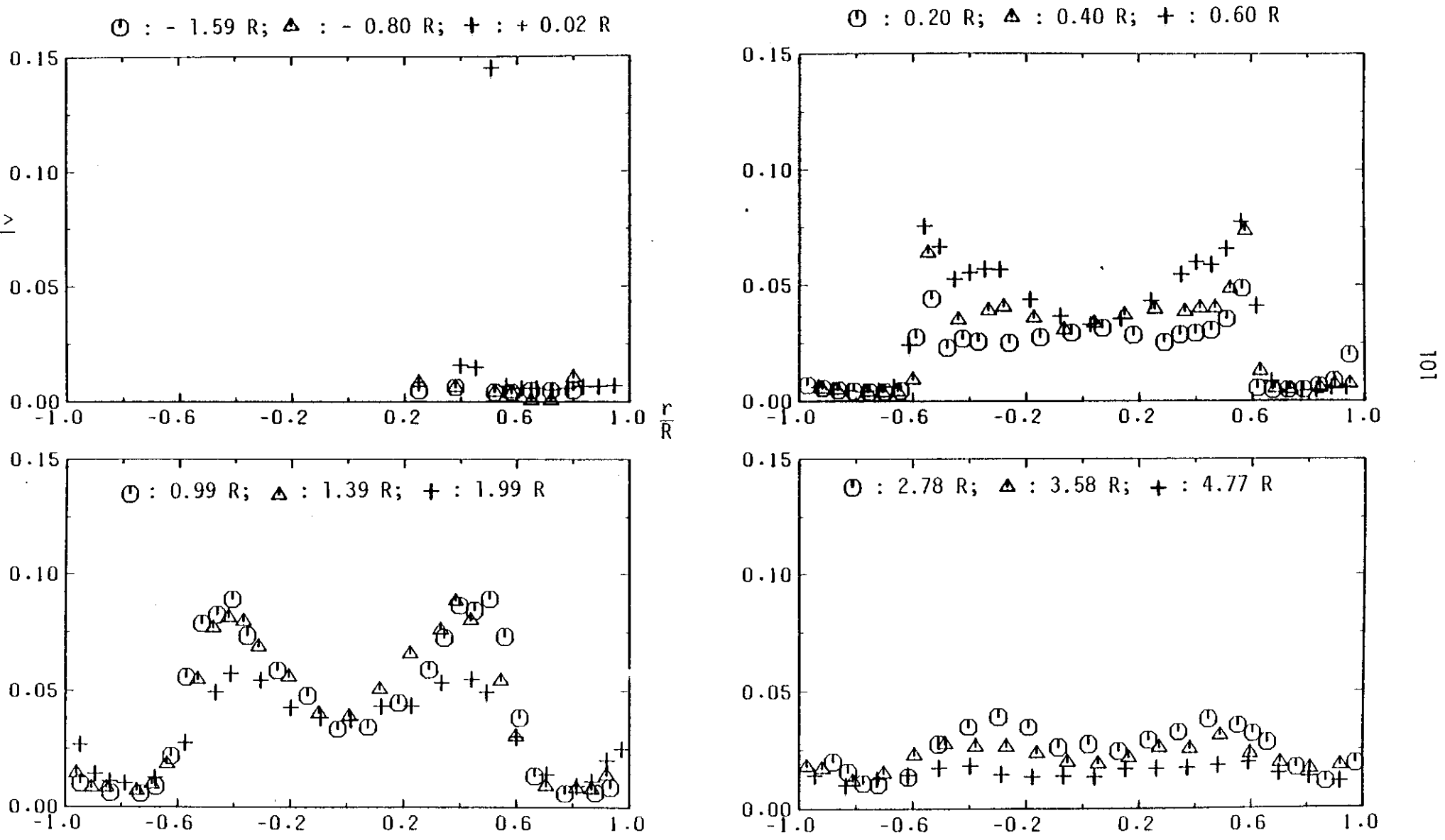

Figure 2.26 Cone 25% blockage: radial profiles of axial Reynolds stress at successive axial stations (U_o = 1.53 ms^{-1})

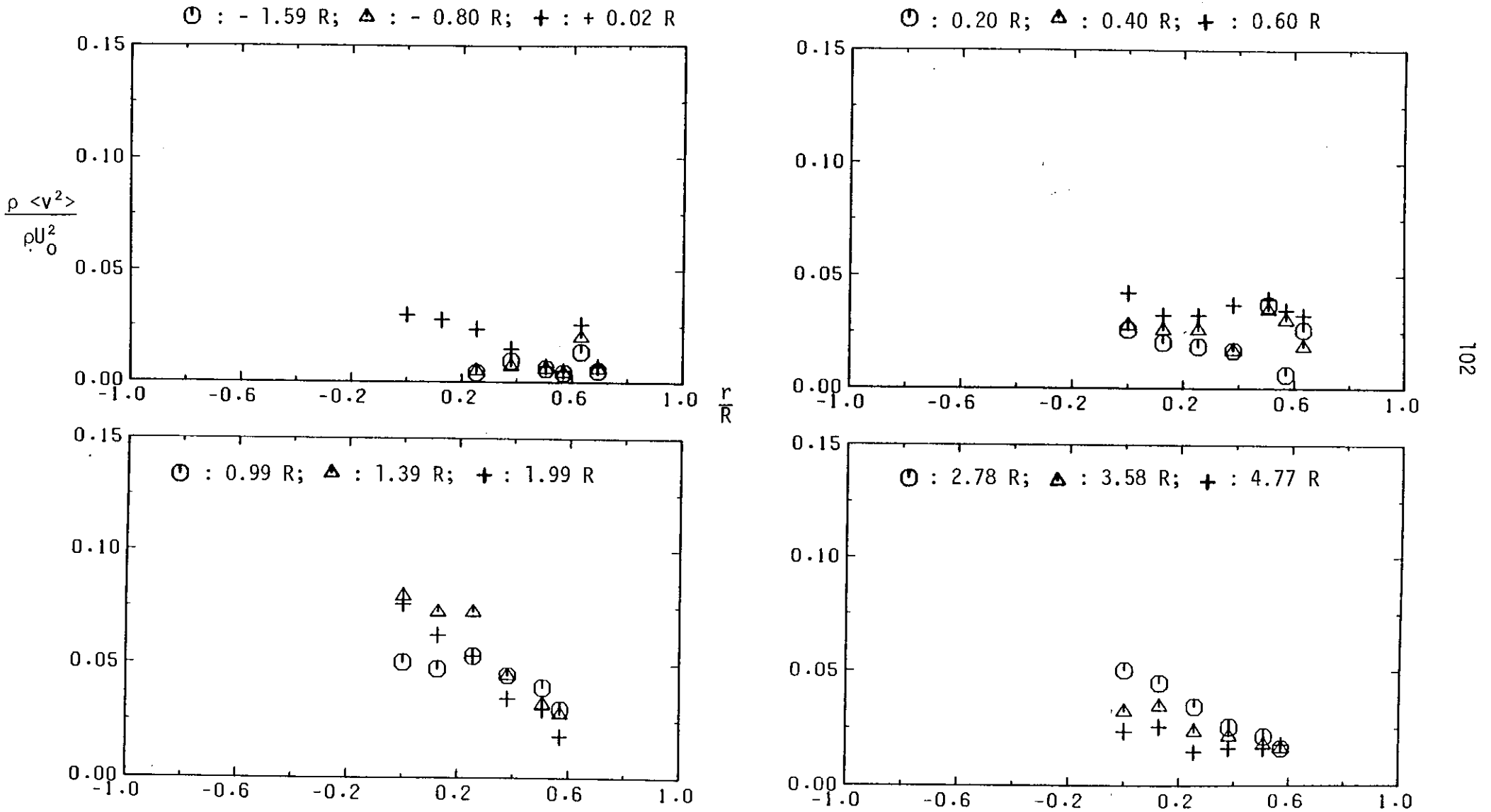

Figure 2.27 Cone, 25% blockage: radial profiles of radial Reynolds stress at successive axial stations (U_o = 1.53 ms^{-1})

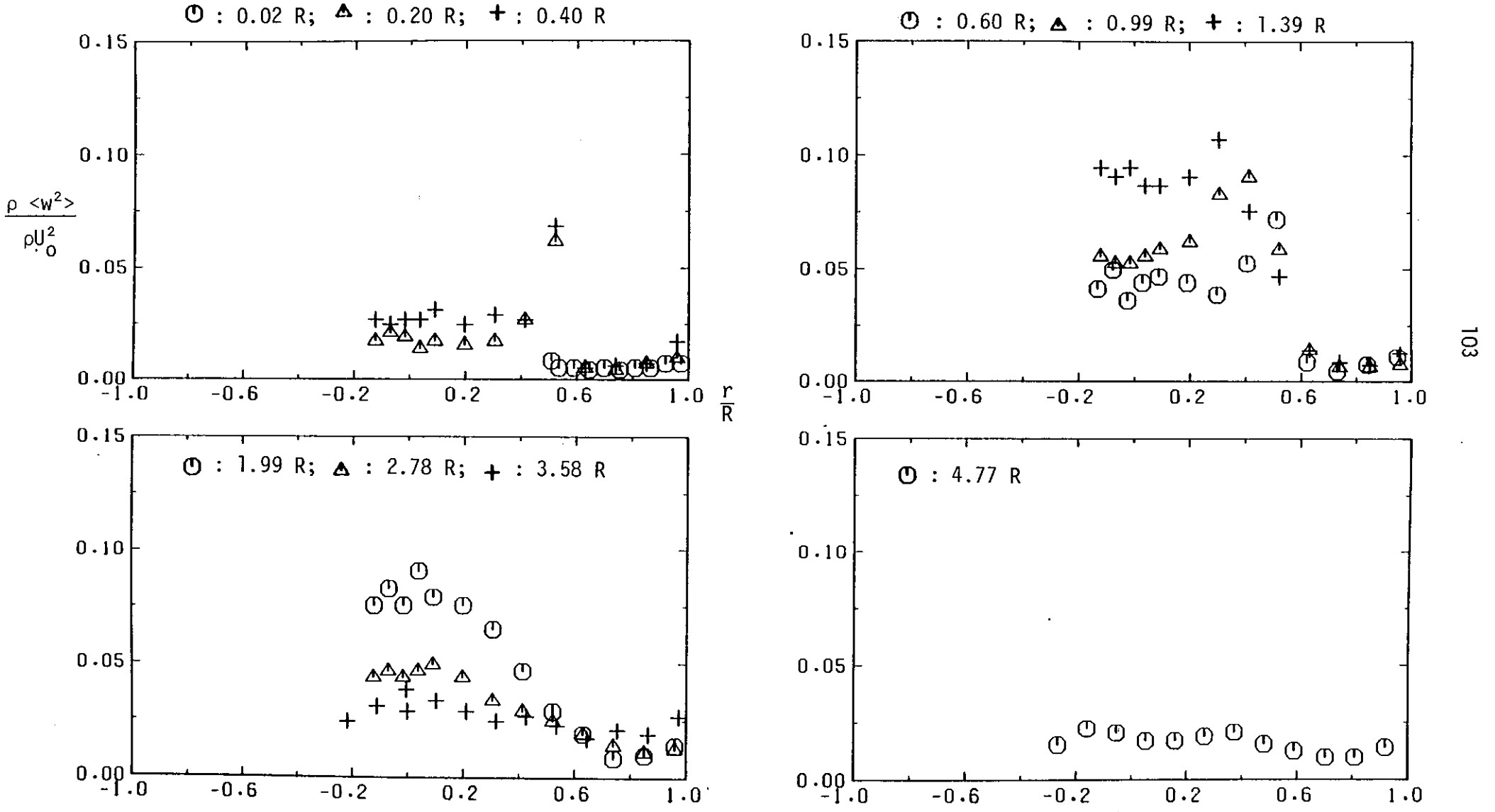

Figure 2.28 Cone, 25% blockage: radial profiles of azimuthal Reynolds stress at successive axial stations (U_o = 1.53 ms^{-1})

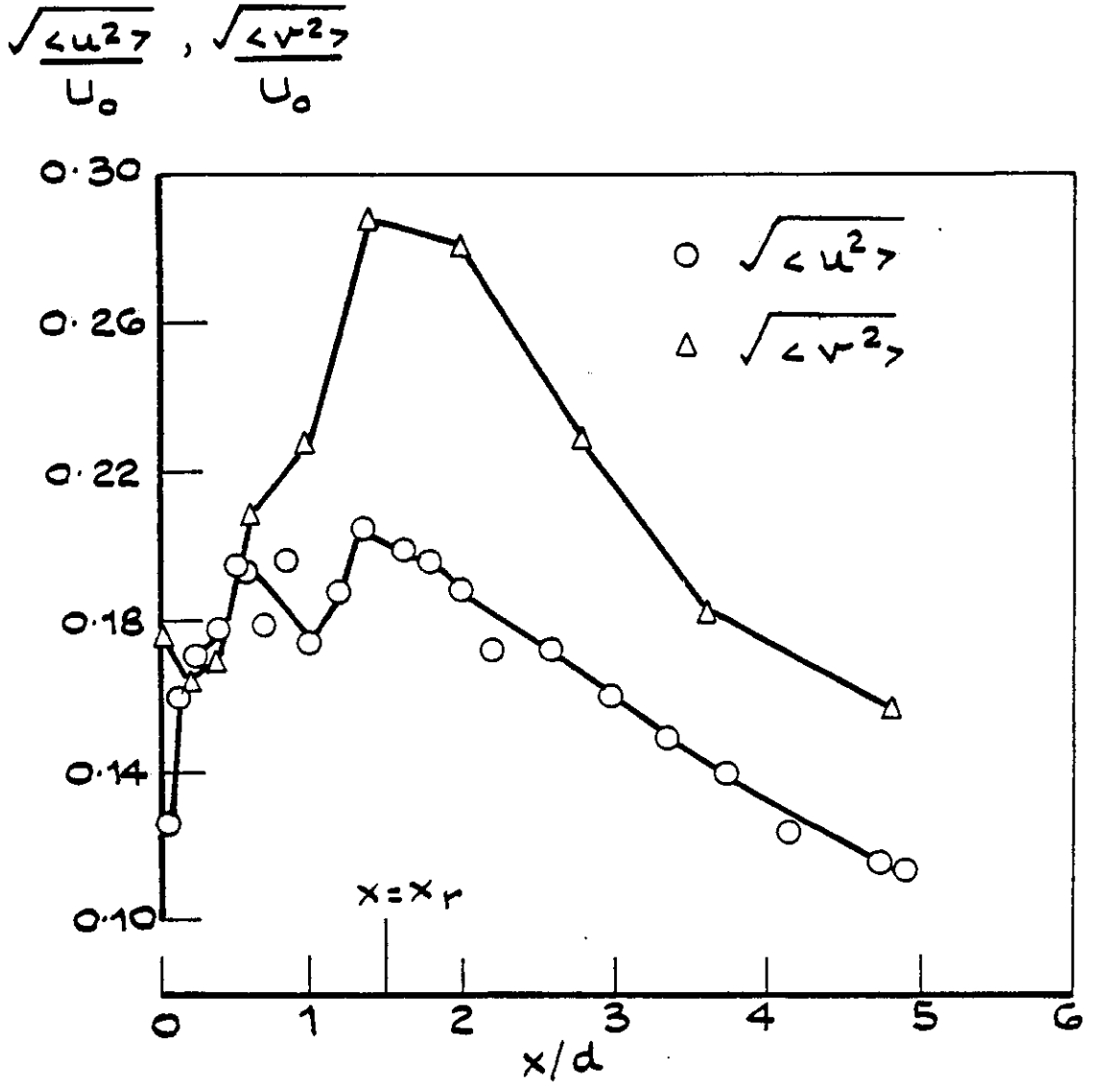

Figure 2.29 Cone, 25% blockage: centreline values of turbulence intensity

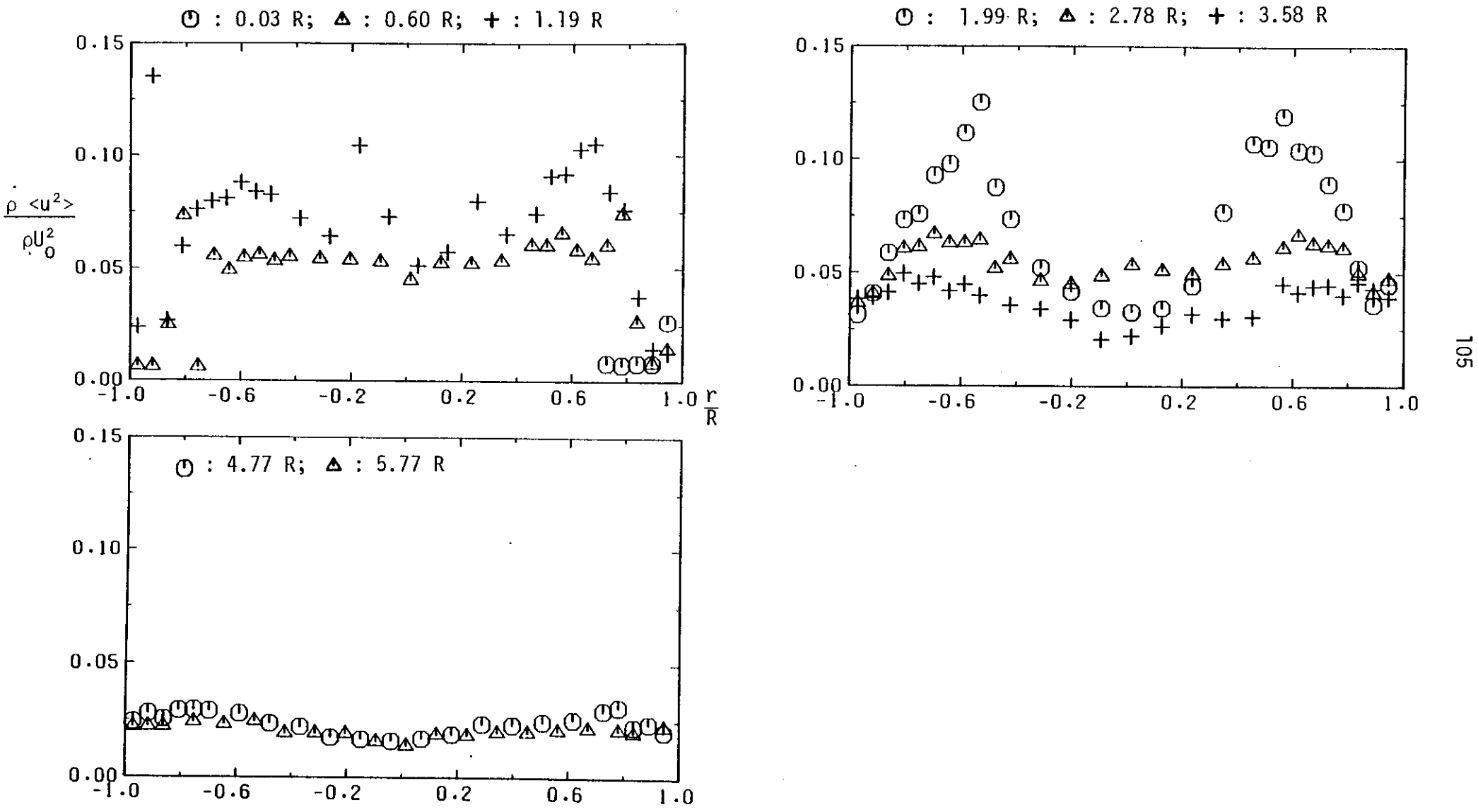

Figure 2.30 Disc, 50% blockage: radial profiles of axial Reynolds stress at successive axial stations (U_0 = 1.62 ms^{-1})

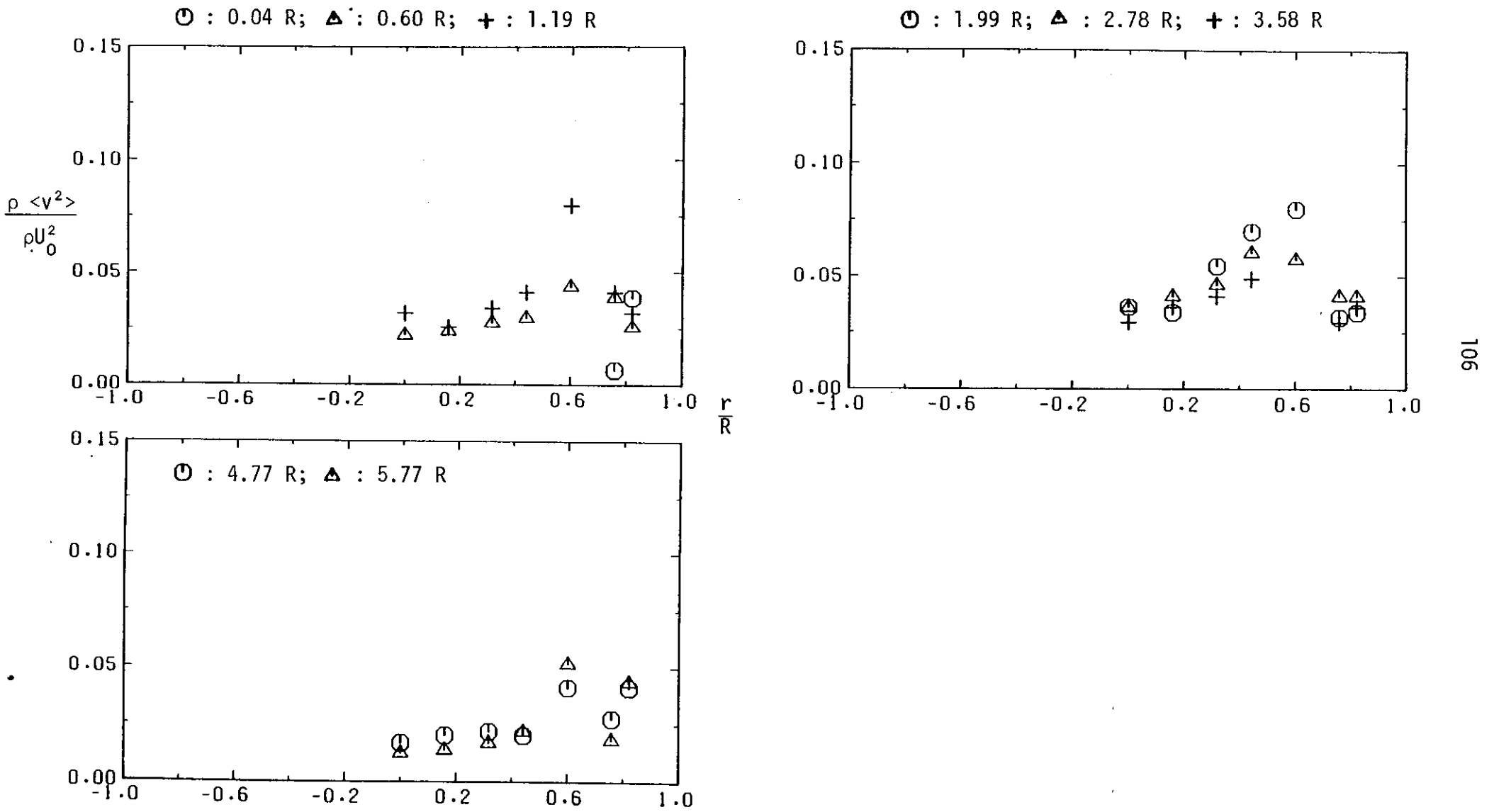

Figure 2.31 Disc, 50% blockage: radial profiles of radial Reynolds stress at successive axial stations (U_0 = 1.62 ms^{-1})

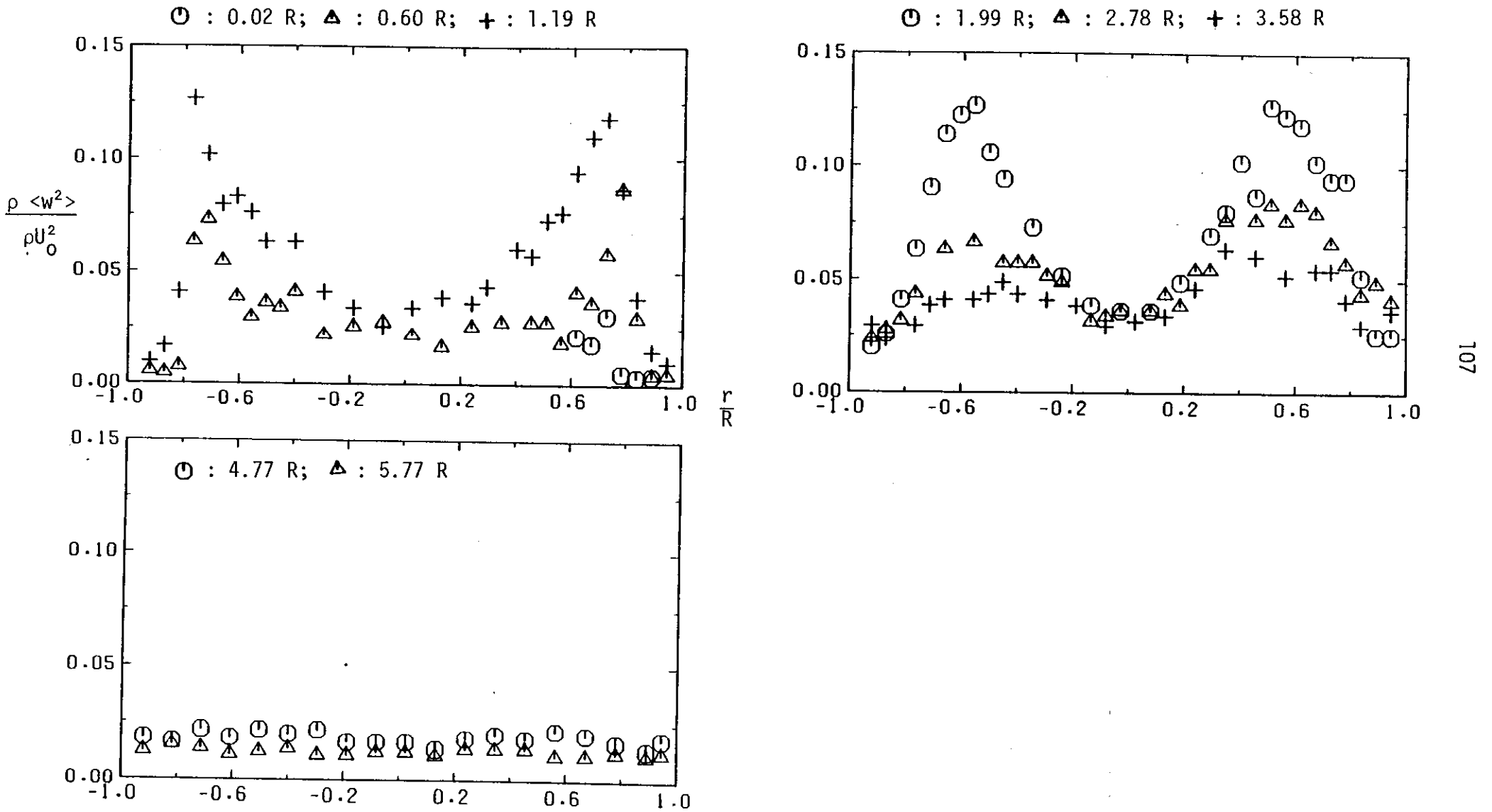

Figure 2.32 Disc, 50% blockage: radial profiles of azimuthal Reynolds stress at successive axial stations (U_0 = 1.62 ms^{-1})

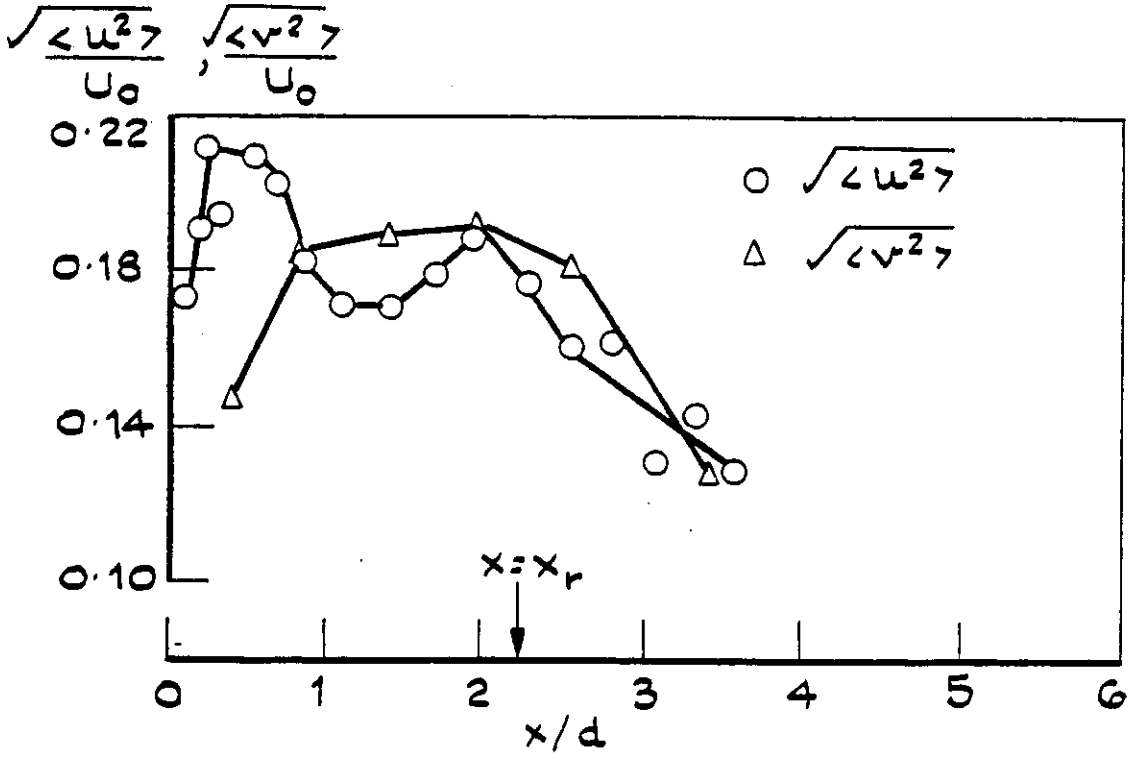

Figure 2.33 Disc, 50% blockage: centreline values of turbulence intensity

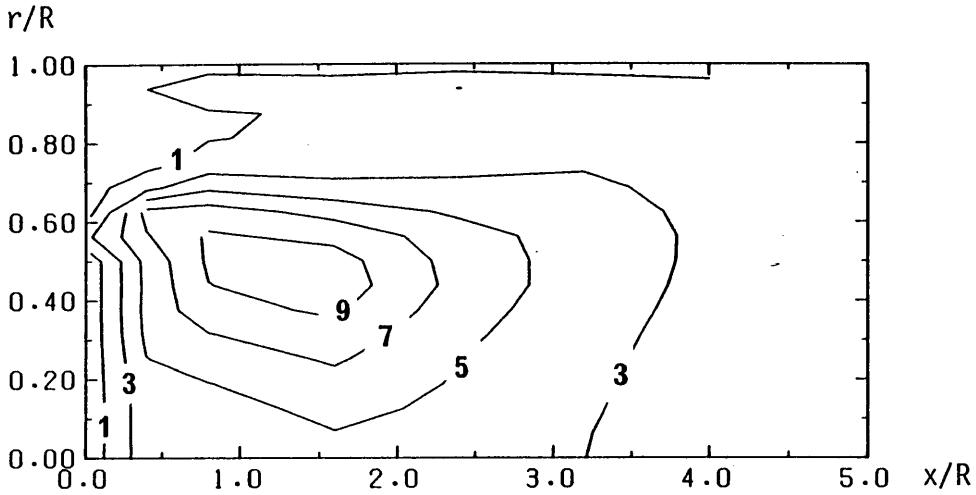

(a) Axial component Reynolds stress

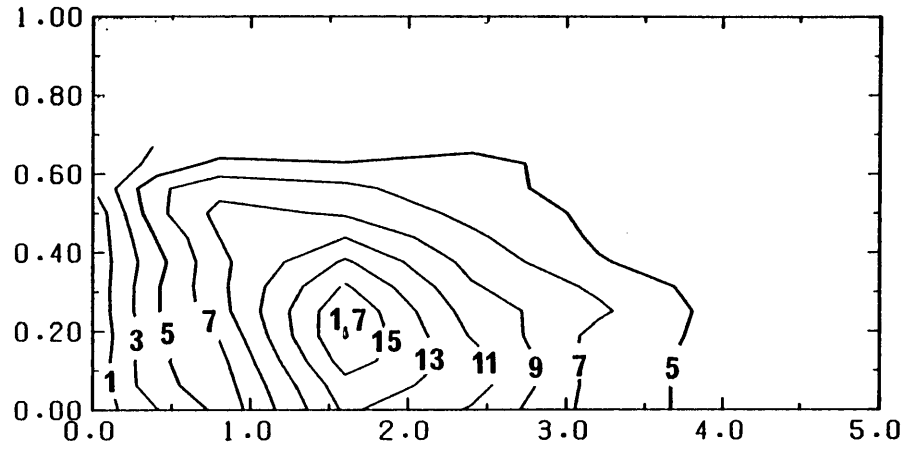

(b) Radial component Reynolds stress

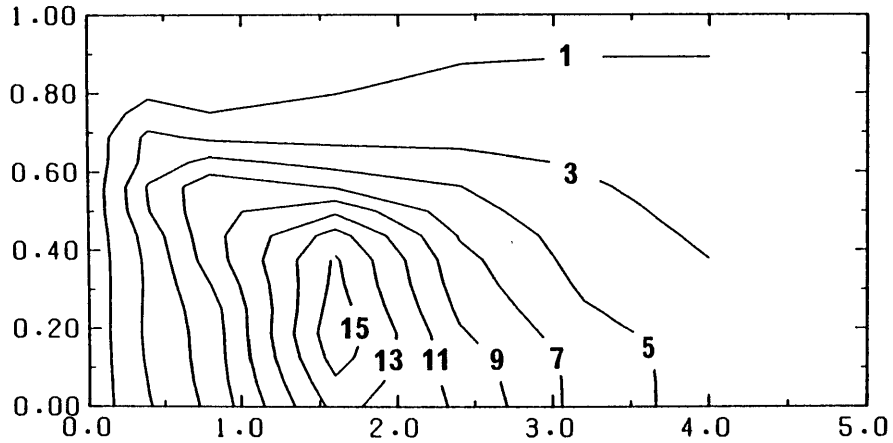

(c) Azimuthal component Reynolds stress

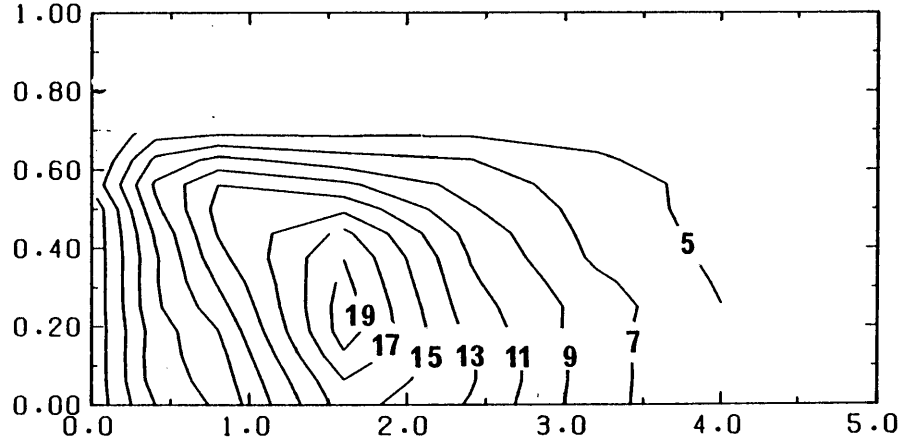

(d) Turbulent kinetic energy

Figure 2.34 Disc, 25% blockage: contours of Reynolds stress (per cent ρU_0^2; U_0 = 1.37 m/s)

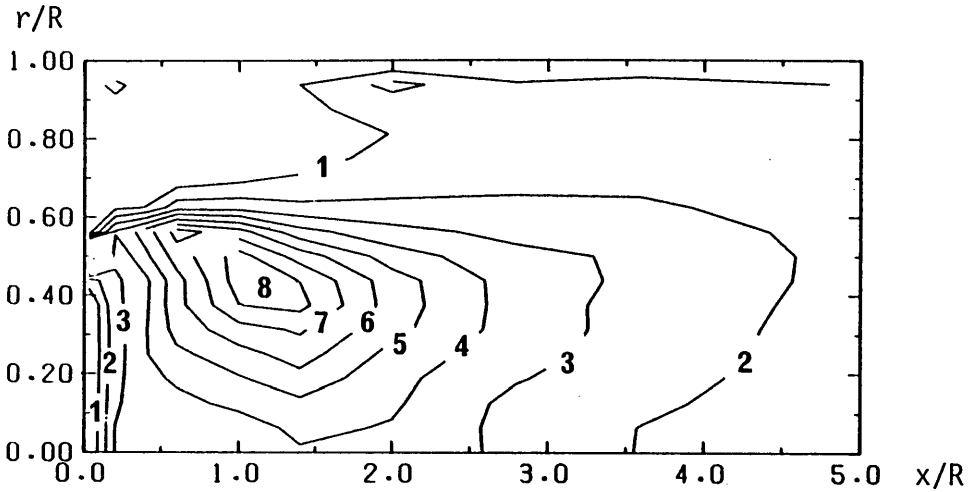

(a) Axial component Reynolds stress

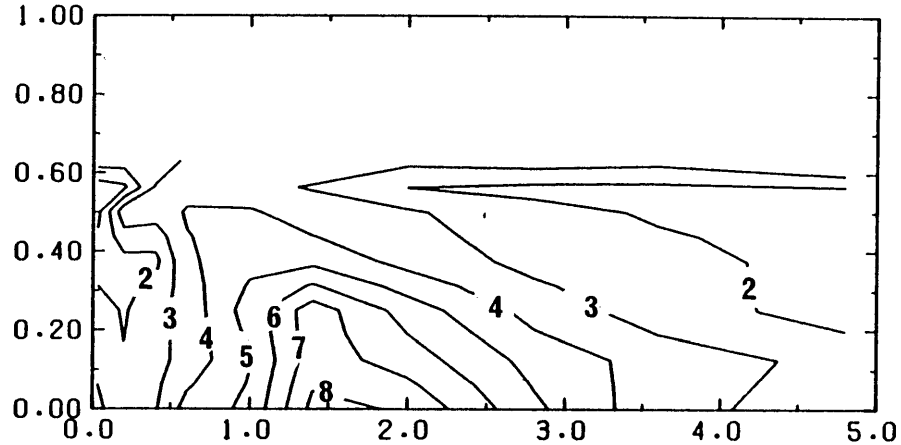

(b) Radial component Reynolds stress

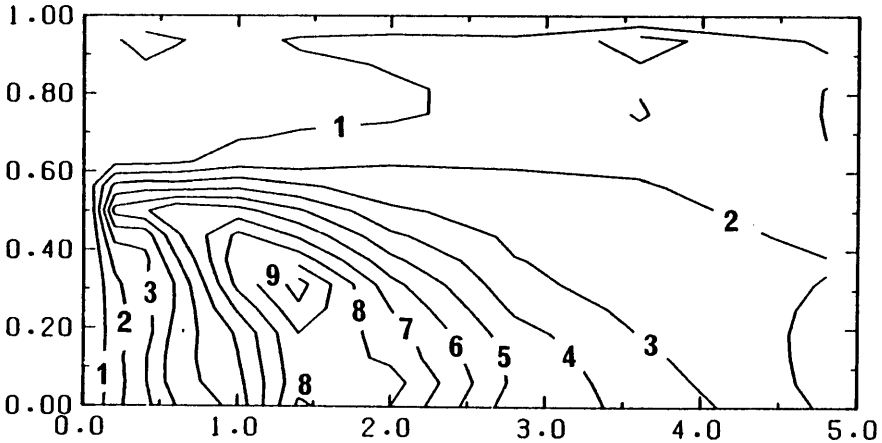

(c) Azimuthal component stress

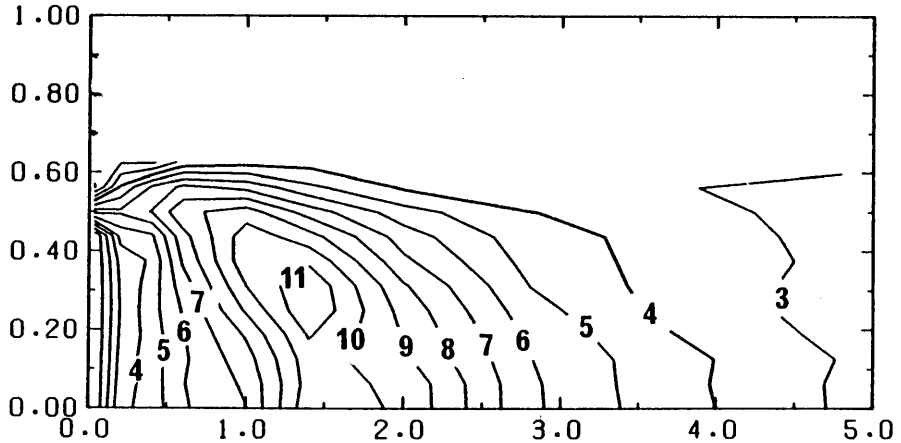

(d) Turbulent kinetic energy

Figure 2.35 Cone, 25% blockage: contours of Reynolds stress (per cent ρU_o^2; U_o = 1.53 ms^{-1})

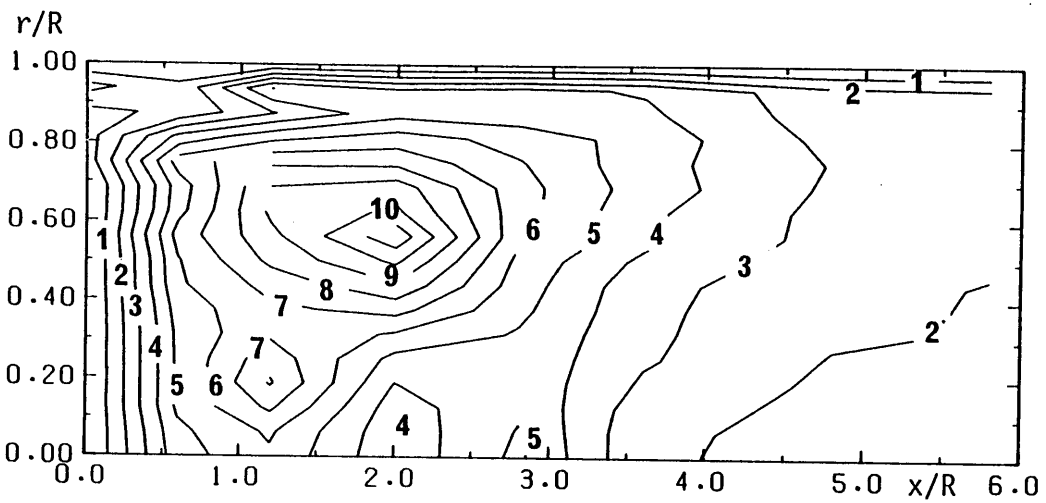

(a) Axial component Reynolds stress

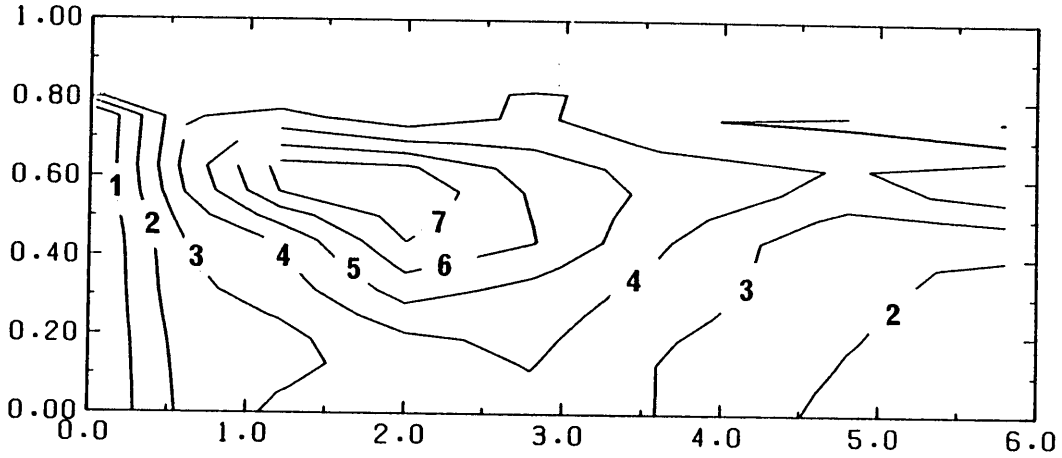

(b) Radial component Reynolds stress

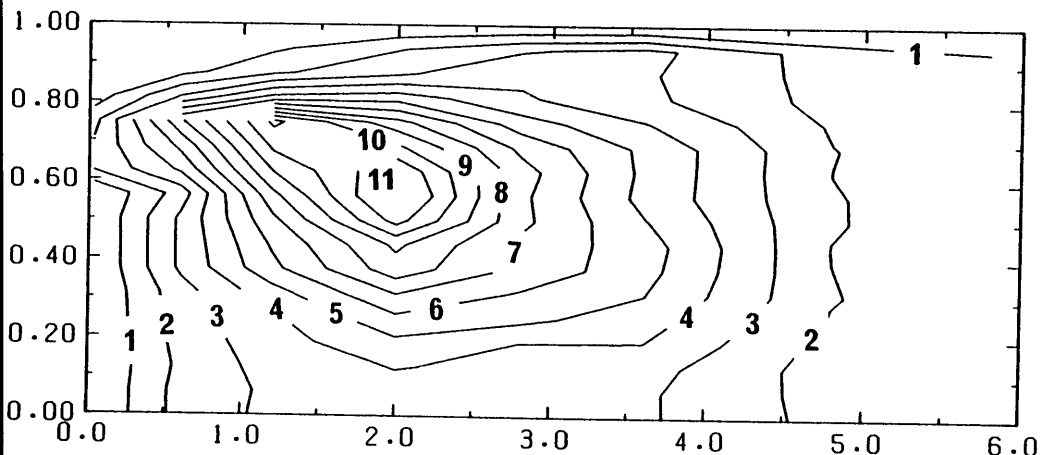

(c) Azimuthal component Reynolds stress

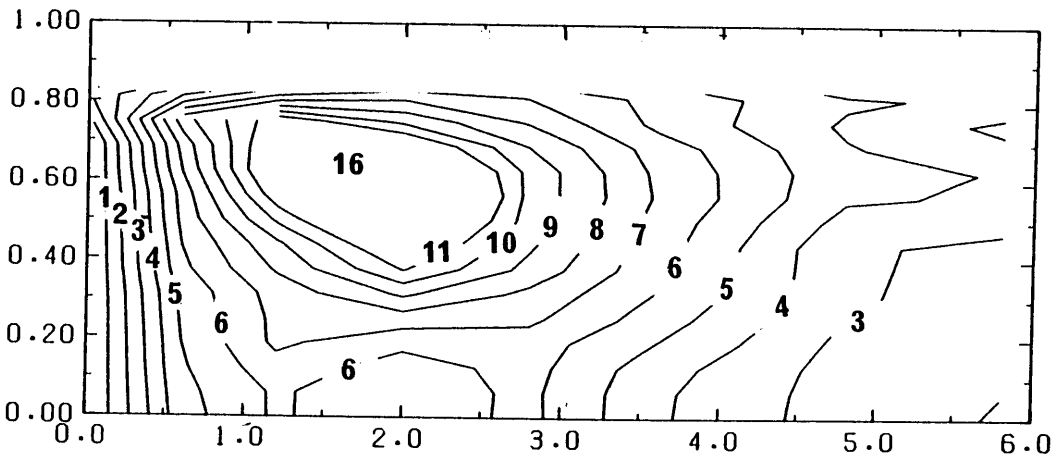

(d) Turbulent kinetic energy

Figure 2.36 Disc, 50% blockage: contours of Reynolds stress (per cent ρU_o^2; U_o = 1.62 m/s)

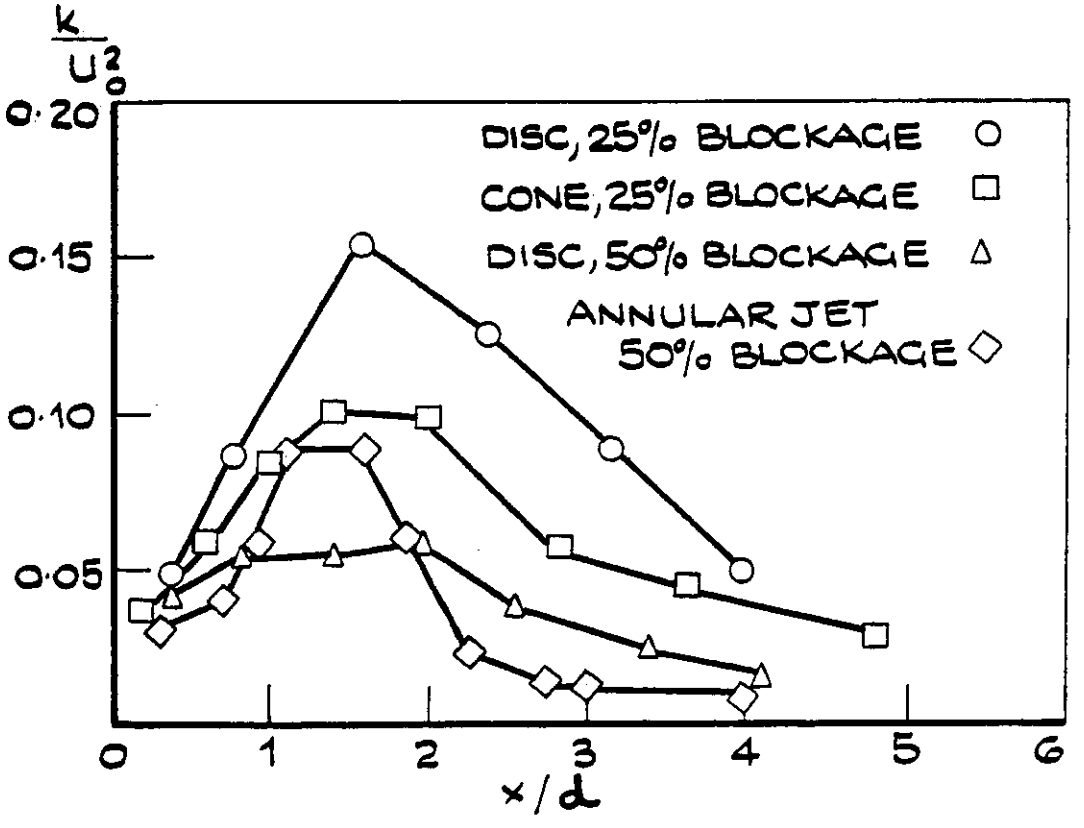

Figure 2.37 Centreline values of turbulent kinetic energy

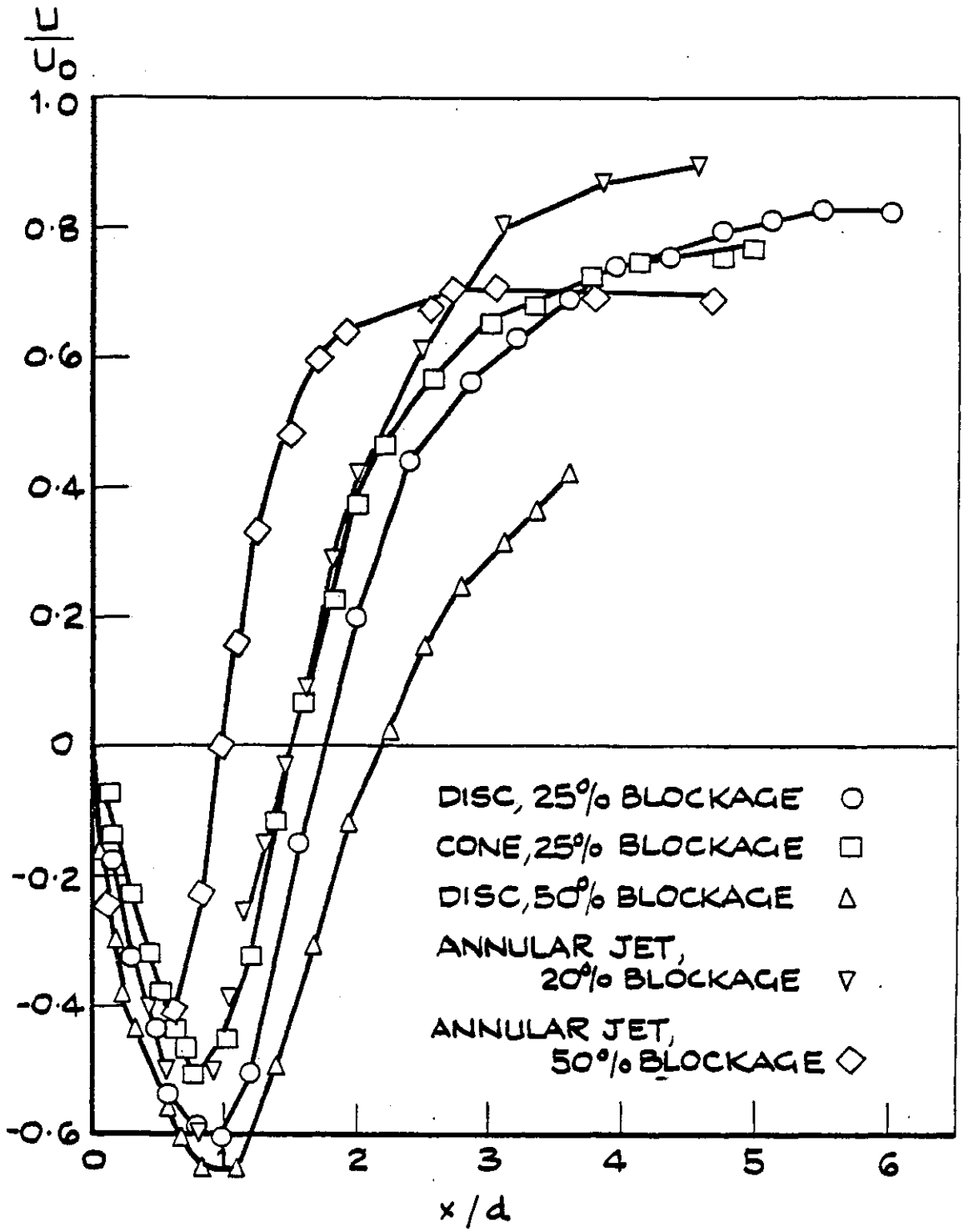

Figure 2.38 Centreline profiles of axial velocity for confined flows and annular jets

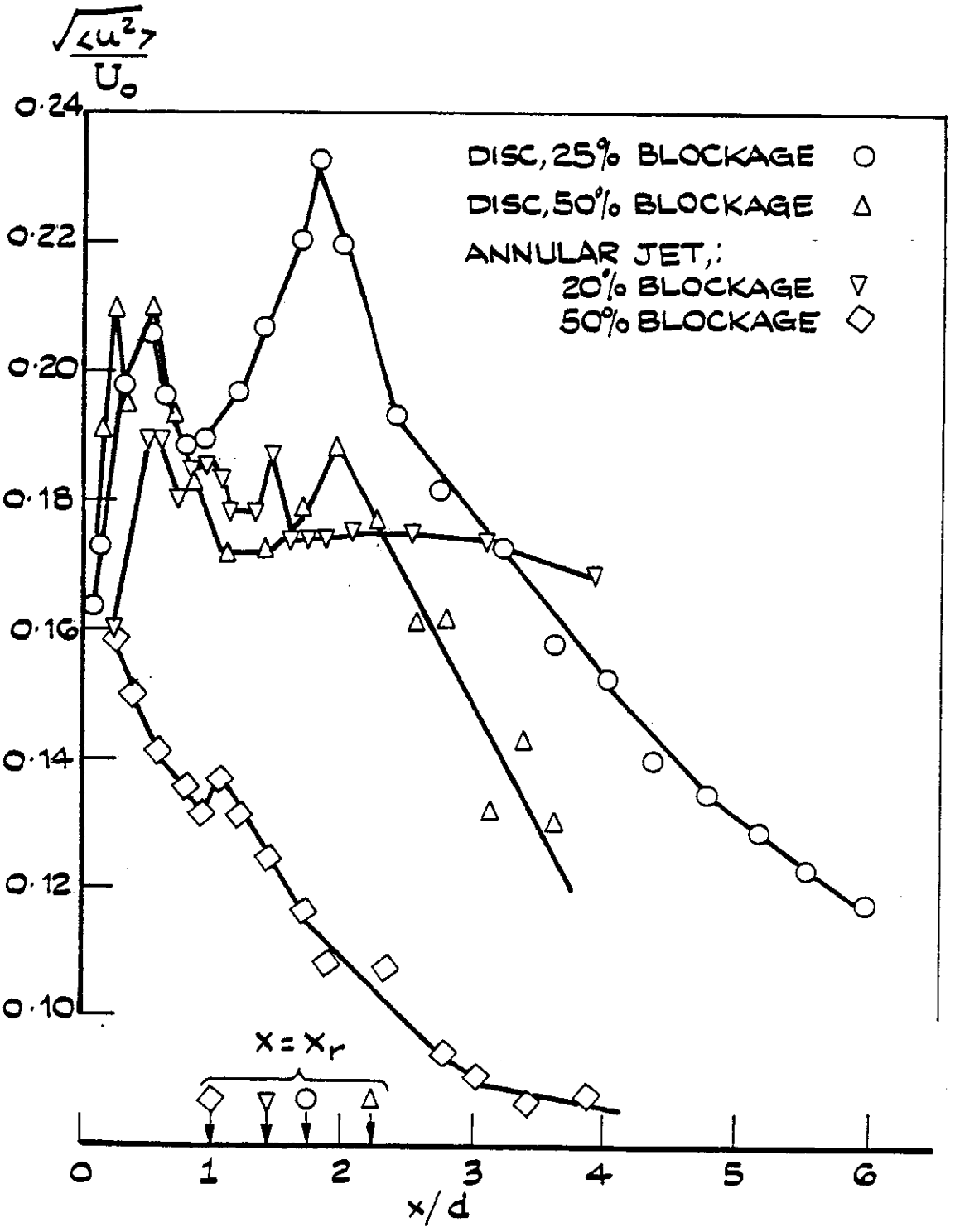

Figure 2.39(a) Centreline values of turbulence intensity for confined flows and annular jets

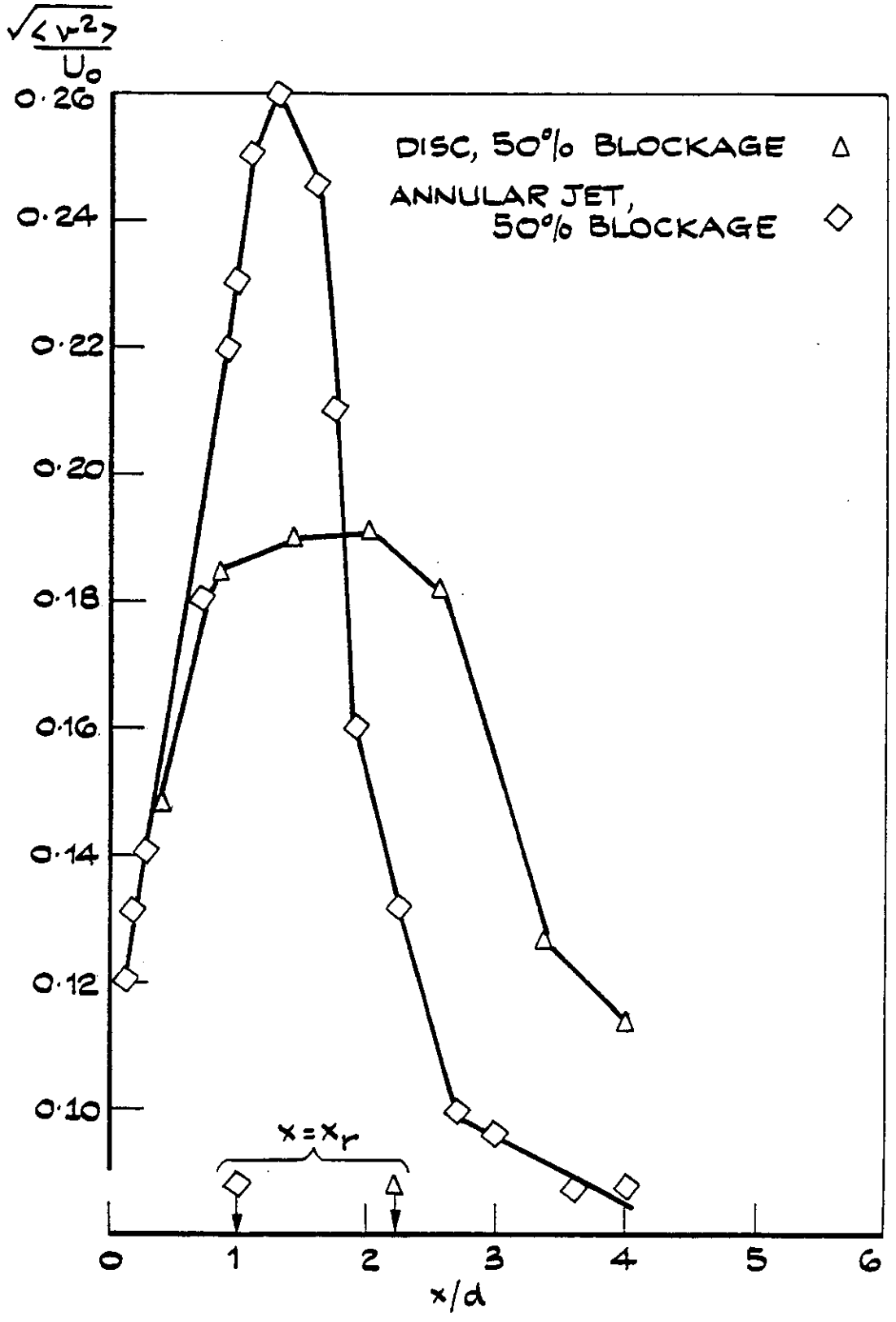

Figure 2.39(b) Centreline values of turbulence intensity for confined flows and annular jets

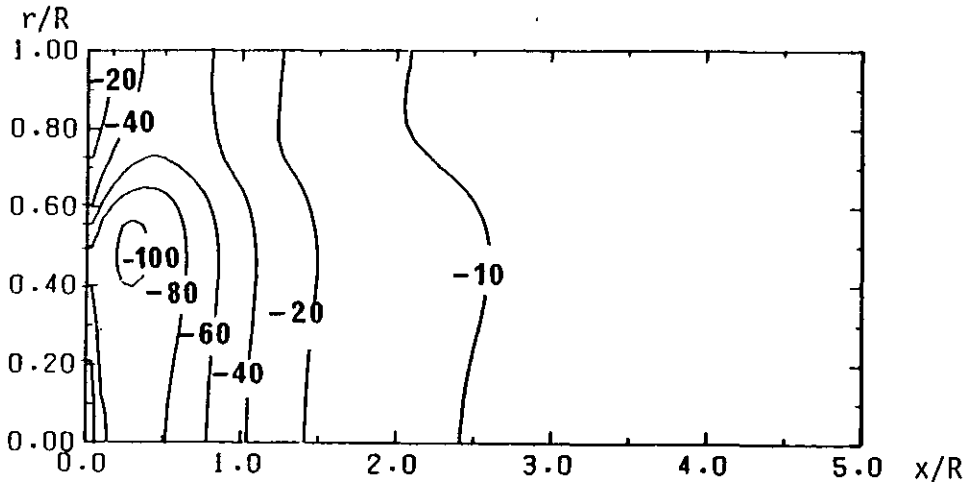

(a) Disc, 25% blockage

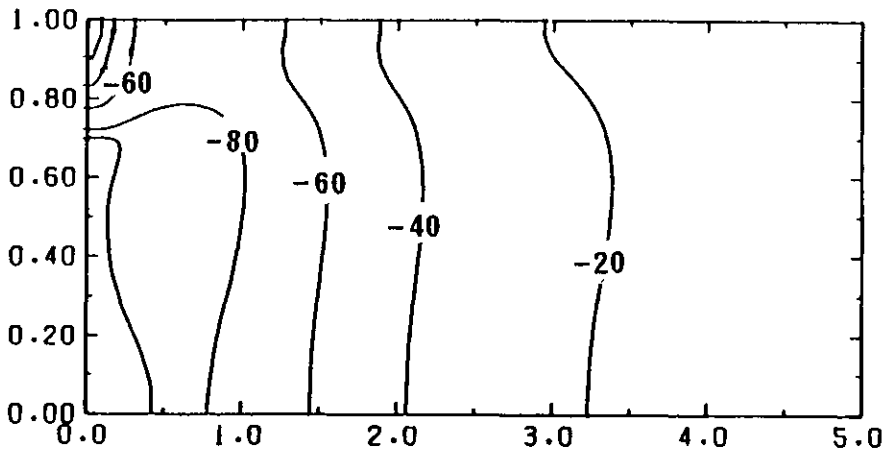

(b) Disc, 50% blockage

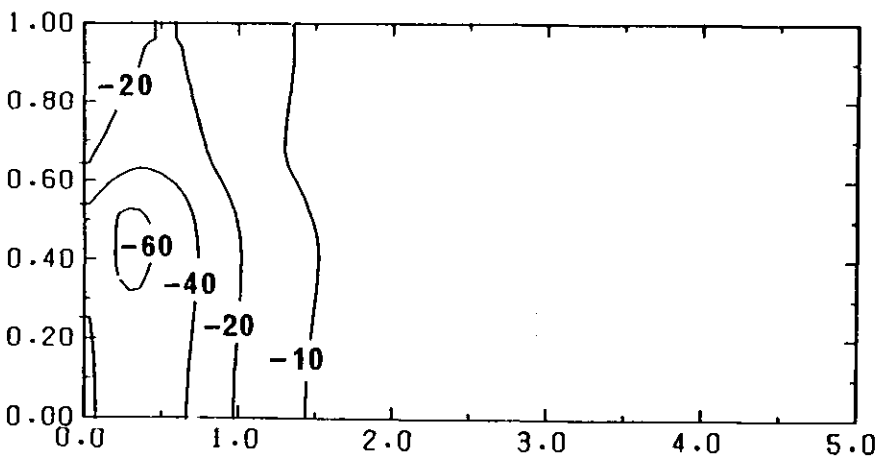

(c) Cone, 25% blockage

Figure 2.40 Calculated isobars for three baffles (per cent $\frac{1}{2}\rho U_o^2$)

CHAPTER III

CALCULATIONS OF ISOTHERMAL FLOWS

3.1 Introduction

This chapter describes the calculation of the isothermal flows for the three baffles of Chapter II and for the related case of the annular jet measured by Durão and Whitelaw (1978). The calculations are made by numerical integration of the partial differential equations of motion, with a turbulence model representing the Reynolds stress tensor. The solutions are compared with experiment and, for the case of the annular jet, with previously reported calculations. The results demonstrate the importance of minimising numerical truncation error, which can be large in recirculating flows. The purposes of the work in this chapter are:-

(a) to examine, more closely than in previously reported investigations, the question of the numerical accuracy in calculations of turbulent, recirculating flows.

(b) to evaluate and criticize the performance of the two equation ("k-ε") model in the calculation of the near-wake of bluff bodies by comparison with the experimental observations of the previous chapter.

(c) to examine the sensitivity of the calculations to the boundary conditions.

(d) to assess a suggestion for the improvement of the two equation model.

(e) to recommend the direction in which future work is required.

The following section gives details of the calculation method, beginning with the equations to be solved, their boundary conditions and the procedure for the numerical integration of the equations on a finite difference grid. Section 3.3 considers the importance of numerical truncation errors in limiting the solution accuracy and describes a rational method for the refinement of the mesh so as to minimise their influence. Section 3.4 presents the results of the calculations of the flows of Chapter II and of the annular jet and compares these with measurement and, for the annular jet, previous calculations. Section 3.5 criticizes the performance of the turbulence model and suggests the use of a more advanced model to overcome the defects of an effective viscosity hypothesis. The final section, 3.6, presents a summary of the main findings and conclusions of the series of calculations.

3.2 Calculation method

3.2.1 Equations to be solved

Partial differential equations

The equations to be solved are the equations of motion of a fluid and are given below in the Reynolds-averaged form, assuming constant density, axisymmetric flow in cylindrical polar co-ordinates

with zero mean azimuthal velocity:-

Mass conservation:

$$\frac{\partial U}{\partial x} + \frac{\partial V}{\partial r} + \frac{V}{r} = 0 \qquad (3.1)$$

Conservation of axial momentum:

$$\rho \frac{\partial (U^2)}{\partial x} + \frac{\rho}{r} \frac{\partial}{\partial r} (rUV) = - \frac{\partial p}{\partial x} - \frac{\partial \rho}{\partial x} \langle u^2 \rangle - \frac{1}{r} \frac{\partial}{\partial r} (r\rho \langle uv \rangle) \qquad (3.2)$$

Conservation of radial momentum:

$$\rho \frac{\partial}{\partial x} (UV) + \frac{\rho}{r} \frac{\partial}{\partial r} (rV^2) = - \frac{\partial p}{\partial r} - \frac{\partial \rho}{\partial x} \langle uv \rangle - \frac{1}{r} \frac{\partial}{\partial r} (r\rho \langle v^2 \rangle) + \rho \frac{\langle w^2 \rangle}{r} \qquad (3.3)$$

(The Reynolds number of the flows is assumed sufficiently high for laminar transport effects to be negligible in equations (3.2) and (3.3)).

The equation set (3.1), (3.2) and (3.3) is insoluble because the number of unknowns (seven - U, V, p, $\langle u^2 \rangle$, $\langle v^2 \rangle$, $\langle w^2 \rangle$, $\langle uv \rangle$) exceeds the number of equations. Although the instantaneous equation of motion (that is, conservation of mass and the Navier-Stokes equations) do form a soluble set, the spatial resolution which would be required of the numerical integration for an accurate solution of a flow of engineering interest is far greater than available computer storage. This is because such flows are generally turbulent and therefore the range of length scales which must be resolved is of the order of (Reynolds number)$^{3/4}$ (Tennekes and Lumley, 1972). The excess of unknowns is referred to as the closure problem and the mathematical

constructs by which the number of equations is made equal to the number of unknowns are referred to as turbulence models.

Turbulence model

The literature survey of Chapter I has mentioned three turbulence models which have been used to calculate recirculating flows. In ascending order of complexity, and therefore also in ascending requirement of computer storage and time, the models are: the two equation "k-ε" model (Jones and Launder, 1972), the three equation model (Hanjalić and Launder, 1972) and the Reynolds stress model (Launder, Reece and Rodi, 1975). The results of previously reported work suggests that the two equation model was as accurate as the others and accordingly it is this model which is used for the calculations of this chapter. This conclusion may, however, have to be revised after consideration of the following sections on the numerical accuracy of these published works.

The model relates the Reynolds stress tensor to the mean rate of strain via a scalar turbulent viscosity hypothesis:-

$$\rho \langle u^2 \rangle = \frac{2}{3} \rho k - 2\mu_t \frac{\partial U}{\partial x} \tag{3.4a}$$

$$\rho \langle v^2 \rangle = \frac{2}{3} \rho k - 2\mu_t \frac{\partial V}{\partial r} \tag{3.4b}$$

$$\rho \langle w^2 \rangle = \frac{2}{3} \rho k - 2\mu_t \frac{V}{r} \quad \text{(for axisymmetric flows with no mean azimuthal velocity)} \tag{3.4c}$$

$$\rho \langle uv \rangle = - \mu_t \left(\frac{\partial U}{\partial r} + \frac{\partial V}{\partial x} \right) \tag{3.4d}$$

where:-

$$k \equiv \left[\frac{\langle u^2\rangle + \langle v^2\rangle + \langle w^2\rangle}{2}\right] \tag{3.5}$$

The turbulent viscosity is a spatial variable, determined by the local values of turbulent kinetic energy, k, and its rate of isotropic dissipation, ε, using a Kolmogorov-Prandtl expression (see, for example, Launder and Spalding, 1972):-

$$\mu_t = C_\mu \rho \frac{k^2}{\varepsilon} \tag{3.6}$$

where C_μ is a constant, and:-

$$\varepsilon = \nu \left\langle \frac{\partial u_i}{\partial x_j} \frac{\partial u_i}{\partial x_j} \right\rangle \tag{3.7}$$

where the summation convention applies to equation (3.7). The designation of the model as "two equation" refers to the means by which the spatial variations of k and ε are found. Exact transport equations can be derived from the Navier-Stokes equations for each of the scalars k and ε and these are given in table 3.1. As a further manifestation of the closure problem, however, these equations introduce new correlations for which a finite number of closed defining equations cannot be written. Thus the unknown correlations are modelled by empirical functions of the mean velocity, Reynolds stresses and ε so as to form a closed set of equations. The process of modelling is facilitated by identifying particular physical processes with certain terms and these are identified in table 3.1. In general, mean advection along a streamline is balanced by sources (positive or negative) and turbulent transport, with the latter being approximated by gradient diffusion.

TABLE 3.1

EXACT AND MODELLED TRANSPORT EQUATIONS FOR THE TURBULENT KINETIC ENERGY, k, AND ITS RATE OF ISOTROPIC DISSIPATION, ε

Exact transport equation for k (Rodi, 1970)

$$\frac{\partial}{\partial x}(Uk) + \frac{1}{r}\frac{\partial}{\partial r}(rVk) = -\langle u^2\rangle \frac{\partial U}{\partial x} - \langle v^2\rangle \frac{\partial V}{\partial r} - \langle w^2\rangle \frac{V}{r} - \langle uv\rangle \left(\frac{\partial U}{\partial r} + \frac{\partial V}{\partial x}\right) +$$

advection along a mean streamline

deformation work (turbulence production)

$$+ \nu\nabla^2 k - \frac{\partial}{\partial x}\left[\left\langle u\left(\frac{u_i u_i}{2} + \frac{p'}{\rho}\right)\right\rangle\right] - \frac{1}{r}\frac{\partial}{\partial r}\left[r\left\langle v\left(\frac{u_i u_i}{2} + \frac{p'}{\rho}\right)\right\rangle\right]$$

transport by viscous stress and velocity fluctuations and pressure gradient work

$$- \mu\left[\left\langle \frac{\partial u_i}{\partial x_j}\frac{\partial u_i}{\partial x_j} + \frac{v^2}{r^2} + \frac{w^2}{r^2}\right\rangle\right]$$

deformation work: rate at which viscous stresses perform work against fluctuating strain rate (viscous dissipation)

(NB $u_1 = u$ $u_2 = v$ $x_1 = x$ $x_2 = r$. Summation convention applies to repeated indices)

TABLE 3.1 (continued)

Modelled transport equation for k (Rodi, 1970)

$$\rho \frac{\partial}{\partial x}(Uk) + \frac{\rho}{r}\frac{\partial}{\partial r}(rVk) = -\rho \langle u^2 \rangle \frac{\partial U}{\partial x} - \rho \langle v^2 \rangle \frac{\partial V}{\partial r} - \rho \langle w^2 \rangle \frac{V}{r} - \rho \langle uv \rangle \left[\frac{\partial U}{\partial r} + \frac{\partial V}{\partial x}\right] +$$

$$+ \frac{\partial}{\partial x}\left[\frac{\mu_t}{\sigma_k}\frac{\partial k}{\partial x}\right] + \frac{1}{r}\frac{\partial}{\partial r}\left[r\frac{\mu_t}{\sigma_k}\frac{\partial k}{\partial r}\right] - \rho\varepsilon$$

(NB (i) transport by viscous diffusion neglected.
(ii) Reynolds stresses given by equation (3.4))

TABLE 3.1 (continued)

Transport equation for ε at high Reynolds number (Launder, Reece and Rodi, 1975)

$$\frac{D\varepsilon}{Dt} = -2\nu \left\langle \frac{\partial u_i}{\partial x_k} \frac{\partial u_i}{\partial x_\ell} \frac{\partial u_k}{\partial x_\ell} \right\rangle - 2 \left[\nu \left\langle \frac{\partial^2 u_i}{\partial x_k \partial x_\ell} \right\rangle \right]^2$$

advection along a mean streamline

generation of ε due to vortex stretching of turbulent filaments and its destruction by viscous action

$$- \frac{\partial}{\partial x_k} \left[\nu \left\langle u_k \frac{\partial u_i}{\partial x_\ell} \frac{\partial u_i}{\partial x_\ell} \right\rangle + \frac{\nu}{\rho} \left\langle \frac{\partial p'}{\partial x_i} \frac{\partial u_k}{\partial x_i} \right\rangle \right]$$

transport by turbulence and pressure fluctuations (transport by viscous diffusion neglected)

(NB The equation is written in cartesian tensor notation. Summation convention applies)

TABLE 3.1 (concluded)

Modelled transport equation for ε (Launder and Spalding, 1974)

$$\frac{\partial}{\partial x}(U\varepsilon) + \frac{1}{r}\frac{\partial}{\partial r}(rV\varepsilon) = -C_{\varepsilon_1}\left[\frac{\langle u^2\rangle}{k}\frac{\partial U}{\partial x} + \frac{\langle v^2\rangle}{k}\frac{\partial V}{\partial r} + \frac{\langle uv\rangle}{k}\left(\frac{\partial U}{\partial r} + \frac{\partial V}{\partial x}\right) + \frac{\langle w^2\rangle}{k}\frac{V}{r}\right]\varepsilon - C_{\varepsilon_2}\frac{\varepsilon^2}{k}$$

$$+ \frac{\partial}{\partial x}\left[-\frac{\mu_t}{\rho\sigma_\varepsilon}\frac{\partial \varepsilon}{\partial x}\right] + \frac{1}{r}\frac{\partial}{\partial r}\left[\frac{r\mu_t}{\rho\sigma_\varepsilon}\frac{\partial \varepsilon}{\partial r}\right]$$

(NB (i) transport by viscous diffusion neglected.
(ii) Reynolds stresses given by equation (3.4))

The detailed derivation of the modelled transport equations is available in the literature (Hanjalić, 1970 {cited by Jones and Launder, 1972}; Launder, Reece and Rodi, 1975; Reynolds, 1976; Lumley, 1978) but the justification for the analogue of the source terms in the ε equation is presented here because a modification to this term is considered in section 3.5. The physical processes represented by these source terms (table 3.1) are the generation of strain rate fluctuations (see equation 3.7) due to vortex stretching and their viscous dissipation. The decay of isotropic turbulence suggests that part of the source term is, on dimensional grounds:-

$$- C_{\varepsilon_2} \frac{\varepsilon^2}{k} \tag{3.8}$$

When turbulence is subjected to a rate of mean strain, then there is, in contrast to isotropic decay, a source of production in the energy equation which can be expected to change the level of dissipation. Lumley (1978) has argued that the rate of strain must appear with the anisotropy tensor b_{ij}:-

$$b_{ij} \equiv \frac{\langle u_i \, u_j \rangle}{k} - \frac{2}{3} \delta_{ij} \tag{3.9}$$

By analysing the source of dissipation as a functional of quantities such as the rate of strain, Reynolds stress and dissipation, collecting non-dimensional groupings, expanding in a series and assuming slow changes, another part of the source term is represented as:-

$$C_{\varepsilon_1} \, b_{ij} \, k \frac{\partial U_i}{\partial x_j} \tag{3.9a}$$

$$\equiv C_{\varepsilon_1} \frac{P}{k} \cdot \varepsilon \qquad (3.9b)$$

where $U_1 = U$; $U_2 = V$; $x_1 = x$; $x_2 = r$, and P represents the production of turbulent kinetic energy. Assuming that the influence of mean velocity gradients is weak (Lumley, 1978), the sum of equations (3.8) and (3.9) are taken to be the analogue for the source term.

Equations (3.1) - (3.4), together with the effective viscosity hypothesis (equation (3.6)) and the two modelled equations for the transport of k and ε (table 3.1) form a soluble equation set. The set includes, however, five unknowns the value of which are taken as constant and part of the turbulence model: table 3.2 summarizes these unknowns.

The value of C_μ is derived from the conditions of near-wall turbulence, where to a good approximation the rate of production of turbulence equals its rate of decay. Under this simplification, the equation for the transport of k reduces to:-

$$\langle uv \rangle \frac{dU}{dr} = \varepsilon$$

and using the law of the wall (equation (3.21) below) to eliminate dU/dr there results:-

$$C_\mu = (\langle uv \rangle / k)^2 = (0.3)^2$$

This value of C_μ is derived under restrictive assumptions and it has been found that in general it is a function of the flow conditions (Rodi, 1975). The implications of this are considered in section 3.5. C_{ε_2} is fixed by matching the experimentally observed rate of decay of

isotropic grid turbulence with the solution of the modelled equations for k and ε in such a flow:-

$$U \frac{dk}{dx} = - \varepsilon$$

$$U \frac{d\varepsilon}{dx} = - C_{\varepsilon_2} \frac{\varepsilon^2}{k}$$

The values of σ_k and C_{ε_1} are determined by optimising the agreement between calculation and experiment for a number of free shear flows. The values in table 3.2 are those recommended by Launder and Spalding (1974). Optimisation is necessarily subjective and a slightly increased value for C_{ε_1} (1.45) is suggested by Hanjalić and Launder (1972); the sensitivity of calculations to the values of C_{ε_1} and C_{ε_2}, and the source term for ε in general, is mentioned in the discussion of section 3.5. The entry for σ_ε in the table is a relation derived from the limiting case of the modelled equation for ε where, in near wall flows, convection is unimportant. The differential equation then reduces to an algebraic relation between the constants.

The two equation model appears to involve two quite separate postulates; that of an eddy viscosity and the determination of the eddy viscosity by the transport equations for k and ε. It can be shown, however, that if the turbulent motion is characterised by only one characteristic length and one characteristic velocity scale, then an eddy viscosity becomes a dimensional necessity (Tennekes and Lumley, chapter 2, 1972). An eddy viscosity can thus be regarded as the corollary of the decision to use two scalars (k and ε) to characterise turbulence.

TABLE 3.2

CONSTANTS IN THE TWO EQUATION MODEL OF TURBULENCE (LAUNDER AND SPALDING, 1974)

SYMBOL	VALUE	BASIS FOR DETERMINATION
C_μ	0.09	Value of $\langle uv \rangle / k$ in near-wall turbulence
C_{ε_1}	1.44	Computer optimisation
C_{ε_2}	1.92	Rate of decay of isotropic (grid) turbulence
σ_k	1.0	Computer optimisation
σ_ε	1.3	$\dfrac{\kappa^2}{(C_{\varepsilon_2} - C_{\varepsilon_1}) C_\mu^{1/2}}$

Finite difference equations

The numerical solution of the partial differential equations (3.1) - (3.3), together with the turbulence model, is achieved by using a standard finite difference method, called TEACH-T, which has been reported by Gosman and Pun (1973) and Gosman and Ideriah (unpublished work). The following paragraph briefly outlines the derivation of the finite difference equations and introduces the 'pressure-correction' variable. A more detailed exposition can be found, for example, in Patankar (1980). Sub-section 3.2.3 considers the method by which the finite difference equations are solved.

The area of integration (to be defined in sub-section 3.2.2) of each equation is overlayed by a rectangular, non-uniform grid, part of which is shown in figure 3.1(a). (It is noted that the grids for the axial and radial components of velocity are staggered with respect to the grid for the remaining variables, as shown in figure 3.1(b). The reason for this is given below).

The approximate solution to the partial differential equation for each dependent variable is found at every grid node by representing the spatial derivatives in the equations by finite difference approximations. Each of the modelled equations for the transport of momentum, k and ε, can be written in the common form:-

$$\rho \frac{\partial}{\partial x}(U\phi) + \frac{\rho}{r}\frac{\partial}{\partial r}(rV\phi) = \frac{\partial}{\partial x}\left(\frac{\mu_t}{\sigma_\phi}\frac{\partial}{\partial x}\phi\right) + \frac{1}{r}\frac{\partial}{\partial r}\left(r\frac{\mu_t}{\sigma_\phi}\frac{\partial \phi}{\partial r}\right) + S_\phi \qquad (3.10)$$

where ϕ is a surrogate variable standing for either U, V, k or ε, σ_ϕ is the appropriate effective turbulent Prandtl number and S_ϕ represents all remaining source terms. The following outline derivation, given for the variable ϕ, thus applies to all four dependent variables.

Consider a control volume which surrounds node P in figure

3.1(a), where the faces of the volume lie mid-way between P and the four surrounding nodes. Using the Gauss divergence theorem, equation (3.10) becomes:-

$$C_E - C_W + C_N - C_S = D_E - D_W + D_N - D_S + \int\int S_\phi \, dx \, rdr \qquad (3.11)$$

where:-

C_i represents the advective flux of ϕ across the appropriate control volume face;

D_i represents the diffusive flux of ϕ across the appropriate control volume face;

and the double integral is taken over the area of the control volume in the $x \sim r$ plane.

The object of using the Gauss divergence theorem before making finite difference approximations is to ensure that the numerical solution of equation (3.11) will satisfy all the conservation relations on flux flow rates as the original partial differential equation, (3.10). The resulting finite difference method then possesses the conservative property (Roache, 1976).

With appropriate (see section 3.3) approximations for the value of ϕ at each control volume face and using the equation for continuity there results the following algebraic equation for ϕ at node P:-

$$\phi_P \, (A_E + A_W + A_N + A_S) = A_E\phi_E + A_W\phi_W + A_N\phi_N + A_S\phi_S + S_\phi \, \delta x \, r\delta r \qquad (3.12)$$

where A_i are influence coefficients, accounting for the net effect

(through convection and diffusion) of the value of ϕ at node "i" on the value of ϕ_p.

The calculation of these coefficients is considered at greater length in section 3.3: here it is noted that when ϕ represents a component of velocity, these coefficients are themselves functions of ϕ and equation (3.12) is then non-linear. This property affects the method of its solution (sub-section 3.2.3).

Pressure is an unknown in the source terms (S_ϕ) in the equations for momentum transport, but does not appear explicitly in the equation for the conservation of mass, (3.1). It is determined through the solution of a Poisson-type equation for a variable called "pressure correction" (Patankar and Spalding, 1972), which adjusts a given pressure and velocity field and moves the solution closer to simultaneous satisfaction of the equations of motion. Suppose equation (3.12) to have been solved for ϕ = U, V using a guessed pressure field, p*. Let the corresponding solutions be U* and V* which will not, in general, satisfy conservation of mass. If the correct pressure, p, is:-

$$p = p^* + p' \tag{3.13}$$

where p′ is the pressure correction field, then the resulting change in the velocity field is:-

$$U = U^* + U' \tag{3.14a}$$

$$V = V^* + V' \tag{3.14b}$$

where U′ and V′ are the corresponding velocity corrections required to achieve the correct velocity field, U and V. The following, local, relation between velocity correction and pressure correction is obtained:-

$$A_E \, U_E' = (p_P' - p_E') \, r \, \delta r \qquad (3.15a)$$

$$A_N \, V_N' = (p_P' - p_N') \, \delta x \qquad (3.15b)$$

by neglecting the effect of pressure correction on the velocities at neighbouring nodes. If equation (3.14) is applied to the equation for the conservation of mass, there results:-

$$G_E - G_W + G_N - G_S = 0 \qquad (3.16)$$

where G_i represents the mass flow across the appropriate control volume face. Substitution of equations (3.15) into (3.16) gives an equation identical in form to equation (3.12), where ϕ now represents the pressure correction variable. The simplification used in (3.15) is made so as to arrive at this common form because it is convenient when solving the system of equations for ϕ = U, V, p', k and ε. It can be shown, however, that the simplification does not affect the solution which is ultimately obtained.

It is now possible to explain the reason behind the use of a staggered grid. In an unstaggered grid (where velocity nodes and pressure nodes coincide) it is possible to obtain solutions to the difference equations which satisfy all constraints and yet are spatially oscillatory, with a period of twice the grid spacing and arbitrary amplitude (see, for example, Patankar, 1980). The staggering of the pressure and velocity nodes removes this possibility.

3.2.2 The specification of the boundary conditions

The domain of dependence of the equation set (3.1) - (3.3),

together with the equations for the transport of k and ε, is similar to that of a classical elliptic differential equation. A mathematically well-posed problem therefore requires boundary conditions to be prescribed for U, V, k and ε on the closed curve describing the boundary of the area of integration. (It is noted that independent boundary conditions for two, and only two, of the variables U, V and pressure correction can be specified for the solution of the equations of motion). The chosen area of integration is the rectangle shown in figure 3.2 and the following paragraphs discuss the conditions which are applied along each of its four sides.

Boundary at x = 0

Two physically and computationally distinct boundaries occur at x = 0. This heading considers the conditions for the annular space between the baffle tip (r = d/2) and the confining pipe wall (r = R); the line adjacent to the baffle surface is treated below under the heading of "wall functions". The radial profiles of axial velocity (U), presented for each baffle in Chapter II, were used directly. For the radial profiles of radial velocity (V) measurements extend only to $r/R \simeq 0.8$ and hence interpolation to zero velocity at r/R = 1 was used to obtain the remaining values: figure 3.3(a) shows the resulting curves fitted to the measurement points for each baffle. The corresponding restriction on $\langle v^2 \rangle$ at this station affects the specification of k, the turbulent kinetic energy. The boundary condition was specified as:-

$$k = \frac{1}{2} \left(\langle u^2 \rangle + 2 \langle w^2 \rangle \right) \qquad (3.17)$$

from the measured values of $\langle u^2 \rangle$ and $\langle w^2 \rangle$ at this station, which can

be expected to be a good approximation. These profiles are shown in figure 3.3(b). The exception was the profile for the 25 per cent blockage disc for which a uniform profile, $k = 0.01\ m^2s^{-2}$, was assumed, shown in figure 3.3, derived from a typical value of k in the annular gap. Sub-section 3.4.2 examines the sensitivity of the solution to this boundary condition by using:-

$$k = \frac{3}{2} \langle u^2 \rangle \tag{3.18}$$

The value of ε was found from:-

$$\varepsilon = \frac{k^{3/2}}{\ell} \tag{3.19}$$

The result (Tennekes and Lumley, 1972) is an inertial estimate for the dissipation rate, obtained by interpreting ε as the rate of transfer of energy from large-scale to small-scale eddies and estimating this rate from the length (ℓ) and time ($\ell/k^{1/2}$) scales associated with the large eddies. The length scale was taken as the width of the annular gap:-

$$\ell = R - \frac{d}{2} \tag{3.20}$$

Wall functions

Wall functions are used as boundary conditions for grid nodes adjacent to the baffle surface and to the confining pipe wall. The physical boundary conditions for velocity at an impervious wall are zero normal and slip velocity. The former condition is retained, but the rapid variation of the dependent variables in a direction

normal to a solid wall would necessitate many grid nodes to resolve the near-wall variation. In many cases, algebraic prescriptions known as wall functions (see, for example, Launder and Spalding, 1974) obviate the need for a fine grid to resolve the distributions near the viscous sublayer (which are not of interest in this case) while allowing for the effect of the wall on the remainder of the flow.

For the velocity component parallel to the wall, the importance of the wall lies in determining the diffusive efflux of momentum across the appropriate control volume face. This can be found from the shear stress at the wall, τ_a:-

$$\tau_a = \rho \, (C_\mu^{1/2} \, k_a)^{1/2} \left[\frac{\kappa \, U_a}{\ell n \, (E y^+)} \right] \qquad (3.21a)$$

and k_a, U_a and y^+ are all evaluated at the grid node adjacent to the wall. The formula is based on the logarithmic law of the wall (see, e.g., Townsend, 1980):-

$$U^+ = \frac{1}{\kappa} \ell n \left[E y^+ \right] \qquad (3.21b)$$

where:-

$$U^+ \text{ is } \frac{U \, (C_\mu^{1/2} \, k_a)^{1/2}}{(\tau_a / \rho)}$$

and:-

$$y^+ \text{ is } \frac{y_a \, (C_\mu^{1/2} \, k_a)^{1/2}}{\nu}$$

In local equilibrium flows:-

$$(C_\mu^{1/2}\ k)^{1/2} \simeq \tau/\rho \qquad (3.21c)$$

so that the above forms for U^+ and y^+ reduce to the usual definitions. For this empirical law to hold, the near wall grid spacing should be such that:-

$$30 \lesssim y^+ \lesssim 300 \qquad \text{(say)} \qquad (3.22)$$

The near wall turbulent kinetic energy is found by assuming that diffusive transport of k to the wall is negligible (Bradshaw, 1971) and evaluating the average value of ε over the control volume near the wall as (the limits of integration being over the control volume):-

$$\int\int \varepsilon r\, dx\, dr \simeq (C_\mu^{1/2}\ k_a)^{3/2}\ U_a \sqrt{\frac{\rho}{\tau_a}} \qquad (3.23)$$

The value of ε near the wall is fixed by a length scale as:-

$$\varepsilon_a \equiv (C_\mu^{1/2}\ k_a)^{3/2}\ (\kappa y_a)^{-1} \qquad (3.24)$$

A brief consideration of the appropriateness of the wall functions is deferred to sub-section 3.4.2.

Axis of symmetry

The following conditions are imposed by virtue of symmetry of the flow:-

$$\frac{\partial U}{\partial r} = \frac{\partial k}{\partial r} = \frac{\partial \varepsilon}{\partial r} = V = 0 \qquad (3.25)$$

Boundary far downstream of the baffle

The boundary conditions sufficiently far downstream of the baffle would be those of a fully-developed turbulent pipe flow. It is neither desirable nor necessary to extend the solution domain so far downstream of the baffle. Instead, the following conditions are chosen:-

$$\frac{\partial U}{\partial x} = \frac{\partial k}{\partial x} = \frac{\partial \varepsilon}{\partial x} = V = 0 \qquad (3.26)$$

and are applied at a downstream station sufficiently far ($\simeq$ 10 R) from the baffle so that these conditions do not affect the flow in the region of interest.

3.2.3 Solution of the difference equations

The simultaneous solution of the algebraic relations, of the form of equation (3.12), is required at each grid node internal to the area of integration for five dependent variables. The coefficients A_i and the source term S_ϕ are functions of the dependent variables, so these equations are non-linear. Because of this property, and also because the matrix of coefficients A_i is sparse, an iterative solution algorithm (called 'SIMPLE' by Patankar and Spalding, 1972) is used and is summarised in table 3.3. The method of solution involves two separate operations:-

(i) solutions to equation (3.12) are obtained, assuming A_i and S_ϕ to be constant, by means of line-by-line application of the standard tri-diagonal matrix algorithm (see, for example, Roache, 1976). A condition for the stable (that is, no growth of rounding errors) application of this algorithm

TABLE 3.3

THE 'SIMPLE' ALGORITHM
(PATANKAR AND SPALDING, 1972)

Each iteration of the 'SIMPLE' algorithm involves the following calculations:-

1. Guess a pressure field, $p^*(x, r)$.

2. Solve (3.12) for $U^*(x, r)$ and $V^*(x, r)$ using the 'line-by-line' application of the tri-diagonal matrix algorithm and appropriate under-relaxation.

3. Solve (3.12) for the pressure correction variable, $p'(x, r)$, using the same procedure as step 2.

4. Calculate $p(x, r)$ from (3.13).

5. Calculate $U(x, r)$ and $V(x, r)$ from (3.15).

6. Solve (3.12) for $k(x, r)$ and $\varepsilon(x, r)$, using the same procedure as step 2.

7. Examine the solution for iteration convergence.

8. If insufficiently converged, treat the corrected pressure, $p(x, r)$ from step 4, as a new guess for pressure, $p^*(x, r)$ and return to step 2.

(Smith, 1978, p. 26) is that the matrix formed by the influence coefficients satisfies:-

$$A_i > 0 \qquad \text{for } i = N, S, E, W$$

at all grid nodes; this automatically ensures that the matrix is also diagonally dominant, which is a further condition for stability. The maintenance of this condition depends, however, on the form of the finite difference approximation used for convection and this is discussed in sub-section 3.3.1. The assumption of constant coefficients is not a good one, so that iteration is not pursued to convergence but merely to obtain improved estimates of ϕ.

(ii) The improved estimates are used to calculate new values of A_i and S_ϕ and then step (i) is repeated.

The use of an iterative scheme for solving non-linear equations makes the use of under-relaxation, to limit the changes in A_i, necessary. Table 3.4 below summarises information on the computer storage and central processor time requirements and the total number of iterations of step (ii) above to reach a converged solution. The table refers to two grid sizes, one being used for the results of sub-section 3.4.1 (30 x 36) and the other for the results of sub-section 3.4.3 (40 x 55).

The use of an iterative procedure requires a criterion, at each completion of step (ii), for assessing the extent to which the current values of ϕ satisfy the original difference equation. Three

TABLE 3.4

COMPUTER STORAGE AND CENTRAL PROCESSOR TIME REQUIREMENTS FOR EXECUTION OF PROGRAM

	GRID SIZE	
	30 x 36	40 x 55
Storage requirement (in decimal words)	44 000	65 000
Number of iterations of 'SIMPLE' algorithm	≃ 600	> 1000
Central processor time per iteration of 'SIMPLE' (seconds)	1.0	2.1

NB (i) values apply for the University of London computer centre on the CDC 6600.

(ii) number of iterations refers to that required for the residual R_U to fall to 1% of inlet momentum flow rate.

different criteria were used:-

(a) Rearrangement of equation (3.12) leads to:-

$$R_\phi \equiv |A_P \phi_P - \sum_i A_i \phi_i - S_\phi| \qquad (3.27)$$

where $A_P \equiv \sum_i A_i$ for i = N, S, E, W. For a converged solution, R_ϕ is zero at all grid nodes. The sum of R_ϕ over all grid nodes was examined for each dependent variable; sufficiently converged solutions generally occurred when R_U was less than one per cent of the inlet momentum flow rate.

(b) The changes in the field solutions for the dependent variables were examined every 100 iteration steps. It was found that the field values close to the baffle converged much quicker than the field close to the downstream boundary. It is likely that the slow convergence downstream of the recirculation zone is due to the application of an elliptic solution procedure in a region of parabolic flow. In this study it is the values near the baffle that are of interest and iteration could be stopped when this region was adequately converged.

(c) The third criterion for assessing convergence is conveniently considered after the analysis of sub-section 3.3.2 and its presentation is postponed.

3.3 Solution accuracy

Provided that iteration convergence can be attained, and that computer round-off errors are negligible, the accuracy of the numerical solution is limited only by the approximation of the partial derivatives by their finite difference analogues. The analogues are approximate because these represent truncated Taylor series expansions. Sub-section 3.3.1 examines the truncated terms in the finite difference approximations for convection and establishes the importance of numerical diffusion. Local grid refinement is chosen to minimise this error, but successful grid refinement depends on being able to identify the magnitude and location of numerical diffusion within the finite difference grid. Sub-section 3.3.2 presents two methods for doing this.

3.3.1 Truncation errors: origin and importance

In what follows, it is convenient to focus attention on the steady-state, one-dimensional, uniform flow (i.e. $U \neq U(x)$), constant property transport of a passive scalar, for which the governing equation is:-

$$\rho \frac{d}{dx}(U\phi) - \mu \frac{d^2\phi}{dx^2} = 0 \qquad (3.28)$$

The extension to two-dimensional flow with source terms involves no new principle, but complicates the mathematics to be used and is not, therefore, given here. For the control volume shown in figure 3.4 the flux balance is, for unit area normal to the x direction:-

$$\rho U_e \phi_e - \frac{\mu}{\delta x}\left[\phi_E - \phi_P\right] - \rho U_w \phi_w + \frac{\mu}{\delta x}\left[\phi_P - \phi_W\right] = 0 \qquad (3.29)$$

where the lower case subscripts (e and w) denote values at the relevant control volume faces in figure 3.4 and space-centred differencing has been used to represent diffusion. If $\phi_e \equiv \frac{1}{2}(\phi_E + \phi_P)$ and $\phi_w \equiv \frac{1}{2}(\phi_P + \phi_W)$ then equation (3.29) becomes:-

$$\phi_P (A_E + A_W) = A_E \phi_E + A_W \phi_W \tag{3.30}$$

using $(U_e - U_w) \equiv 0$ and with:-

$$A_E \equiv \left(\frac{\mu}{\delta x} - \rho \frac{U_e}{2}\right) \quad ; \quad A_W \equiv \left(\frac{\mu}{\delta x} + \rho \frac{U_w}{2}\right) \tag{3.31}$$

The resemblance of equation (3.30) with equation (3.12) is obvious. The above assumptions for ϕ_e and ϕ_w constitute a central difference approximation for convection, because equations (3.30) and (3.31) are equivalent to approximating:-

$$U \frac{d\phi}{dx} \simeq \frac{U}{2\delta x}(\phi_E - \phi_W) \tag{3.32}$$

assuming that the grid line spacing is uniform. If this is not the case, then further truncation terms, in addition to those given below, are introduced and the non-uniformity should be kept small (see sub-section 3.3.2) to minimise these terms.

It can be shown that, provided the function ϕ and its derivatives are single valued, finite and continuous on x and using a Taylor series expansion, that:-

$$\frac{U}{2\delta x}(\phi_E - \phi_W) = U \frac{d\phi}{dx} + \frac{U}{6} \frac{d^3\phi}{dx^3} \delta x^2 + \ldots. \tag{3.33}$$

where the expansion is centred on $x = x_p$ (figure 3.4) and the ellipsis denotes higher powers of δx. Equation (3.33) shows that (3.32) is a good approximation when the terms in $(\delta x)^2$ and higher are small compared to the leading term in the expansion. It can be similarly shown that the approximation for the diffusion results in truncated terms of the same order of (δx) (i.e. δx^2). The numerical solution of equations (3.30) and (3.31) is thus equivalent to exact solutions of the following differential equation:-

$$\rho \frac{d}{dx}(U\phi) = \mu \frac{d^2\phi}{dx^2} + \underline{\frac{U}{6}\frac{d^3\phi}{dx^3}\delta x^2 + \ldots} = 0 \qquad (3.34)$$

where the underlined terms in (3.33) and (3.34) have been introduced by the finite difference approximations.

It is noted that when the computational Péclet number, Pe, is such that:-

$$Pe \equiv \left| \rho \frac{U\delta x}{\mu} \right| > 2 \qquad (3.35)$$

then the coefficients, A_i, in (3.31) may become negative and thus the matrix of coefficients A_i in equation (3.30) ceases to be diagonally dominant, so that solution by the tri-diagonal matrix algorithm is no longer possible (see sub-section 3.2.3). Solutions can be obtained by other means which show unphysical (Spalding, 1972), spatially oscillatory variations which violate the boundedness condition of equation (3.28) (the analytical solution for ϕ (x) of (3.28) must lie within the values of the boundary conditions). The reason for this behaviour is that the wavelength (grid line spacing) of the finite difference grid is too long to resolve the (shorter) wavelengths of the solution, leading to

an aliasing error (Roache, 1976). Thus the short wavelength part of the solution is folded about that of the grid to appear as long wavelengths. This behaviour is unacceptable in the numerical solution.

The limits to the available computer time and storage do not allow the use of grids for which Pe is less than two everywhere. A common (Roache, 1976; Gosman et al, 1969) device for obtaining unconditionally (numerically) stable differencing schemes is to use upwind differencing. In this scheme, the value of ϕ at a control volume boundary is supposed to be that obtaining at the grid node immediately upstream (upwind). In the example used above, this means that:-

$$\phi_e \equiv \phi_P \quad \text{and} \quad \phi_w \equiv \phi_W$$

and the coefficients A_E, A_W in equation (3.30) are then:-

$$A_E \equiv \left[\frac{\mu}{\delta x}\right] \quad ; \quad A_W \equiv \left[\frac{\mu}{\delta x} + \rho\, U_w\right] \tag{3.36}$$

The use of upwind differencing is sufficient to ensure that the coefficients, A_i, remain positive and the matrix of coefficients is thus diagonally dominant for all values of the Péclet number, so that the tri-diagonal matrix algorithm can be used, and the solution remains bounded. Comparison of the performance of the central and upwind differencing schemes with the analytical solution to equation (3.28) suggests that (Spalding, 1972) the coefficients A_i should be evaluated:-

* for Pe < 2 : central differencing
* for Pe > 2 : upwind differencing with neglection of diffusion by μ

The coefficients in equation (3.36) become, for Pe > 2:-

$$A_E \equiv 0 \quad ; \quad A_W \equiv \rho U_W$$

This differencing scheme is referred to as hybrid differencing (Gosman et al, 1969).

The use of upwind differencing, equation (3.36), for convection is equivalent to:-

$$U \frac{d\phi}{dx} \simeq \frac{U}{\delta x} (\phi_P - \phi_W) \tag{3.37}$$

for which the Taylor series expansion is:-

$$\frac{U}{\delta x} (\phi_P - \phi_W) = U \frac{d\phi}{dx} - \underline{\frac{U}{2} \frac{d^2\phi}{dx^2} \delta x} + \frac{U}{6} \frac{d^3\phi}{dx^3} \delta x^2 + ... \tag{3.38}$$

The numerical solution of upwind differenced equations is equivalent to exact solutions of the following differential equation:-

$$\rho \frac{d}{dx} (U\phi) \rightarrow \mu \frac{d^2\phi}{dx^2} + \underline{\left(\frac{U}{2} \delta x\right) \frac{d^2\phi}{dx^2}} + ... = 0 \tag{3.39}$$

where the underlined terms have again been introduced by the finite difference approximations. The disparity between the central difference representation, equation (3.33) and the upwind difference representation, equation (3.38), is that the latter has a leading truncation term of order (δx) which is one order smaller than the leading term for the approximation for diffusion (or pressure gradient, when this is introduced). As a result, it is likely that upwind differencing will

give rise to the dominant error in the solution of the finite difference equations. The reason for particular concern with the term of order (δx) is that, comparing equations (3.39) and (3.34), it results in the solution of a differential equation with an artificially increased (by $\frac{U}{2}\,\delta x$) diffusion term. The coefficient multiplying the second gradient of ϕ is thus referred to as a numerical diffusion coefficient, and numerical solutions of ϕ obtained with upwind differencing can have overdiffused profiles. The neglect of physical diffusion in the hybrid differencing scheme, when Pe > 2, is an attempt to reduce this overdiffusion. It should be emphasized that under these conditions, the amount of diffusion in the solution is then determined without reference to the details of the turbulence model.

The preceding paragraphs have been concerned with the case of a passive scalar. Similar results attend the finite difference approximation to the representation of momentum transport. The central difference approximation for $\rho \frac{\partial U^2}{\partial x}$ is:-

$$\rho \frac{\partial U^2}{\partial x} \simeq \frac{\rho}{4\delta x} \left(U_E^2 - U_W^2 + 2U_P \, (U_E - U_W) \right) \tag{3.40}$$

for which the Taylor series expansion is:-

$$\frac{\rho}{4\delta x} \left(U_E^2 - U_W^2 + 2U_P \, (U_E - U_W) \right) = 2\rho U \frac{dU}{dx} + \frac{\rho}{2} \frac{dU}{dx} \frac{d^2U}{dx^2} \delta x^2 + \ldots . \tag{3.41}$$

and an upwind difference approximation, which retains the conservative property, is:-

$$\rho \frac{\partial U^2}{\partial x} \simeq \frac{\rho}{2\delta x} \left(U_P \, (U_P + U_E) - U_W \, (U_P + U_W) \right) \tag{3.42}$$

for which the Taylor series expansion is:-

$$2\rho U \frac{dU}{dx} - \underline{\left(U \frac{d^2U}{dx^2} - \frac{dU}{dx}\frac{dU}{dx}\right) \frac{\delta x \rho}{2} + \left(U \frac{d^3U}{dx^3} - \frac{dU}{dx}\frac{d^2U}{dx^2}\right) \frac{\delta x^2 \rho}{2} + \ldots.} \qquad (3.43)$$

The central difference, equation (3.41), also results in a coefficient of numerical diffusion $\left(\frac{1}{2}\frac{dU}{dx}\delta x^2\right)$ because the term being approximated is non-linear. It does not, however, give rise for concern because it is of order $(\delta x)^2$ and thus similar to the truncation terms introduced by the approximations for diffusion and pressure gradient. In contrast, the coefficient of numerical diffusion introduced by equation (3.43) is of order (δx) and thus likely to be the dominant error.

Numerical diffusion is particularly undesirable in calculations which are made to evaluate the performance of turbulence models. Castro (1979) has suggested that such numerical inaccuracies in recirculating flows can be as important as deficiencies in turbulence models; the results of sub-section 3.4.3 below support this suggestion. The calculation of simple shear flows, such as a jet or wall boundary layer, usually presents no numerical problem. This is because the relevant equation set can be solved by a marching procedure and the finite difference grid can be arranged so that streamlines are closely aligned with one set of grid lines. The cross-stream spacing is then sufficiently fine that central differencing can be used. Although upwind differencing may be used in the streamwise direction, the resulting numerical diffusion is negligible compared with the remaining terms in the momentum equation, because streamwise gradients are small in such flows. If, however, the same flow type is calculated with streamlines at large angles to the grid lines and the resulting

computational Péclet numbers are such that upwind differencing is used, then numerical diffusion is important and does affect the solution (e.g. Wolfshtein, 1968). The calculation of recirculating flows, which inevitably involves the calculation of shear flows at large angles to grid lines, can thus be expected to be subject to large numerical diffusion if upwind differencing and coarse grids are used.

Improvements in the accuracy of numerical calculations have been attempted in several ways. For example, higher-order approximations to the convection terms (e.g. Leonard, Leschziner and McGuirk, 1978; Leschziner, 1980) are proposed as being more accurate because the leading term in the truncated series is a higher power of (δx), the grid line spacing. Another method is the skew-upwind differencing procedure (Raithby, 1976; cited by Leschziner, 1980) which is derived by extending the concept of upwind differencing in streamline co-ordinates. The application of these differencing schemes is still under development, but both suffer from violation of the boundedness conditions of the partial differential equations and hence are not suitable for the solution of inherently positive definite quantities, such as k or ε.

A widely used alternative for improving the accuracy of solutions has been to increase the number of grid node points within the area of integration ("grid refinement") together with the use of non-uniform grid line separation so as to cover some regions more densely than others. In some flows, regions of the solution domain are covered by locally fine grids (e.g. Johns, 1979) which lie within a coarser grid. Grid refinement is pursued until the change between consecutive solutions is small: the results are then claimed to be "grid independent" and hence uninfluenced by large truncation errors.

The procedure by which grid independence is attained is mostly arbitrary and relies on being able to identify, intuitively, areas in which further grid refinement is unnecessary.

In order to be effective, grid refinement must be used in conjunction with a rational method for assessing the magnitude and location of truncation errors. The following sub-section describes two such methods.

3.3.2 Truncation errors: assessment of magnitude

There exist a number of methods for the local assessment of the magnitude of truncation errors (e.g. Roache, 1976). This sub-section presents two which were used in this thesis. The first is due to De Vahl Davis and Mallinson (1972) who established that the coefficient of numerical viscosity could be approximated by:-

$$\mu_{num} \simeq \rho \frac{|\underline{V}| \ \delta x \ \delta r \ |\sin 2\alpha|}{4 \ (\delta r \ |\sin^3 \alpha| + \delta x \ |\cos^3 \alpha|)} \tag{3.44}$$

where:-

$|\underline{V}|$ is the magnitude of the velocity vector at a node

α is the direction of the velocity vector to the x direction grid lines

A sufficient, though not necessary, condition for numerical diffusion to be large is that the quotient μ_{num}/μ_t (where μ_t is defined by equation (3.6)) should be of order one. The condition is only sufficient because the magnitude of diffusion (whether numerical or physical) must be compared with the remaining terms in the equations of motion. Equation (3.44) is used in sub-section 3.4.3 below in

comparing the calculations of Leschziner and Rodi (1980) with those of this chapter.

The second method, which assesses the truncation error itself, is due to McGuirk and Rodi (1978). Suppose that an iteratively converged solution to equation (3.12) has been obtained, designated $\Phi^*(x, r)$, using the hybrid differencing scheme. Consider a location at which upwind differencing has been used only in the x-direction, because Pe > 2. Then $\Phi^*(x, r)$ satisfies the differential form of momentum conservation equation (3.10) with:-

$$\rho \frac{\partial}{\partial x}(U\phi) \simeq \rho \left[\frac{U_e \Phi_P^* - U_w \Phi_W^*}{\delta x}\right] \tag{3.45}$$

with obvious extension of notation from sub-section 3.3.1. If this term is re-evaluated using a central difference approximation:-

$$\rho \frac{\partial}{\partial x}(U\phi) \simeq \rho \left[\frac{U_e (\Phi_E^* + \Phi_P^*) - U_w (\Phi_P^* + \Phi_W^*)}{2\delta x}\right] \tag{3.46}$$

then in general, the terms in equation (3.11) will no longer satisfy the equality but will give rise to an out-of-balance term, T, which is arithmetically the difference between (3.45) and (3.46). Formally, T is due to the difference in the truncation series for upwind and central differencing which is, from (3.33) and (3.38) (assuming $U_e = U_w$ for simplicity):-

$$\rho T \equiv \rho \left(\frac{U_e}{2} \frac{\partial^2}{\partial x^2} \Phi^* \delta x + \ldots.\right) \tag{3.47}$$

which is the numerical diffusion term. A partial derivative is used in

(3.47) in recognition of the two-dimensionality of the solution space. Whether numerical diffusion is important or not is found by comparing the magnitude of ρT with the original terms (convection, diffusion, pressure gradient) in equation (3.11). It is noted that the convective term should be evaluated as the single term:-

$$\rho \frac{\partial}{\partial x} (U\phi) + \frac{\rho}{r} \frac{\partial}{\partial r} (rUV\phi)$$

rather than as two separate terms, because it is net convection that must be balanced by the remaining terms in equation (3.10).

At the grid nodes where T is comparatively large, numerical diffusion is important and hence grid refinement is required. By reducing the grid spacing, δx say, the magnitude of the terms in the truncation series become smaller. It is noted, however, that the condition for T to be small is a necessary, but not sufficient condition for grid independence. This is because T is evaluated by differencing approximations which are accurate only to terms up to (δx^2). Higher-order truncated terms can be evaluated by using higher-order differencing approximations. This has not been done because, for the grid spacings used, it seems that it is the terms in (δx) which dominate the truncation series. It is plausible that if this were not the case, then upwind differencing would also suffer from boundedness problems.

Numerical diffusion affects the solution of U, V, k and ε. The evaluation of numerical diffusion was only applied, however, (by obvious extension of the preceding one-dimensional description) to the solutions of U and V. This is because, as noted by Castro (1979) and Leschziner (1980), the equations for k and ε are dominated by their respective source terms and hence the details of the representation

of convection are not crucial.

In summary, the method of McGuirk and Rodi (1978) is applied as follows. Converged solutions to the finite difference equations (3.12) are obtained for a given grid. The values of convection, axial and radial diffusion and pressure gradient are evaluated, a posteriori, together with the out-of-balance term, T, for each grid node for both momentum equations. Radial profiles of these quantities are plotted at selected axial stations and the magnitude of T is examined to see whether it constitutes an important term in the local balance of momentum at any grid node. If this is the case, then the grid line spacing in the vicinity of this node is selectively refined, typically by halving the original grid line spacing in the direction in which upwind differencing is being taken (halving the grid line spacing halves the leading truncation term). Non-uniform grid line spacing was used but the ratio of successive line spacing was always kept below 1.3, and usually much less than this, for the reason given in sub-section 3.3.1. A new solution is then generated on the refined grid and again checked for large values of T; the method is repeated until a grid with acceptably small values of T is attained. The advantage of the method is greatest whenever the computer storage which is available is limited and the numerical errors cannot be minimised by indescriminate grid refinement.

The grid line spacings which were eventually arrived at are given in Appendix 3.1 for the 25 per cent blockage baffles and in Appendix 3.2 for the 50 per cent blockage baffle. The radial grid spacing used is particularly fine in the vicinity of the baffle tips, where the separation streamline originates. This is because the shear layer near the baffle tip is directed at large angles to the grid lines and is associated with steep gradients. The presence of large

numerical diffusion in this region would be particularly pernicious to the solution because this would effectively destroy the influence of the boundary conditions at x = 0 which are crucial to the remaining flow field. The sensitivity of solutions to grid refinement near the separation point has also been observed by Castro (1979).

In concluding this section, the third criterion for assessing convergence, mentioned on page 142, is introduced. Given a solution field it is possible to form the individual partial derivatives which constitute the original partial differential equation. In contrast to the method for evaluating T, however, the convection terms are constructed according to the local requirements of the hybrid differencing scheme. The sum of these derivatives at each node will sum to a residual which, in this case, is due to non-convergence of the iterative solution. The magnitude is an indication of the iteration convergence.

3.4 Results

The results of the calculations, using the two equation model of turbulence, are presented in three parts. The first (3.4.1) compares experiment with calculation for the three flows of chapter II and the second (3.4.2) examines the sensitivity of the solutions to the imprecision of the boundary conditions. In the discussion of section 3.5, reference is made to the conclusions of Pope and Whitelaw (1976) and Leschziner and Rodi (1980) concerning the relative merits of the Reynolds stress and two equation models when applied to the annular jet flow measured by Durão and Whitelaw (1978). Their numerical accuracy is examined by re-performing the calculations on finer grids and the details are given in the final part of this section, 3.4.3. The solutions are also compared with the observations

of Durão and Whitelaw (1978).

3.4.1 Calculation of flows of chapter II

These results are discussed in terms of profiles of mean axial velocity, wall pressure and the distribution of turbulent kinetic energy.

Profiles of mean velocity and wall pressure

Figure 3.5 shows the comparison between experiment and calculation for the radial profiles of axial velocity for the 25 per cent blockage disc. The axial stations have been selected to occur within the recirculation zone (x/R = 0.80) close to the free stagnation point (x/R = 1.59) and far downstream of the baffle (x/R = 5.97). At x/R = 0.80 and 1.59 the calculated value of $\partial U/\partial r$ in the mixing layer is smaller than that measured, indicating that the calculated diffusion of axial momentum towards the centreline is too large. The result is that the negative axial velocities near the centreline are generally too small; figure 3.6 depicts the centreline development of axial velocity in which the maximum reversed velocity is too small by 12 per cent and the length of the recirculation bubble is short by 11 per cent. Far downstream, figure 3.5 shows that the calculations retain a marked velocity deficit on the centreline, and figure 3.6 supports the view that the reform of the profile is substantially slower than the experiment. This suggests that radial diffusion of axial momentum is too small, in contrast to the result for the region near the recirculation bubble.

Table 3.5 compares the measured and calculated values of the length and width of the recirculation bubble, and the recirculating mass flow rate. The calculated width is narrow by 5 per cent and from

TABLE 3.5

MEASURED AND CALCULATED DIMENSIONS OF RECIRCULATION BUBBLE AND RECIRCULATING MASS FLOW RATE FOR FLOWS OF CHAPTER II

	x_r/R	W/R	$\dot{m}_r/\dot{m}_o$
Disc, 25% blockage			
measured	1.75	0.63	11 %
calculated	1.56	0.60	8.2 %
Cone, 25% blockage			
measured	1.55	0.56	7 %
calculated	1.41	0.54	5.4 %
Disc, 50% blockage			
measured	3.11	0.79	24 %
calculated	2.78	0.74	14.4 %

the analysis presented in chapter II, equation (2.18), this will result in a smaller minimum wall pressure. Figure 3.7 shows the profiles of wall pressure and confirms the expected discrepancy. Far downstream the pressure recovery is slower and smaller than experiment, indicating that losses due to wall friction are overestimated.

The comparisons for the cone of 25 per cent blockage are given in figures 3.8, 3.9 and 3.10 for the radial profiles of axial velocity, centreline development of axial velocity and profile of wall pressure respectively. In figure 3.8, the close agreement between experiment and calculation at $x/R = 0.60$ is fortuitous because this axial location happens to be where the centreline profiles coincide (see figure 3.9). As for the disc, radial diffusion (that is, turbulent transport) of axial momentum is too great in the mixing layer surrounding the recirculation bubble but too small far downstream. This is because the profile of axial velocity (that is, $\partial U/\partial r$) within the mixing layer is primarily influenced by the turbulent transport of momentum rather than by pressure gradients. However, outside this layer both become important and, for example, are equally large at the rear stagnation point. Reference to table 3.5 shows that the dimensions of the recirculation bubble are again smaller than those measured, although the relative differences occurring between a 25 per cent blockage disc and cone are present. For example, the calculated recirculating mass flow rate behind the cone is about 0.6 that behind a disc. Figure 3.10 compares the measured and calculated variation of wall pressure, and shows that the pressure recovery downstream is too small due to excessive wall friction.

Figure 3.11 gives the radial profiles for the 50 per cent blockage disc at axial stations within the bubble and far downstream; the excessive diffusion of axial momentum is again evident at $x/R =$

1.19 and 2.78. The calculated dimensions of the recirculation bubble, table 3.5, are again small and thus the recirculating mass flow rate and the minimum wall pressure (see figure 3.13) are poorly calculated although the proportional increase in the calculated recirculation zone length, between discs of 25 and 50 per cent blockage, is similar to that found experimentally (≃ 78 per cent). Figure 3.12 shows that the calculated centreline development of axial velocity results in an underestimation of the magnitude of the reversed velocity. The discussion of sub-section 2.4.1 associated the magnitude of the reversed velocity to the pressure minimum near the eye of recirculation vortex, and, therefore, to the magnitude of the centripetal force associated with streamline curvature. The under-estimation of the reversed velocity is the consequence of the excessive diffusion of axial velocity because the latter results in smaller axial velocity maxima (e.g. figure 3.11, x/R = 1.19) and hence a smaller pressure minimum near the eye of the vortex.

Distribution of turbulent kinetic energy

In principle distributions of $\langle u^2 \rangle$, $\langle v^2 \rangle$ and $\langle w^2 \rangle$, as well as k, can be determined from the numerical solution using equations (3.4a) - (3.4c). In practice, a scalar viscosity model does not give satisfactory levels of partioning of turbulent kinetic energy, even in flows where $\langle uv \rangle$, and hence the mean field, are well represented. For example, measurements in a nearly homogeneous shear flow (Champagne et al, 1970) where $\partial U/\partial y$ is the only non-zero strain show that:-

$$\frac{\langle u^2 \rangle}{k} - \frac{2}{3} = 0.3$$

$$\frac{\langle v^2 \rangle}{k} - \frac{2}{3} = -0.18$$

$$\frac{\langle w^2 \rangle}{k} - \frac{2}{3} = -0.12$$

$$\frac{\langle uv \rangle}{k} = 0.3$$

whereas a scalar viscosity model would give, at best, no anisotropy with $\langle uv \rangle / k = 0.3$. Hence only the distribution of turbulent kinetic energy is presented in this sub-section.

Figure 3.14 compares the experimental and calculated distributions of turbulent kinetic energy, k, for the disc of 25 per cent blockage. The generation of k is, in both cases, vigorous immediately downstream of the baffle tip because of the large shear strain, $\partial U/\partial r$. However, the numerical solution has already produced the maximum value of k ($\simeq 0.13\ U_o^2$) by $x/R = 1$, whereas measurements show that k is still increasing at this station. This result is consistent with the calculated mean flow which gives a low value for $\partial U/\partial r$ and hence an underestimation of the production of k in this region. The maximum value of k is calculated to lie at $r/R \simeq 0.5$ for any axial station, in contrast to the measurements which show that this maximum should lie increasingly closer to the centreline with increasing x. Figure 3.15 shows that the centreline distribution of k is substantially underestimated, particularly in the region of the free stagnation point.

The distributions of k for the 25 per cent blockage cone, given in figure 3.16, show similar results to those of the corresponding disc, although the calculated maximum value ($\simeq 0.09\ U_o^2$) is closer to that measured ($\simeq 0.11\ U_o^2$). As before, the centreline distribution of

k is too small near the free stagnation point (see figure 3.17). In the discussion of the measurements of chapter II, it was suggested that the increase in $\langle v^2 \rangle$ and $\langle w^2 \rangle$, and hence k for the 25 per cent blockage baffles was due to normal stress ∿ normal strain generation terms. The inability of a scalar viscosity hypothesis to represent normal stresses adequately, together with the low value of $\partial U/\partial x$ (normal strain) can thus account for the low levels of k on the centre-line and in the vicinity of the free stagnation point.

The calculated distribution of k for the 50 per cent blockage disc, shown in figure 3.18, gives the closest qualitative agreement of the three baffles. Although the position of the maximum value of k is correct, the magnitude is only half that measured. This large discrepancy reinforces the suggestion, made in chapter II, that the shear layer emanating from the baffle tip does not closely resemble a simple mixing layer. In contrast to the low values of k in the free shear layer, the centreline distribution, illustrated in figure 3.19, is in good agreement. This may be because production of k by normal stress ∿ normal strain is unimportant in comparison to the remaining transport processes.

3.4.2 Sensitivity of the solution to the boundary conditions

With the possible exception of the requirement of flow symmetry at the axis of the pipe, the boundary conditions which are specified in sub-section 3.2.2 are imprecise. The purpose of this section is to examine the influence of two separate imprecisions on the solutions presented in sub-section 3.4.1 and thus to assess their importance. The first concerns the conditions in the annular gap at $x = 0$; the second is the use of wall functions.

Boundary conditions at $x = 0$ for $d/2 < x < R$

The boundary conditions for U, V and k are derived from experiment and for ε by estimation. To assess the likely influence of the imprecision in these conditions, calculations were reperformed for the 25 per cent blockage disc. The calculation presented in sub-section 3.4.1 for this case, with the boundary conditions of sub-section 3.2.2, is referred to as the base case.

Whereas the experimental profile of U is accurately known, that of V is subject to greater uncertainty, such as the extrapolation from the measurements to the wall shown in figure 3.3(a). Accordingly, solutions were obtained for the following modifications:-

$$V\ (x = 0,\ r) = \frac{1}{2}\ V_m\ (x = 0,\ r) \quad ; \quad \frac{d}{2} < x < R$$

$$V\ (x = 0,\ r) = \frac{3}{2}\ V_m\ (x = 0,\ r) \quad ; \quad \frac{d}{2} < x < R$$

where V_m are the measured conditions used in the base case of 3.4.1. These modifications make generous allowance for the estimated error (table 2.5) in the measurement of radial velocity. The uniform profile for k used in 3.4.1 was set by reference to a typical value in the annular gap. The specification of k by equation (3.18) is probably more realistic, although it is expected that these conditions are less important than the effects of generation in the shear layer. The profile specified by (3.18) is shown in figure 3.3(b) and the solution corresponding to this was obtained.

The boundary condition for ε, estimated by equation (3.19), should similarly be less important than the effects of its generation within the subsequent shear layer. However, in an attempt to increase the solution values of k, ε was replaced by:-

$$\varepsilon\ (x = 0,\ r) = (0.01)^{3/2}/2\ell \quad ; \quad \ell \equiv R - d$$

which is half that used in the base case.

The effect of these alterations on the radial profiles of axial velocity is shown in figure 3.20. The change in the boundary conditions for radial velocity has the greatest influence on the solutions because of the corresponding variations in the maximum bubble width. Increasing the values of radial velocity results in a wider recirculation bubble and hence a larger maximum in the profile of axial velocity; the converse is true when radial velocity is decreased. Neither solution, however, gives better agreement with experiment and this is particularly evident in figure 3.21, which represents the centreline development of axial velocity. The solutions for the modified values of k and ε, also given in figures 3.20 and 3.21, show that the differences occur mostly within the recirculation region which suggests that it is the values of k and ε very close to the baffle tip which are important. The change in the solution, however, does not result in better agreement with experiment.

Figure 3.22 shows that the profiles of wall pressure are greatly influenced by the change in the radial velocity at x = 0, as would be expected from the discussion of the preceeding paragraph. (The profiles for the modified values of k and ε are virtually indistinguishable from the base case and are not plotted). Both profiles in this figure lie further from the measurements than that for the base case and this may be regarded as <u>a posteriori</u> confirmation of the accuracy of the radial profile in figure 3.3(a).

Figures 3.23(a) and (b) show that the field values of turbulent kinetic energy are also more influenced by the boundary conditions for radial velocity than for k or ε because of the influence

of the former on the strain field, and consequently on the generation of k. The solutions in figure 3.23(b) still retain the maximum value of k away from the centreline, in the mixing layer for the axial station close to the rear stagnation point (x/R = 1.69). The modifications cannot be said, therefore, to represent an improvement over the base case.

The use of wall functions

The wall functions specified in sub-section 3.2.2 are based on the 'law of the wall' for the wall shear stress and the value of dissipation near the wall. This assumes the existence of a Couette-type flow and the presence of a constant stress layer near the wall. The conditions of the flow along the baffle surface at x = 0 do not closely satisfy these conditions, with large spatial gradients of pressure, but the influence of this region on the flow field will be small. For example, it would be expected that changing the hydraulic roughness of this surface in the experiment will not influence the results of chapter II, principally because the separation point is fixed by the geometry of the baffle to lie at r = d/2. The use of the law of the wall at the confining pipe wall is likely to be a good approximation. Also, the shear stress at the wall is determined by the flow remote from the wall, rather than vica versa, so that departures from the constants of the law, should they occur, will not be important.

Summary

The influence of the imprecision attached to the specification of the boundary conditions for radial velocity, turbulent kinetic energy and its dissipation has been determined by numerical experiment.

The changes in the solution caused by the likely tolerances are insufficient to account for the discrepancy between measurement and calculation. It is concluded, therefore, that the errors are due to the inadequacies of the turbulence model.

3.4.3 Calculation of an annular jet

The measurements of the flow in an annular jet, made by Durão and Whitelaw (1978), have been used for the evaluation of various turbulence models (e.g. Pope and Whitelaw, 1976; Leschziner and Rodi, 1980) and finite differencing schemes (e.g. Leonard, Leschziner and McGuirk, 1978; Leschziner and Rodi, 1980). The solutions published by Pope and Whitelaw show comparison with experiment (in terms of, say, the recirculation length) which is worse than that of 3.4.1 above; in contrast, those of Leschziner and Rodi (using a higher order differencing scheme and a turbulence model modification) result in very close agreement with observation.

There would seem to be two reasons, other than the differencing scheme and turbulence model, for these diverse results. The first is that the published calculations have been performed on finite difference grids which are coarser than those used in this work and substantially so in the crucial region surrounding the baffle's tip (Pope and Whitelaw used 30 x 30 nodes; Leonard et al used 25 x 25 nodes; Leschziner and Rodi used 38 x 37 nodes). This is emphasized in figure 3.24 which shows that the area of integration must extend farther radially than for the confined flows of 3.4.1 (cf. figure 3.2). It is, therefore, possible that numerical truncation errors have affected these solutions. The second, equally important reason is that different boundary conditions have been adopted for the flow in the annular gap at $x = 0$ (the jet inlet).

This sub-section presents calculations, on a grid based on that of 3.4.1, for the boundary conditions specified by Pope and Whitelaw (1976) and Leschziner and Rodi (1980). The solutions are compared with the published solutions and experiment and demonstrate the importance of numerical truncation errors and of the boundary conditions assumed to exist at x = 0.

Boundary conditions and finite difference grid

The principle obstacle to the satisfactory calculation of this flow is that measurements of the profiles of U, V and k are not available at x = 0. This feature is likely to be present in any experiment in which the flow expands from small initial dimensions. The closest profiles are at x = 0.20 R and the measurements of chapter II suggest that this is too far from the trailing edge of the baffle to constitute precise conditions at x = 0, particularly for radial velocity. It thus becomes necessary to postulate these conditions and since the solutions are to be compared against those in the literature, it is desirable to adopt the same boundary conditions.

The boundary conditions used by Pope and Whitelaw were (Pope, 1976, p. 111):-

$$U\ (x = 0,\ r) \equiv \hat{U}_0 = 26.8\ ms^{-1} \qquad (d/2 < r < R)$$

$$V\ (x = 0,\ r) = 0.0 \qquad (d/2 < r < R)$$

$$k\ (x = 0,\ r) = 0.003\ (26.8)^2 \qquad (d/2 < r < R)$$

$$\varepsilon\ (x = 0,\ r) = k^{3/2}/\ell \qquad (d/2 < r < R)$$

$$\ell = 0.03\ R \equiv 0.09\ (R - d/2)$$

For the reassessment of the work of Pope and Whitelaw in this dissertation (hereafter referred to as "calculation I") these conditions were modified as follows:-

(a) Boundary layers, each of thickness 0.2 (R - d/2) were allowed for at r = d/2 and r = R as shown in figure 3.25(a). Such layers must exist and their thickness is an estimate derived from the measurements of chapter II. Calculations were made without these boundary layers but the solution was dominated by numerical diffusion.

(b) The value of turbulent kinetic energy was set at $1.5\ m^2\ s^{-2} \equiv 0.002\ (26.8)^2$. This value is taken from the minimum value of k measured at x = 0.2 R and was not available to Pope and Whitelaw.

(c) The length scale for ε was set as $\ell = (R - d/2)$ which is the same prescription as for the solutions in 3.4.1.

The modifications are of detail and not expected to influence the comparison.

For the reassessment of the work of Leschziner and Rodi (hereafter referred to as "calculation II") the profiles of U and k were made available by Leschziner (unpublished work) and are presented in figures 3.25(a) and (b). Although there are differences in the conditions for U, k and ε between calculations I and II, the differences in k and ε are likely to be unimportant and this is

TABLE 3.6

SUMMARY OF THE BOUNDARY CONDITIONS USED FOR CALCULATIONS OF AN ANNULAR JET

POSITION	CALCULATION I				CALCULATION II			
	U	V	k	ε	U	V	k	ε
$x = 0$, $r < \frac{d}{2}$, $r > R$	Eqn. 3.21	0	Eqn. 3.23	Eqn. 3.24	As for calculation I			
Jet inlet, $\frac{d}{2} < r < R$	Fig. 3.25a	0	1.50	Eqn. 3.19	Fig. 3.25a	0	Fig. 3.25b	$k^{3/2}/0.56R$
Entrainment boundary	0	$\frac{\partial}{\partial r}(rV) = 0$	0	0	As for calculation I			
Symmetry axis	$\frac{\partial U}{\partial r}$	0	$\frac{\partial k}{\partial r} = 0$	$\frac{\partial \varepsilon}{\partial r} = 0$	As for calculation I			
Exit plane	parabolic exit conditions		$\frac{\partial k}{\partial x} = 0$	$\frac{\partial \varepsilon}{\partial x} = 0$	$\frac{\partial U}{\partial x} = 0$	$\frac{\partial V}{\partial x} = 0$	$\frac{\partial k}{\partial x} = 0$	$\frac{\partial \varepsilon}{\partial x} = 0$

supported by the results of sub-section 3.4.2. The differences between the solutions are thus due to the difference in the profile of U. It is pointless to discuss which of the two prescriptions is more realistic since both assume zero radial velocity: judging from the evidence of chapter II this is likely to be a particularly poor assumption.

The remaining boundary conditions for the two calculations are summarised in table 3.6.

The details of the distribution of the finite difference grid are given in appendix 3.3. The same grid was used for both calculations and the radial spacing, for $r < R$, is derived from that of appendix 3.2. The grid for $r > R$ must resolve the shear layer downstream of the shroud and also extend far enough radially to cover the downstream spread of the jet. The increase in the number of grid nodes over that in 3.4.1 adds greatly to the storage requirements and number of iterations for convergence: see table 3.4.

In applying the boundary conditions at the downstream boundary it is necessary to require that the U component of velocity remains positive during iteration convergence, otherwise numerical instability occurs. The requirement does not constitute an over-specification of the boundary conditions because it is not enforced on the converged solution.

Comparison with experiment and previous solutions

The results of calculations I and II were examined to assess the magnitude of numerical diffusion, using the analysis of section 3.3. The solution provided by calculation I was found to include relatively large amounts of numerical diffusion, particularly upstream of the free stagnation point. In contrast, the solution of calculation II suffered from substantially less numerical diffusion, although some is

still present. This emphasizes that numerical diffusion is a function of both the finite difference grid and the solution which is generated. These observations suggest that the use of a grid which is much finer than those of either Pope and Whitelaw or Leschziner and Rodi is still unsatisfactory as far as solutions which are 'grid independent' are concerned. The grid was not refined because the imprecision in the boundary conditions at x = 0 does not justify further effort and, more importantly, would not lead to conclusions which are different from those presented below.

Figure 3.26 compares the radial profiles of axial velocity at three axial stations; x = 0.2 R, which is the closest location to the baffle for which measurements are available, near the rear stagnation point (x = 1.3 R) and at a station far downstream (x = 4.3 R). Neither calculation agrees closely with experiment at x = 0.2 R although the difference between calculation I and II, particularly for $0.7 \lesssim \frac{r}{R} \lesssim 0.9$, is large. This is due to the difference in the boundary conditions for U shown in figure 3.25(a). Figure 3.27 presents the radial profile of radial velocity at x = 0.2 R which shows that both calculations overestimate the velocity in the lee of the baffle. It is noted that the measured maximum negative velocity at $r \simeq 0.7$ R is absent from either calculation and this is almost certainly to do with the assumption of zero radial velocity at x = 0. Both calculations show remarkable agreement over the region $0.75 < \frac{r}{R} < 1.0$, however. Returning to the profiles of axial velocity, the calculations show the familiar excessive diffusion of axial momentum at the first two stations, the difference between calculation I and II being particularly noticeable at x = 1.3 R. Far downstream, at x = 4.3 R, the measurements show that axial velocity decays monotonically with radial distance but both calculations retain a wake-like portion in the profile, because

of insufficient radial transport of axial momentum in this region. The magnitude and radial position of the maximum axial velocity in calculation I is consistently different from that of calculation II and experiment. It is noted that the calculations of 3.4.1, for which reliable boundary conditions of U at x = 0 were available, resulted in good agreement between the calculated and measured radial location of maximum axial velocity. This implies that the inlet boundary condition for U is as important as that for radial velocity itself.

Figure 3.28 compares the measurements of Durão and Whitelaw (1978) for the centreline development of axial velocity with calculation I and the solution of Pope and Whitelaw (1976). Although it is encouraging that calculation I approaches the measurements closer than the solution of Pope and Whitelaw, little more than this can be said for the improvement because of the uncertainty in the boundary conditions (compare this with the results of calculation II, below). The important point is that calculation I is <u>different</u> from the other solution. The minor differences in the boundary conditions, at x = 0, between calculation I and those of Pope and Whitelaw are not to be seen as the cause of this, but rather that calculation I was performed on a finer grid. This shows that the solution published by Pope and Whitelaw is far from grid independent and that numerical diffusion has, therefore, influenced the solution. For the purposes of the discussion in section 3.5, it is stressed that the solution of Pope and Whitelaw refers to that given by the Reynolds stress model as well as that using the two equation model.

Figure 3.29 compares the centreline development of calculation II with the solution of Leschziner and Rodi (1980). The latter solution refers to use of the two equation model without modification and the same differencing procedure as in section 3.3. In this case,

calculation II compares less favourably with the measurements than does the solution of Leschziner and Rodi and the difference between calculation II and I demonstrates the influence of the boundary conditions at x = 0. As for calculation I, the change in the solution on using a finer grid is indicative of grid dependence, and hence numerical diffusion, in the previously reported solution. It is recalled that the boundary conditions used for calculation II are precisely the same as those used by Leschziner and Rodi, so that there can be no doubt as to the origin of the difference in the two solutions.

The work of Leschziner and Rodi includes calculations using the same turbulence model but with two other differencing schemes designated "hybrid-skew-upwind/central" and "quadratic". The details of these schemes are not relevant here; their use is expected (see Leschziner, 1980; Leonard, Leschziner and McGuirk, 1978) to give rise to solutions which suffer less from numerical truncation error than does the scheme of section 3.3 for a given grid. The solutions, using these schemes, are similar to that using the hybrid central/upwind scheme and it is concluded by these authors that the fact that two such different schemes yield solutions close to each other suggests that these must be grid independent. The large difference between their results and those of calculation II suggests, however, that the solutions are also not grid independent so that third-order numerical truncation errors may be important in the quadratic scheme.

Figure 3.30 compares measured radial profiles of k with calculation I and II at the same axial locations given in figure 3.26. Both calculations underestimate k in the shear layer downstream of the tip of the baffle and near the free stagnation point for the same reasons as those given in sub-section 3.4.1. Far downstream the

calculated and measured levels are in closer agreement, with calculation I different from II because of the difference in levels of generation due to cross stream shearing (see figure 3.26, x = 4.3 R).

Figures 3.31(a) and (b) compare the radial and centreline distributions of k of calculation II with Leschziner and Rodi (unpublished work). Large differences between the two solutions are again present, providing further evidence of the grid dependence of the solution of Leschziner and Rodi.

Figure 3.32 compares contours of μ_{num}/μ_t where μ_{num} is an estimate of the coefficient of numerical diffusion defined in sub-section 3.3.2, for the case of a plane twin parallel jet calculated by Leschziner and Rodi and calculation II. The plane twin parallel annular jet is the plane two-dimensional equivalent of an axisymmetric annular jet. The plane geometry was calculated using the same turbulence model and grid density (38 x 37) as the annular jet and so the contours for the plane geometry can be expected to be very similar to those of the axisymmetric case. The maximum value in the solution of Leschziner and Rodi is greater than 50 whereas calculation II gives rise to values smaller than 1. This shows that the calculations presented here involve values of numerical diffusion which are smaller by about one and a half orders of magnitude.

3.5 Discussion

The results of section 3.4 show that although there is qualitative agreement between experiment and calculation there are differences in, for example, the length of the recirculation bubble and the levels of turbulence. Assessment of the magnitude of the second order truncation errors in the solutions of sub-section 3.4.1 suggests that these are not responsible for the discrepancy between

experiment and solution, and sub-section 3.4.2 has shown that uncertainty in the boundary conditions is also not the reason so that this must be due to the limitations of the turbulence model. This section opens by briefly discussing whether the discrepancies are important, with particular reference to the calculation of the equivalent combusting flow. The suitability of the two equation model is then analysed by examination of the modelled form of the transport equations for k and ε and by questioning the applicability of a scalar effective viscosity hypothesis. The section closes by making a recommendation for further work.

The calculations of this chapter are representative of the performance of the two equation turbulence model in a two-dimensional recirculating flow where the separation point is well known and the rear stagnation point is not complicated by reattachment to a solid surface. It can be expected that further intricacies, for example if the separation point is not known a priori, will result in poorer agreement with experiment. Exceptions to this conclusion would involve flows where the recirculation region does not greatly influence the main flow, such as a separating boundary layer with almost immediate reattachment. In recirculating flows where the extent of turbulent transport is important, such as effluent discharge in a river or heat transfer at a solid surface, the defects in the turbulent field are important. Even in those situations where only the mean flow is important, this can be sensitive to the turbulent field (for example, the locus of the separation streamline between successive buildings).

In the application of the calculation procedure to the equivalent combusting flow, it can be expected that the difference between measurement and calculation will increase because of the additional imperfections of the combustion model. The underestimation

of the size of the recirculation bubble is undesirable because this will lead to corresponding errors in the flame extinction limits; the underestimation of the rate of growth of the wake will be associated with incorrect calculation of flame propagation. The levels of turbulence should be correct because, for example, these determine the turbulent exchange between the reactants outside the recirculation region and the products within the bubble and also because the level of turbulence and temperature fluctuations may be related. These fluctuations are important because, for instance, the concentration of pollutants is extremely dependent on the probability density of temperature. As a final example of the importance of calculating the correct turbulence levels, it is noted that the rate of reaction for the combustion of fuel (the source term in the transport equation for the mass fraction of that chemical species) may be given by the "eddy break-up" model (Mason and Spalding, 1973) as:-

$$<\rho> \frac{\varepsilon}{k} C_E \, g^{1/2}$$

where $<\rho>$ is the average value of density, C_E is a constant and $g^{1/2}$ is the root-mean-square fuel-concentration fluctuation.

In presenting the two equation turbulence model in sub-section 3.2.1, the eddy viscosity was presented as a corollary of being able to characterize turbulence correctly using only two scalars, k and ε. The model can thus be usefully criticized in two stages: first, by questioning the assumptions involved in the modelling of the transport equations for k and ε and, second, by inquiring as to whether a scalar effective viscosity hypothesis is tenable in this flow.

Modelling of the equations for k and ε

The equation for the transport of k (table 3.1) involves the use of approximations, such as the representation by gradient diffusion of the turbulent transport of k. Although this is known to be sometimes qualitatively incorrect (e.g. near the centreline of a jet), it is probably the case that the underlying postulate, namely that the components of the Reynolds stress tensor are simply related to its first invariant, is the more suspect. The discussion of sub-section 2.4.1 has shown that the transport of each component of Reynolds stress, particularly for the two smaller baffles near the centreline, requires separate consideration because normal stress $\sim$ normal strain generation is large. In contrast, the two equation model has been developed in flows where turbulence is maintained solely through cross-stream shear.

The equation for the transport of ε (table 3.1) is used both in the two equation model and in more advanced formulations, such as the Reynolds stress closure, so that defects in this equation have extensive repercussions in turbulence modelling. The suspected inadequacies of the form of the source term, the outline derivation of which is given in sub-section 3.2.1, have been held responsible for the poor performance of calculations in many flows by several authors (e.g. Pope and Whitelaw, 1976; Morse and Launder, 1979; Launder, Reece and Rodi, 1975), principally because of the great sensitivity to adjustments in the values of C_{ε_1} or C_{ε_2}. A serious obstacle to progress is that reliable measurement of ε is difficult, so that statements concerning defects and improvements in modelling generally rely on inference. A theoretical difficulty is that the exact transport equation refers to processes at the smallest (Kolmogorov) length scales, whereas closure is to be made by large scale quantities. However, the

magnitude of dissipation is determined by large-scale mechanisms at high Reynolds numbers (Lumley, 1978) because ε is equivalent to the energy flux, in wavenumber space, in the inertial subrange which occurs at length scales much larger than the Kolmogorov scales. Since spectral energy transfer is from the largest to the smallest scales, ε is related to the spectral production of turbulent energy at the large scale end of the spectrum. The significance of the preceeding description is that for flows which are not in local equilibrium (i.e. flows in which there are rapid mean flow changes or large imbalances between production and dissipation) the rate of energy transfer out of the large scales is not the same as ε (Hanjalić and Launder, 1979) because the time scale of the mean flow is comparable to the time scale of the spectral transfer of energy. Hence there is a lag between spectral production of k and its effect on dissipation levels (Morse and Launder, 1979). The condition implicit in the derivation of the modelled source is that changes in the mean flow are sufficiently slow that the small scales are in quasi-equilibrium (Lumley, 1978, p. 128; Tennekes and Lumley, 1972, p. 119). It is certain that this condition is not fulfilled in the near wake region of the flow over a baffle.

The interpretation of ε as a spectral energy transfer process has stimulated several modifications to the modelled equation (e.g. Hanjalić and Launder, 1979; Pope, 1978) or even its complete replacement (Hanjalić, Launder and Schiestel, 1980). The modification proposed by Hanjalić and Launder is to include an additional term to account for the experimentally observed rôle of irrotational strain in promoting energy transfer (increasing ε) across the wavenumber spectrum. The modification was used by Leschziner and Rodi (1980), who reported better agreement between experiment and calculation on its introduction. However, the defects of their solution, which have been shown at

length in sub-section 3.4.3, suggest that the physical plausibility of this modification has yet to be tested in this flow type.

The modification of Pope (1978) was tried in an attempt to improve the results of the previous section. The proposed physical basis for this is that in axisymmetric flows there is spectral transfer of energy produced by the 'hoop' stretching of large scale vorticity which is inadequately represented by the existing model. This stretching is absent in a plane flow and it is this difference which is held to account for the difference in spreading between a plane and an axisymmetric jet. The stretching is accounted for by including the following non-dimensional measure of vortex stretching in the source term of the ε transport equation:-

$$C_{\varepsilon_3} \frac{\varepsilon^2}{k} \cdot \chi \tag{3.48}$$

where:-

$$\chi \equiv \omega_{ij}\, \omega_{jk}\, s_{ki} \tag{3.49}$$

and:-

$$\omega_{ij} \equiv \frac{1}{2} \frac{k}{\varepsilon} \left(\frac{\partial U_i}{\partial x_j} - \frac{\partial U_j}{\partial x_i} \right) \tag{3.50}$$

and:-

$$s_{ij} \equiv \frac{1}{2} \frac{k}{\varepsilon} \left(\frac{\partial U_i}{\partial x_j} + \frac{\partial U_j}{\partial x_i} \right) \tag{3.51}$$

C_{ε_3} is a constant which is determined by reference to the spreading rate

of a round jet ($C_{\varepsilon_3} = 0.79$). Lumley (1978) has criticized the form of (3.48) on the grounds that it is independent of the anisotropy of turbulence and suggests that s_{ij} be replaced by:-

$$b_{ij} \equiv \frac{\langle u_i u_j \rangle}{k} - \frac{2}{3}\delta_{ij} \tag{3.52}$$

It is noted that in the two equation model, $b_{ij} \propto s_{ij}$.

In axisymmetric flows (3.48) reduces to:-

$$\frac{C_{\varepsilon_3}}{4}\frac{k^2}{\varepsilon}\left(\frac{\partial U}{\partial r} - \frac{\partial V}{\partial x}\right)^2 \frac{V}{r} \tag{3.53}$$

This term was incorporated into the solution procedure, with care being exercised so as to ensure that the source terms of the finite difference equations remained positive (note that (3.53) can be positive or negative, depending on the sign of V). Despite various formulations, it proved impossible to arrive at stable solutions to the equations, which may be due to the following property of (3.48). In regions where V is negative, (3.53) tends to reduce ε; however, (3.53) is proportional to ε^{-1} so that the term becomes even larger. In the limit, the modelled equations (for any quantity) should possess the following quality, known as realisability (Schumann, 1977; cited by Lumley, 1978):-

as $\varepsilon \to 0$

$$\frac{D\varepsilon}{Dt} \to 0$$

The inclusion of the term (3.48) violates this property. Similar difficulties were encountered by Leschziner and Rodi (1980) when they attempted to use two different modifications simultaneously.

Although there is good theoretical justification for criticizing the form of the ε equation, there does not yet appear to be any entirely satisfactory modification.

Hypothesis of a scalar effective viscosity

Examination of the exact transport equations for the Reynolds stress shows that no relation resembling an effective viscosity can be derived without severe simplifications. The justification for the use of an effective viscosity is carefully set out in Tennekes and Lumley, 1972, section 2.3 and depends on being able to scale the vorticity of the eddies involved in cross-stream momentum transfer with the cross-stream vorticity of the mean flow and also on being able to scale the shear stress with any component of the Reynolds stress tensor. On dimensional grounds, this is only possible in flows with one characteristic length scale and one characteristic time scale (reciprocal of the strain rate) and these conditions are fulfilled by simple thin shear layer flows (such as jets or wakes) because these are observed to be self-preserving. The physical attribute of these flows is that the production of turbulent kinetic energy equals its dissipation, although convective and diffusive transport may not be negligible (Bradshaw, 1976).

The flow over baffles involves multiple length scales (e.g. the wake width, the recirculation bubble length and the boundary layer thickness on the confining wall) and the strain rates (such as the cross-stream shear and the streamwise gradients of U). One consequence of multiple length scales is the observation (Fujii et al, 1978; Durão and Whitelaw, 1978) that the occurence of zero shear stress does not coincide with zero shear strain, which cannot be accounted for by the effective viscosity hypothesis. It could be argued that the flow downstream of the rear stagnation point approaches the conditions of

a simple shear layer flow and that the effective viscosity hypothesis is applicable. In the vicinity of the centreline, however, ε greatly exceeds the rate of production of k and the flow thus resembles weak shear flows. In these flows, Rodi (1975) found that C_μ (table 3.2) assumed values larger than 0.09. The observed underestimation of the radial diffusion of axial momentum in this region can thus be attributed to the inappropriate value of C_μ. The amelioration of the calculation downstream of the recirculation bubble may involve changes in the turbulence model but is also contingent on improving the calculation of the flow within the recirculation bubble itself. This has been shown by Durst and Rastogi (1979) who calculated the flow downstream of a recirculation bubble using measured profiles at a station just downstream of the rear stagnation point as initial conditions. The solution was in closer agreement with experiment than the calculation of the flow which included the recirculation bubble.

At axial stations upstream of the rear stagnation point the most obvious departure of the flow from the conditions of a simple thin shear layer is the occurence of streamline curvature, which is due to a strain normal to the streamline. Nominally, the two equation model accounts for the presence of this extra strain rate on the level of shear stress:-

$$\langle u_s v_s \rangle \propto \frac{\partial U_s}{\partial n} + \frac{\partial V_s}{\partial s} \qquad (3.54)$$

where U_s, u_s, V_s and v_s are defined in the streamline co-ordinates (s, n) shown in figure 3.33. It is a matter of observation, however, that (Bradshaw, 1973):-

$$\langle u_s v_s \rangle \propto \frac{\partial U_s}{\partial n} + \gamma \frac{\partial V_s}{\partial s} \qquad (3.55)$$

where γ is a coefficient of the order of 10 and the sign of γ is determined according to whether the streamline curvature is stabilising or destabilising. Stabilising curvature exists when the angular momentum of a flow increases with increasing n co-ordinate, so that the curvature associated with the shear layer extending from the baffle tip is of the stabilising kind. Comparison of equations (3.54) and (3.55) suggests that the two equation model should overestimate cross-stream shear stress, and hence turbulent diffusion also, as was inferred in sub-section 3.4.1. Experimental evidence for this overestimation is given in figure 3.34 which shows the results of calculations I and II together with the measurements of Durão and Whitelaw (1978). As expected, the calculated values of <uv> are much greater for x = 0.6 R and 1.3 R. (In passing, it is noted that <uv> at x = 4.3 R is indeed underestimated as expected from the discussion above).

Equation (3.55) is a qualitative, rather than quantitative, statement about the effects of streamline curvature. Changes to the two equation model have been used to account for the effects of streamline curvature, that of Leschziner and Rodi (1980) being perhaps the most soundly based. Their improvisation consists of making C_μ a function of the streamline curvature.

A more fundamental allowance for the effects of streamline curvature involves abandoning an effective viscosity hypothesis in favour of the Reynolds stress model mentioned in sub-section 3.2.1. The details of this model are not directly relevant to this discussion, other than to say that modelled transport equations for all Reynolds stresses, as well as for ε, are solved. The disposable constants have been established by reference to simple shear flows; however, the qualitative effects of curvature, equation (3.55) are predicted (Launder, Reece and Rodi, 1975) without any further changes to the

model. Its quantitative performance has been evaluated for curved wall boundary layers (Irwin and Arnot-Smith, 1975) as well as for a free, plane curved shear layer (Gibson and Rodi, 1981). The latter computational investigation is particularly convincing in validating the physical basis of the model through the comparison of the experimental and calculated budgets of turbulent energy and shear stress, which showed clear improvement over the two equation model. In recommending the adoption of this more advanced model the separate consideration of normal stress ∿ normal strain production, recommended above, is automatically assured. It is thus expected that the near centreline distributions of $\langle u^2 \rangle$ and $\langle v^2 \rangle$ will be better calculated, for the 25 per cent blockage baffles. As a consequence, the qualitative distribution of turbulent kinetic energy should also improve.

The Reynolds stress model has already been applied (Pope and Whitelaw, 1976) to the annular jet flow with results virtually the same as for those of the two equation model: this would appear to refute the recommendation made in the previous paragraph. It is recalled that sub-section 3.4.3 demonstrated that the work of Pope and Whitelaw (1976) was influenced by numerical diffusion. A further reason for the importance of numerical diffusion in their calculation using the Reynolds stress model concerns the method by which the gradients of Reynolds stress were incorporated in the numerical solution technique. Because these were included (Pope, 1976, p. 103) in the source term, S_ϕ (equation (3.12)), it was necessary to use upwind differencing to retain the diagonal dominance of the matrix of coefficients, A_i (see sub-section 3.2.3) at each and every grid node and in both co-ordinate directions. As explained in sub-section 3.3.1 this will increase numerical diffusion as compared with a solution

using hybrid differencing wherever Pe (equation (3.35)) is less than two and can thus mask any benefit which may accrue from the change to the more advanced turbulence model.

The evidence for re-appraising the performance of the Reynolds stress model in recirculating flows, taking particular care to minimise numerical truncation errors, is thus strong.

3.6 Summary

The following is a summary of the more important findings and conclusions of this chapter:-

1. There are two major obstacles to the evaluation of turbulence models in recirculating flows:-

   (a) the presence of large numerical diffusion errors which accompany the use of upwind differencing for the representation of convection;

   (b) the availability of reliable experimental profiles for use as boundary conditions at the plane containing the trailing edge of the baffle.

2. Numerical diffusion errors can be reduced by grid refinement, but to be effective refinement must be accompanied by a method for assessing the magnitude and location of these errors. The method used in this chapter is due to McGuirk and Rodi (1978) and involves the a posteriori estimation of numerical diffusion in the converged solution of the finite difference equations.

3. The experimental results of chapter II provide sufficiently accurate profiles to remove obstacle 1(b).

4. The two equation turbulence model has been used for the calculation of the flows of chapter II. The following discrepancies are observed:-

   (a) the radial diffusion of axial momentum is over-estimated in the region of the recirculation, and underestimated further downstream. As a consequence the length of the recirculation is too short and the rate of reform of the wake is too slow;

   (b) the level of turbulent kinetic energy is too small and, for the 25 per cent blockage baffles, incorrectly distributed;

   (c) the qualitative changes in the mean flow which occur on changing baffle blockage or forebody shape are reflected in the calculations.

5. The two equation model is criticized for the form of the source term in the ε equation and the use of an effective viscosity hypothesis. The greatest demonstrable weakness of the model in this flow is that the scalar effective viscosity is unable to account for the reduction in shear stress in the shear layer surrounding the recirculation zone because of the existence of stabilising streamline curvature.

6. It is proposed that the more advanced Reynolds stress turbulence model be used to account for the effects of streamline curvature. It is expected that the qualitative distribution of turbulent kinetic energy will also improve.

7. A previously reported use of the Reynolds stress model, in a related flow, which was found to give no improvement over the two equation model, is shown to have suffered from large numerical diffusion.

APPENDIX 3.1

25 per cent blockage disc and cone: location of grid lines for finite difference procedure and values of boundary conditions at x = 0.

x- direction		r-direction	
Grid Line Number	Position/(mm)	Grid Line Number	Position/(mm)
1	- 0.819	1	- 0.52
2	0.819	2	0.52
3	2.46	3	1.56
4	4.09	4	2.60
5	5.73	5	3.65
6	7.37	6	4.69
7	9.01	7	5.73
8	10.6	8	7.02
9	12.5	9	8.06
10	14.7	10	8.94
11	17.2	11	9.67
12	20.0	12	10.3
13	23.3	13	10.8
14	27.1	14	11.2
15	31.5	15	11.6
16	36.5	16	11.9
17	42.3	17	12.2
18	48.9	18	12.4
19	56.5	19	12.6
20	65.3	20	12.8
21	75.3	21	13.1
22	86.9	22	13.4
23	100.0	23	13.8
24	116.0	24	14.2
25	133.0	25	14.7
26	153.0	26	15.3
27	177.0	27	16.1
28	204.0	28	16.9
29	234.0	29	18.0
30	270.0	30	19.3
		31	20.3
		32	21.4
		33	22.4
		34	23.4
		35	24.0
		36	26.0

APPENDIX 3.1 (CONTD.)

Disc, 25 per cent blockage: boundary conditions at x = 0

Grid Line Number	Axial Velocity (m/s)	Radial Velocity (m/s)	k (m^2/s^2)
18	0.00	0.00	0.00
19	0.01	0.00	0.01
20	0.02	0.50	0.01
21	0.03	0.86	0.01
22	0.05	0.82	0.01
23	0.50	0.78	0.01
24	1.00	0.70	0.01
25	1.44	0.65	0.01
26	1.45	0.60	0.01
27	1.49	0.52	0.01
28	1.48	0.46	0.01
29	1.48	0.40	0.01
30	1.47	0.33	0.01
31	1.45	0.26	0.01
32	1.42	0.21	0.01
33	1.37	0.15	0.01
34	1.27	0.10	0.01
35	1.20	0.06	0.01
36	0.00	0.00	0.00

APPENDIX 3.1 (CONCLUDED)

Cone, 25 per cent blockage: boundary conditions at x = 0

Grid Line Number	Axial Velocity (m/s)	Radial Velocity (m/s)	k (m^2/s^2)
18	0.00	0.00	0.000
19	0.50	0.00	0.142
20	1.13	0.48	0.130
21	1.23	0.48	0.105
22	1.32	0.48	0.065
23	1.53	0.46	0.043
24	1.64	0.44	0.019
25	1.64	0.41	0.019
26	1.65	0.38	0.018
27	1.65	0.35	0.017
28	1.65	0.32	0.017
29	1.63	0.28	0.016
30	1.61	0.24	0.017
31	1.57	0.18	0.019
32	1.54	0.14	0.021
33	1.50	0.11	0.023
34	1.45	0.07	0.025
35	1.10	0.04	0.015
36	0.00	0.00	0.000

APPENDIX 3.2

50 per cent blockage disc: location of grid lines for finite difference procedure and values of boundary conditions at x = 0.

x-direction	r-direction	
	Grid Line Number	Position /(mm)
As in appendix 3.1	1	- 0.52
	2	0.52
	3	1.56
	4	2.60
	5	3.65
	6	4.69
	7	5.73
	8	6.77
	9	7.81
	10	8.85
	11	9.90
	12	10.9
	13	12.2
	14	13.3
	15	14.1
	16	14.9
	17	15.5
	18	16.0
	19	16.4
	20	16.8
	21	17.1
	22	17.4
	23	17.6
	24	17.8
	25	18.0
	26	18.3
	27	18.6
	28	19.0
	29	19.4
	30	19.9
	31	20.5
	32	21.3
	33	22.1
	34	23.2
	35	24.0
	36	26.0

APPENDIX 3.2 (CONCLUDED)

Disc, 50 per cent blockage: boundary conditions at x = 0

Grid Line Number	Axial Velocity (m/s)	Radial Velocity (m/s)	k (m^2/s^2)
23	0.00	0.00	0.000
24	1.80	0.00	0.010
25	1.82	0.50	0.017
26	1.83	0.52	0.029
27	1.82	0.54	0.040
28	1.80	0.56	0.047
29	1.79	0.57	0.037
30	1.77	0.58	0.028
31	1.75	0.57	0.020
32	1.72	0.55	0.020
33	1.69	0.45	0.022
34	1.66	0.38	0.029
35	1.55	0.30	0.021
36	0.00	0.00	0.000

APPENDIX 3.3

Annular jet (Durão and Whitelaw, 1978): location of grid lines for finite difference procedure.

x-direction		r-direction	
Grid Line Number	Position/(mm)	Grid Line Number	Position/(mm)
1	- 0.318	1	- 0.021
2	0.318	2	0.021
3	0.955	3	0.063
4	1.59	4	1.05
5	2.23	5	1.47
6	2.86	6	1.88
7	3.50	7	2.30
8	4.14	8	2.70
9	4.77	9	3.14
10	5.41	10	3.56
11	6.05	11	3.98
12	6.68	12	4.40
13	7.40	13	4.91
14	8.21	14	5.33
15	9.13	15	5.68
16	10.2	16	5.97
17	11.3	17	6.22
18	12.7	18	6.43
19	14.2	19	6.61
20	15.9	20	6.76
21	17.8	21	6.88
22	19.9	22	6.98
23	22.4	23	7.07
24	25.1	24	7.16
25	28.2	25	7.25
26	31.8	26	7.35
27	35.7	27	7.47
28	40.2	28	7.62
29	45.3	29	7.79
30	51.1	30	8.00

APPENDIX 3.3 (CONCLUDED)

x-direction		r-direction	
Grid Line Number	Position/(mm)	Grid Line Number	Position/(mm)
31	56.8	31	8.25
32	62.6	32	8.54
33	68.3	33	8.90
34	74.0	34	9.31
35	79.8	35	9.76
36	85.5	36	10.2
37	91.3	37	10.8
38	97.0	38	11.6
39	103.0	39	12.5
40	109.0	40	13.8
		41	15.5
		42	17.7
		43	20.5
		44	23.3
		45	26.1
		46	29.0
		47	31.8
		48	34.6
		49	37.4
		50	40.3
		51	43.1
		52	45.9
		53	48.7
		54	51.6
		55	54.4

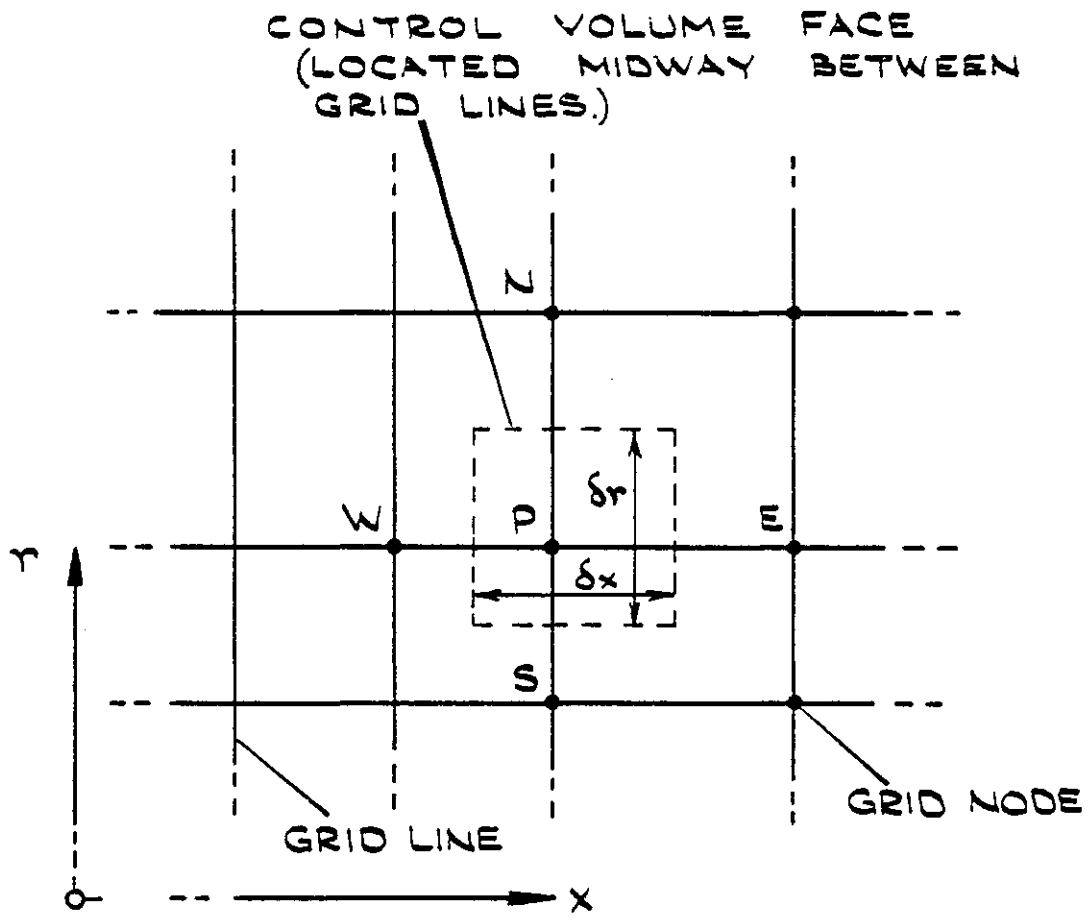

Figure 3.1(a) Rectangular, non-uniform grid (in polar cylindrical co-ordinates showing grid node distributions)

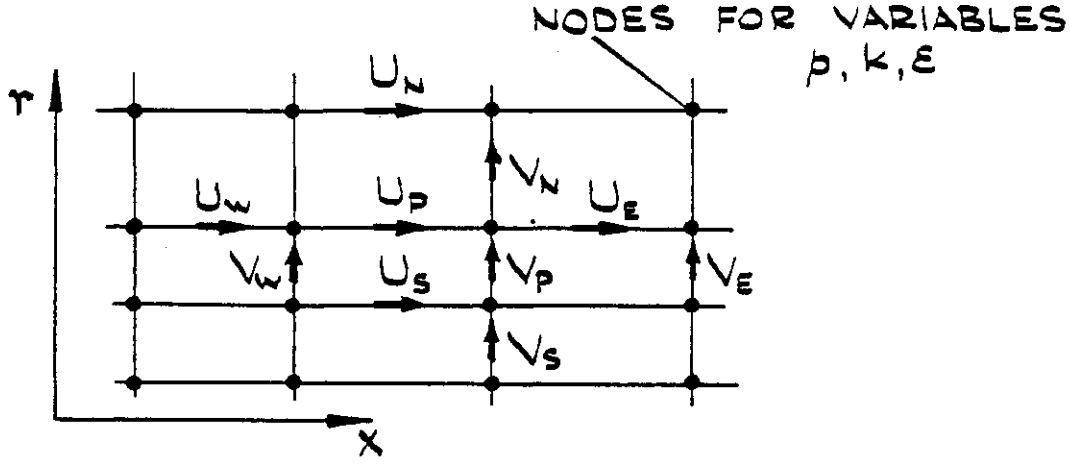

Figure 3.1(b) Relative location of variables in staggered grid

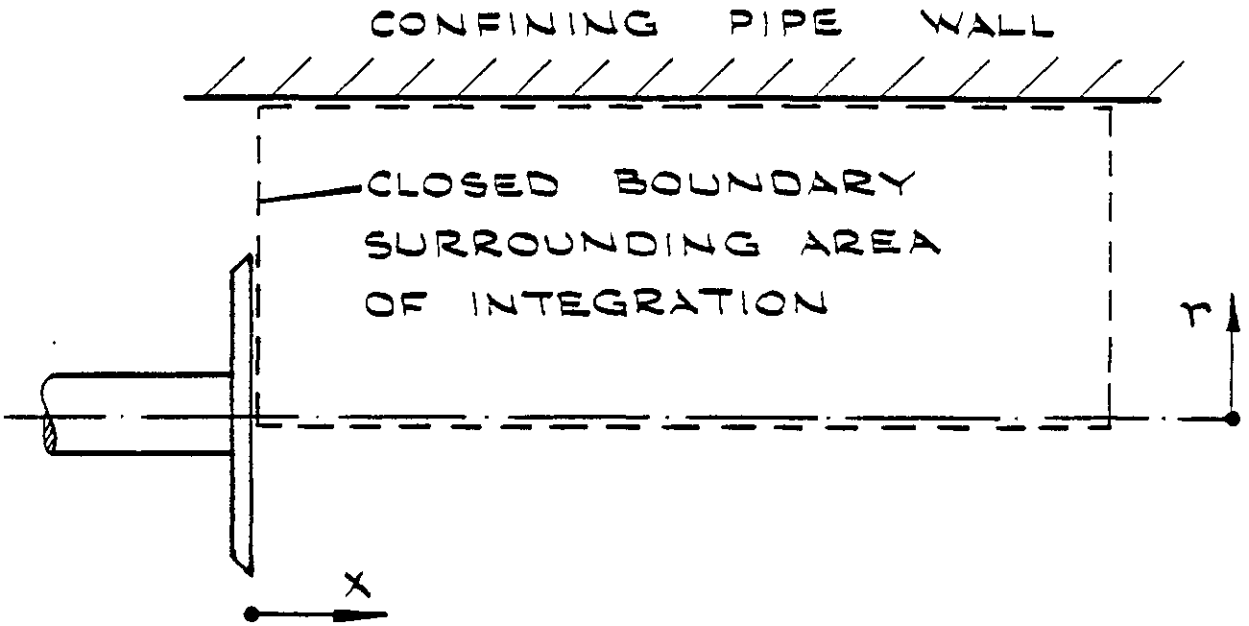

Figure 3.2 Area of integration of the finite difference equations for U, V, k, ε

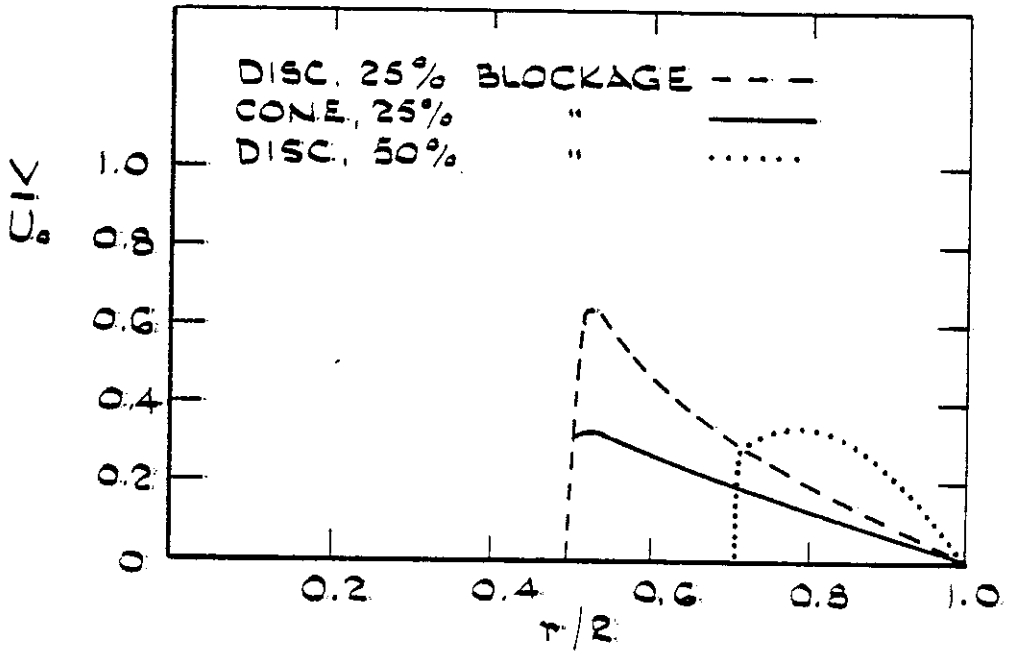

Figure 3.3(a) Boundary (x = 0) profiles of radial velocity for 3 baffles

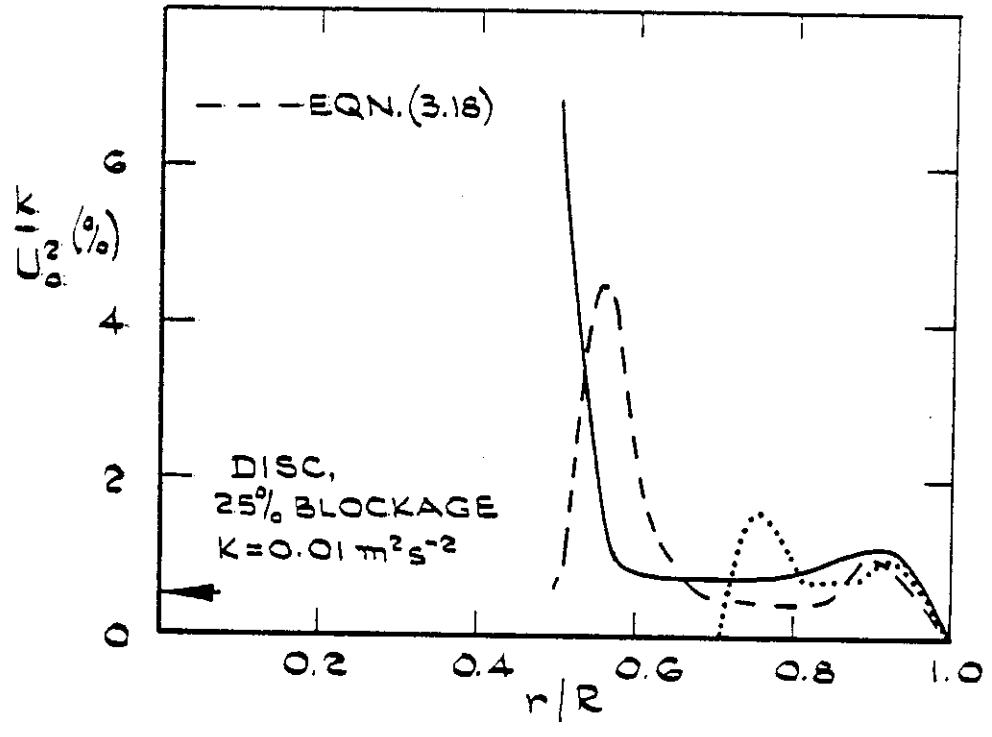

Figure 3.3(b) Boundary (x = 0) profiles of turbulent kinetic energy for 3 baffles

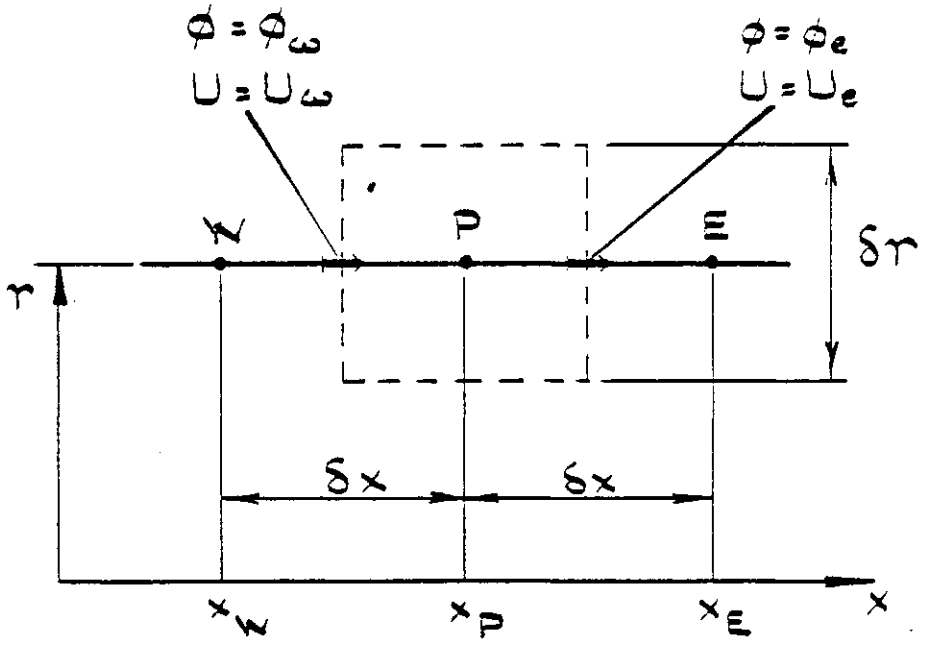

Figure 3.4 Definition sketch for control volume (dotted line) used in section 3.3.1

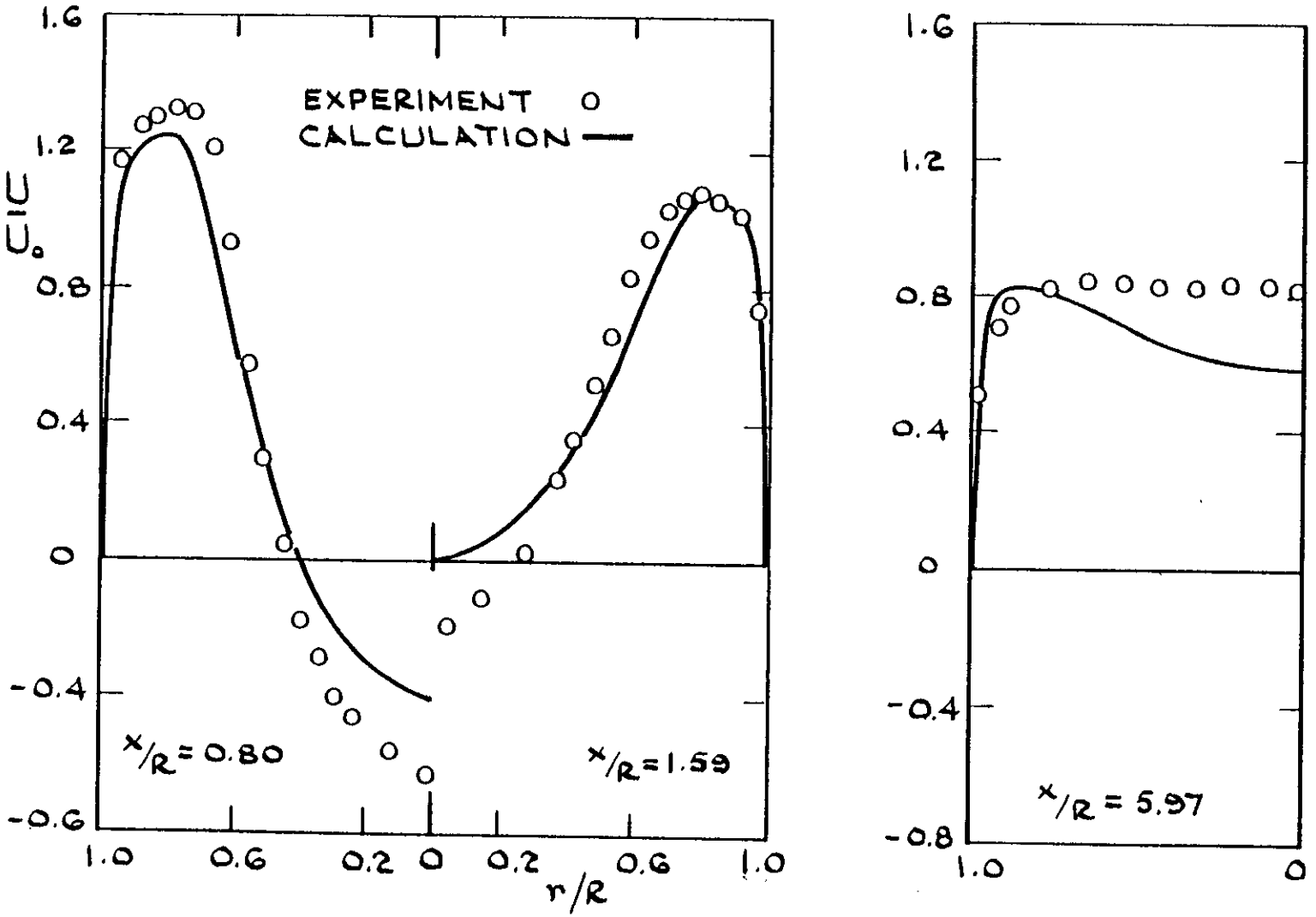

Figure 3.5 Disc, 25% blockage: radial profiles of axial velocity at successive axial stations. Comparison between experiment and calculation.

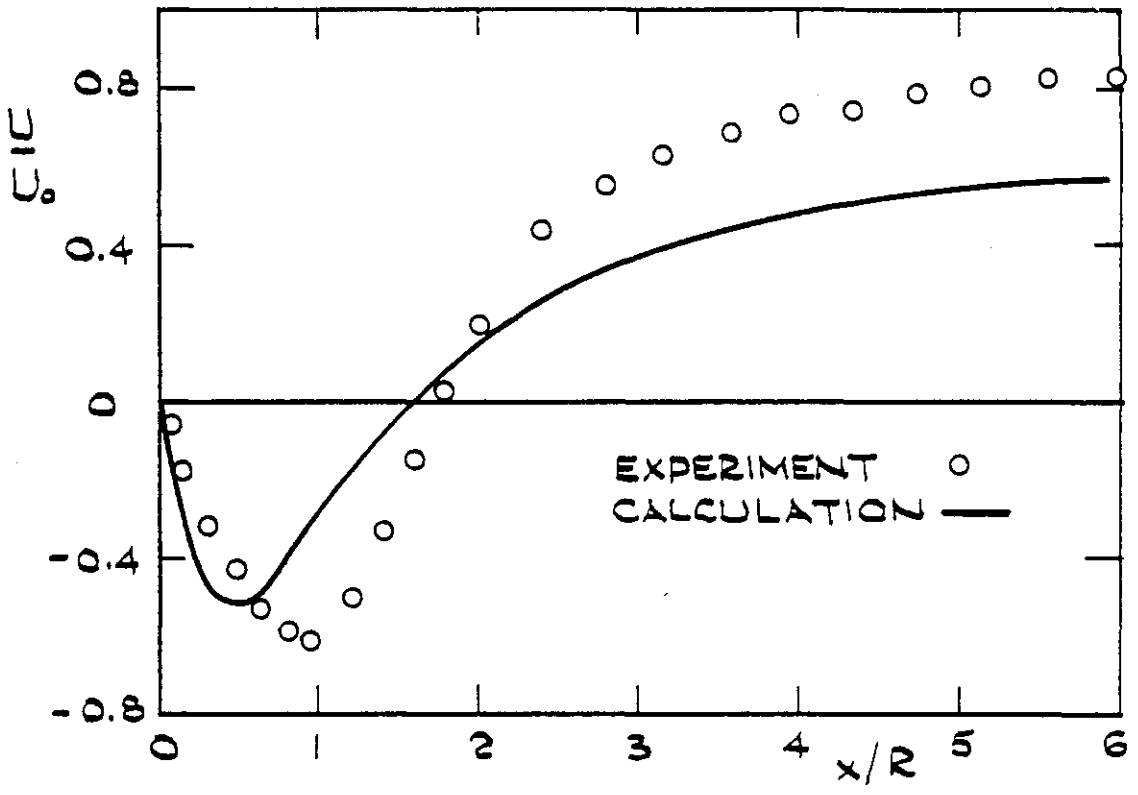

Figure 3.6 Disc, 25% blockage: centreline development of axial velocity. Comparison between experiment and calculation.

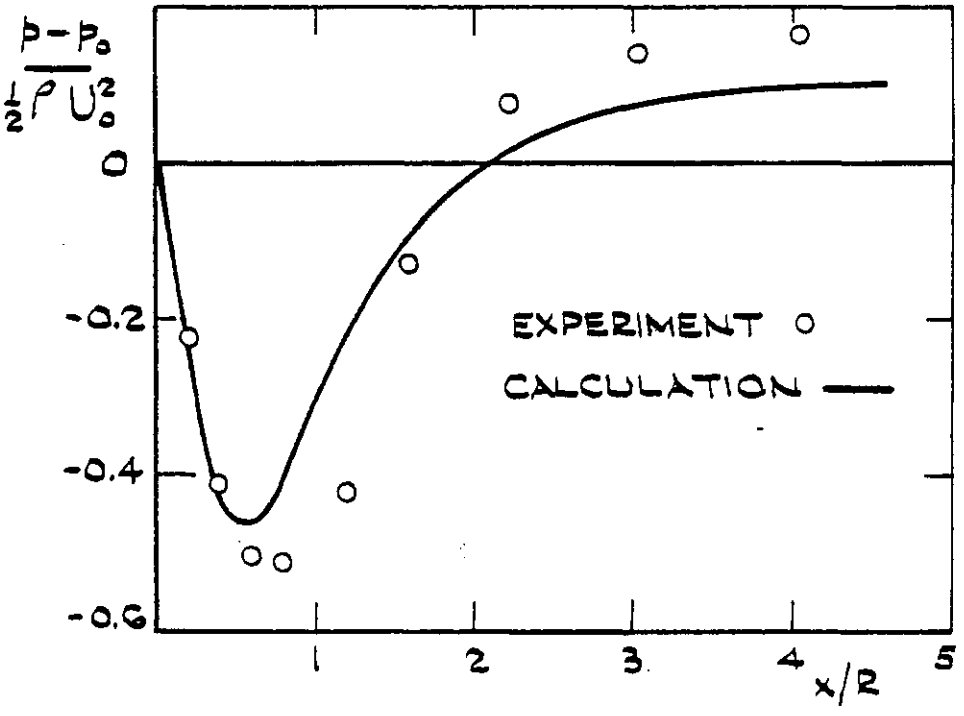

Figure 3.7 Disc, 25% blockage: axial profile of wall pressure. Comparison between experiment and calculation.

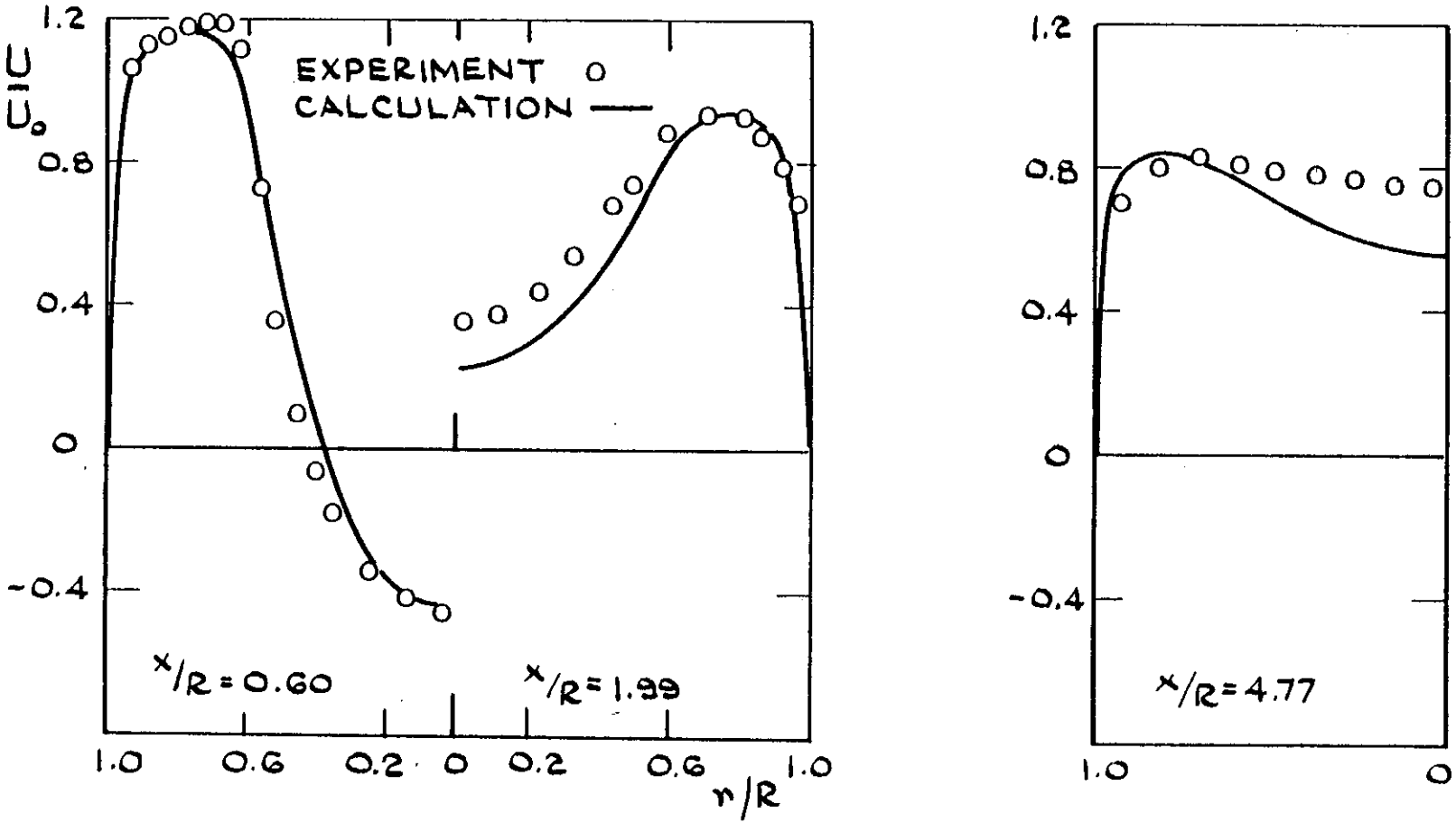

Figure 3.8 Cone, 25% blockage: radial profiles of axial velocity at successive axial stations. Comparison between experiment and calculation.

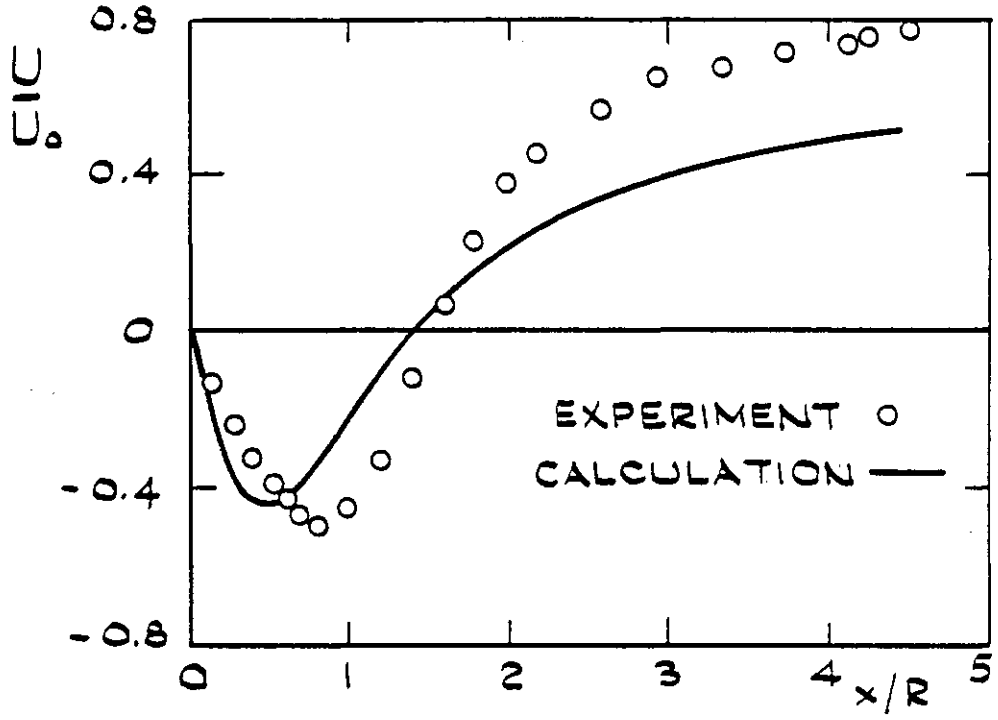

Figure 3.9 Cone, 25% blockage: centreline development of axial velocity. Comparison between experiment and calculation.

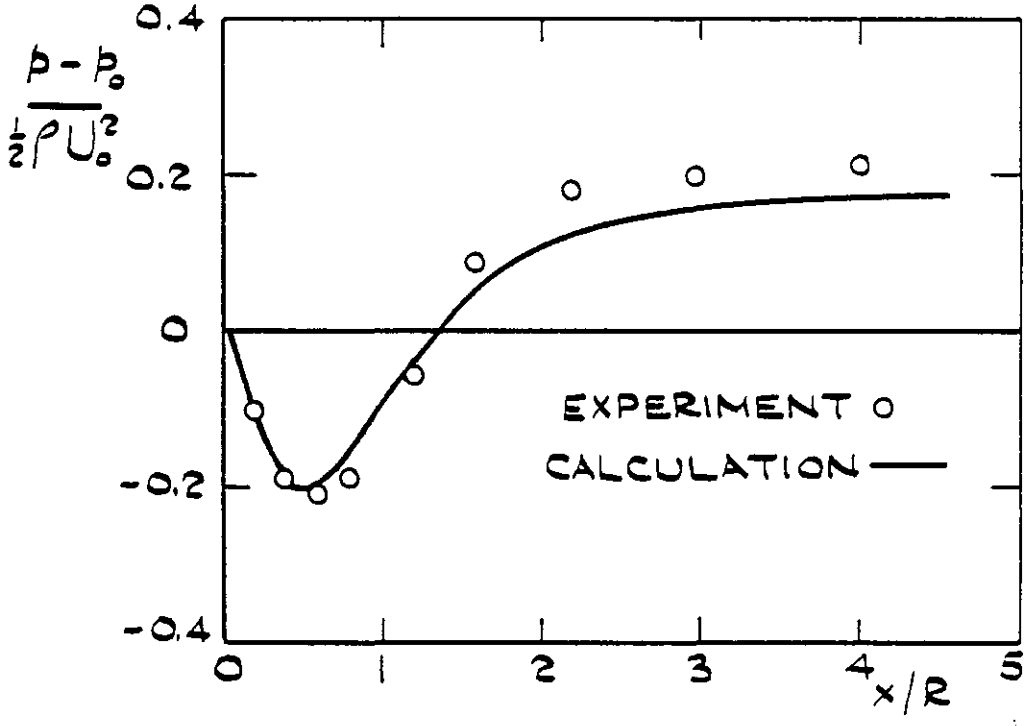

Figure 3.10 Cone, 25% blockage: axial profile of wall pressure. Comparison between experiment and calculation.

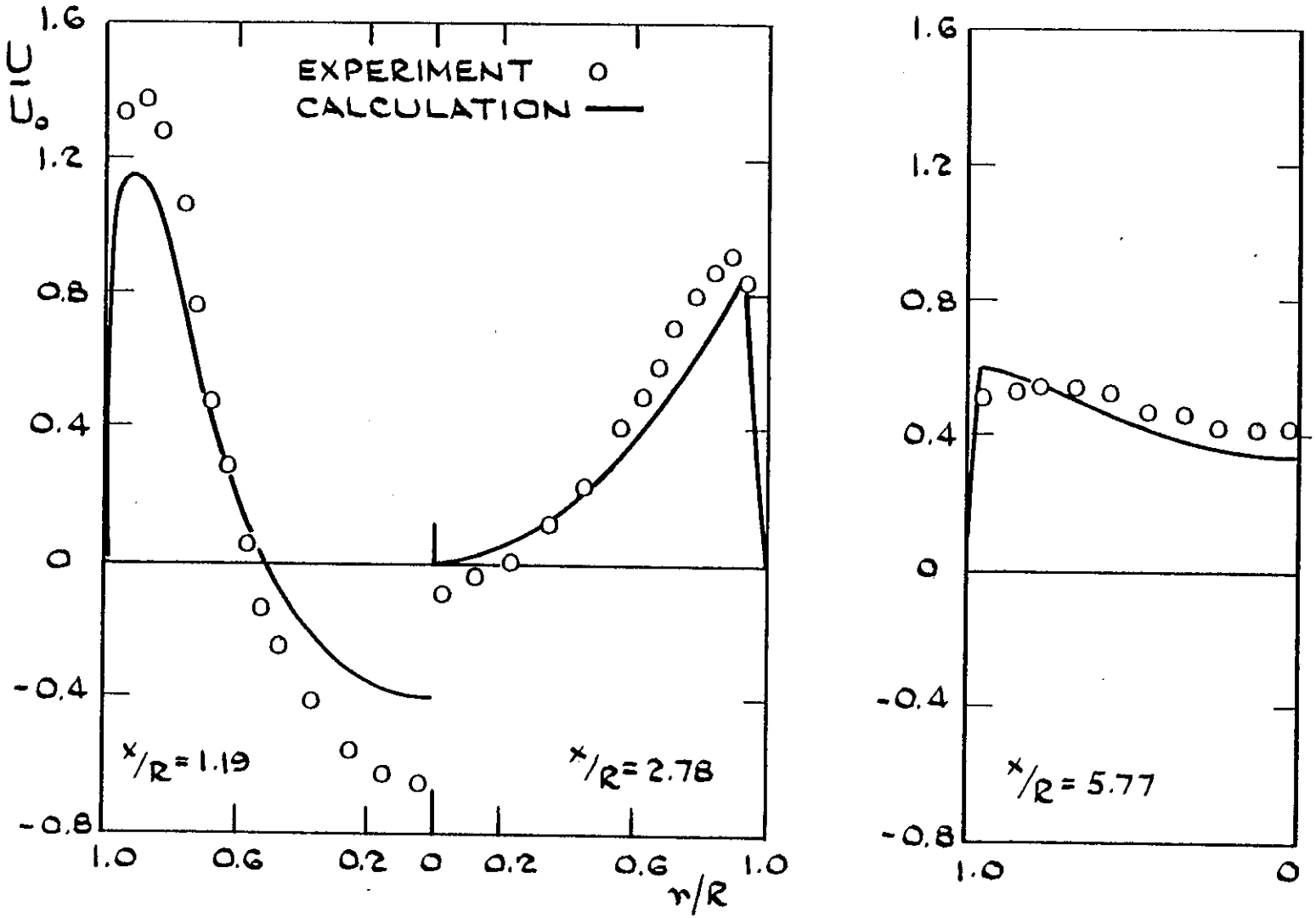

Figure 3.11 Disc, 50% blockage: radial profiles of axial velocity at successive axial stations. Comparison between experiment and calculation.

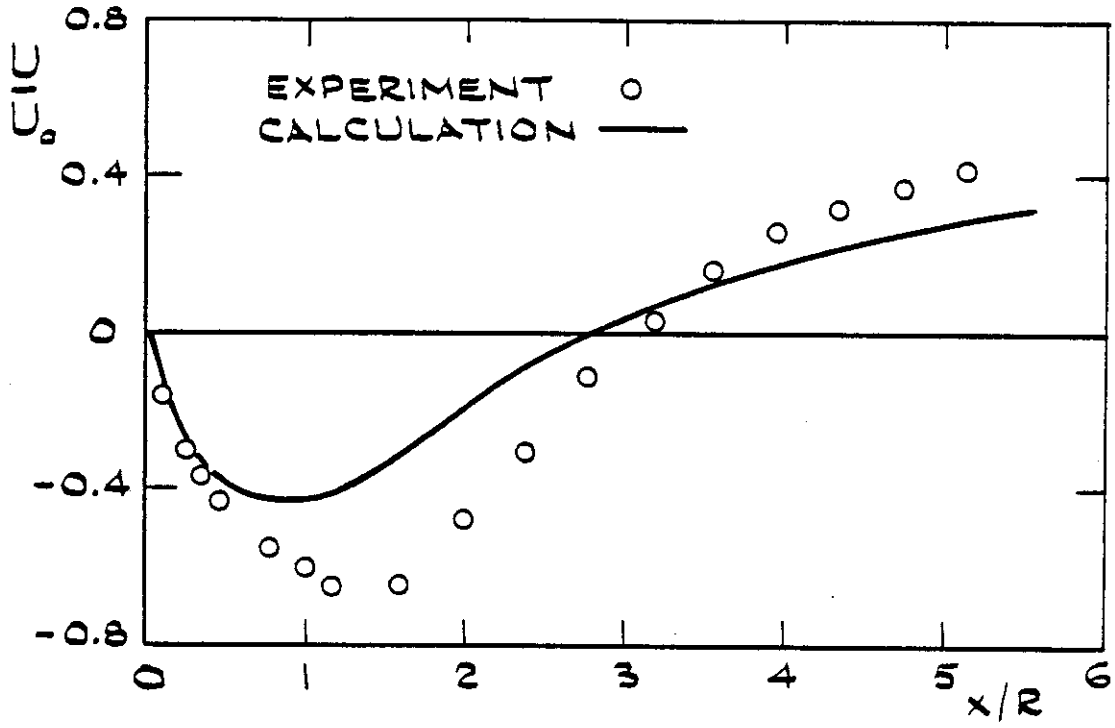

Figure 3.12 Disc, 50% blockage: centreline development of axial velocity. Comparison between experiment and calculation.

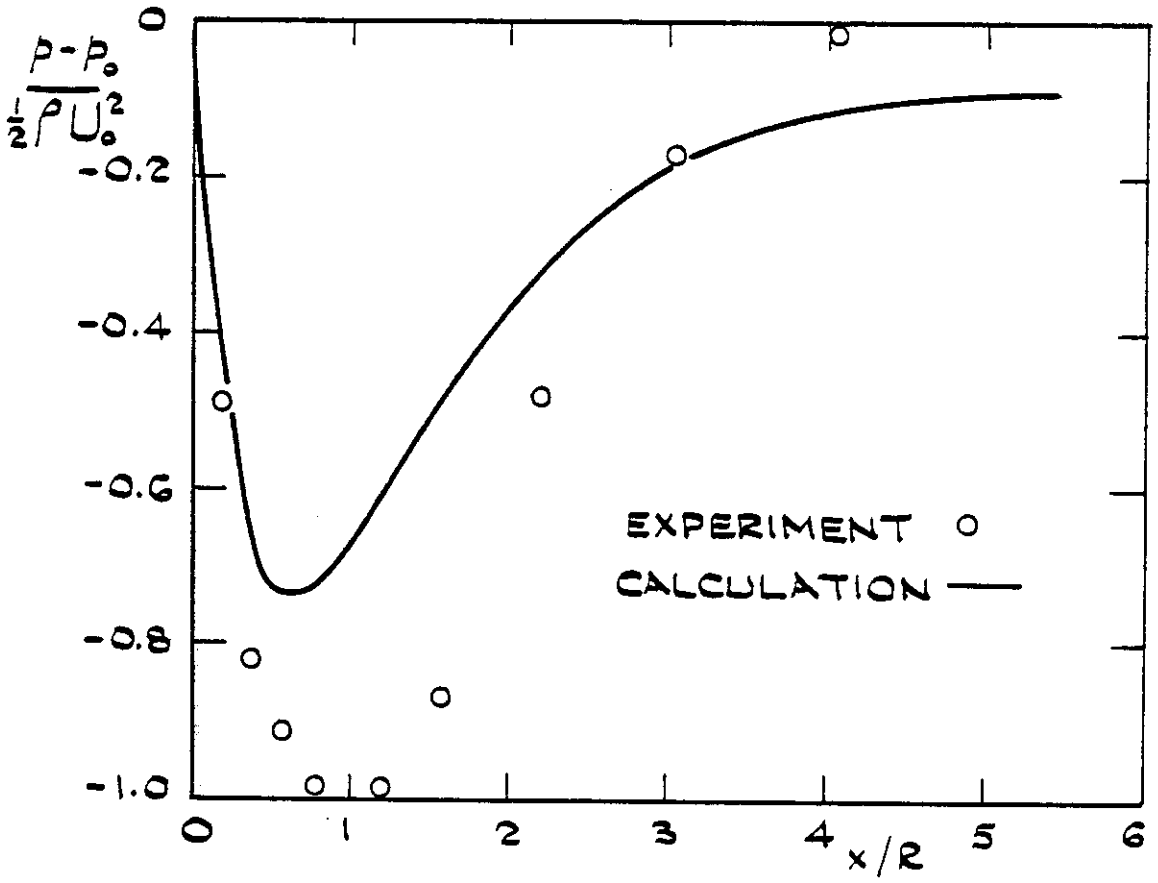

Figure 3.13 Disc, 50% blockage: axial profile of wall pressure. Comparison between experiment and calculation.

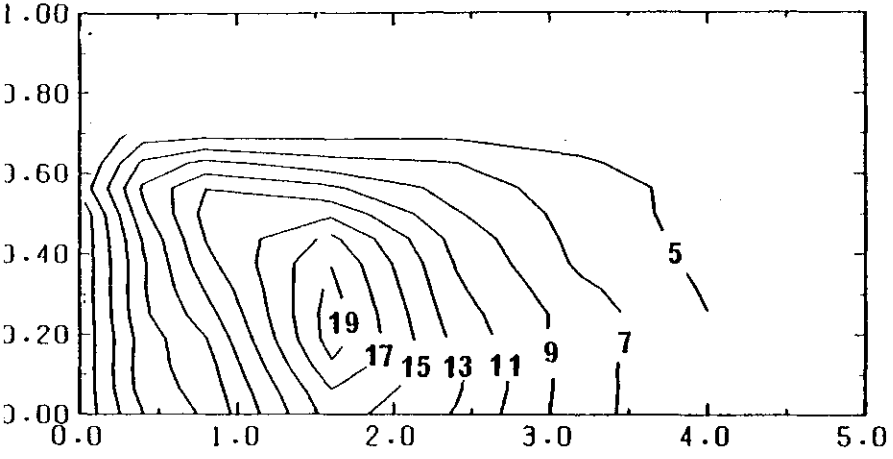

(a) Experiment

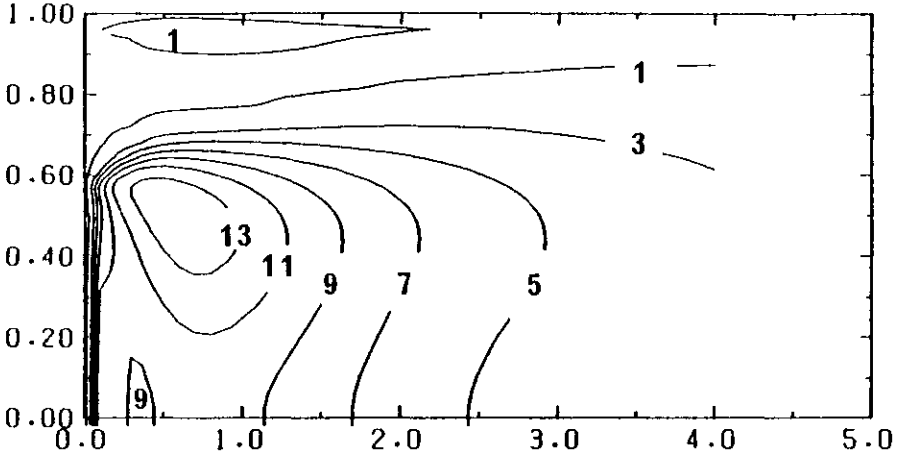

(b) Calculation

Figure 3.14 Disc, 25% blockage: comparison of distribution of turbulent kinetic energy (contour levels in % U_o^2)

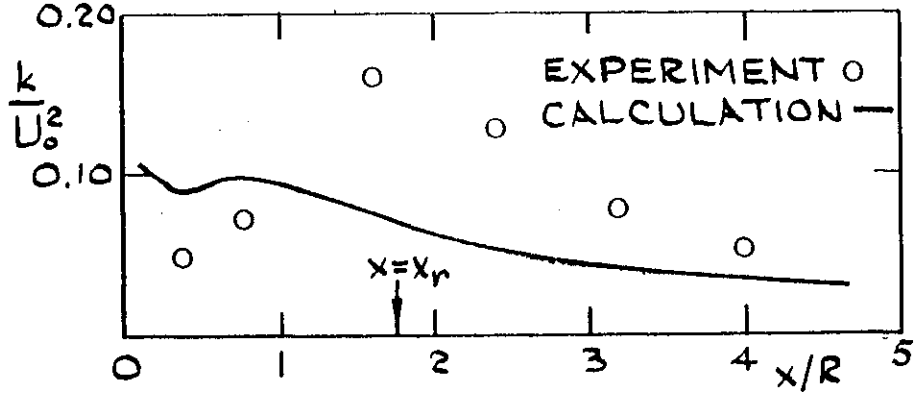

Figure 3.15 Disc, 25% blockage: centreline development of turbulent kinetic energy. Comparison between experiment and calculation.

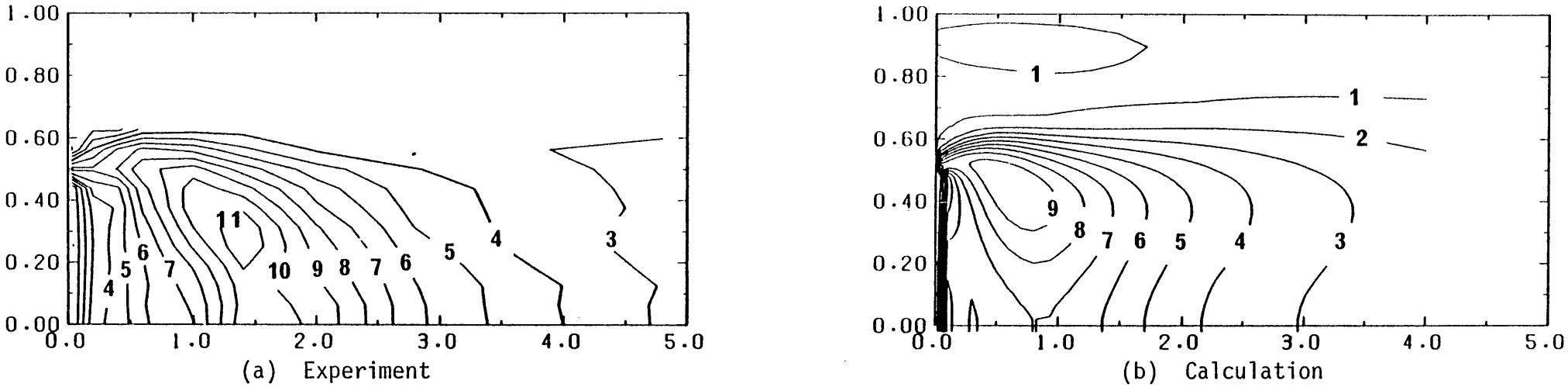

Figure 3.16 Cone, 25% blockage: comparison of distribution of turbulent kinetic energy (contour levels in % U_0^2)

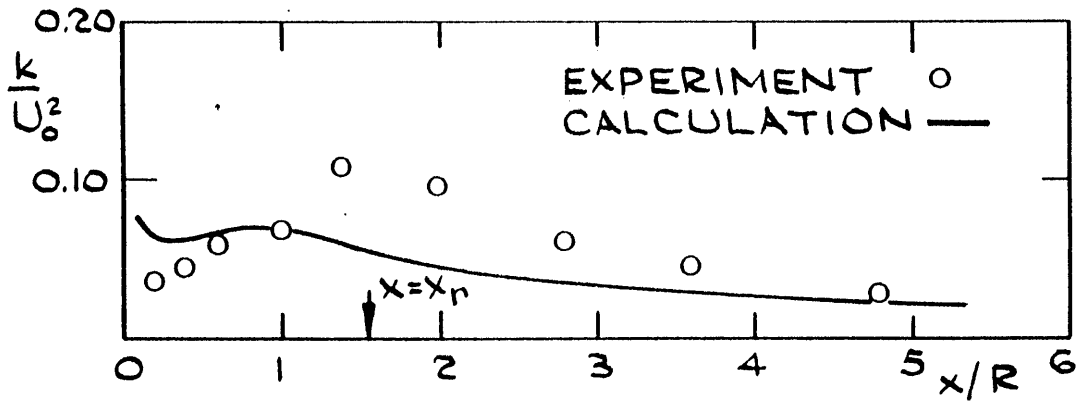

Figure 3.17 Cone, 25% blockage: centreline profile of turbulent kinetic energy. Comparison between experiment and calculation.

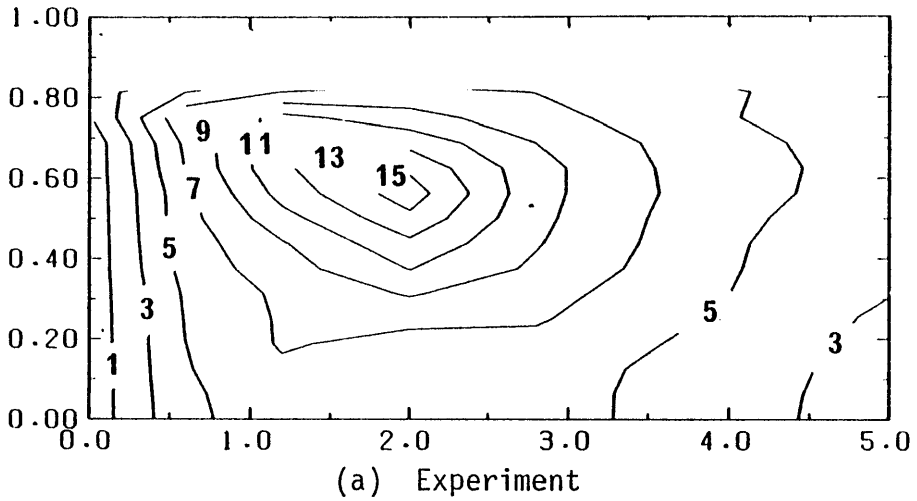

(a) Experiment

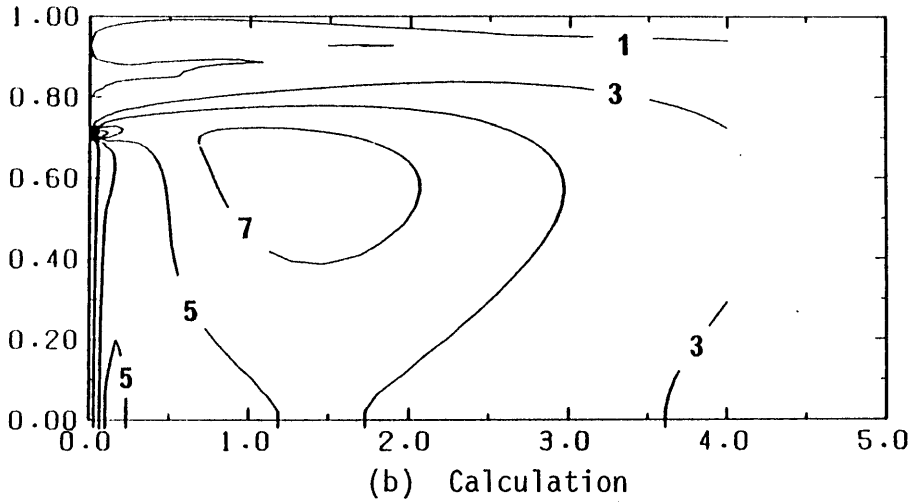

(b) Calculation

Figure 3.18 Disc, 50% blockage: comparison of distribution of turbulent kinetic energy (contour levels in % U_o^2)

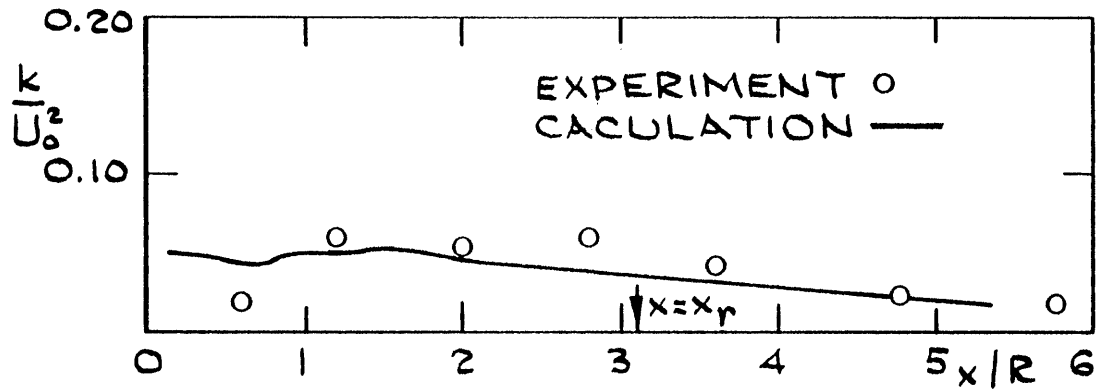

Figure 3.19 Disc, 50% blockage: centreline profile of turbulent kinetic energy. Comparison between experiment and calculation.

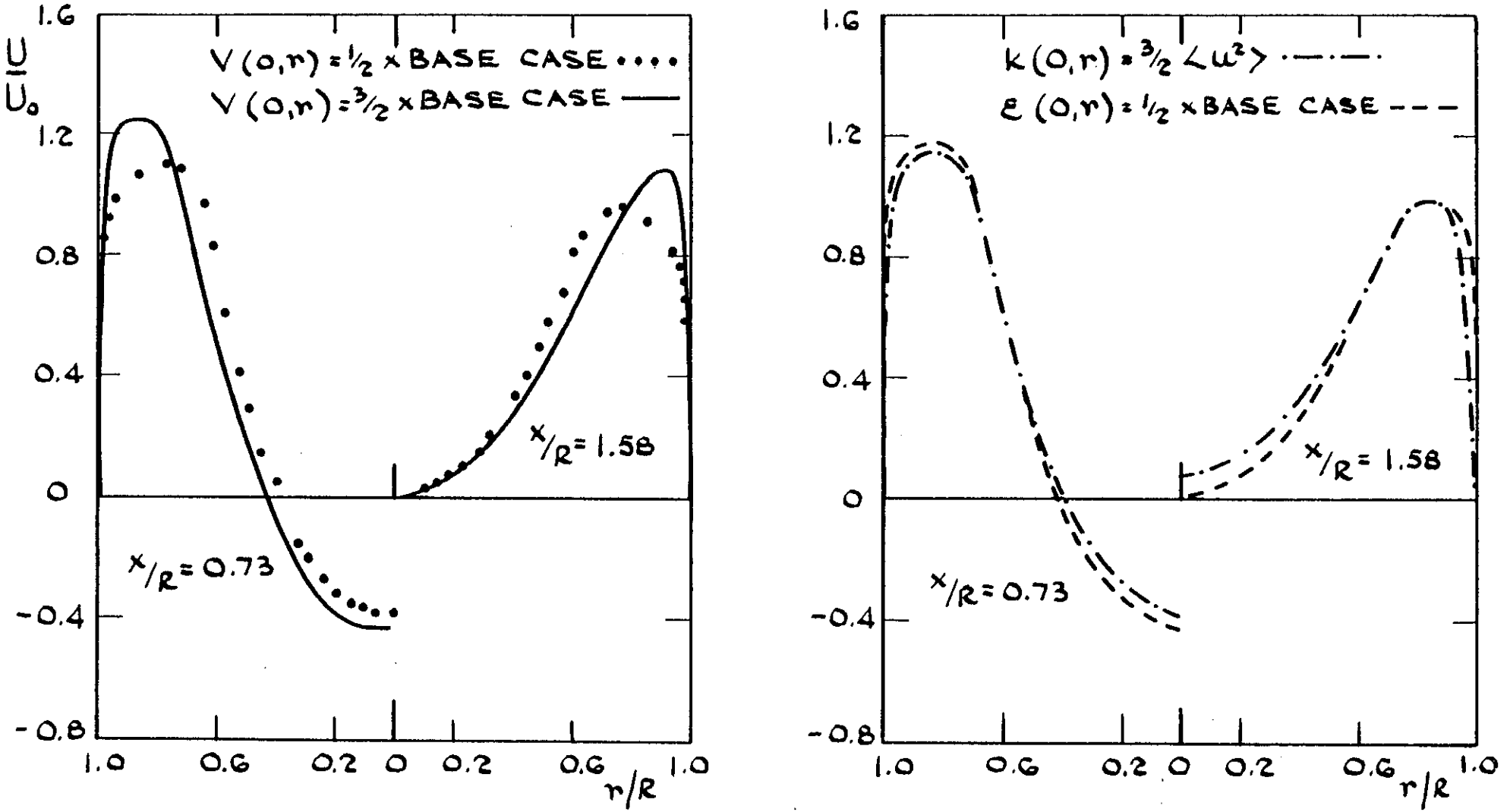

Figure 3.20 Disc, 25% blockage: sensitivity of radial profiles of axial velocity to boundary conditions at x = 0

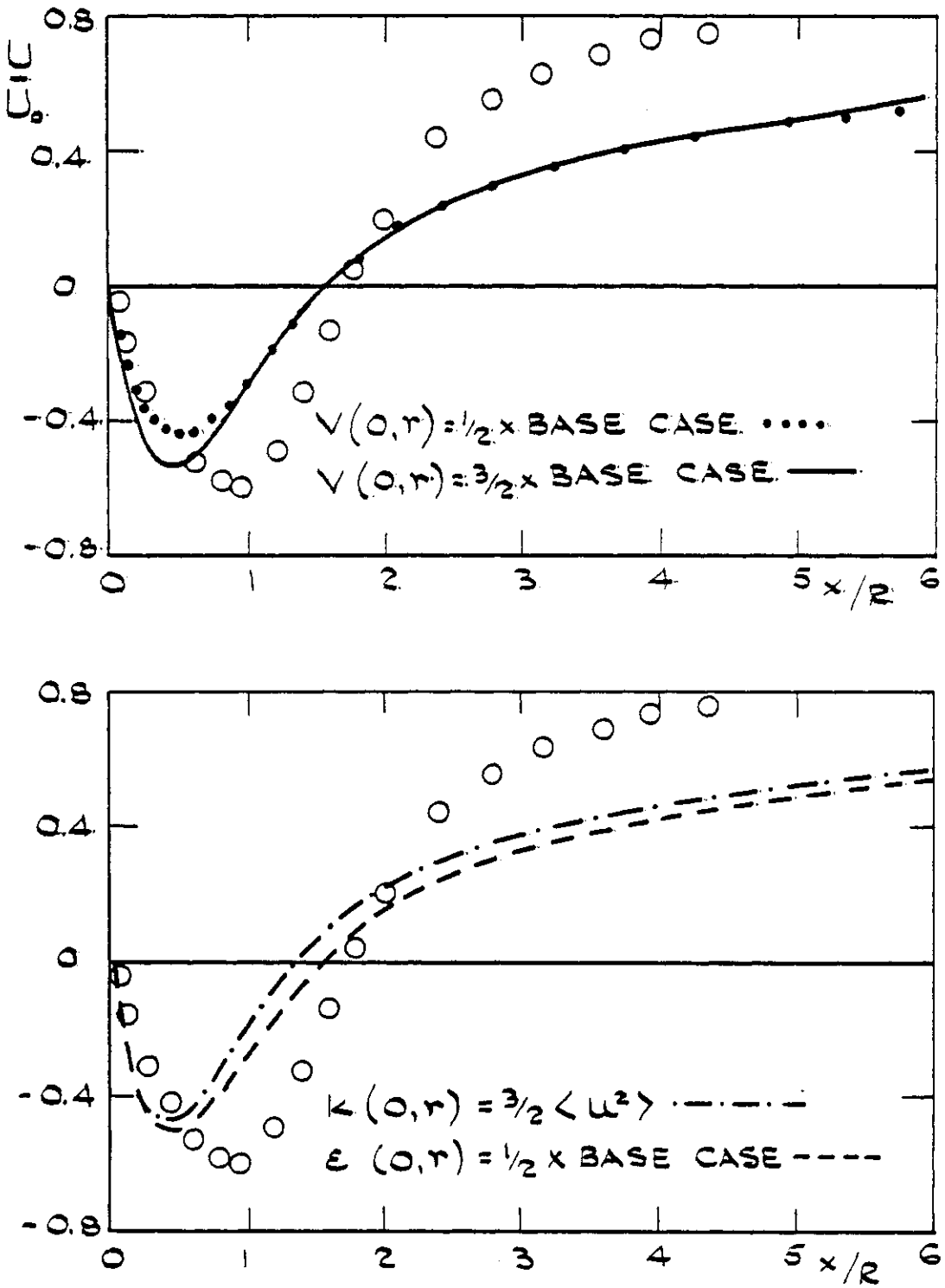

Figure 3.21 Disc, 25% blockage. Sensitivity of centreline profiles of axial velocity to boundary conditions at x = 0

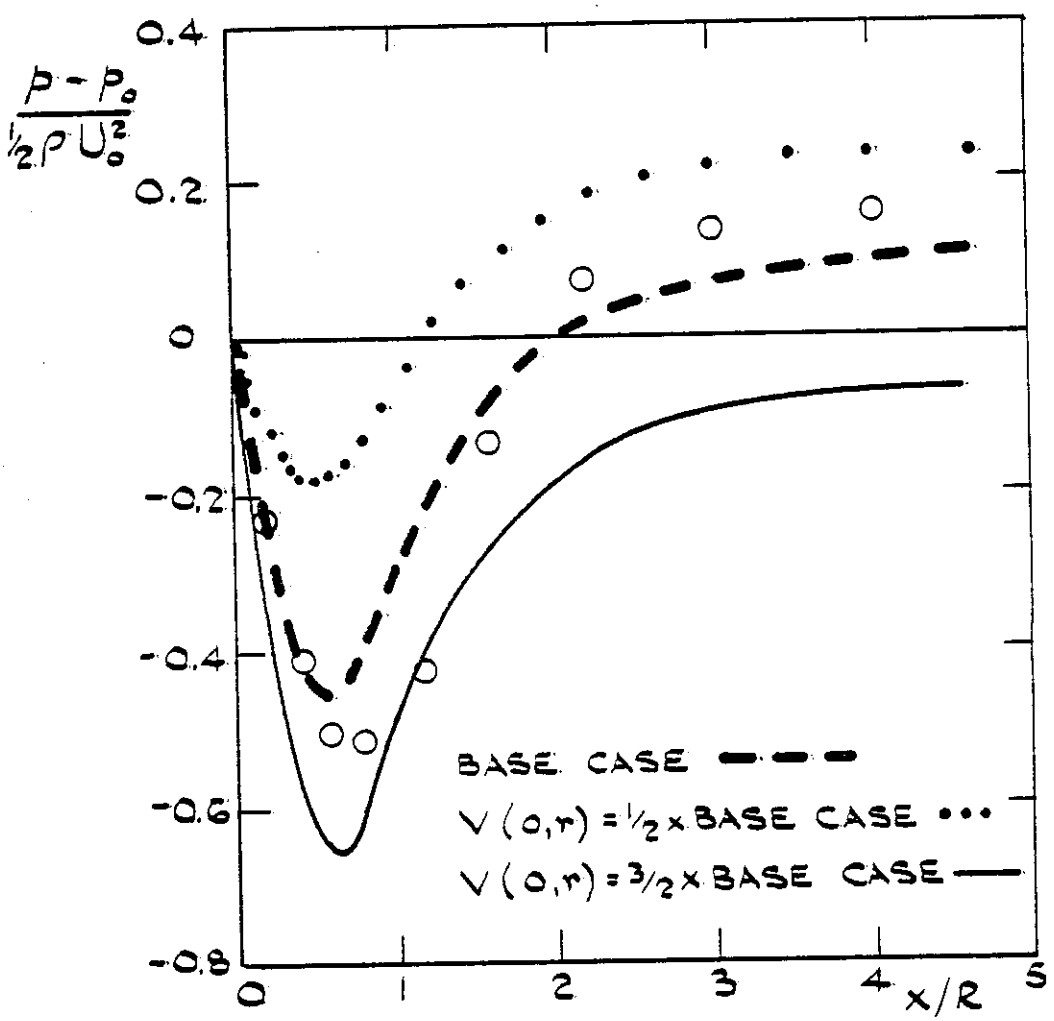

Figure 3.22 Disc, 25% blockage. Sensitivity of wall pressure to boundary conditions at x = 0.

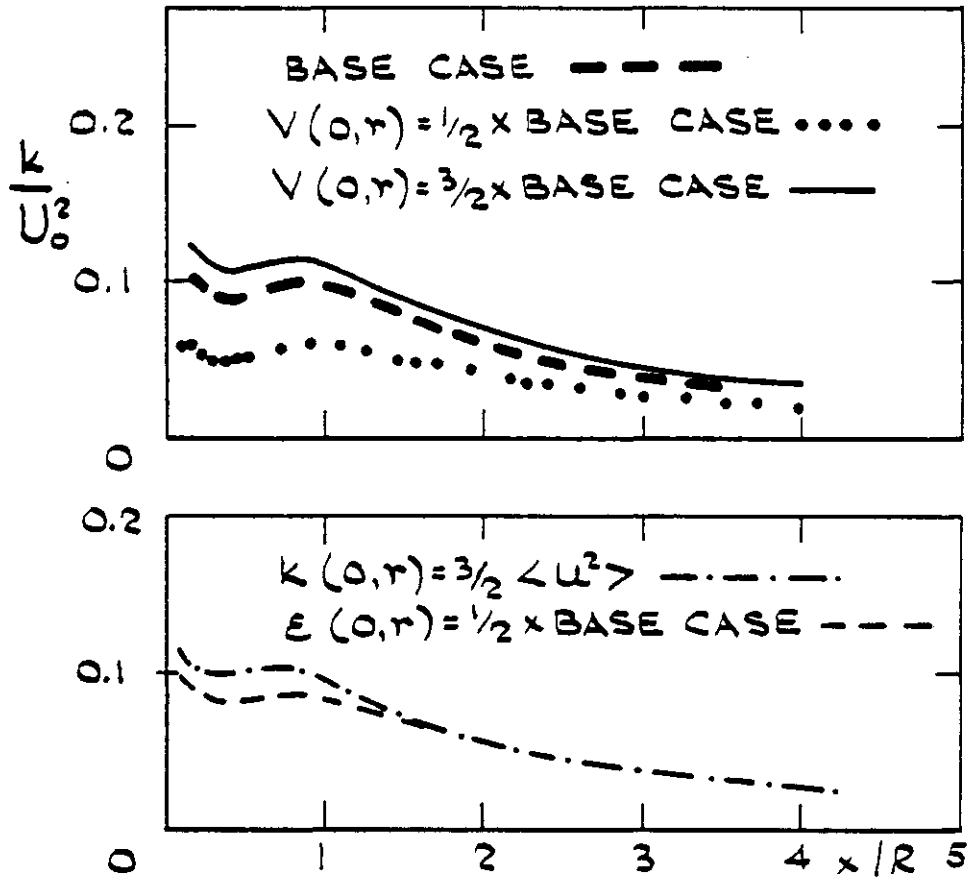

Figure 3.23(a) Disc, 25% blockage: sensitivity of centreline development of turbulent kinetic energy to boundary conditions at x = 0

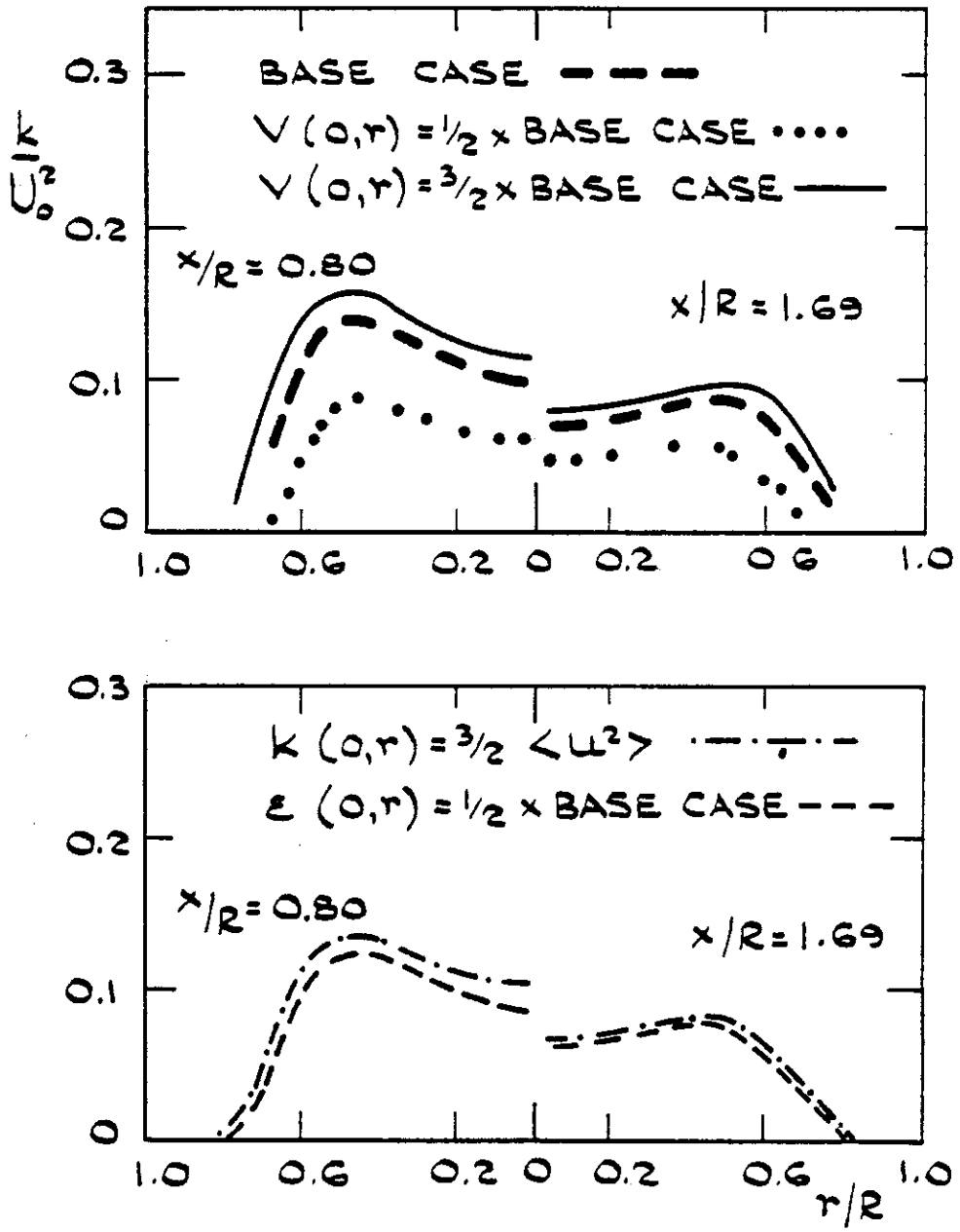

Figure 3.23(b) Disc, 25% blockage: sensitivity of radial profiles of turbulent kinetic energy to boundary conditions at x = 0

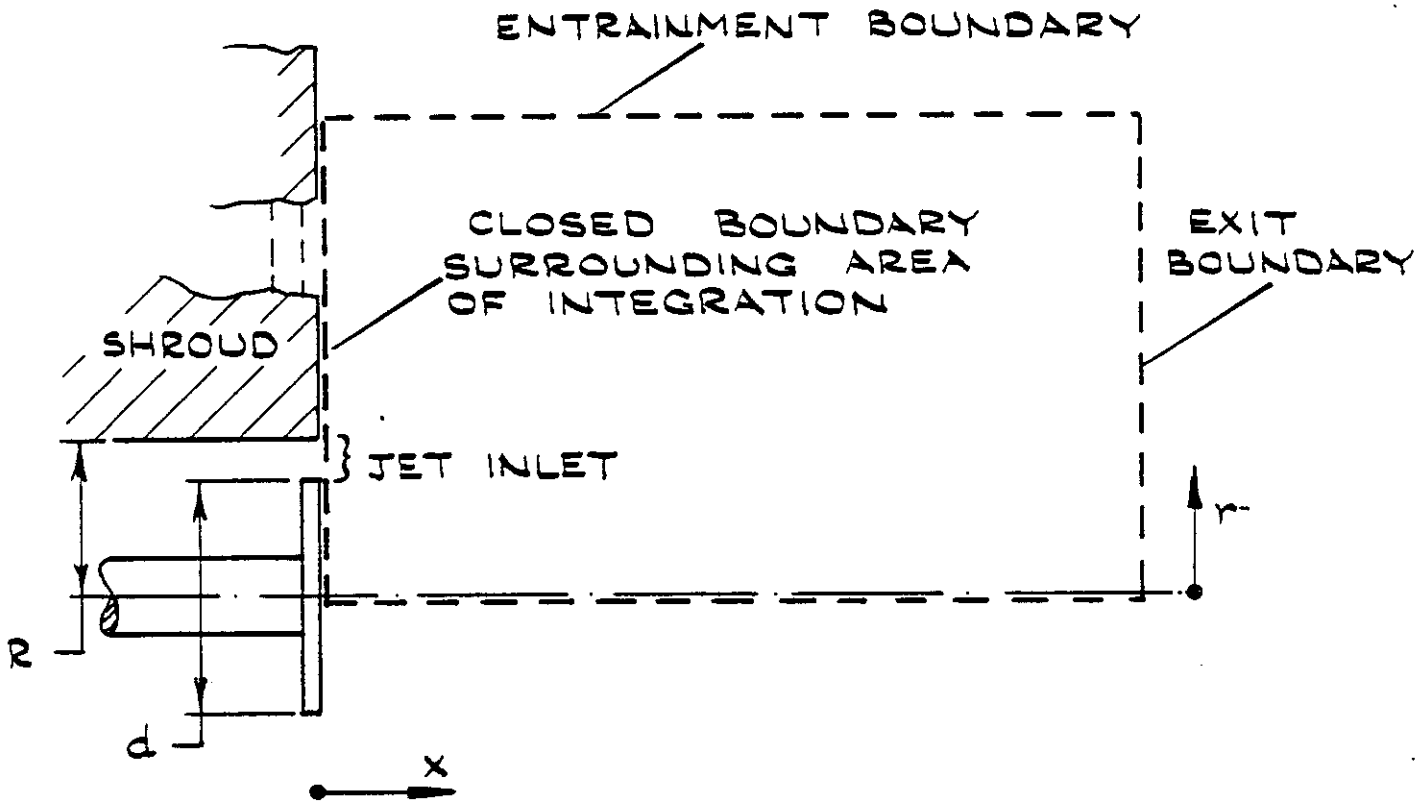

Figure 3.24 Area of integration of the finite difference equations for annular jet

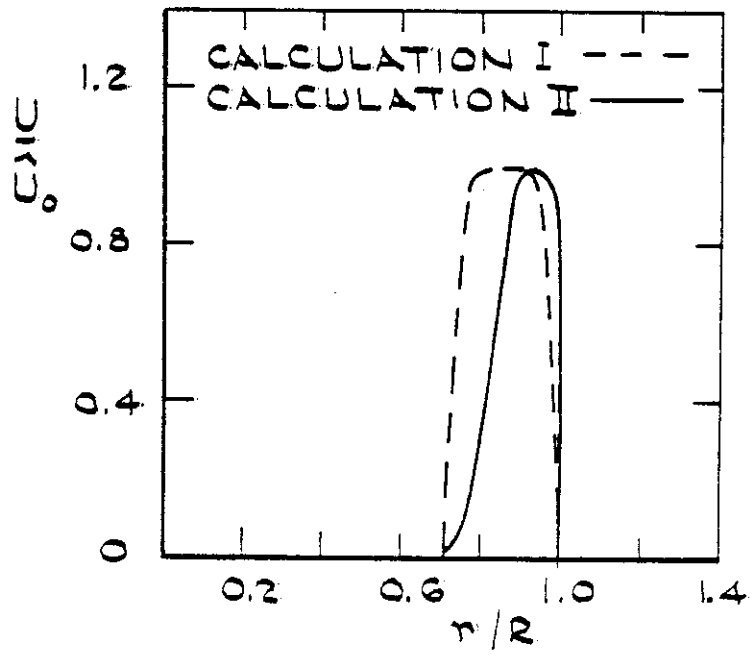

Figure 3.25a Boundary (x = 0) profiles of axial velocity for an annular jet (U_0 = 26.8 m/s)

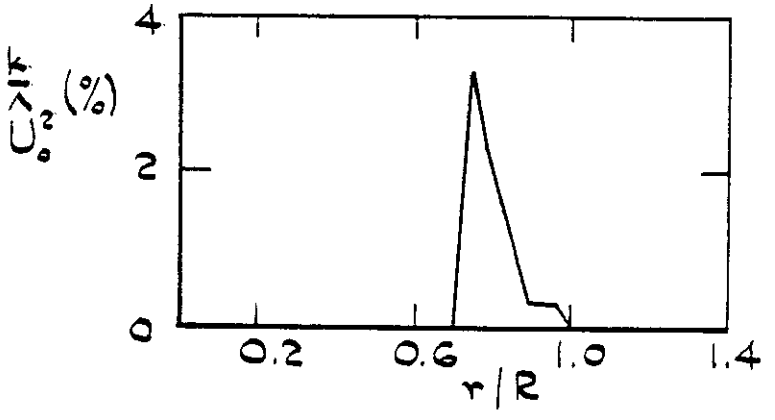

Figure 3.25b Boundary (x = 0) profile of turbulent kinetic energy for calculation II of an annular jet ($\hat{U}_0$ = 26.8 m/s)

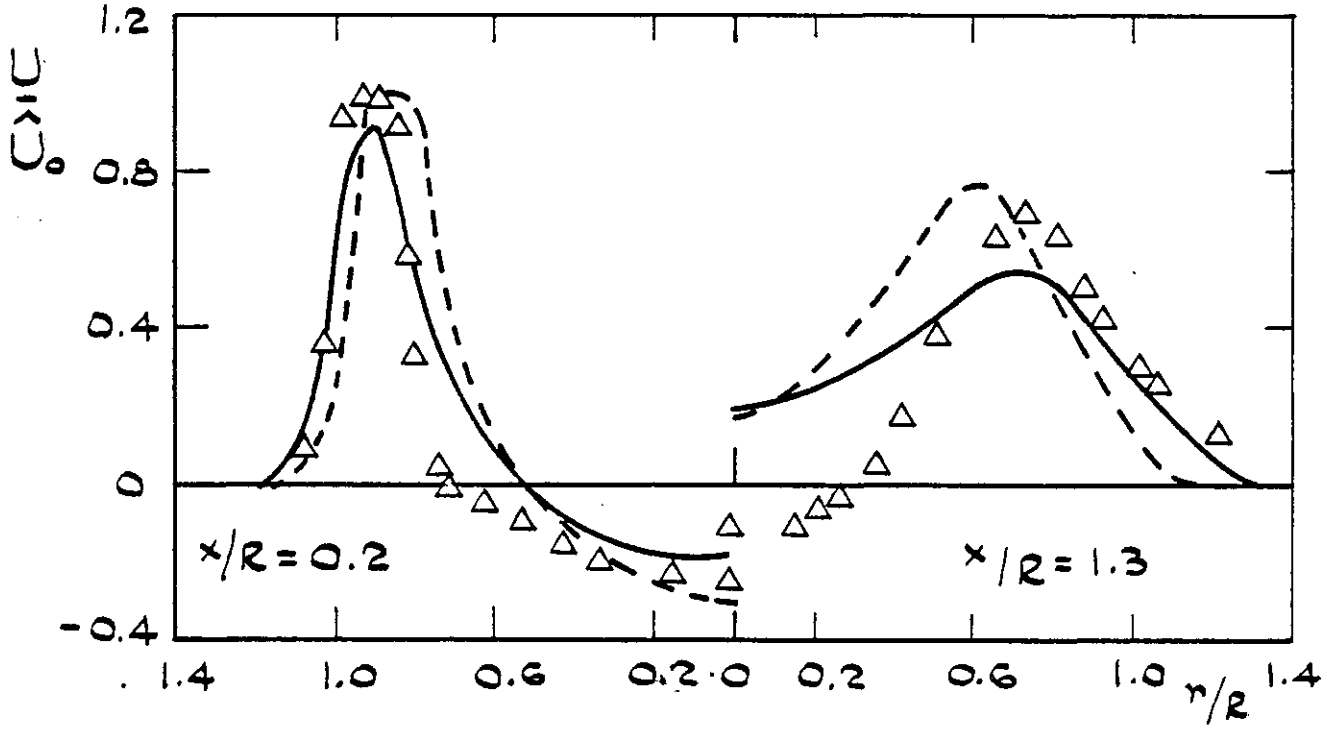

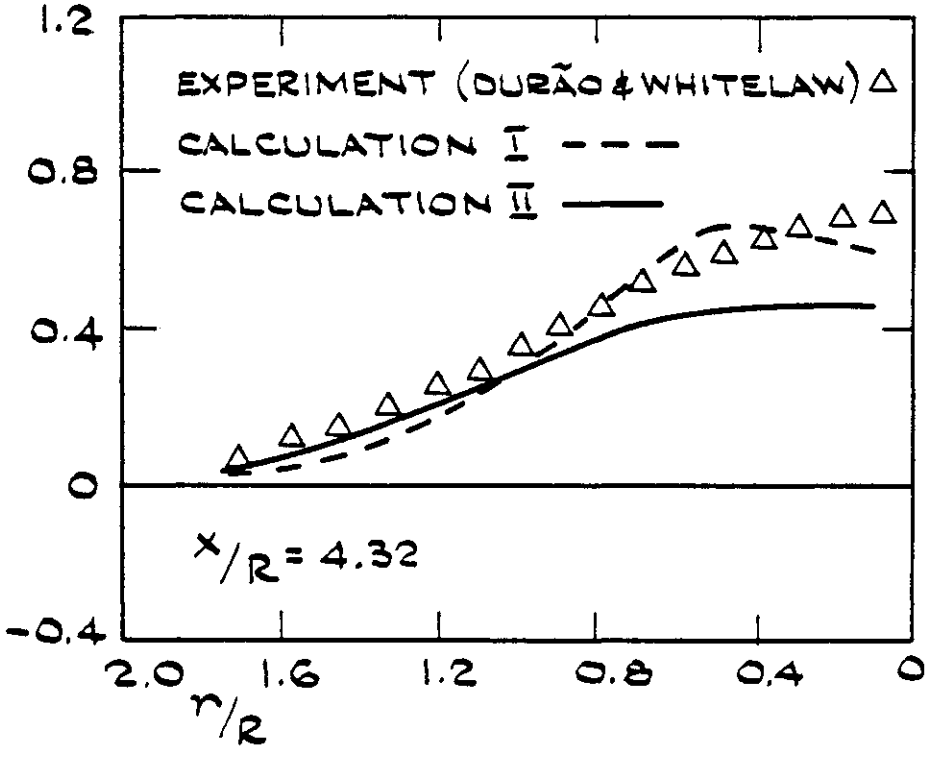

Figure 3.26 Annular jet: radial profiles of axial velocity at successive axial stations. Comparison between experiment and calculations.

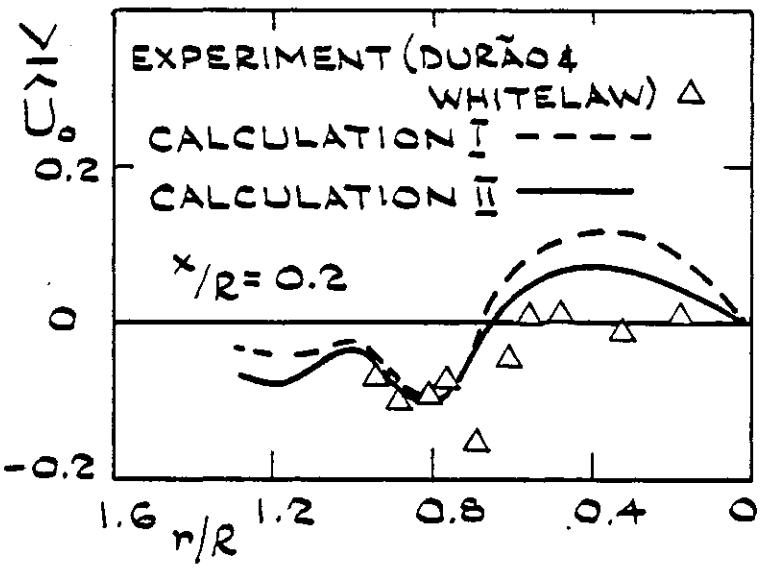

Figure 3.27 Annular jet: radial profile of radial velocity near jet origin. Comparison between experiment and calculations.

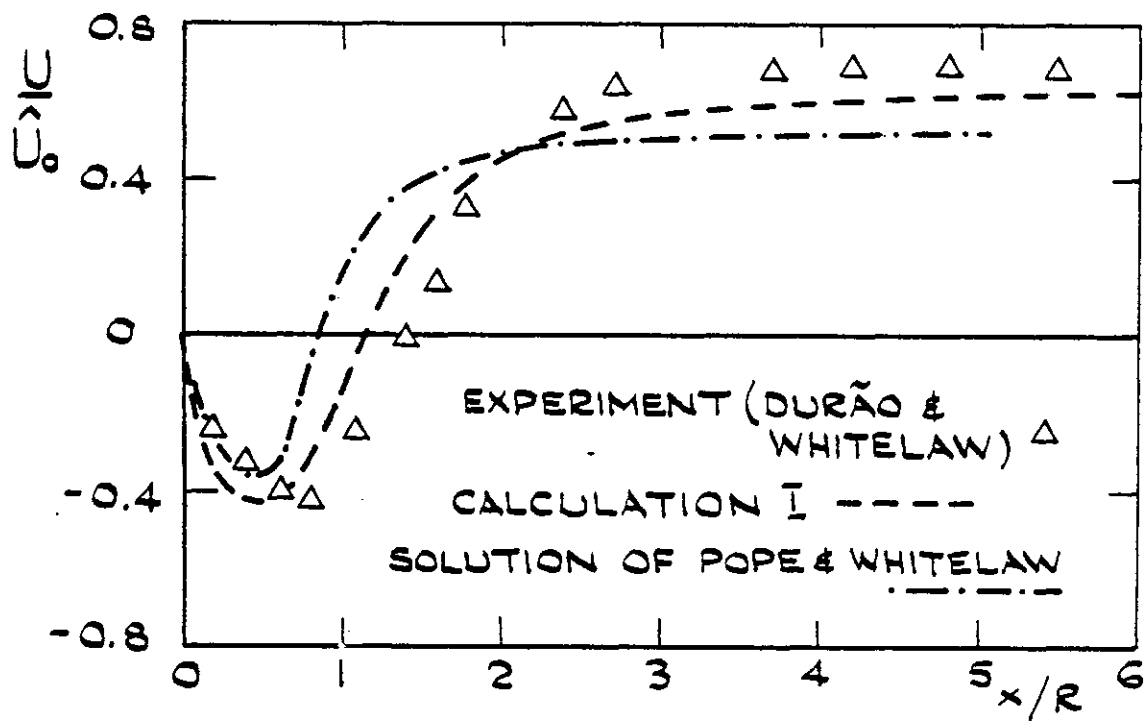

Figure 3.28 Annular jet: centreline development of axial velocity. Comparison between experiment and calculations.

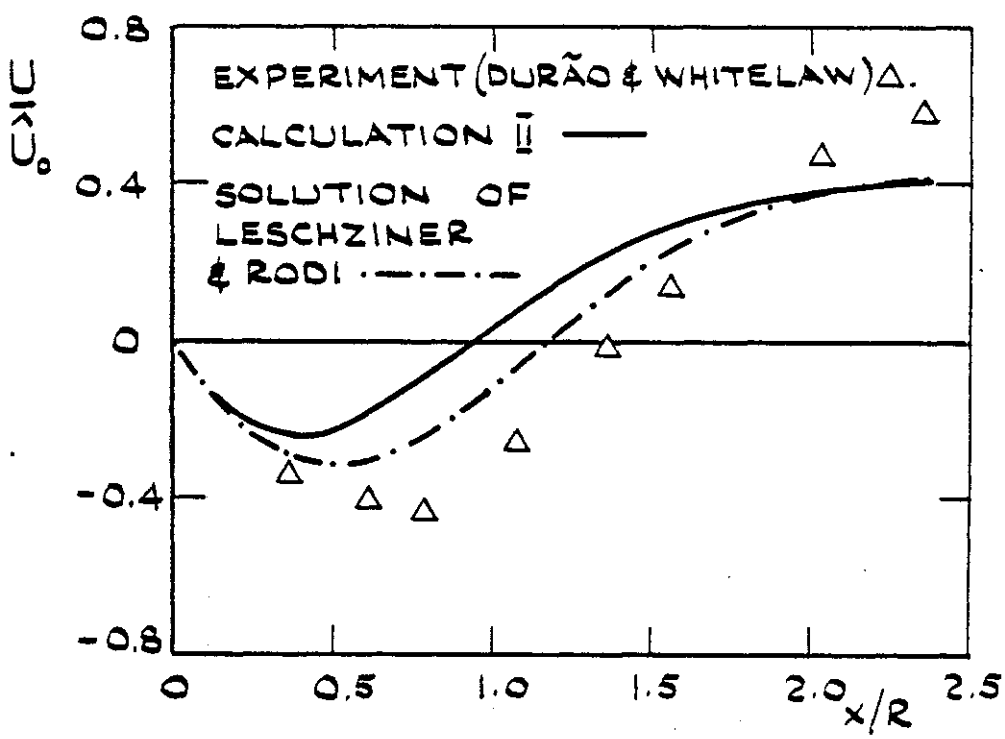

Figure 3.29 Annular jet: centreline development of axial velocity. Comparison between experiment and calculations.

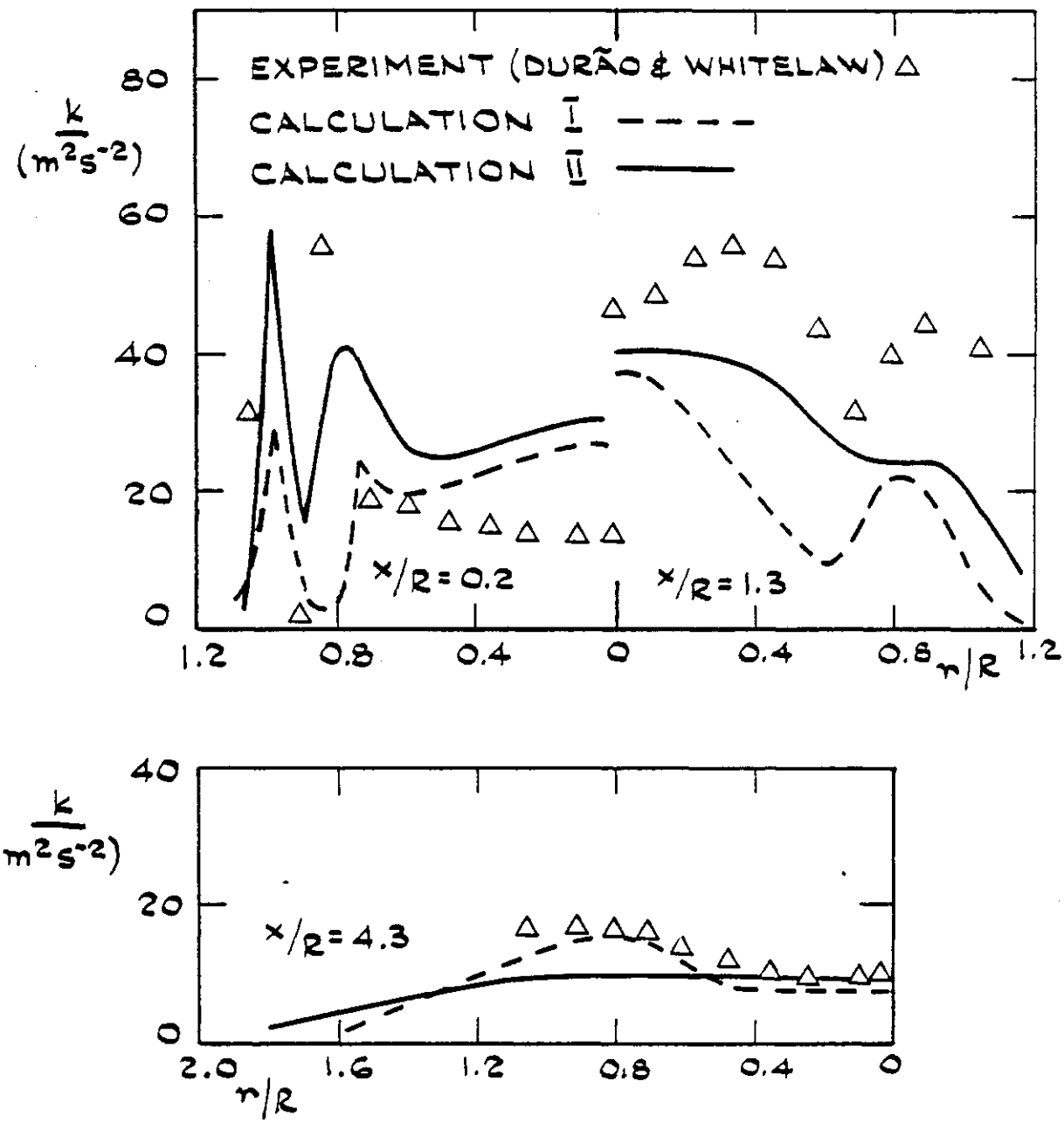

Figure 3.30 Annular jet: radial profiles of turbulent kinetic energy at successive axial stations. Comparison between experiment and calculations.

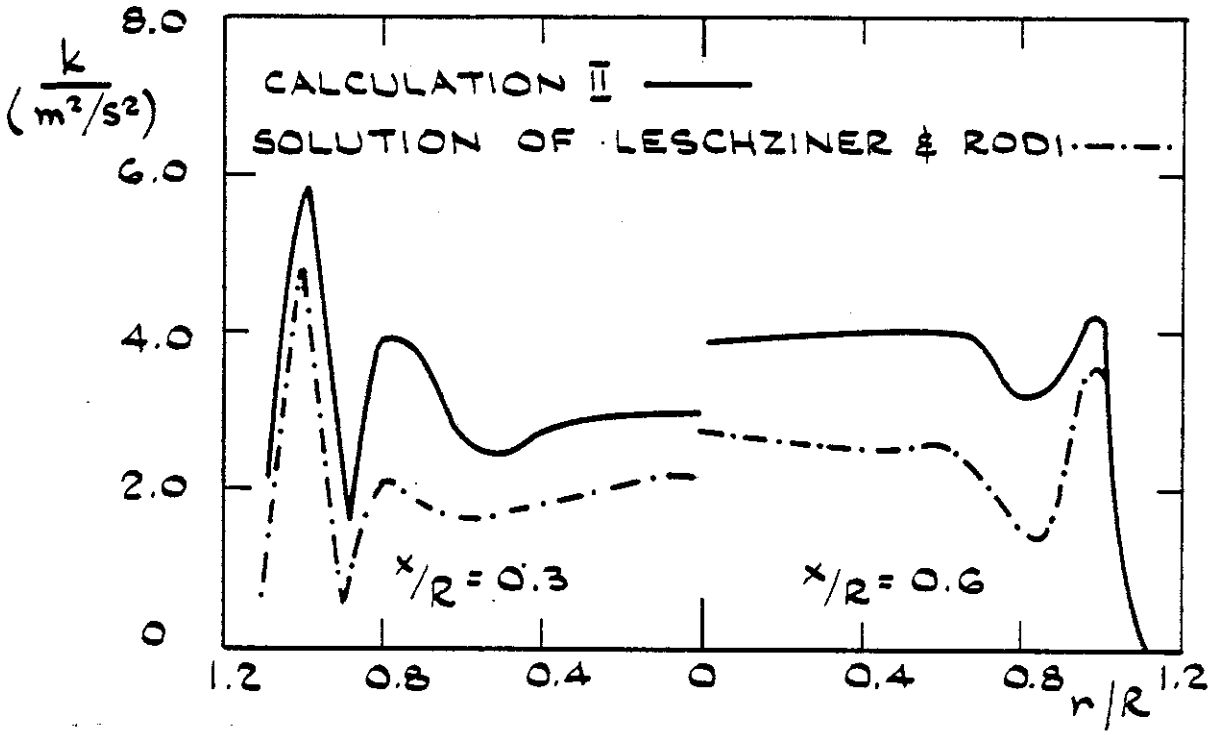

Figure 3.31(a) Annular jet: radial profiles of turbulent kinetic energy. Comparison between two calculations.

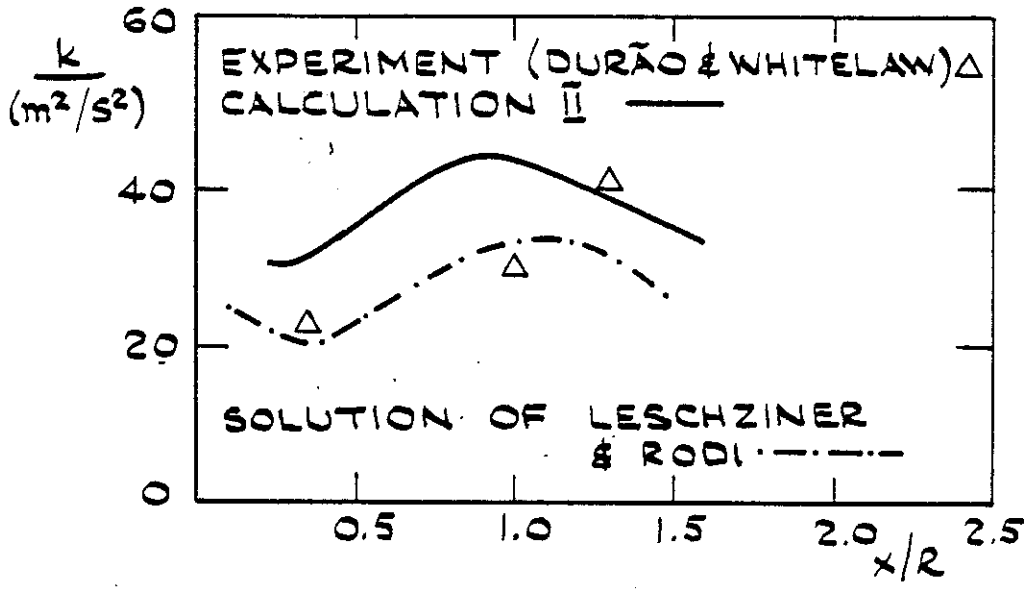

Figure 3.31(b) Annular jet: centreline development of turbulent kinetic energy. Comparison between experiment and calculations.

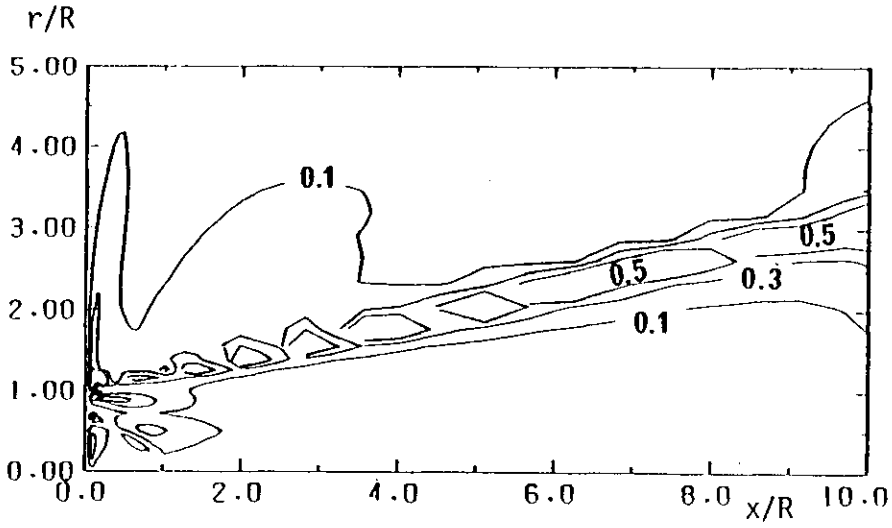

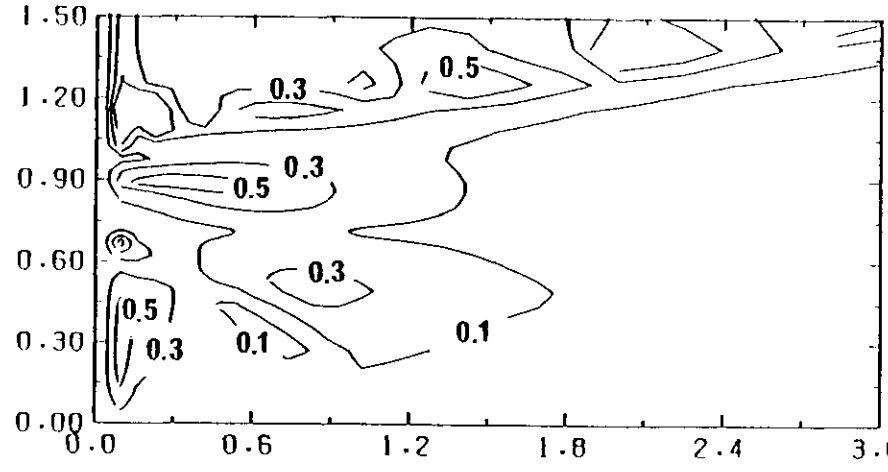

(a) Calculation II: annular jet (annular gap 0.7 < r/R < 1.0). Contours drawn to two different scales

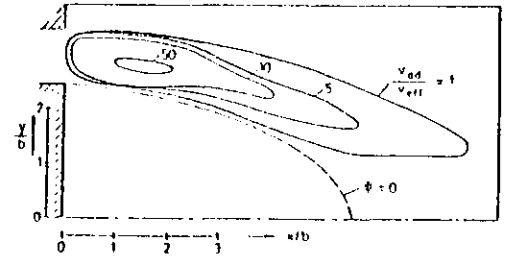

(b) Plane parallel jet (Leschziner and Rodi, 1980)

Figure 3.32 Contours of (numerical/turbulent) viscosity for calculations of annular jet and plane parallel jet

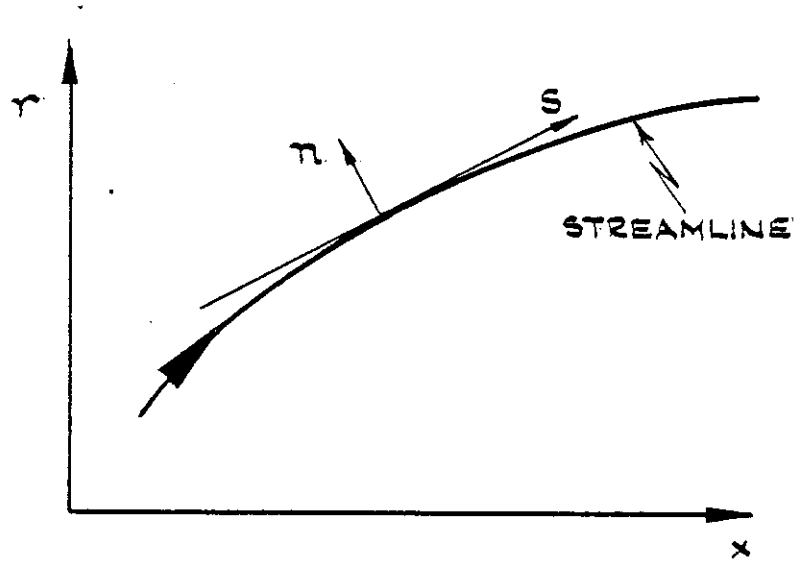

Figure 3.33 Definition sketch for directions of streamline co-ordinates, s and n

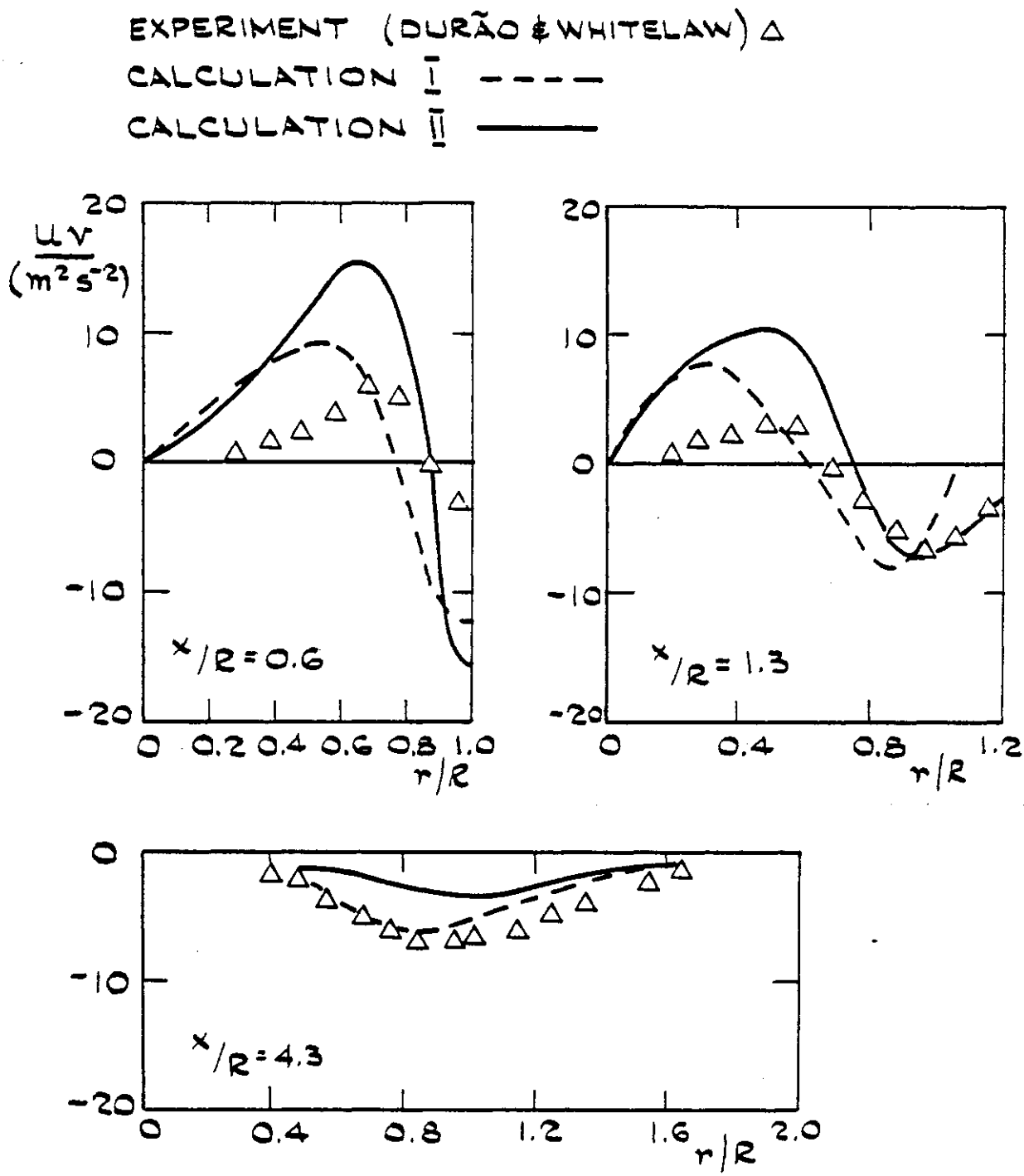

Figure 3.34 Annular jet: radial profiles of cross-correlation <uv> at successive axial stations. Comparison between experiment and calculations.

CHAPTER IV

EXPERIMENTS IN COMBUSTING FLOWS

4.1 Introduction

This chapter describes experiments with premixed, low Mach number, baffle-stabilised flames for geometries which are, as far as possible, similar to those of chapter II. The reactants were air and natural petroleum gas. Field measurements of the mean and variance of axial velocity are presented, together with the mean temperature, for a disc and a cone of 25 per cent area blockage ratio and a disc of 50 per cent blockage. These are compared and contrasted with those which have been obtained in isothermal air flows, and allow the study of the influence of the forebody shape and blockage. The ratio of fuel to air in the reactants is found to influence the aerodynamics greatly and hence some of the experiments are concerned with the effects of this ratio.

Section 4.2 describes the experimental method under the headings of flow configuration, measurement techniques and estimation of errors. Although laser-Doppler velocimetry has again been used, its method of application differs from that of chapter II, as do the experimental tolerances. The results are described in section 4.3. Sub-section 4.3.1 describes the influence of the fuel to air ratio, particularly on flow oscillations. The detailed field measurements of velocity and temperature, for fuel-lean operation, are given in sub-section 4.3.2. The discussion, section 4.4, is presented in two parts: the first considers the possible origins of the combustion-induced flow oscillations and the second examines the influence of the forebody shape and blockage. The final section, 4.5, presents a summary of the main findings and conclusions of the chapter.

4.2 Experimental method

4.2.1 Flow configuration

The combustion chamber was manufactured from a length of mild steel pipe, shown schematically in figure 4.1, with its axis of symmetry in a horizontal plane. The pipe was circular to within about 1 mm, except in the vicinities of the observation windows (see figure 4.1) which reduced the local diameter by up to 3 mm. The air and natural gas, the composition of which is given in table 4.1, were supplied separately to a swirl register, shown in figure 4.2, at one end of the chamber. The flow rates of each reactant stream were measured with 'D, D/2' orifice plates, constructed according to B.S.1042. For the lowest gas flow rates, independently calibrated rotameters were used. The two gas flows mixed immediately downstream of the register through the swirl imparted to the air, with the remaining length upstream of the baffle being occupied by flow straighteners and wire meshes to destroy the swirl and act as flame arrestors for safety. These were held in position by the steel collars indicated in figure 4.1. The length of the chamber downstream of the baffle was sufficient for combustion to be complete for fuel lean conditions, at its exit.

The laboratory compressed air supply was capable of delivering up to about 120 m^3/hour through this configuration, corresponding to pipe bulk velocities of about 6 ms^{-1}. Table 4.2 lists typical values of the Archimedes, Damkoehler, Mach and Reynolds numbers appropriate to these flows. The Archimedes number is sufficiently small for buoyancy forces to be small compared with inertial forces. The Damkoehler number suggests that a typical chemical reaction time is smaller than the timescale of the turbulence, so that the combustion is controlled mainly by the rate of turbulent mixing rather than by

TABLE 4.1

PHYSICAL PROPERTIES AND CHEMICAL COMPOSITION OF NORTH SEA NATURAL GAS (MONEIB, 1980)

Physical Properties

Properties	
Density Kg/m^3	0.7283
Molecular weight Kg/Kmol	17.18
Specific heat MJ/(Kmol K)	0.03634
Net calorific value MJ/m^3	35.05

Volumetric Chemical Composition

Gas	% Volume
Methane	93.63
Ethane	3.25
Nitrogen	1.78
Propane	0.69
Butane	0.27
Carbon Dioxide	0.13
Pentanes	0.09
Helium	0.05
Hexanes	0.03
Benzene	0.02
Toluene	0.01
Octanes	0.01

TABLE 4.2

TYPICAL VALUES OF ARCHIMEDES, DAMKOEHLER, MACH AND REYNOLDS NUMBERS FOR COMBUSTING EXPERIMENTS

NUMBER	FORMULA	CONDITIONS	VALUE
Archimedes	$\frac{2Rg\ (T_b - T_u)}{U_o^2\ T_u}$	$U_o \simeq 10\ ms^{-1}$ $R = 40\ mm$ $T_b \simeq 2000\ K$ $T_u \simeq 300\ K$	0.044
Damkoehler	$\frac{\ell}{\sqrt{\langle u^2 \rangle}} \cdot \frac{S_L}{\delta_L}$	$\ell \simeq 20\ mm$ $\sqrt{\langle u^2 \rangle} \simeq 2.4\ ms^{-1}$ $S_L \simeq 0.9\ ms^{-1}$ $\delta_L \simeq 0.19\ mm$	39
Mach	$\frac{U_o}{c}$	$c \simeq 880\ ms^{-1}$	0.01
Reynolds	$\frac{U\ .\ d}{\nu}$	Disc, 25% blockage: $U_o = 8.7\ ms^{-1}$	22 970
		Cone, 25% blockage: $U_o = 8.7\ ms^{-1}$	22 970
		Disc, 50% blockage: $U_o = 13\ ms^{-1}$	48 900

NB Values of the laminar flame speed, S_L, and the flame thickness, δ_L, are taken from Vinickier and van Tiggelen (1968), cited by Gökalp, 1980.

chemical kinetics. The Mach number is low and so frictional heating is negligible and pressure fluctuations will not influence the chemical kinetics. The Reynolds number is based on the equivalent isothermal air flow and although its value is almost as high as in the flows of chapter II, it is likely that the increase in kinematic viscosity due to the temperature increase will result in an effective Reynolds number much lower than that given in table 4.2. It is noted that U_o, the annular bulk velocity of the flow, is always calculated from the air flow rate in this chapter.

For the isothermal flow experiments to be described below, the air flow was laden with a mist of compressor oil and was suitable for use as seeding. During combustion it was necessary to seed with refractory (titanium dioxide) particles. These have a nominal diameter of 0.3 μm (Asalor and Whitelaw, 1974) before agglomeration and about 3 μm after agglomeration and are thus (Durst et al, 1976) sufficiently small to follow the turbulent flow accurately while remaining inert at the temperatures encountered in the flame. The particles were introduced into the air line, upstream of the swirl register, using a generator constructed according to the guidelines of Asalor and Whitelaw (1974). In general the introduction of small particles can influence combustion, for example by quenching the reaction: however, the concentration of scattering particles in the flows is sufficiently low that, according to Durst and Kleine (1973), the effect is negligible.

Optical access to the flow was through plane, vitreous silica plate windows set into the observation ports, allowing velocity profiles to be measured in a horizontal plane. For the isothermal measurements reported in sub-section 4.3.2, single pieces 26.7 cm long

were used: for the combusting flow shorter lengths ($8\frac{1}{2}$ cm) were considered safer, with the remainder of the observation port being filled with steel inserts. As a result, axial profiles of velocity could only be made over lengths of 5 cm at a time without extinguishing the flame and repositioning the windows.

The thermocouple probe, described in sub-section 4.2.2, was passed through the observation ports as shown in figure 4.3(a). In contrast to the measurement of velocity, it was possible to take the temperature profile in the axial direction without extinguishing the flame.

As for chapter II, the forebody shapes which were chosen were a disc and a cone (45 degrees included angle) and area blockages of 25 and 50 per cent. The details of the shapes are given in figure 4.4 and the co-ordinate system is as for chapter II. Each baffle was held in place by eight 5 mm diameter pylons, shown in figure 4.1. The accuracy with which a baffle could be centred was limited by the tolerance on the pipe's circularity.

4.2.2 Measurement techniques

Velocimeter configurations

The velocities and fluctuation levels in the flows of this chapter are larger than those of chapter II and the magnitude of the light frequency shift which is required to provide direction sensitivity is correspondingly greater. It is not convenient to derive such a shift from the rotation of a radial diffraction grating: instead, acousto-optic cells, exploiting the Debye-Sears effect, are used and the magnitude of the shift (21.002 MHz) is that of a travelling ultrasonic wave in a liquid. The full details of the design

of the cells and of the velocimeter itself are to be found in Durão (1976): figure 4.5 shows the instrument schematically and gives details of the optics used to gather the forward-scattered light.

Table 4.3 below summarises the principal characteristics of the velocimeter. The laser power is higher than used in the water flows because the number of photons scattered is related to the residence time of the particle in the measuring volume: hence the higher velocities call for increased power. The size of the measuring volume and the fringe spacing are given by formulae similar to equations (2.1) to (2.4). There is, however, only one lens in the transmitting optics, equivalent to lens L_3 in figure 2.3, and equation (2.3) is modified to:-

$$b = \frac{4\lambda f}{\pi b_o^3} \qquad (4.1)$$

The influence of the gradients in refractive index, which occur because of the chemical reaction, is negligible (Durst et al, 1976) over the comparatively short diameter of the chamber.

The radial velocities in the plane of the trailing edge of the baffle could not be measured in the way shown in figure 2.5(c) because of the steel walls. Figure 4.6 shows the method that was used for the measurements of this chapter which involved recording the radial profile of axial velocity along x = 0 and the same profile of the resultant velocity at about 45 degrees to the axis of symmetry. It is then possible to deduce the profile of mean radial velocity at x = 0. (This strategy was also attempted for the flows of chapter II, but it proved impossible to image the measuring volume adequately because of the flare associated with the many air, Perspex and water interfaces).

TABLE 4.3

PRINCIPAL CHARACTERISTICS OF
THE LASER-DOPPLER VELOCIMETER

800 mW, Argon Ion Laser	λ = 514.5 nm
Focal length of lens:	
L_3 (nominal)	f_3 = 300 mm
Beam diameter, b_o, at e^{-2} intensity, of laser	1.5 mm
Measured half-angle of intersection, θ	6.63 degrees
Fringe separation (line pair spacing)	2.228 μm
Calculated dimensions of measuring volume:	
b_x	0.13 mm
b_y	1.13 mm
b_z	0.13 mm
Calculated number of fringes within e^{-2} intensity level	58
Velocimeter transfer constant, K^{-1}	0.449 MHz/ms^{-1}

Doppler signal processing

The Doppler signals were detected by a photomultiplier tube (RCA model 4836), the frequency response of which is higher than that used in chapter II so as to accommodate the larger frequencies. The Doppler frequency lay between about 10 and 40 MHz and is beyond the passband of frequency trackers. The signals were demodulated by a swept-tuned spectrum analyzer (Hewlett-Packard model 141T/8552A/8553B) using a system described by Durão, Laker and Whitelaw (1978). The method is briefly outlined below.

A window in frequency space is selected on the analyzer

which is sufficiently wide to accommodate the range of Doppler frequencies at the point under consideration. The analyzer is swept through this window in 64 equal steps, with the bandwidth, δf, of the analyzer being adjusted to match the interval between steps. The control of the analyzer, the logging of results and data reduction is assigned to a microprocessor (Intersil model IM 6101) with the arrangement shown schematically in figure 4.7. The amplitude output of the analyzer is proportional to the r.m.s. voltage of the signal at each interval and the presence or absence of a Doppler signal (the information of interest in this application) is determined by establishing a threshold amplitude of the analyzer's output via a Schmitt trigger. The input to the analyzer is demodulated at each of the 64 intervals for 0.47 seconds and the number of Doppler signals occurring during this time is recorded. The threshold amplitude can be exceeded only <u>once</u> for every Doppler signal and, for reasons concerned with the operation of the microprocessor, the minimum time between consecutive recordings is 42 μs. On completion of the sweep across the frequency window, the microprocessor has a record (histogram) of the number of scattering centres (N_i) occurring within each frequency interval, $(f_i \pm \frac{1}{2}\delta f)$, and can be regarded as a discrete probability distribution of velocity from which moments can be calculated.

This method of demodulation, in contrast to frequency tracking, entails the loss of information regarding the temporal variation of velocity and so the frequency content of the velocity fluctuations is lost. However, there is no restriction on the particle arrival rate (compare equation (2.5)). The results are population-, rather than time-, averages and this distinction is important when estimating the errors which are incurred.

Temperature measurement

Temperatures were measured with a bare-wire thermocouple (platinum : 13% rhodium-platinum) constructed from 80 μm diameter wire. This arrangement was preferred to a suction pyrometer partly because it was smaller but also because of the dependence of the pyrometer measurements on the suction velocity as shown, for example, by Attya (1980). The junction of the thermocouple was formed at the centre of a 6 mm length of wire by butt-welding. It was mounted on the probe illustrated in figure 4.3(b), with the suspending wires aligned with isotherms to minimise conduction errors. The diameter of the wire was chosen as a compromise between durability, which favours large diameters, and small radiative heat loss and high frequency response, which require small diameters. The output voltage was passed to a differential amplifier (OP-07A) via compensating leads and the output of the amplifier was time-averaged.

Measurement of sound levels

The sound levels, presented in sub-section 4.3.1, were measured by microphones (General Radio model 1560-P4 and Dawe type 99D401B) which were located approximately two metres away from the combustion chamber. The sound levels were measured by a Dawe sound level meter type 1400 H (sound levels relative to 2×10^{-5} Nm^{-2}) and the frequency content was measured by a spectrum analyzer (General Radio model 1564-A).

4.2.3 Data reduction and error estimates

This sub-section begins with the data reduction for velocity and then considers errors associated with the measurement of velocity and temperature. It concludes with estimates of the errors in the

measured quantities to be presented in section 4.3.

Velocity

The relation between the velocity of a scattering centre and its Doppler frequency is given by equation (2.6). For the acousto-optic cells, the shift frequency is a constant (21.002 MHz) rather than being given by equation (2.8). The population's mean is:-

$$U = \langle U(t) \rangle \equiv K \frac{\sum_i N_i f_i}{\sum_i N_i} \tag{4.2}$$

and the variance is:-

$$\langle u^2 \rangle \equiv K^2 \cdot \frac{\sum_i N_i f_i^2}{\sum_i N_i} - U^2 \tag{4.3}$$

where K has been defined by equation (2.6).

Errors in velocity measurement

Table 4.4(a) summarises the errors in the measurement of velocity under five headings. The first is non-turbulent Doppler broadening: the effects have been considered in table 2.4 and are not repeated here because these are less important than others to be considered below. The second considers the error (strictly, the confidence interval) corresponding to the sample size from which the mean and variance are constructed: it is analagous to the integration time in time-averaging. A related error is the use of a discrete representation of the probability density of a continuous random variable. Estimates for the confidence intervals for the mean and

TABLE 4.4(a)

ERRORS INCURRED IN THE MEASUREMENT OF THE MEAN AND VARIANCE OF VELOCITY

SOURCE	TYPICAL MAGNITUDE OF ERROR U	TYPICAL MAGNITUDE OF ERROR $\langle u^2 \rangle$
1. Non-turbulent Doppler broadening	Similar to values in table 2.4	
2. (a) Influence of sample size on confidence interval	< 1% (% of local values)	< 3% (% of local values)
(b) Representation of a continuous probability density distribution by a discrete probability function	Does not alter above estimates	
3. Velocity bias:		
within recirculation bubble	$< + 0.08\ U_o$	$< - 10\% \sqrt{\langle u^2 \rangle}/U$ (% local value)
outside recirculation bubble	$< + 0.01\ U_o$	$< - 2\% \sqrt{\langle u^2 \rangle}/U$
4. Scattering-particle concentration bias	$\lesssim - 0.05\ U_o$	negligible
5. Scattering-particle concentration-gradient broadening	Negligible except in immediate region of flame front	

TABLE 4.4(b)

ERRORS INCURRED IN THE MEASUREMENT OF MEAN TEMPERATURE

SOURCE	TYPICAL MAGNITUDE OF ERROR
1. Probe disturbance	Small
2. Catalytic activity of Platinum	
3. Losses by radiation and conduction	- 40 K
4. Temperature-dependence of heat transfer, influencing averaging process	Similar in magnitude, but opposite sign, to difference between true time-mean and Favre-mean. See equation 4.5.

variance have been given by Yanta (1973), based on the student t and chi-squared distributions respectively. In all the measurements reported here, 10 000 samples or more were used. This results in a confidence interval of better than 1 per cent for the mean value, for turbulence intensities up to 30 per cent, and 3 per cent for the variance, both intervals estimated for a confidence level of 95 per cent. These estimates are derived on the assumption that the number of intervals which form the discrete distribution is of the same order as that of the sample size. It has been recommended (Bendat and Piersol, 1971) that the error for approximately Gaussian random data is small for interval widths of about one-fifth of the standard deviation. In practice it has been found (Clare et al, 1976) that the confidence intervals given above hold good for such cases.

The third source of error is velocity bias, which arises because the rate at which particles arrive in the measuring volume, $\dot{R}$, is proportional to the volumetric flux of fluid through the measuring volume:-

$$\dot{R} = \mu A \, |\underline{U}(t)| \tag{4.4}$$

where:-

μ is the instantaneous scattering-particle density (m^{-3})

A is the cross-sectional area of the measuring volume projected in the direction of the instantaneous velocity vector, $\underline{U}(t)$

Assuming for simplicity that μ and A are constants, then the sampling rate is proportional to the magnitude of velocity and because this

rate is related to the quantity (a component of $\underline{U}(t)$) for which the probability distribution is required, the sample space (population) of the experiment will be biassed. In other words, the sampling rate and the instantaneous velocity are not independent variables (because the particle arrival rate is slower than the sampling rate of the microprocessor) and, in general, the probability function of the measured velocity component will be biassed towards high velocities, with the result that the measured mean and variance are too large and too small respectively. The effects of biassing are unimportant at turbulence intensities less than about 10 per cent and give rise to errors of less than 5 per cent for intensities between 15 and 20 per cent. Velocity biassing has been analysed by a number of workers (McLaughlin and Tiederman, 1973; Barnett and Bentley, 1974; George, 1975; Buchhave, 1975; Durão and Whitelaw, 1975; Dimotakis, 1976; Buchhave, George and Lumley, 1979; Durão, Laker and Whitelaw, 1980).

Averaging algorithms which properly account for velocity biassing require (Dimotakis, 1976; Buchhave, 1975) either knowledge of the joint probability density function for the three components of velocity or involve the use of the residence time of the particle (Buchhave et al, 1979). Neither of these was used, so that some error has been incurred in the measurements and an estimate of this error can be made. The estimate is likely to be too large for the reasons given in the following paragraph.

The extent to which the variation in the data rate, given by equation (4.4), biasses the population of velocity measurements depends on the relative magnitude of the particle arrival timescale, τ_p ($\equiv 1/\dot{R}$) and the timescale of the energy-containing turbulent fluctuations, τ_t. Biassing will be greatest when τ_p is less than τ_t, and decreases as τ_p becomes larger than τ_t. (This seems to be the

reason for some publications reporting poor correlation between data rate and velocity, such as Smith and Meadows (1974) and Durão, Laker and Whitelaw (1980), while others find good correlation, such as Karpuk and Tiederman (1976), Quigley and Tiederman (1977) and Erdman and Gellert (1976), cited by Buchhave et al (1979). Here, the particle arrival rate was less than five thousand per second so that τ_p is slightly larger than τ_t and hence the bias is smaller than that suggested by application of equation (4.4). A further effect which occurs is that the signal amplitude of high velocity particles may be smaller than that of low velocity particles (Tiederman, 1977, cited by Buchhave et al, 1979; Durão and Whitelaw, 1979) so that if the signal validation criterion depends on the amplitude, a "reverse" bias exists. The effect depends on the laser power, the speed of response of the photomultiplier tube and the presence or absence of frequency shift. The results of Durão and Whitelaw (1979), using the same instruments as described in this chapter, suggest that the velocity biassing is mitigated.

The magnitude of the velocity bias is now estimated using the calculated corrections given by McLaughlin and Tiederman (1973). These corrections are based on a two-dimensional, Gaussian representation of the velocity probability density distribution. Estimates are made for two points on the centreline: the one at the maximum negative mean velocity and the other far downstream. The corrections depend on the local (measured) values of $\sqrt{\langle u^2 \rangle}/U$ and $(\langle v^2 \rangle / \langle u^2 \rangle)^{1/2}$ and these are summarised below. The values in the extreme right-hand column are taken from the isothermal measurements of chapter II. The errors ($\equiv$ (estimate-true)/true) for each position are given in table 4.5 and are largest within the recirculation zone because of the high turbulence intensities present and negligible

Position x/R	$\frac{U}{U_o}$	$\frac{\langle u^2 \rangle}{U_o^2}$ (%)	$\frac{\sqrt{\langle u^2 \rangle}}{U}$ (%)	$\left[\frac{\langle v^2 \rangle}{\langle u^2 \rangle}\right]^{1/2}$
0.75	- 0.60	5.3	38	≃ 1.0
4.50	1.45	≃ 1.2	8	≃ 1.5

far downstream. The values of the errors given in table 4.5 are certainly worst estimates because the presence of a third component of fluctuating velocity (ignored by the analysis of McLaughlin and Tiederman) serves to reduce further the correlation between a component of velocity with the instantaneous, three-dimensional velocity vector's magnitude. In recognition of this, the typical error in a measurement, quoted in table 4.4, is smaller than that derived from the analysis of McLaughlin and Tiederman (1973).

TABLE 4.5

ESTIMATES OF ERROR DUE TO VELOCITY BIASSING FOR TWO POSITIONS. ESTIMATES DERIVED FROM THE TWO-DIMENSIONAL ANALYSIS OF McLAUGHLIN AND TIEDERMAN (1973)

Position x/R	U/U_o	$\sqrt{\langle u^2 \rangle}/U_o^2$
0.75	+ 8%	- 12%
4.50	+ 1%	- 1%

The fourth source of error in table 4.4(a), which arises because $\dot{R}$, equation (4.4), varies with the instantaneous scattering-particle density, (μ), is present if, and only if, fluctuations in μ and U(t) are correlated. Since μ is a function of the instantaneous pressure and temperature, it is likely that some correlation does exist. An analysis similar to that of McLaughlin and Tiederman has been made by Asalor and Whitelaw (1975) which gives the error as a function of the pressure- or temperature-fluctuation intensity, assuming unity correlation factors with velocity. This can be interpreted as a bias towards the (unburnt) reactant conditions. The level of pressure fluctuations is small (proportional to {Mach number}^{2}) and even during violent combustion-induced oscillations (see sub-section 4.3.1) this will only be of the order of 5 per cent (Clare et al, 1976) and the errors incurred are small. For the purposes of this section a representative value of $\sqrt{\langle T'^2 \rangle}/T$ is, say, 0.20. This gives rise to an important error in the value of mean velocity alone, amounting to a possible 5 per cent underestimation of the local value.

An alternative approach to the variation of the rate of particle arrival due to variations in the local concentration of particles is to say that since this concentration is proportional to the local density, then the measurement made by the velocimeter is density weighted. This is a useful result because density weighted variables are frequently used in mathematical models of combustion. In these experiments, however, the timescale of particle arrival is slightly larger than that of the turbulence and the measurements are thus closer to unweighted results.

The final effect in table 4.4 is due to broadening which arises because of gradients of both velocity and particle concentration across the measuring volume. The effect is analagous to mean velocity

gradient broadening, table 2.4. Baker (1974, cited by Asalor and Whitelaw, 1975) has found that gradients of 25 per cent mm^{-1} do not introduce large errors and, with the possible exception of the small ($\sim$ 2 - 3 mm) regions of large radial temperature gradient, evident in figures 4.31 - 4.33, the effect can be considered small.

The reproducibility of the flow should also be considered when determining the accuracy of the measurements, particularly because the centreline profiles of velocity (figures 4.17, 4.20, 4.23, 4.28 - 4.30) were determined by extinguishing the flame and re-positioning the windows during the profile. The limits to the reproducibility are set by the tolerance to which the volume flow rates of reactants could be maintained. The flow rates of gas and air could be measured to much better than 1 per cent from the pressure drop across the orifice plate meters and the laboratory supply of compressed gas could be maintained constant to much better than 1 per cent. However, the laboratory supply of compressed air would fluctuate by up to $\pm$ 1½%, so that a comparable error exists in the values of equivalence ratio. The importance of this error can be estimated by referring to figures 4.9, 4.10, 4.17, 4.20, 4.23, 4.28, 4.29 and 4.30. The latter six figures show profiles in which the flame was extinguished and relighted twice, so as to reposition the observation windows. The consistency of the profiles suggests errors of less than 3 per cent for mean velocity and 1 per cent for the turbulence intensity.

In concluding in this section, it is apparent that the dominant error remains the effect of velocity biassing for the region within the recirculation zone: table 4.4 summarises a representative value of this error.

Errors in temperature measurement

Table 4.4(b) summarizes the errors incurred in the measurement of mean temperature. Probe interference can be important in premixed flames because the probe can act as a secondary flame holder, thereby changing the flow. The probe shown in figure 4.3(b) was not observed to give rise to any flame holding. A phenomenon related to probe interference is the catalytic activity of the platinum on the reaction. Some (Alvermann and Stottmann, 1964; cited by Pein, Peschel and Fetting, 1970) claim that catalytic effects are unimportant; others (Lewis and Moss, 1978; Bilger, 1977) assert the opposite. No coating was applied to the thermocouple in these experiments: catalysis will partly compensate for the radiation errors discussed below.

The thermocouple bead gains heat from the surrounding gases through surface heat transfer and loses heat by conduction from the supporting wires and by radiation. For large ratios (Bradshaw, 1971) of the length-to-diameter ratio of these supporting wires, conduction errors are negligible and radiation loss dominates. The magnitude of the radiation correction has been shown (Attya, 1980) to be of the order of 80 K at 1700 K in a free flame and, with the lower mean temperatures in the present arrangement, was about 40 K.

The average temperature measured by the thermocouple will be (Bilger, 1977):-

$$\langle T_{g,m} \rangle = \frac{\langle K_f \; Nu \; T_g \rangle}{\langle K_f \; Nu \rangle} \qquad (4.5)$$

where:-

K_f is the thermal conductivity at some varying film

temperature and composition

Nu is the corresponding Nusselt number

(The equation assumes that the thermocouple bead is sufficiently massive not to follow the temperature fluctuations). Bilger (1977) suggests that $\langle T_{g,m} \rangle$ will differ from the time mean temperature by more than the Favre-averaged temperature, but with opposite sign. As noted by Kent and Bilger (1973) this source of error is largely unquantifiable although the results of Attya (1980) suggest that it is small.

The limits of flow reproducibility are also important for the accurate measurement of temperature, as indicated in figure 4.11 by the steep variation of temperature with equivalence ratio. The small scatter in the temperature profiles, presented below, suggests an error of about 40 Kelvins due to this source.

4.3 Results

The results are presented under two headings. The first describes the influence of the fuel-to-air ratio on the flame extinction limits, the flame's position, local values of velocity and temperature and on the sound levels. The second gives the field measurements of velocity and temperature for fuel-lean operation.

4.3.1 Influence of the equivalence ratio

The equivalence ratio, ϕ, is defined as:-

$$\phi \equiv \frac{\text{volumetric fuel-to-air ratio}}{\text{stoichiometric (volumetric) fuel-to-air ratio}} \qquad (4.6)$$

where the denominator has a value (1/9.52). The flame extinction

limits of the baffles were examined by keeping the air flow rate constant and changing the gas flow rate. Figure 4.8 shows these limits for the three baffles as a function of the annular bulk air velocity, U_o. The shaded areas define the fuel-lean ('blow-out') and -rich ('blow-off') extinction limits. Adjacent to these limits are regions designated as 'stable' which refer to the presence of a well-defined, comparatively smooth flame sheet originating at the baffle tip and extending downstream only of the baffle. Between these regions is a range marked 'unstable' which corresponds to operation with the flame visible upstream, as well as downstream, of the trailing edge. The boundary between each flow regime is subject to an uncertainty of about $\pm$ 0.03 ϕ. At the highest values of the annular bulk velocity, the width of the unstable range is similar ($0.9 \lesssim \phi \lesssim 1.4$) for all three baffles. At lower values this width changes erratically, with the only identifiable trend being that of the cone (figure 4.8(b)) for which the unstable range becomes smaller.

As will be seen below, the flow is markedly different between the stable and unstable states of combustion with the onset of unstable combustion being an abrupt occurence. At small values of U_o (less than about 6 ms^{-1} and 12 ms^{-1} for the 25 and 50 per cent blockages respectively) the flame stabilised in the boundary layer of the sting, upstream of the trailing edge of the baffle. At higher values of U_o, the flame was not attached to any boundary layer.

The following three graphs present the influence of the equivalence ratio on the local values of velocity and temperature. The measurements of velocity during unstable combustion were limited to just one point because the violence of the pressure fluctuations was such as to damage both the glass windows and the flame trap upstream of the baffle. Figure 4.9 shows the variation of mean

velocity with ϕ for the 25 per cent blockage disc at a point which is, during stable combustion, close to the free stagnation point. The results show that the bubble is longest for equivalence ratios near the extinction limits and that as the value of ϕ is moved away from these limits, so the mean velocity becomes larger and eventually positive. This implies that the recirculation length becomes shorter and that stoichiometric conditions are associated with large velocities on the centreline, even quite close to the baffle. This is seen by comparing the maximum centreline velocities measured during fuel-lean conditions ($\simeq 1.6\ U_o$; figure 4.19) and during stoichiometric conditions ($\simeq 3\ U_o$). The decrease in the length of the recirculation zone as conditions approach stoichiometric is in agreement with the results of Winterfeld (1965) and Wright (1959), although these authors observed a smaller dependence on the equivalence ratio than is implied by the results of figure 4.9.

Figure 4.10 presents the behaviour of the variance of velocity, $\langle u^2 \rangle$, at the same point: attention is drawn to the use of a logarithmic scale for the ordinate. For fuel-rich, stable combustion, the variance changes comparatively little; the onset of unstable combustion gives rise to an extremely large and rapid increase which is then relatively insensitive to further changes in ϕ. During unstable combustion the probability function of velocity was either heavily skewed or sometimes bimodal, the latter suggesting a periodic oscillation; the use of frequency analysis for demodulation of the Doppler signal precludes the substantiation of this speculation, however. The increase in $\langle u^2 \rangle$ during unstable combustion, at least over that obtaining in the equivalent isothermal flow, has also been observed by El Banhawy, Melling and Whitelaw (1978).

Figure 4.11 demonstrates the change in mean temperature with

increasing equivalence ratio: results could not be taken during unstable combustion because the thermocouple would break. Although an increase in the mean temperature is expected, the figure shows that this is greater than the proportional increase in the adiabatic flame temperature. If the state of the gas is taken as alternating between completely burnt products and completely unburnt reactants, then departures from the adiabatic flame temperature are simply related to the time during which the point is occupied by unburnt reactants. Physically, this view depends on the Damkoehler number being large and the reaction zone being very thin (Bray, 1980): experimental evidence, at least for the qualitative correctness of the supposition, comes from the measurement of the probability density functions of temperature measured by Lewis and Moss (1978), Yoshida and Guenther (1980) and Dibble and Hollenbach (1980). The variance of temperature fluctuations for the supposed temporal variation (a castellated wave-form) is then related to the mean temperature by:-

$$\langle T_+'^2 \rangle = T_+ \ (1 - T_+) \tag{4.7}$$

where:-

$$T_+(t) = \frac{T(t) - T_u}{T_b - T_u} \tag{4.8}$$

and:-

$$T_+(t) = T_+ + T_+' \tag{4.9}$$

Using equation (4.7), the results of figure 4.11 suggest that the

variance of temperature is smallest near the flame extinction limit and near the transition to unstable combustion. The latter observation implies that the point under consideration (x = 3.13 R, r = 0.63 R) lies increasingly downstream of the flame front.

Figure 4.12 shows the sound levels emitted by the chamber for each of the three baffles at high values of U_o during combustion. For isothermal flow the sound level radiated is, for the 25 per cent blockage disc, 8.5 dB (ref. laboratory background) and comparison with the results of figure 4.12 indicates that during stable combustion the sound level is similar to the inert flow. As the unstable regime is approached, this sound level increases by between 15 and 25 dB and is accompanied by a perceived increase in the proportion of low frequency noise.

The sound that is radiated from the chamber comes partly from the fluctuating pressure, associated with the fluctuating shear stresses, which is present in all (reacting or isothermal) turbulent flows and partly from individual elements of reactants as these ignite, burn and expand (Bragg, 1963). Both of these sources are broadband and random. A third source is due to combustion-induced oscillations of pressure which are characterised by specific frequencies and are maintained by feedback energy derived from the rapid expansion of the gas during combustion. The presence of combustion-induced oscillations is conveniently established experimentally by the occurence of peaks in the spectral analysis of the sound level fluctuations. Figures 4.13(a) - (c) present the frequencies of such oscillations in the 25 - 250 Hz band for the three baffles as a function of the equivalence ratio, with U_o as parameter. The results show that up to four different peak frequencies co-exist at any given value of equivalence ratio for all baffles, at all values of U_o and independently of

whether combustion is stable or unstable (repetition of the experiment during isothermal flow confirmed the absence of any similar 'preferred' frequencies). These frequencies make larger contributions to the sound level during unstable combustion. In each of the figures, combustion-induced oscillations always occur at about 25 and 200 Hz, irrespective of the operating conditions. It is likely that these frequencies are harmonically related and that they derive from the frequency of the rotary compressor which was used to supply the gas (speed of rotation: 1430 r.p.m. ≡ 24 Hz). In the classification of Barrère and Williams (1969) this is a 'system instability' and no more attention will be devoted to it.

Within the range 50 - 150 Hz, there exist up to two further peaks in the spectrum which are not harmonically related, however. When only one of these two frequencies was present, the microphone output was sometimes, but by no means always, recognisably periodic. (The Strouhal number of the flow (based on the baffle diameter, U_o, and a frequency of 80 Hz) is about 0.4 and is higher than that (0.2) occuring in isothermal flows). If the periodicity were related to free vortex shedding, then a systematic dependence on U_o or the diameter is expected. Although the frequency of the oscillations is sensitive to U_o, the diameter of the baffle and the equivalence ratio, no systematic dependence is apparent and thus free vortex shedding can be discounted as a source.

In very many case studies (e.g. El Banhawy, Melling and Whitelaw, 1978; Putnam, 1971; Kilham, Jackson and Smith, 1961) the frequency of combustion-induced oscillations has been identified with acoustic oscillations. Two possible standing pressure "quarter" waves are shown in figure 4.14: their frequency is now estimated using an analysis similar to that presented by Putnam and Dennis (1955) (cited

by Putnam, 1971). (The reason for placing the pressure antinode at the baffle for the short wavelength is given in the discussion of sub-section 4.4.1 below). In general, the frequency of oscillation for the quarter wave in a pipe closed at one end is, for isothermal operation:-

$$f_a = \frac{c}{4L} \tag{4.10}$$

where:-

c is the velocity of sound

L is the length of the tube

For the purposes of this calculation it is assumed that the chamber downstream of the baffle is occupied by air at a temperature of 2000 K and upstream of the baffle by air at 300 K, that the velocity of sound in air at 300 K is 340 ms^{-1} and that no end corrections are applicable to the length L. In addition, the length occupied by hot air ($\simeq$ 0.9 m) is equivalent to a length:-

$$0.9 \sqrt{\frac{300}{2000}} \tag{4.11}$$

at 300 K. The two frequencies, corresponding to the two lengths, returned by calculation are then 68 and 94 Hz which are close to those observed experimentally. The coincidence of experiment and the result of the simple calculation is evidence for identifying the combustion-induced oscillations of pressure with the quarter-waves shown in figure 4.14. The similarity between the graphs of the variance of velocity, figure 4.10, and the sound level, figure 4.12(a), can now

be explained. The standing pressure wave in an acoustic resonance is accompanied by a similar fluctuating velocity field, except that the velocity antinode occurs at the pressure node. Hence the increase in the amplitude of the pressure wave, which is equivalent to the increase in sound level, results in the increase in the variance of velocity.

The results so far have shown the existence of combustion-induced oscillations of pressure and possibly of velocity also. The spectrum of fluctuations of the flow, particularly of temperature, is important to the elucidation of the mechanism by which combustion sustains the oscillations (Rayleigh's criterion, sub-section 4.4.1). The effects of thermal inertia cause the frequency response of the thermocouple to roll-off at about 20 dB/decade (Lenz and Guenther, 1980) at a break frequency which depends on the operating conditions but is of the order of, say, 10 Hz for the thermocouple described in sub-section 4.2.2 (Yoshida and Guenther, 1980). The interest here is the detection of peaks in the spectrogram of temperature fluctuations, rather than information on their strength, so that frequency compensation was not necessary. Figure 4.15 shows two spectrograms (that is, spectra uncorrected for the change in the analyser's filter bandwidth, equation (2.15), or for the effects of thermal inertia) of temperature and sound level fluctuations. The operating conditions correspond to stable combustion. The figure shows that there is only one peak in the temperature spectrogram, at about 100 Hz, which coincides with the higher of the two acoustic frequencies.

The confinement of the flame gives rise to the possibility of acoustically-related, combustion-induced pressure oscillations which, during unstable combustion, modify the mean flame position. This may be due either to the instantaneous pressure becoming large

enough to stagnate the flow locally, so that the flame propagates upstream through the temporarily stationary reactants (Mellor, personal communication, 1980) or because the velocity fluctuations (due to the acoustic resonance) become strong enough to convect flame kernels upstream of the baffle. The behaviour of the corresponding unconfined flame was investigated by repositioning the baffle so that its trailing edge lay at the exit of the chamber and the flame was established in the annular jet. A particularly strong oscillation could also be promoted in this configuration with a frequency of 120 Hz. This frequency corresponds to an unrealistically short quarter-wavelength and the most plausible explanation for this resonance is that the pipe upstream of the baffle and the annular gap act as a Helmholtz resonator. {The natural frequency of such a resonator is (Putnam, 1971):-

$$f_H = \frac{c}{2\pi}\left[\frac{A_t}{V_c\, \ell_{eff}}\right]^{1/2} \qquad (4.12)$$

where:-

A_t is the area of the annular gap (throat)

V_c is the chamber's volume

ℓ_{eff} is the effective length of the throat

$\simeq 0.85\ (2R)\left[1 - 0.7\ (A_t/A_c)^{1/2}\right]$

A_c is the area of the chamber

The value of f_H returned by this calculation is about 150 Hz and is sufficiently close to that measured to confirm the existence of the Helmholtz resonance. Both the Helmholtz resonance and the quarter wave oscillation are acoustic resonances: which of the two is present in a chamber depends on the details of the geometry and does not represent

a fundamental difference in the mechanism of oscillation}. The resonance could be stopped by partially opening the observation windows which is strong evidence for believing the combustion-induced oscillations of the chapter to be acoustic in origin rather than derived from vortex shedding, low Reynolds number effects or from aerodynamic instabilities. A detailed consideration of how these acoustic resonances are maintained is deferred to the discussion of sub-section 4.4.1.

In this work only the acoustic responses of the chamber are considered, but these are not the only ones possible. The flame surface is an interface separating high density gas (the reactants) from low density (the products) and can thus reflect and transmit acoustic waves. Recently Marble and Candel (1979) and Marble et al (1980) have calculated the response of this surface when excited by periodic acoustic disturbances. Their results suggest that the energy from combustion feeds into the flow field fluctuations by means of a phenomenon similar to Landau instability (Bray, 1980). The calculation is involved and requires assumptions concerning the turbulent flame speed, which is necessary to specify the flame sheet's position.

The presence of large-amplitude oscillations during unstable combustion is undesirable because of the damage which is wreaked on the chamber. Also, the measurements taken under such conditions will be less suitable for comparison with calculation procedures which incorporate models of turbulence and combustion that are unable to account for the oscillations. The field measurements of the following sub-section were, therefore, taken at an equivalence ratio (ϕ = 0.69) which corresponds to stable combustion and thus combustion-induced oscillations represent only a comparatively small part of the

fluctuating field.

4.3.2 Velocity and temperature fields at 0.69 equivalence ratio

This sub-section presents field measurements of the mean and variance of axial velocity, wall pressure and mean temperature at an equivalence ratio of 0.69 for three baffles. For the purposes of comparison, a number of isothermal (air only) velocity and wall pressure profiles have been measured and are presented. Preliminary results for the disc of 25 per cent blockage have been published (Taylor and Whitelaw, 1980). Since then, a damaged flame arrestor has been replaced with an improvement in the symmetry of the flow.

Mean velocity and wall pressure

Figure 4.16 shows the radial profiles of mean axial velocity for the case of the 25 per cent blockage disc at axial stations in the plane of the trailing edge of the baffle, at two stations within the recirculation zone and one far downstream. The asymmetry in the radial direction is due both to the lack of circularity of the pipe and to the inhomogeneous obstruction of the flame arrestor with seeding particles. The qualitative features of these profiles are similar to those in isothermal flow, such as the acceleration of the fluid because of the presence of a recirculation bubble which is wider than the baffle. In the plane of the baffle, the influence of combustion on the axial velocity profile is no greater than would be expected from the greater volume flow rate associated with the presence of natural gas. Figure 4.17 presents the radial profile of mean radial velocity during, and without, combustion at the same station. For this baffle, the changes in the profile due to combustion are small with the

exception of the point closest to the baffle where the radial velocity, and hence the angle of the separation streamline, is greater in the presence of reaction. The differences as compared with isothermal flow are best illustrated by the centreline development of axial velocity, figure 4.18. The repositioning of the observation windows, mentioned in sub-section 4.2.2, entails a small error which has been discussed in sub-section 4.2.3. The recirculation length (table 4.6) is longer (as found by Winterfeld, 1965) by about 38 per cent, the maximum reversed

TABLE 4.6

LENGTH OF THE RECIRCULATION ZONE DURING FUEL-LEAN OPERATION AND ISOTHERMAL FLOW

CASE	COMBUSTING[b] LENGTH[a]	ISOTHERMAL LENGTH[a]
Disc, 25% blockage	2.20	1.60
Cone, 25% blockage	2.20	1.45
Disc, 50% blockage	2.26	1.98

[a] Lengths expressed in baffle diameters

[b] Equivalence ratio = 0.69

velocity is larger by about 40 per cent and the acceleration of the flow downstream of the rear stagnation point is greater and more prolonged. The latter is the result of the dilatation due to heat release and is obvious over much of the radius of the chamber: the effects are particularly evident at x = 4.25 R.

The acceleration of the gases downstream of the baffle is

financed by a favourable pressure gradient. Figure 4.19 shows this gradient for the region $x \gtrsim 3$ R and the result is to be contrasted with the pressure recovery which takes place in the isothermal flow. The pressure minimum, which is associated with the maximum width of the recirculation bubble, is larger during combustion and this suggests that the bubble's maximum width is greater (see equation (2.18)). This result is consistent with the increase in mean radial velocity at x = 0, noted above.

Figure 4.20 shows that in the case of the 25 per cent blockage cone, the acceleration of the axial velocity around the recirculation bubble is smaller than for the disc. Figure 4.17(b) indicates that the radial velocity at x = 0 is, at locations close to the baffle's tip, larger during combustion although the magnitudes involved are, as expected, smaller than for the disc. Figure 4.21 compares the centreline development of axial velocity both with and without combustion; the reacting flow is virtually indistinguishable from that of the disc, figure 4.18. Figure 4.22 shows the corresponding profiles of wall pressure: the trends are similar to those of figure 4.19 although the magnitude of the pressure minimum during combustion is similar to isothermal flow. The apparent similarity between the wall pressure for the 25 per cent blockage disc and cone (figures 4.19 and 4.22) is spurious because the position of the reference pressure, p_0, is not the same in the two cases.

Figure 4.23 shows that the influence of combustion on the radial profile of axial velocity at x = 0, for the 50 per cent blockage disc, is small. The influence on the corresponding profile of radial velocity, figure 4.17(c), is to increase the magnitude by almost half, a more noticeable change than for the previous baffles.

Figure 4.24 shows the by now familiar increase (about 14 per cent) in the recirculation bubble length and in the maximum reversed velocity (about 36 per cent) over isothermal flow, although the former is relatively smaller than for the two other baffles. Figure 4.25 shows that there is virtually no difference in the wall pressure up to the occurence of the minimum value implying that the maximum width of the bubble is similar in isothermal and combusting flow, in common with the result of the cone, figure 4.22. This is in agreement with the results of Winterfeld (1965) but is surprising in view of the large change in the radial velocity at x = 0. As before, the subsequent pressure recovery downstream of this point is less during combustion because of the axial acceleration of the mean flow.

Comparison with measurements of chapter II

The comparison between the isothermal flows of this chapter and those in chapter II is briefly considered here. Tables 4.6 and 2.7 show that the recirculation lengths in this chapter are consistently smaller. A small part of this may be due to velocity biassing (see sub-section 4.2.3) but the remainder is due to differences in the flows. The profiles of wall pressure for the 25 per cent blockage cone and 50 per cent blockage disc provide corroborating evidence for this point of view.

In all three cases, the radial profile of axial velocity at x = 0 is larger than for the corresponding flows in chapter II. This is due to the effects of the constriction of the annular gap, caused by the plane glass observation windows, and also to the wake downstream of the retaining collars (figure 4.1), giving rise to a region of low velocity near the walls. It is known from the numerical experiments of chapter III that changes in the radial velocity in the plane of the trailing edge can alter the wall pressure distribution

greatly (see figure 3.22). The profiles of radial velocity (figures 4.17(a) - (c)) show both agreement (cone, 25% blockage; figure 2.17) and disagreement (disc, 50% blockage; figure 2.20) with the water flows. Taken together with the change in the axial velocity profiles, these results imply a difference in the angles of the streamlines and illustrate the dangers of extrapolating results between different configurations.

Variance of velocity

Figures 4.26, 4.27 and 4.28 present the radial profiles of the variance of velocity of axial velocity, $\langle u^2 \rangle$, for the disc and cone of 25 per cent blockage and the disc of 50 per cent blockage respectively. This quantity is not simply related to the Favre-averaged Reynolds stress (see Libby and Bray, 1977) which appears in the mean axial momentum equation, although it is indicative of the level of turbulence.

As for the isothermal flows of chapter II, $\langle u^2 \rangle$ is largest in the free shear layer downstream of the baffle tip; the radial maxima during combustion are, however, much larger than for the isothermal flow. Values of $\langle u^2 \rangle / U_o^2$ greater than about 0.12 within the shear layer represent regions in which the axial velocity can be expected to become instantaneously negative. (This corresponds to a standard deviation of about 35 per cent and, assuming that the width of a Gaussian distribution is approximately six standard deviations, gives rise to a distribution which extends to negative velocities). The measurements, particularly for the larger disc (figure 4.28), show that flow reversal occurs at locations quite remote from the axis, which is not the case for isothermal flow. It is possible that these reversals are responsible, in the case of unstable

combustion, for the convection of the flame front upstream of the trailing edge of the baffle.

Westenberg and Rice (1959) reported that, at locations far downstream of the recirculation zone, the forebody shape of the baffle did not have an important bearing on the turbulence level. The evidence of figures 4.26 - 4.28 shows that this is not the case within the recirculation bubble, being higher for the smaller disc than for the cone and largest for the 50 per cent blockage disc. It is plausible to associate this observation with the increase in the flame widths (compare below) from the cone to the larger disc.

Figures 4.29, 4.30 and 4.31 show the centreline development of turbulence intensity for the three baffles in a form suitable for comparison with the isothermal flow observations of figures 2.24, 2.29 and 2.33. The isothermal measurements of this chapter are very similar to those of chapter II. The profiles in the presence of combustion possess features similar to those in its absence. For example, $\sqrt{\langle u^2 \rangle}$ has a local maximum at the rear stagnation point (not clear in figure 4.30 because the observation window was repositioned); there is a further maximum near the baffle where $\partial U/\partial x$ is negative; and values decay monotonically downstream of the rear stagnation point. In contrast to isothermal flow, however, the two maxima are not of similar intensity.

Mean temperature

The field distributions of mean temperature for the baffles are given in figures 4.32, 4.33 and 4.34. The profiles describe, in a quantitative way, the rate of propagation into the unburnt reactant stream and knowledge of the mean flame position is useful in the interpretation of the velocity profiles. For each figure, one profile

spans the width of the combustor and shows the departures from symmetry.

If the thin flame model (equations (4.7) - (4.9)), introduced above, is assumed then the mean flame position can be defined as those points at which reaction products are present for half of the time. At an equivalence ratio of 0.69, this corresponds to a temperature of 1100 Kelvins. Comparing figure 4.32 with 4.33 shows that the flame spreads more rapidly from the disc than for the cone, in accordance with the steeper trajectory of the shear layer. The mean flame width decreases in both cases downstream of $x \simeq 0.8$ R until, by the end of the recirculation zone ($x \simeq 2.5$ R) it is only 0.3 R wide. In the case of the disc, the flame spreads radially while for the cone the width remains constant. Figure 4.34 indicates that for the 50 per cent blockage disc, the flame width decreases monotonically with axial distance until the end of the recirculation bubble, at $x \simeq 3$ R, where it is about 0.6 R wide. The decrease in width is smaller, in proportion to the diameter of the baffle, than for the smaller baffles and suggests more vigorous flame propagation.

The radial temperature distribution within the recirculation zone is initially comparatively uniform and similar ($\simeq$ 1300 - 1400 K) for all baffles. The value is, however, substantially smaller than the adiabatic flame temperature ($\simeq$ 1800 K) and implies that unburnt gases are present within this region. According to the thin flame approximation of equation (4.7), about one-fifth of the time is occupied by such gases. The radial homogeneity decreases with axial distance as the mean flame width becomes narrower. As could be expected, the larger disc retains a large region ($\simeq$ 0.4 R) of constant mean temperature in the radial direction even at the furthest axial measurement station, corresponding to the wider flame.

4.4 Discussion

The discussion of the results of section 4.3 falls into two independent parts. The first part deals with the presence of the combustion-induced flow oscillations which were shown in sub-section 4.3.1 to be acoustically related. Sub-section 4.4.1 thus is devoted to a consideration of the origin of these oscillations and concludes with recommendations for further work. The second part is concerned with the flow during stable combustion, during which these oscillations do not play a major rôle in the fluid flow. The discussion proceeds by comparing and contrasting the influence of the forebody shape and blockage (on the recirculation length and the level of turbulence) during combustion with that in the corresponding isothermal flow.

4.4.1 Combustion-induced oscillations

This sub-section examines three aspects of the combustion-induced, acoustic oscillations. The first concerns the mechanisms by which periodic heat release may arise. The second inquires as to why these oscillations should increase in amplitude during what has been termed unstable combustion. The final aspect is accounting for the absence of unstable regimes in combustion chambers which, superficially at least, resemble that used in this study.

The identification of acoustic oscillations, whether quarter-wave or Helmholtz resonance, is part of a description of the phenomenon but does not constitute an explanation for its occurence. The energy source for the maintenance of the oscillations, to compensate for the irreversabilities inevitably present, is the periodic heat release or gas expansion. An explanation of the existence of oscillations, therefore, involves discussing how periodic heat release might occur.

Various mechanisms have been postulated as being responsible

for periodic heat release: some of these can, however, be dismissed for the cases of this chapter. For example, Howland and Simmonds (1953) (cited by Putnam, 1971) postulated the existence of an ignition time lag. As noted by Marble et al (1980), this constitutes a plausible explanation for frequencies of the order of a kilohertz, because this corresponds to the time scale typical of chemical reactions but for frequencies of the order of one hundred hertz, such timescales are unimportant. Free vortex shedding from the baffle can also be discounted as a likely mechanism because, as noted in subsection 4.3.1, the Strouhal number of the flow and the dependence of the frequency with baffle diameter and U_o do not support this conclusion. Finally, the influence of pressure on the rate of reaction can also be dismissed because the Mach number is low and the rate of reaction is limited by mixing rather than by the chemical kinetic constants (Bragg, 1963; Spalding, 1971).

That mixing is the rate determining step in the reaction suggests that periodicity in the mixing can give rise to periodic heat release, thereby sustaining oscillations. There are three possible ways for periodic mixing to take place: aerodynamic instability, large scale 'coherent structures' and fluctuations in the reactant flow rates. These are now discussed in turn.

Aerodynamic instability can arise in flows with points of inflexion in the mean velocity profiles, as is the case in the flows of this chapter. In a study of oscillating, unconfined diffusion flames, Durão and Whitelaw (1974)* concluded that aerodynamic instability was responsible for the combustion-induced oscillations that they observed. The instability mechanism, however, amplifies

---

* Reference: DURÃO, D. F. G. and WHITELAW, J. H. (1974) Instantaneous velocity and temperature measurements in oscillating diffusion flames. Proc. R. Soc. Lond. A. 338, 479.

only a narrow range of frequencies and it is unlikely, in general, that this will always coincide with the particular acoustic frequencies of the duct under consideration. The observed subsidence of the Helmholtz oscillations, which accompanied the partial opening of the observation windows (see sub-section 4.3.1), is further evidence against aerodynamic instability being an important process.

Large-scale 'coherent structures' (Roshko, 1976; Bradshaw, 1980) have been reported (Ganji and Sawyer, 1979, 1980; Pitz and Daily, 1979) to be important in the combusting flow stabilised downstream of a plane, backward facing step. The frequency with which these large-scale structures are shed is susceptible to a wide range of forcing frequencies (Hussain and Zaman, 1978; cited by Pitz and Daily, 1979), and in this case the forcing frequency would be that of the acoustic resonance. Experimentally, Blackshear (1956) has also shown that the shear flow downstream of a baffle is responsive to externally-applied acoustic disturbances. The experimental evidence for large-scale structures is almost always primarily photographic and such evidence is very difficult to obtain in axisymmetric, combusting flows. The results of this chapter can, therefore, neither confirm nor refute the presence of this postulated mechanism.

The third mechanism for periodic heat release to be considered involves the fluctuating flow rate of the reactants, which is the counterpart of the fluctuating pressure field in any acoustic vibration. An increase in the reactant flow rate at, say, the velocity antinode (pressure node) will give rise to an increase in the rate of heat release. This oscillatory heat release has been advanced as the way in which oscillatory combustion (with acoustic standing quarter waves) is maintained in a premixed flame stabilised by a sudden pipe expansion (Kilham et al, 1961, 1965). The same explanation is

applicable in the flows considered here and together with a suitable time lag (compare below) appears to be the most plausible cause of periodic mixing.

The results of sub-section 4.3.1 show that the amplitude of the pressure oscillations is large over the particular range of equivalence ratio corresponding to unstable combustion. A possible reason for the sensitivity of the oscillation's amplitude to the equivalence ratio is now examined.

If fluctuations in the reactant flow rate are to maintain oscillations, then there must be a suitable time lag (Putnam, 1971) between the increment in flow rate and that of the corresponding heat release in order that the latter be positively correlated with the pressure oscillation. This requirement is imposed by Rayleigh's criterion (e.g. Thring, 1969) which asserts that acoustic oscillations, whatever their origin, can be maintained only if heat is being released as the pressure increases. The time lag arises physically from the 'time of flight' of the increment in mass flow rate between the velocity antinode (the origin of the increment) and its combustion at the flame sheet: the position of the flame, therefore, determines whether the time lag will be suitable or not. At the Reynolds numbers appropriate to the experiments of this chapter, flame propagation is sensitive to the equivalence ratio, with the width increasing as conditions approach stoichiometric (Williams, Hottel and Scurlock, 1949; Wright and Zukoski, 1962). The variation in the flame width gives rise to variations in the time lag and the transition to unstable combustion thus occurs because the relative phasing between heat release and pressure fluctuations improves, giving rise to stronger pressure oscillations. The estimation of the value of the time lag in a given flow is particularly difficult but a value, based on U_o and

X_r, is at least of the required magnitude.

An implication of Rayleigh's criterion is that the frequency of the temperature and pressure fluctuations, which are responsible for coupling the release of chemical energy with the flow oscillation, must be the same. The spectrograms of the temperature fluctuations in figure 4.15 suggest that the driving pressure-oscillation is only the higher of the two acoustic frequencies and the temperature peak is, as expected, weak during stable combustion (i.e. the conditions under which the results of figure 4.15 were taken). The higher frequency corresponds to the shorter quarter-wavelength in figure 4.14 so that if the temperature fluctuation is to be able to perform work against the pressure fluctuation, the pressure antinode must lie near the plane of the baffle, as shown in the figure. These arguments suggest that the lower frequency oscillation is passively excited by the higher and plays no part in the maintenance of the combustion-induced oscillations.

The sensitivity to the flame's shape, which is implied by the importance of the time lag, suggests that the presence or absence of combustion-induced oscillations will depend crucially on the details of flow. Thus some experiments have been reported concerning confined, premixed flames but stabilised by means other than a baffle - for example by a pilot flame (Lefebvre and Reid, 1966), by an opposed jet (Peck and Samuelsen, 1976) or by a hot mixing layer (Moreau and Boutier, 1976) - which have not reported the existence of large combustion-induced oscillations of pressure. It is concluded that this is due to the flame shapes giving rise to time lags which are unfavourable to the maintenance of oscillations.

It is possible, however, to arrange confined, bluff body stabilised, premixed flames which are free of large combustion-induced

oscillations (e.g. Winterfeld, 1965; Wright and Zukoski, 1962). These experiments were carried out at high Reynolds numbers (that is, fully turbulent), for which the flame shape is independent of the equivalence ratio. This means that the time lag between the increase in the reactant flow rate and its combustion is independent of the equivalence ratio and there is no way to improve the correlation between the temperature and pressure fluctuations.

Further research is required to confirm the nature of the acoustic oscillations by measuring, with a probe microphone, the r.m.s. amplitude of the pressure fluctuation at frequencies corresponding to the shorter wavelength. The identification of the variation in the phase relation between pressure and temperature as a function of the equivalence ratio is important for establishing, experimentally, how the oscillation is maintained.

The nature of the flow which accompanies the pressure oscillation should be investigated by measurements of instantaneous velocity and temperature, together with the relative phasing of these fluctuations. Conditional sampling techniques can be used, with the conditioning signal being derived from either pressure or temperature.

The principal obstacle to the execution of this work is the measurement of the temperature fluctuations particularly during unstable combustion. The experience of this work is that a thermocouple made of 80 μm diameter wire is too fragile to withstand unstable combustion and thicker wires will be needed. This entails a drastic loss in the frequency reponse of the probe for which it may be difficult to compensate, even over the small frequency range (say up to 150 Hz) which is necessary to describe the oscillations. It is likely that this crucial measurement can be better made by optical techniques, such as Rayleigh scattering.

4.4.2 Influence of forebody shape and blockage during fuel-lean operation

Forebody shape

Figures 4.16 to 4.24 show that the qualitative features of combusting flow are similar to those in isothermal flow. The differences, as compared with the isothermal flows, are the lengthening of the recirculation bubble, with the lengths being the same for both disc and cone, and the increase in the maximum reversed velocity. With regard to the turbulent field, $\langle u^2 \rangle$ is larger and the details of the centreline distribution within the recirculation bubble are different. The following paragraphs discuss these points.

The recirculation length at $\phi = 0.69$ is longer than during isothermal flow, a result which also holds for plane baffles (Clare et al, 1976). The extent of the increase in length depends critically on the flow geometry under consideration. Clare et al (1976) report a 50 per cent increase, but Bespalov (1967), cited by Beér and Chigier (1974) reports a four-fold increase. The measurements of figure 4.17 show that the angles of the streamlines in the plane of the trailing edge of the baffles are larger in the presence of combustion than in its absence, with the increase being distributed over a larger radial distance from the tip of the baffle in the case of the cone. This gives rise to the larger increase in the recirculation length during combustion in the case of the cone (see table 4.6). The increase in length is also due to a reduction in the transport of momentum from the high-speed flow surrounding the bubble. This conclusion is drawn because in the limit of inviscid flow the separation streamlines never meet or, what is equivalent, the 'recirculation zone' is infinitely long. Further evidence comes from the increase in the residence time of a passive scalar in the recirculation zone during

combustion as compared to isothermal flow (Winterfeld, 1965; Bovina, 1958). The transport of the scalar out of the time-mean recirculation bubble is due principally to the turbulent transport:-

$$\langle \rho\, c'' v_s'' \rangle \qquad (4.13)$$

{where:-

c'' represents fluctuations of scalar concentrations from a Favre-averaged mean

v_s'' represents fluctuations of velocity normal to the local streamline, from a Favre-averaged mean}

across the surface defined by the separating streamline. The increase in the residence time is due to the turbulent transport being smaller than the isothermal counterpart, since the increase in the surface area of the bubble during combustion is insufficient to account for the increase in the residence time. Invoking the analogy between mass and momentum transport, it follows that the shear stress $\langle \rho\, u_s'' v_s'' \rangle$ must also have decreased.

The experimental evidence concerning the behaviour of the magnitude of the maximum reversed velocity, as compared with isothermal flow, is not unanimous. Clare et al (1976) report an increase for a ducted flow, Bespalov (1967) reports a decrease for unconfined flow, Durão, Founti and Whitelaw (1979) report a decrease for an annular jet diffusion flame and Durão and Whitelaw (1977) observed a decrease for a premixed annular jet flame. As discussed in the isothermal flow of chapter II, a fluid particle on the centreline is accelerated by the pressure gradients which are associated with the pressure

minimum near the eye of the recirculation bubble. During combustion, at least the following three changes will have taken place:-

(i) The streamline curvature, which is responsible for establishing the pressure minimum, will be smaller because the recirculation length is longer in the flows of this chapter. This tends to reduce the pressure minimum.

(ii) The velocity of fluid particles in the vicinity of the flame surface is larger, because of the dilatation. This increases the pressure minimum.

(iii) The gas density in (ii) is smaller because of combustion. This tends to reduce the pressure minimum, but the effect is partly counterbalanced because the fluid on the centreline is also less dense and hence more susceptible to acceleration.

The effects are competing ones and thus give rise to different effects on the centreline velocity in different cases. In the present case it seems that (ii) is the prevalent modification over the isothermal flow.

The magnitudes of individual terms in the budget for turbulent kinetic energy are modified by the presence of combustion (as discussed by Bilger, 1980, and Bray, 1980) so that for example dilatation (that is normal strain) can become an important sink term. The discussion of chapter II has already suggested that, even in isothermal flow, production by the interaction of normal stresses and strains is an important term. It can be expected that the analagous terms, appropriate to combusting flow, will retain this importance.

The mixing layer surrounding the separation streamline is

dominated by shear stress production and the increase in $\langle u^2 \rangle$ over the values in isothermal flow is generated by the increased rate of mean strain, $\partial U/\partial r$, which is observed. As noted in sub-section 4.3.2, the local maximum in $\langle u^2 \rangle$ on the centreline, within the recirculation bubble, is larger than that at $x = x_r$, in contrast to the result in isothermal flow. This is due to the larger values of $\langle u^2 \rangle$ which exist in the free shear layer in the combustion flow and which are transported in the recirculation bubble.

There arises in the Favre-averaged equation for turbulent kinetic energy the following term on the right hand side:-

$$\frac{D}{Dt} (\langle \rho \rangle \tilde{U}_j \tilde{K}) = ... - \langle u_j'' \frac{\partial p}{\partial x_j} (t) \rangle \qquad (4.14)$$

Now:-

$$- \langle u_j'' \frac{\partial p}{\partial x_j} (t) \rangle = - \langle u_j'' \rangle \frac{\partial \langle p \rangle}{\partial x_j} - \langle u_j'' \frac{\partial p'}{\partial x_j} \rangle \qquad (4.15)$$

where the summation convention applies. The first term on the right hand side of equation (4.15) can represent a source of turbulent kinetic energy. In the case of a one-dimensional reaction zone it has been shown (Libby and Bray, 1980: Bray et al, 1981) that, with sufficient heat release, this term dominates the production of turbulence. The analagous term in the balance for species concentrations fluctuations gives rise to a counter-gradient diffusion of concentration.

There appear to be two regions in these flows where these terms, involving the mean pressure gradient, could become important. The first is in the vicinity of the maximum width of the recirculation bubble, where the radial pressure gradient is large (see figure 2.40)

and has the same sign as that of density gradient. Because of this, the mean pressure gradient will accelerate hot products preferentially to cold reactants in this region and a counter-gradient flux will be established. The effect may be comparatively small but will act in the balance equation for turbulent kinetic energy, or that for the correlation between velocity and concentration, as an "extra rate of strain" in the terminology of Bradshaw (1971). It is known that even small extra rates of production, as are present in streamline curvature, can have large effects on the turbulent flow's structure and the term should be incorporated into any turbulence model which may be used in calculating these flows. The second region where $- \langle u_j'' \rangle \frac{\partial \langle p \rangle}{\partial x_j}$ may be important is on the centreline. Large pressure gradients occur both upstream and downstream of the free stagnation point so that it is possible that $- \langle \rho u_i'' u_j'' \rangle \partial \tilde{U}_i / \partial x_j$ and $- \langle u_j'' \rangle \frac{\partial \langle p \rangle}{\partial x_j}$ are of similar magnitude. Hence, because the first term is likely to be important, so by implication is the second.

Blockage

The result of increasing blockage is to give rise to a recirculation zone which is longer than the corresponding isothermal flow although the percentage difference in length (table 4.6) between the 25 and 50 per cent blockage discs during combustion ($\simeq$ 3 per cent) is much smaller than that which exists during isothermal flow ($\simeq$ 25 per cent). This occurs despite the large increase in the streamline angles in the plane of the trailing edge of the larger disc (see figures 4.17(a) and (c)). As for isothermal flow, the results of Winterfeld (1965) and Wright (1959) show that increasing blockage (up to 36 per cent) results in the decrease of the non-dimensional bubble length. The reason for the change in this trend with still higher blockage has

been discussed for isothermal flows in sub-section 2.4.2 and applies here as well.

The results of Durão and Whitelaw (1977) and Durão, Founti and Whitelaw (1979) represent virtually the only detailed aerodynamic measurements in the near wake of bluff body stabilised flames available. In both cases the flows were unconfined annular jets. In contrast to the results of this chapter, the recirculation length remains unchanged from that of the isothermal flow, irrespective of whether the reactants are premixed or not. An explanation of this is that, since combustion starts at the outer radius of the annular jet, the aerodynamics of the near wake involves, solely, hot gases. The flow is, in all major respects, that of a high temperature gas around the bluff body which is, therefore, similar to an isothermal inert flow. Once the flow is confined, however, there is a region of interaction between the cold (high density) flow surrounding the bubble and the hot (low density) gases within it which gives rise to a reduction in the momentum transfer process and thus increases the length of the recirculation bubble.

4.5 Summary

The following is a summary of the more important findings and conclusions of this chapter:-

1. For a wide range of equivalence ratios on either side of the stoichiometric, combustion is characterised as unstable for all three baffles. Within this range, the flame front originates upstream of the trailing edge of the baffle and, as compared with stable combustion, the sound levels emitted are higher, the recirculation lengths are shorter

and the axial velocity fluctuations are larger. Stable combustion is restricted to regions adjacent to the flame extinction limits. The width of the unstable range is affected by the magnitude of the annular bulk velocity.

2. Combustion-induced oscillations are always present, for all three baffles, and two frequencies are associated with two separate, standing acoustic quarter waves. The transition to unstable combustion occurs because of the improved phasing between the heat release and pressure fluctuations corresponding to the shorter acoustic wavelength. The improvement is brought about by the alteration in the flame's shape with changes in the equivalence ratio.

3. During fuel-lean (ϕ = 0.69), stable operation:-

   (a) the influence of changing the baffle's forebody shape from a disc to a cone, both of 25 per cent blockage is to:-

      (i) leave the recirculation length unaltered

      (ii) leave the maximum reversed velocity unaltered

      (iii) reduce the maximum measured value of $\langle u^2 \rangle$ by 18 per cent

   (b) the influence of increasing the area blockage ratio

of the disc from 25 to 50 per cent is to:-

(i) increase the recirculation bubble length (expressed in baffle diameters) by about 3 per cent

(ii) increase the maximum dimensionless velocity by 12 per cent

(iii) increase the maximum measured dimensionless value of $\langle u^2 \rangle$ by 95 per cent.

4. During fuel-lean, stable combustion the flow is similar to the corresponding isothermal flow. Quantitatively, the influence of combustion is to:-

(a) increase the magnitude of the radial velocity in the plane of the trailing edge of the baffle.

(b) increase the recirculation bubble length by 38 and 14 per cent for the 25 and 50 per cent blockage discs respectively.

(c) increase the maximum reversed velocity by 40 and 36 per cent for the 25 and 50 per cent blockage discs respectively.

(d) increase the values of $\langle u^2 \rangle$ within the free shear layer surrounding the recirculation zone.

5. (a) The increase in the recirculation length, noted in 4, is attributed both to the modification in the magnitude of the radial velocity at the trailing edge of the baffle and to the reduction in momentum transfer between the cold reactants and the hot gases within the recirculation zone.

(b) The increase in $\langle u^2 \rangle$ within the free shear layer, noted in 4, is produced by the increase in the rate of shear strain.

6. During fuel-lean, stable combustion, the mean flame widths decrease towards the rear stagnation point, where these are about 0.3 R and 0.6 R for the 25 and 50 per cent blockage discs respectively. The thin flame approximation suggests that even at the end of the recirculation bubble, unburnt reactants are present for up to one-fifth of the time.

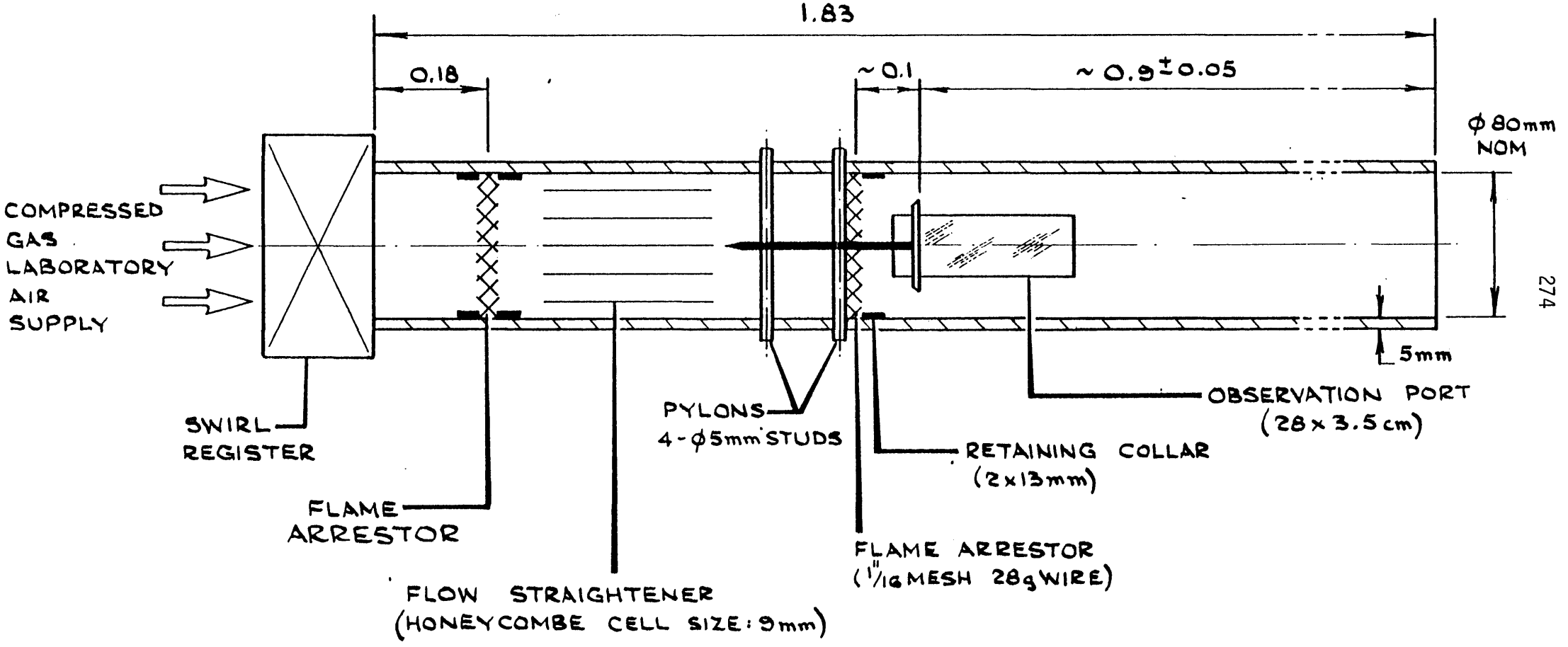

Figure 4.1 Diagram of combustion chamber

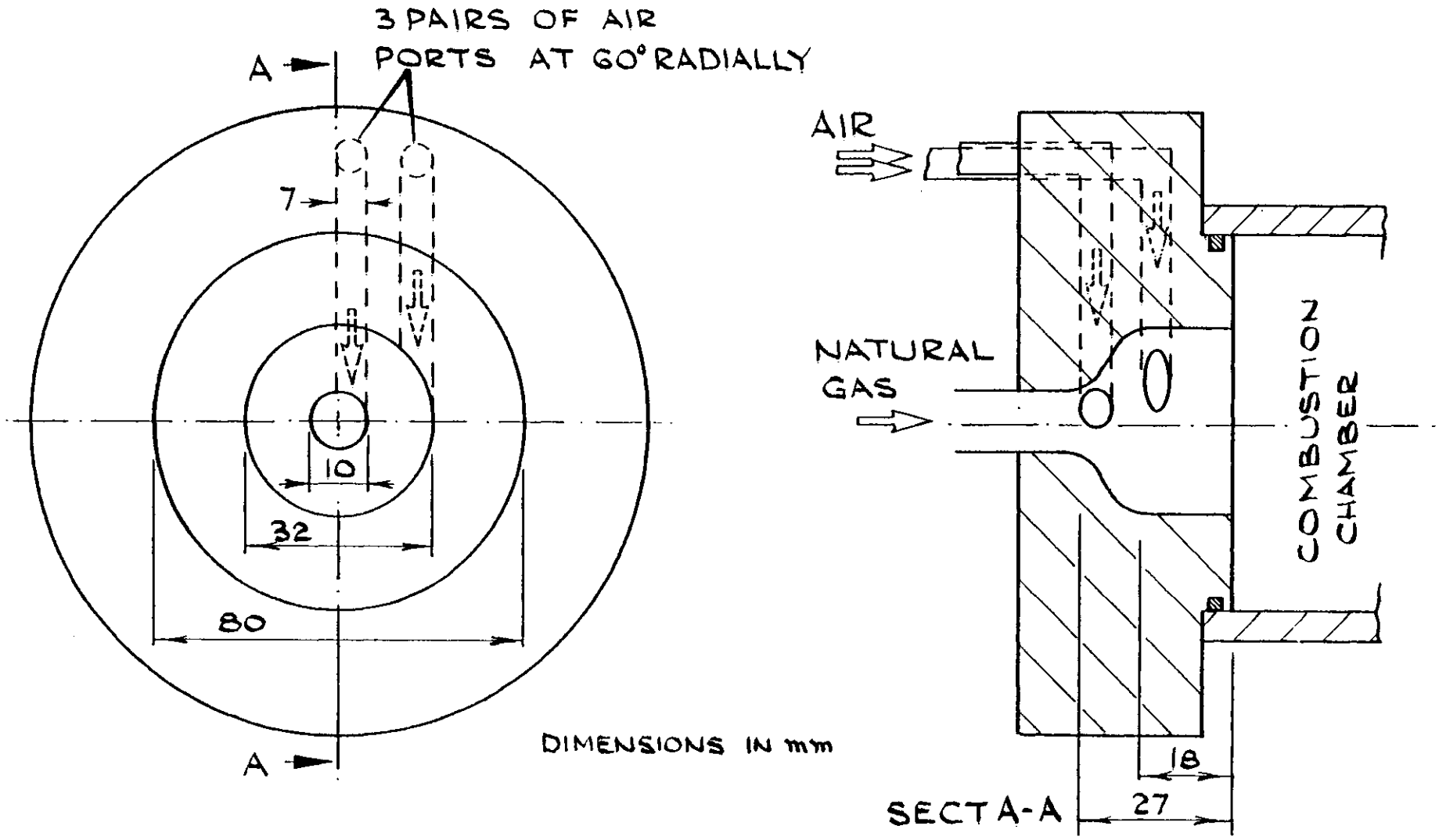

Figure 4.2 Diagram of swirl register (not to scale)

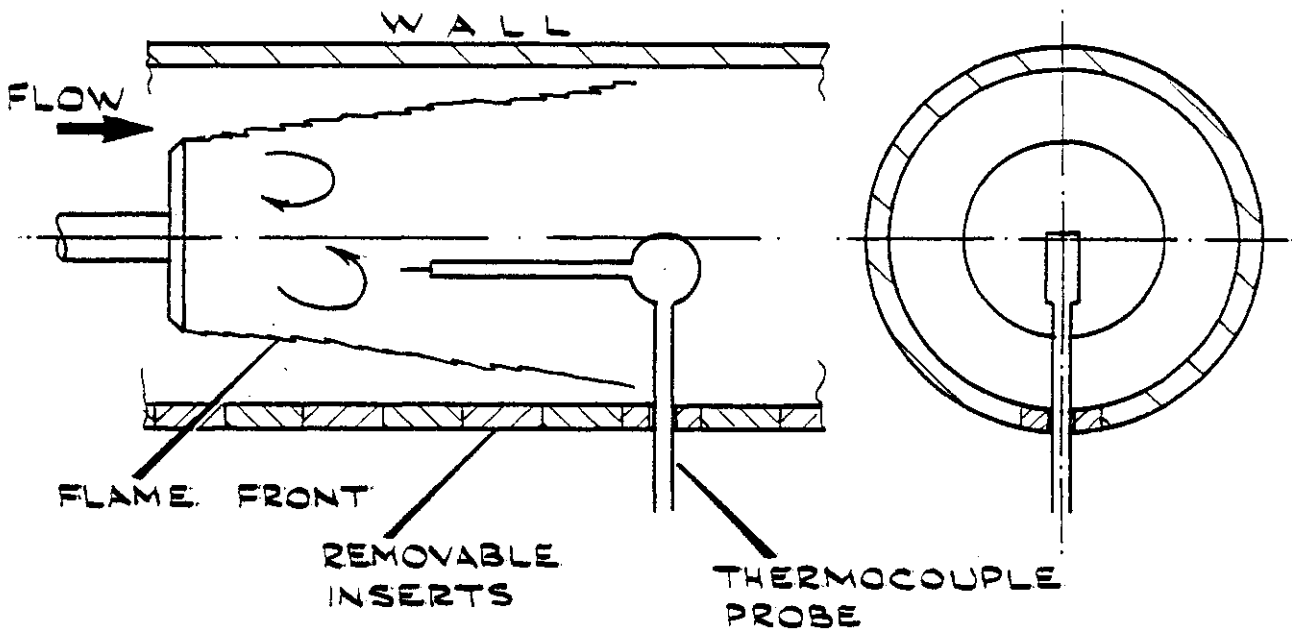

Figure 4.3(a) Diagram of thermocouple probe within combustor

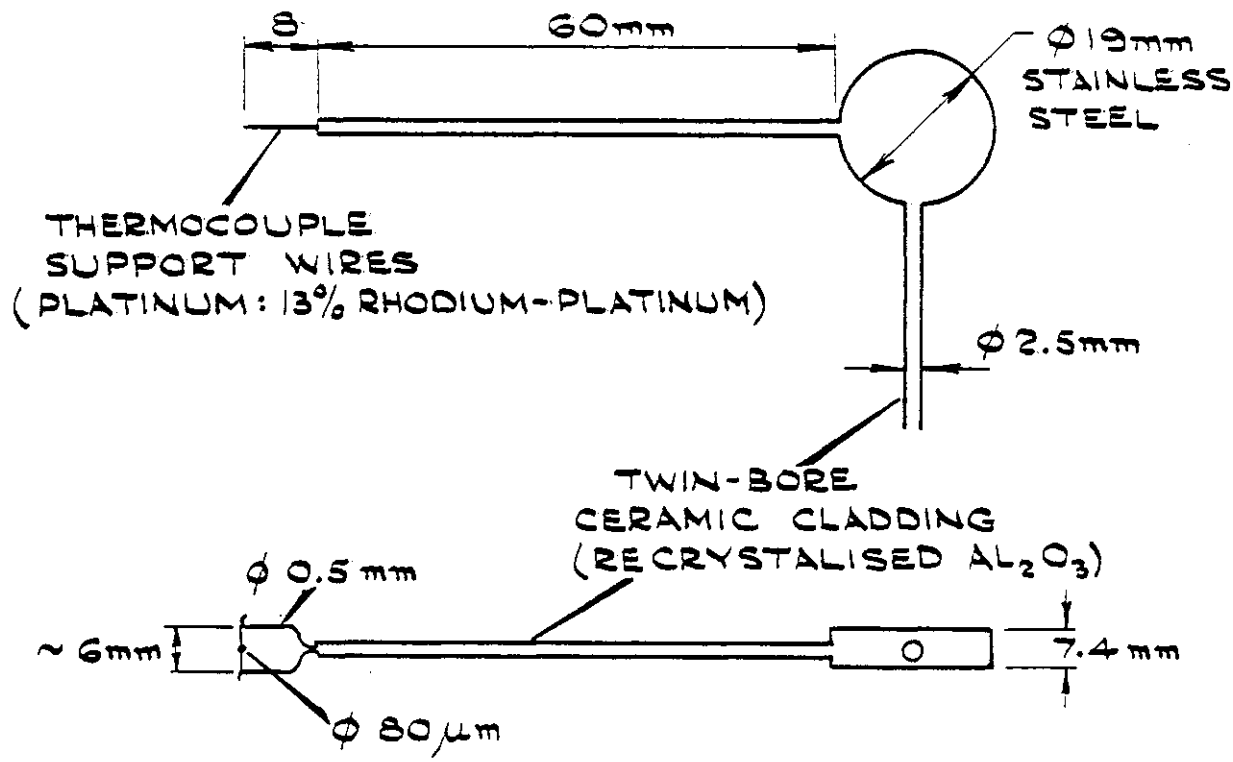

Figure 4.3(b) Diagram of thermocouple probe

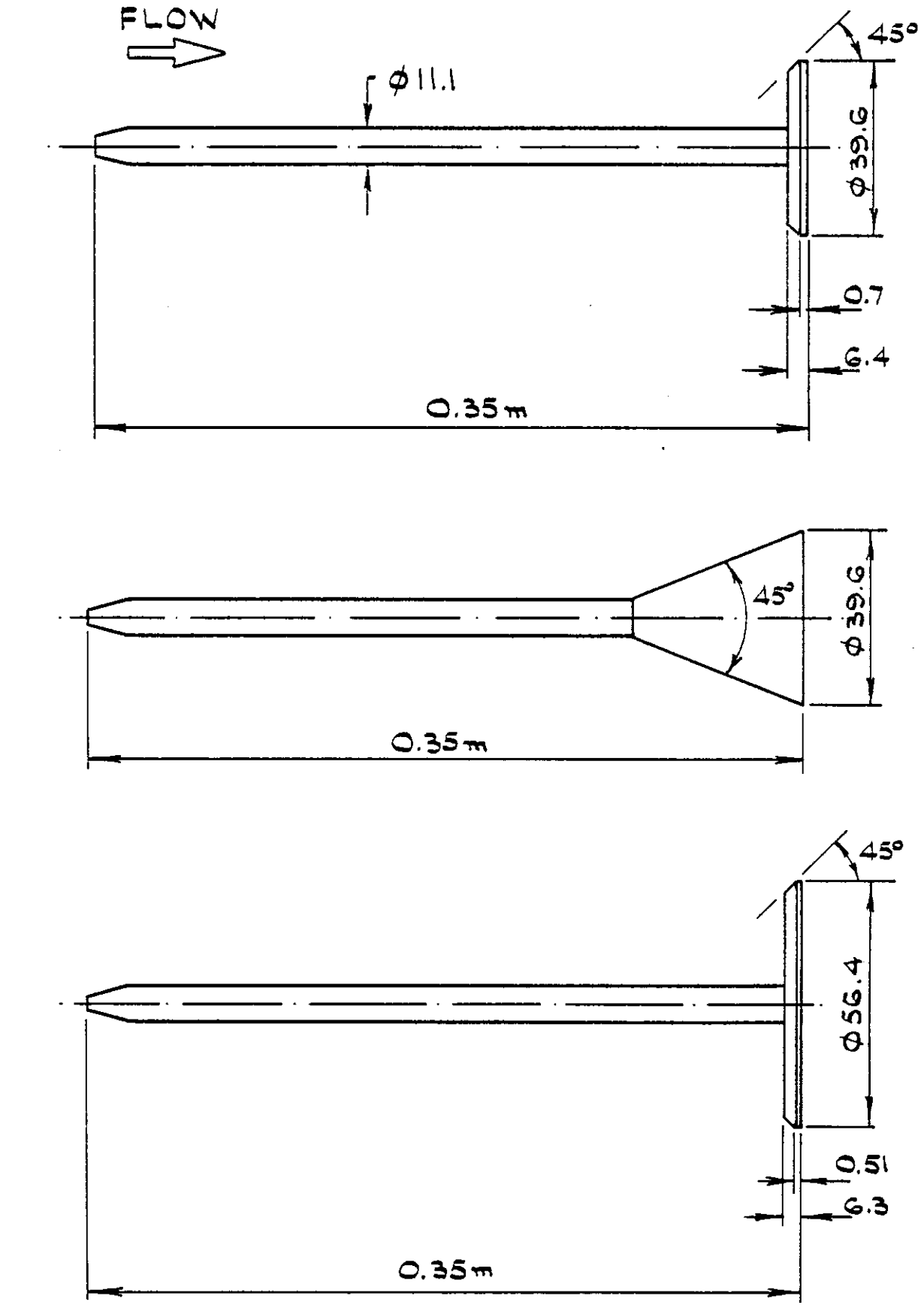

Figure 4.4 Shapes and dimensions of baffles

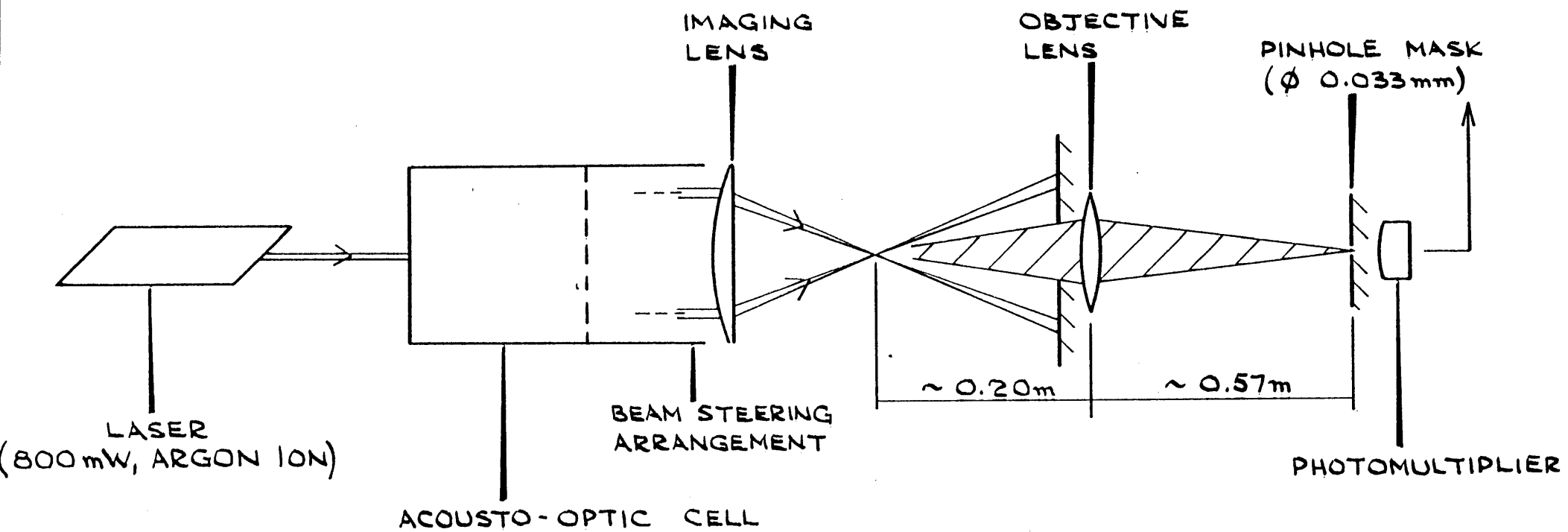

Figure 4.5 Optical arrangement of laser-Doppler velocimeter

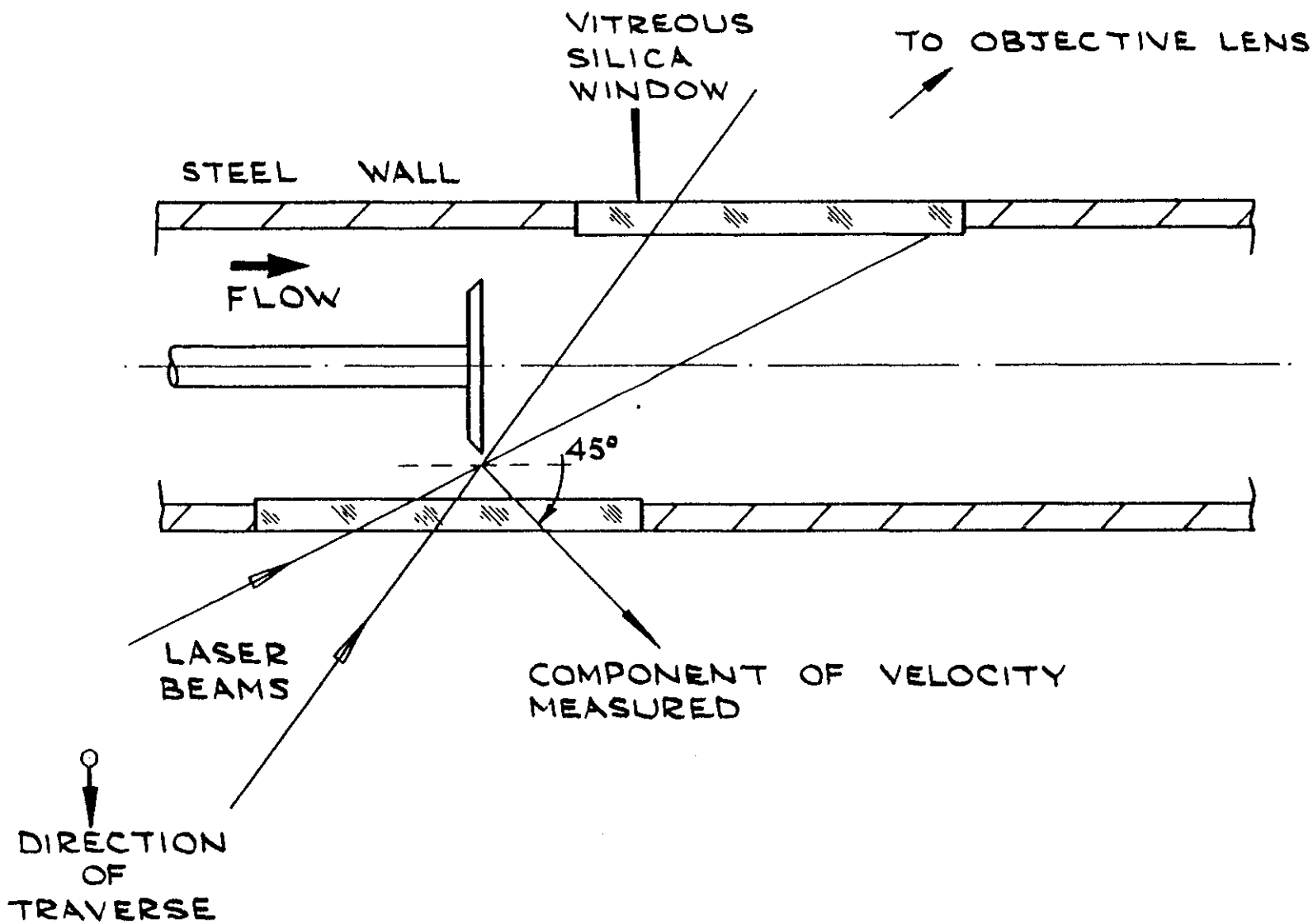

Figure 4.6 Beam attitude and direction of traverse for measurement of resultant velocity at 45^0 to axis of chamber

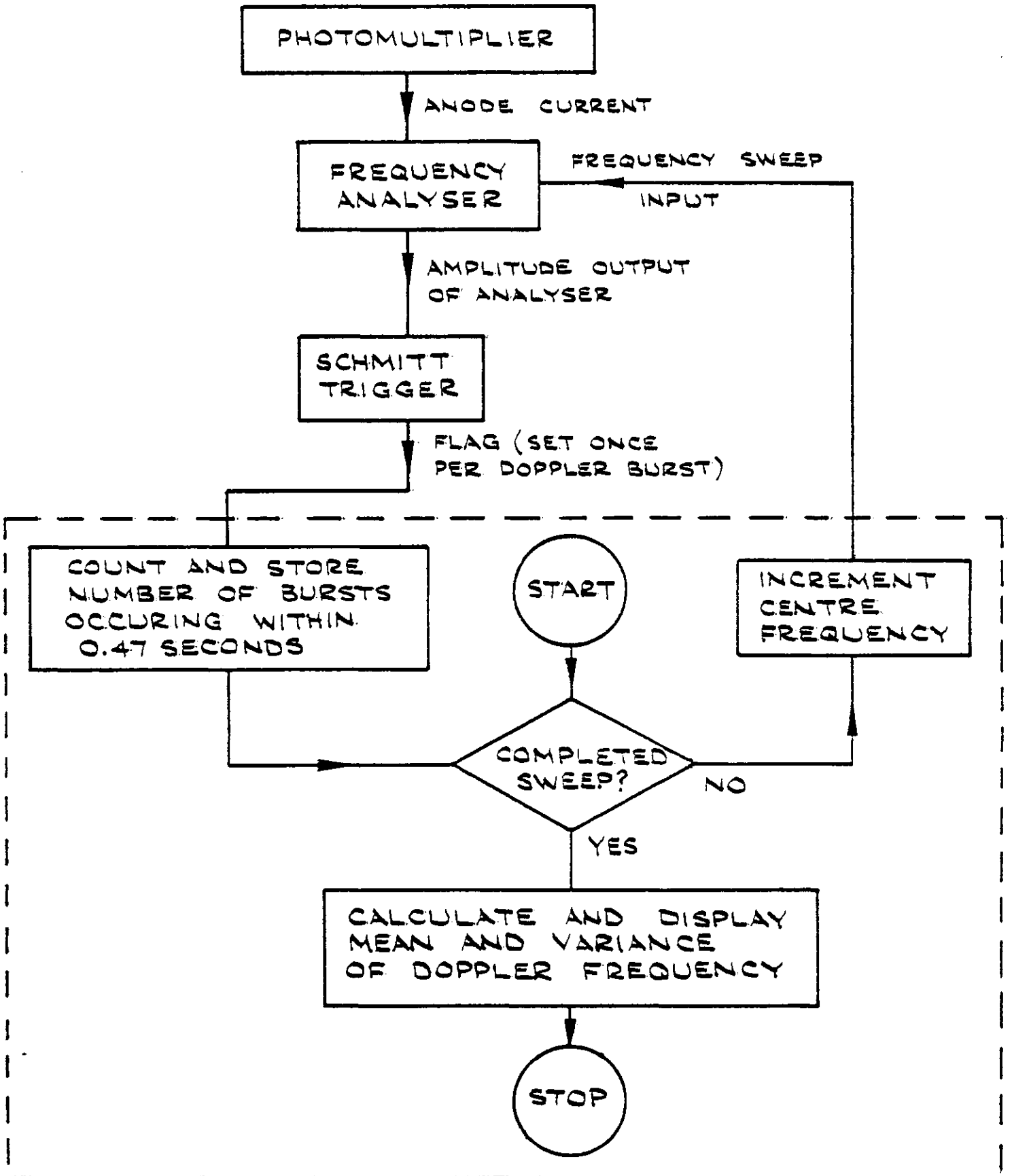

Figure 4.7 Block diagram of Doppler signal processing arrangement

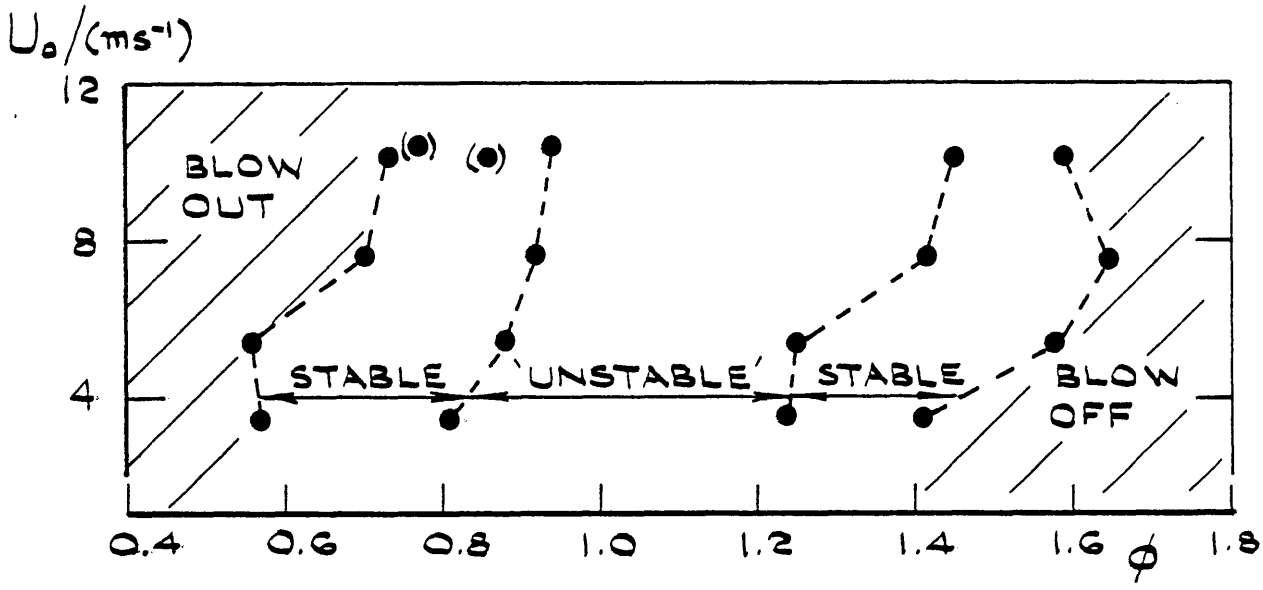

(a) Disc, 25% blockage

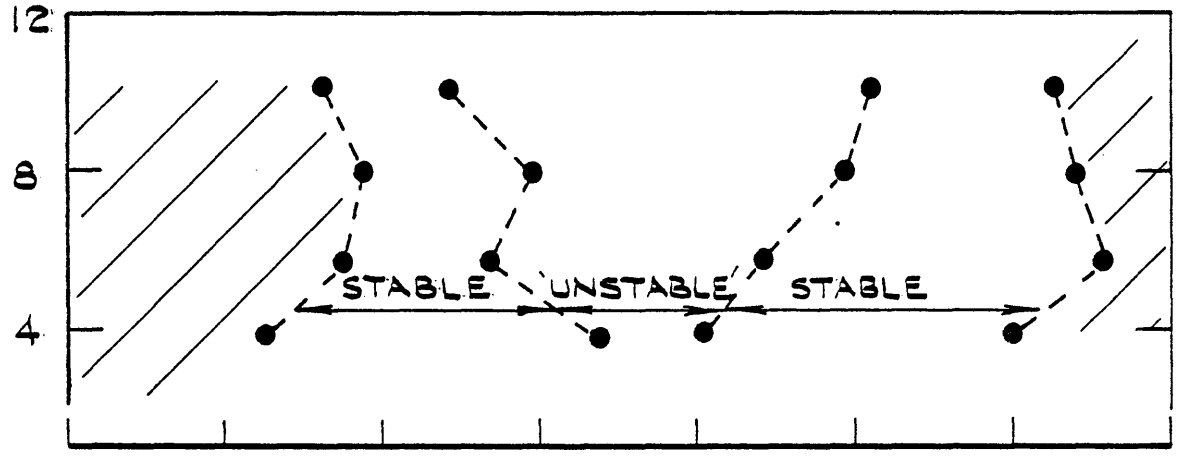

(b) Cone, 25% blockage

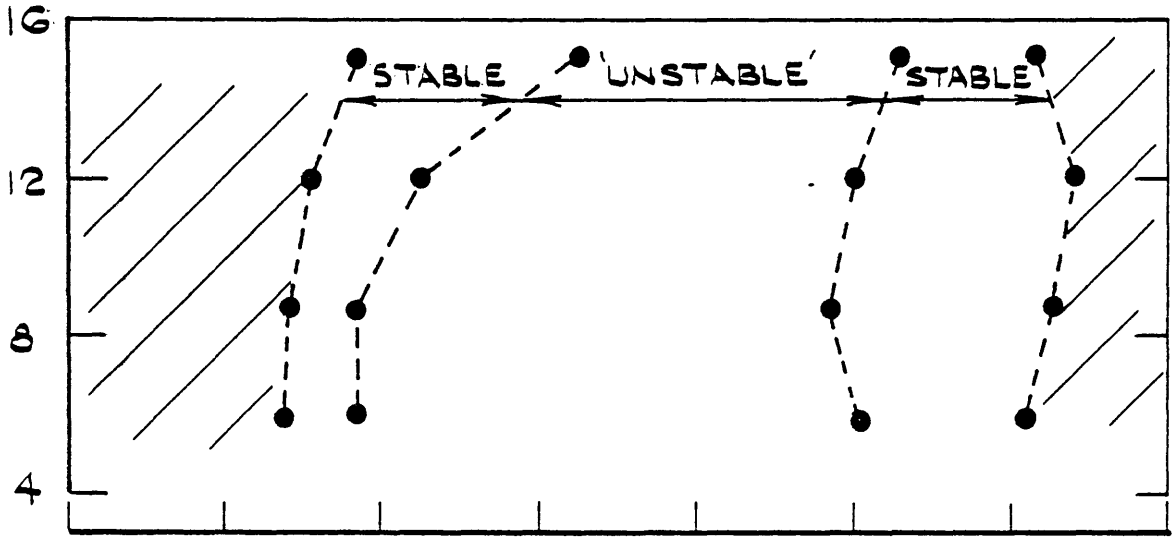

(c) Disc, 50% blockage

Figure 4.8 Flame extinction data with U_o as parameter

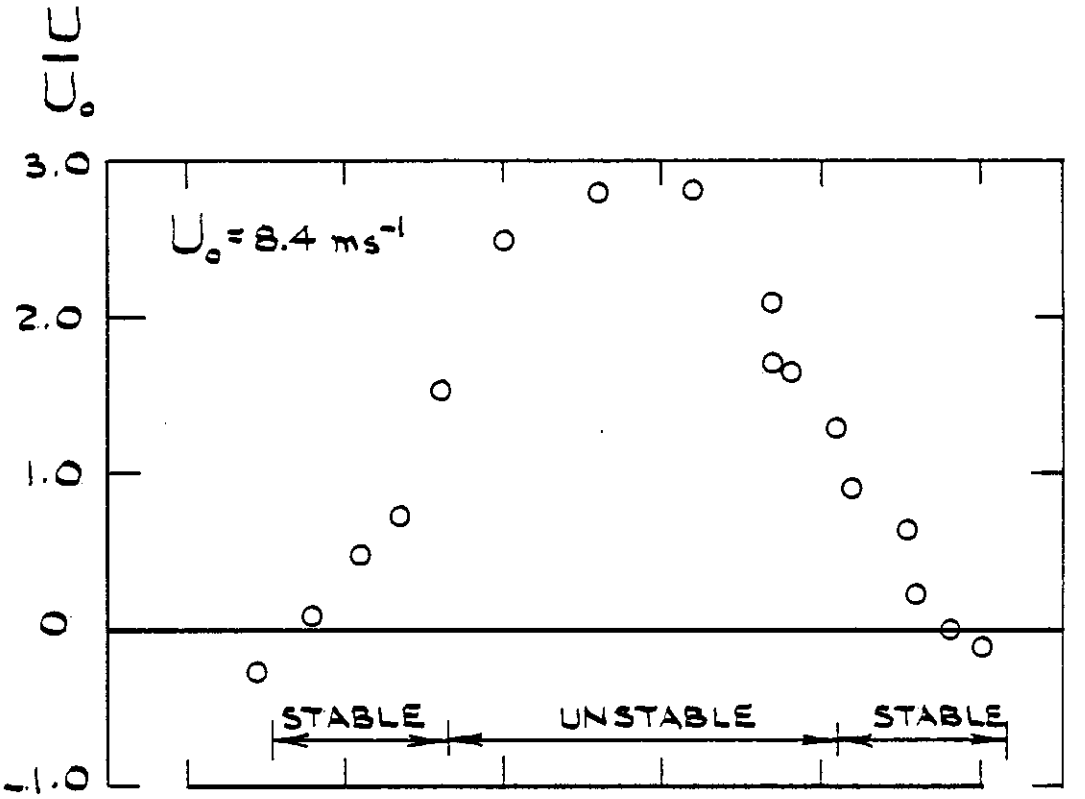

Figure 4.9 Disc, 25% blockage: mean velocity as a function of equivalence ratio on centreline; x = 1.63 R

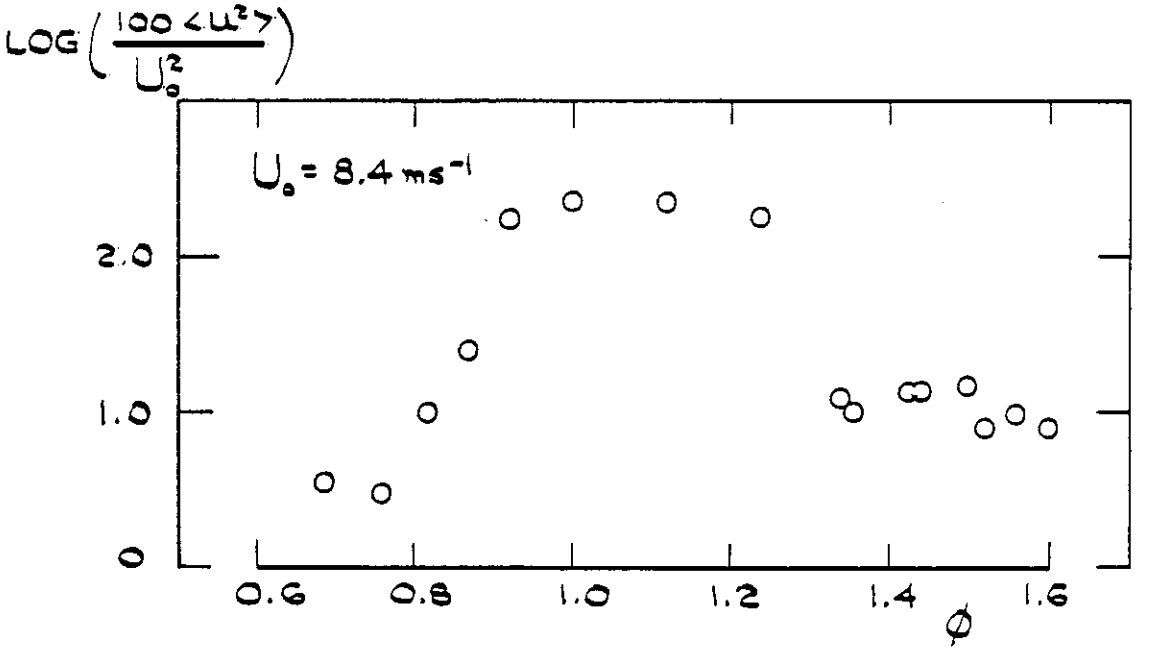

Figure 4.10 Disc, 25% blockage: variance of velocity as a function of equivalence ratio on centreline; x = 1.63 R

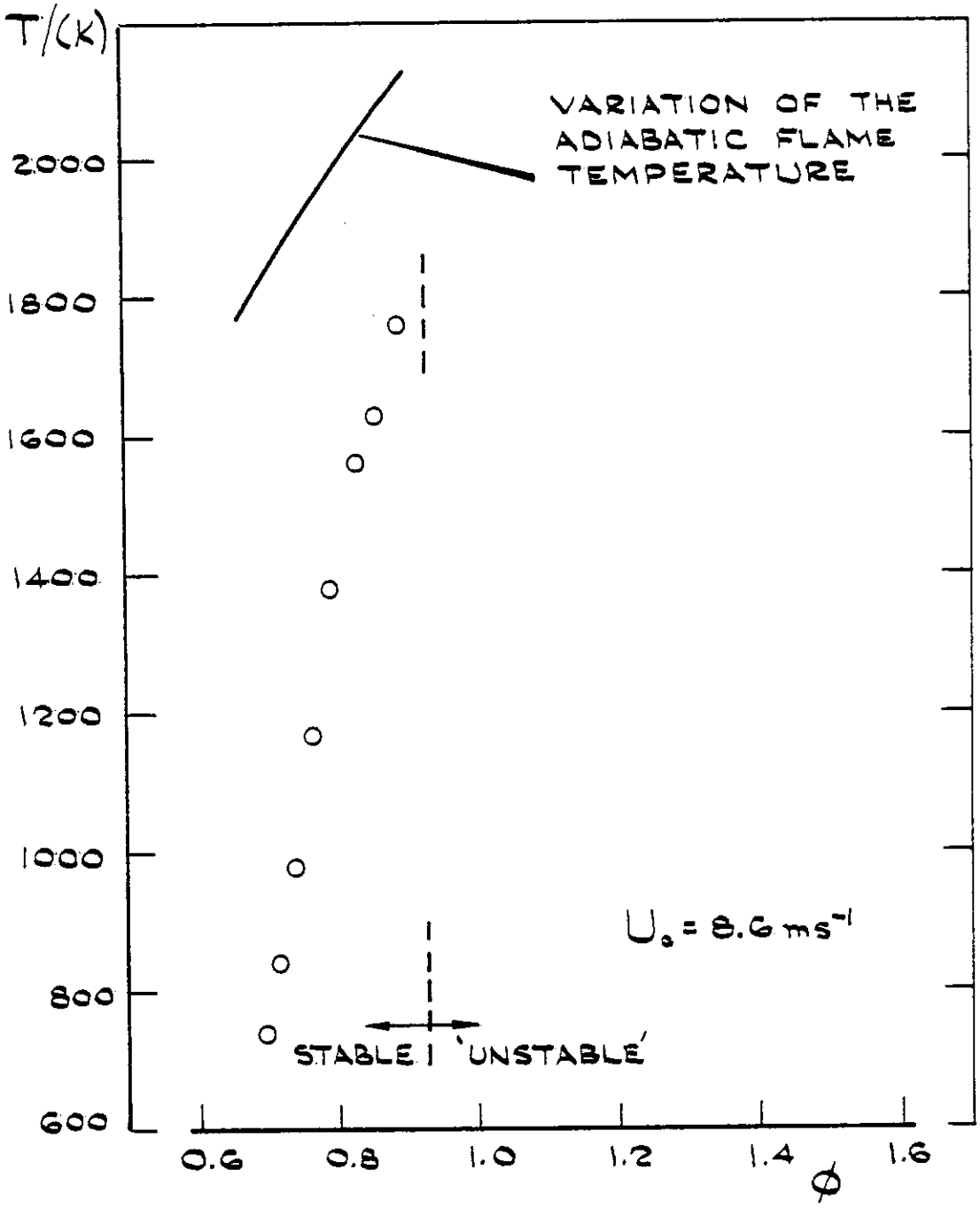

Figure 4.11 Disc, 25% blockage: mean temperature as a function of equivalence ratio; (x = 3.13 R, r = 0.63 R)

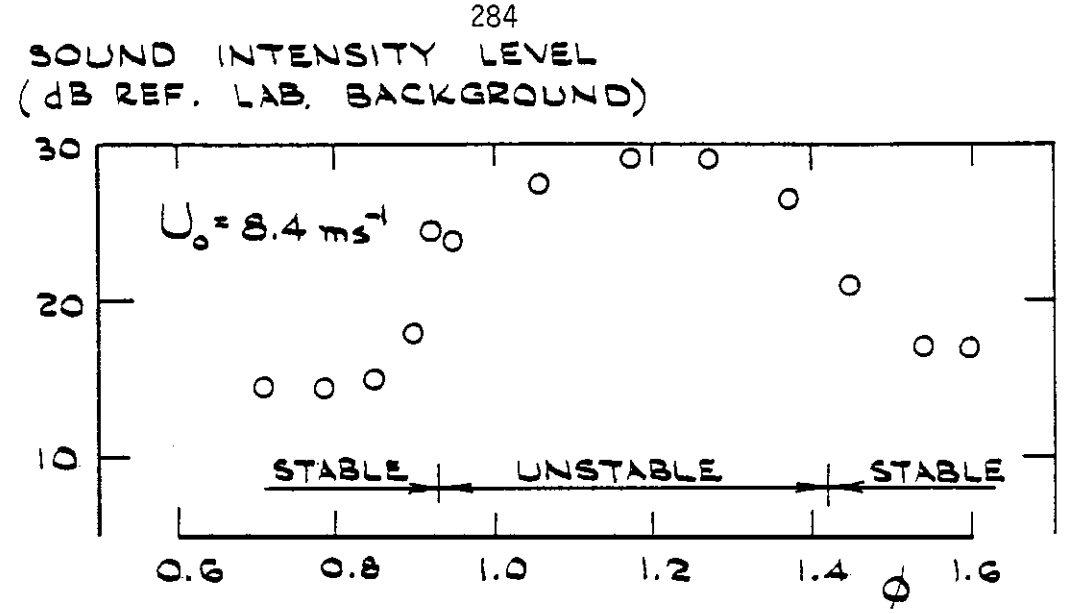

(a) Disc, 25% blockage

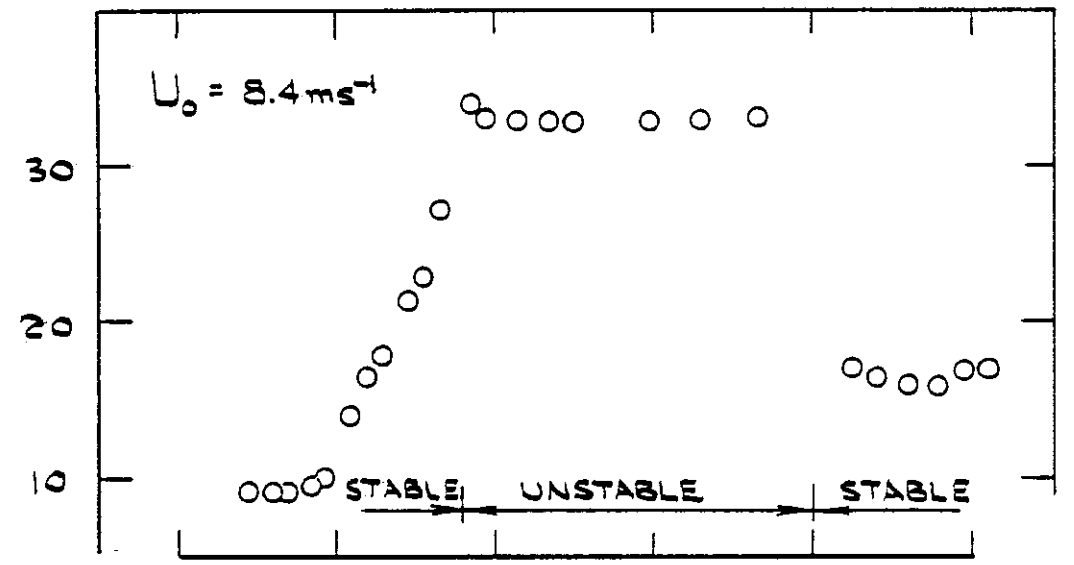

(b) Cone, 25% blockage

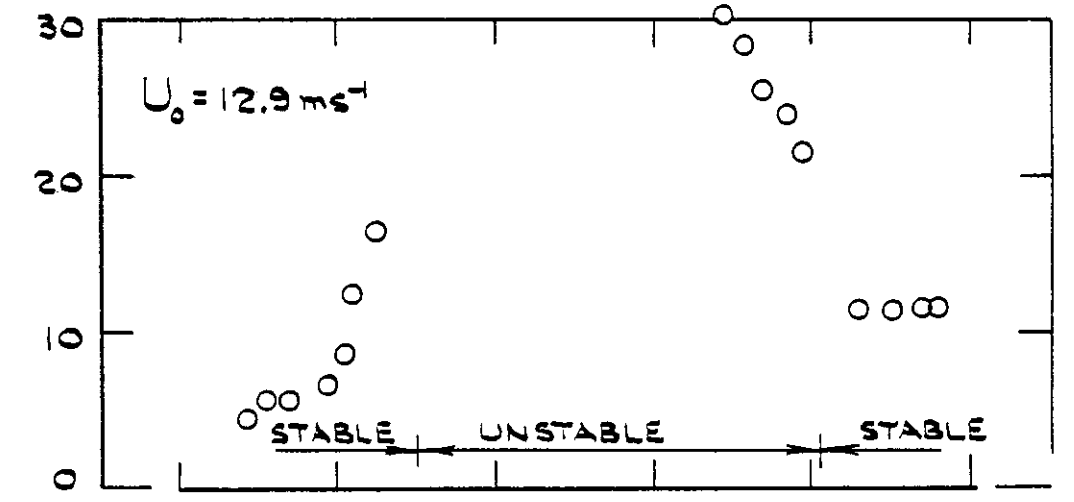

(c) Disc, 50% blockage

Figure 4.12 Sound intensity level as a function of equivalence ratio, ϕ

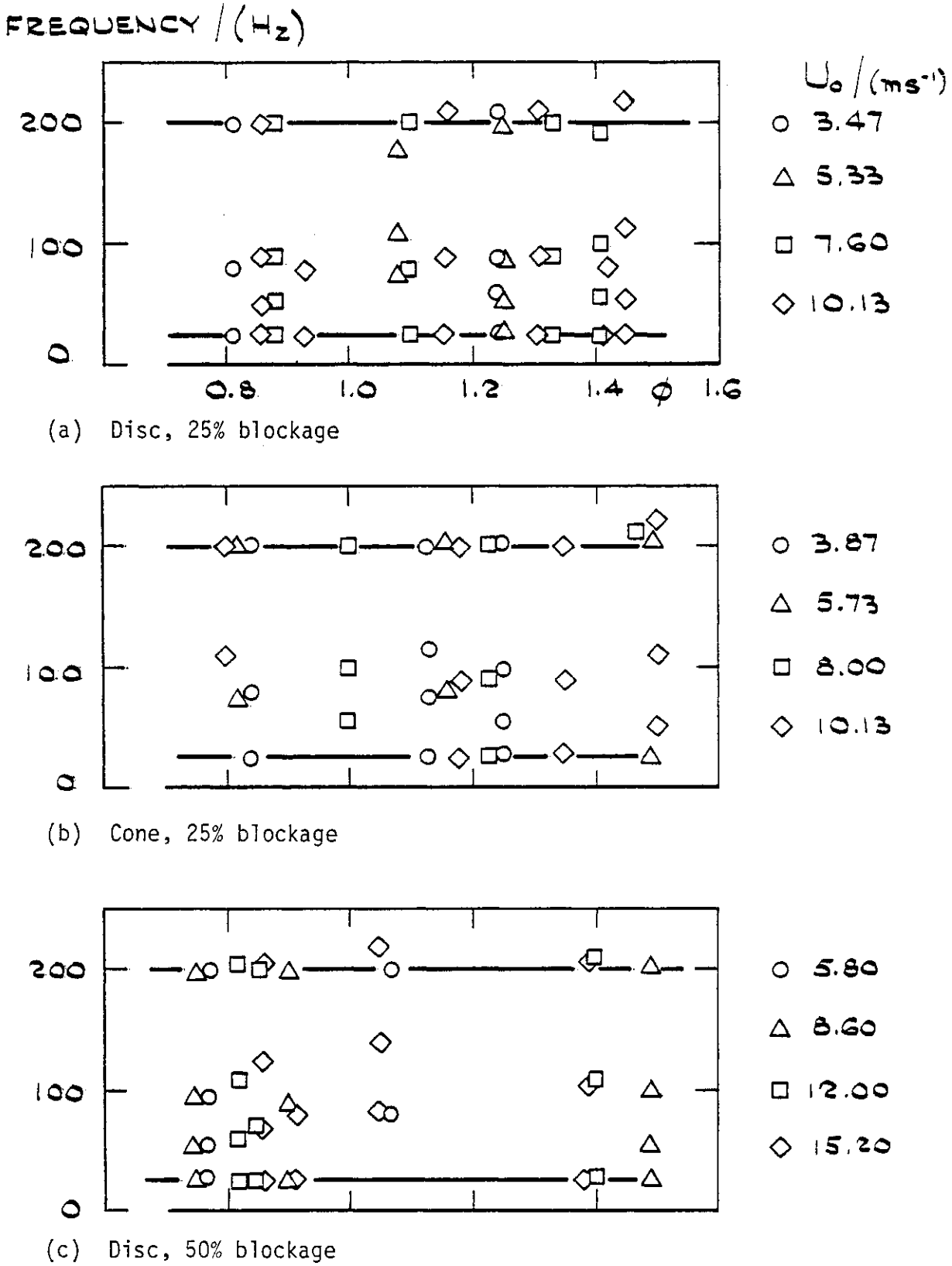

Figure 4.13 Frequency of amplitude peaks in sound spectrogram as function of equivalence ratio, with U_o as parameter

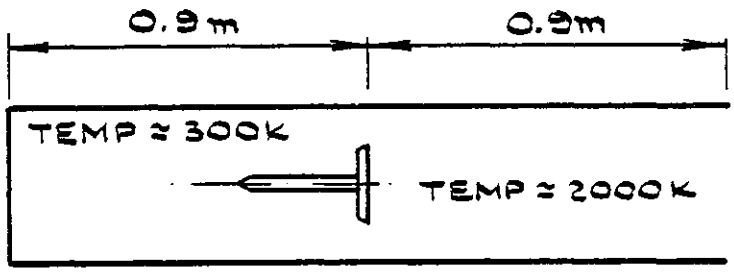

(a) Axial length of combustion chamber drawn to scale

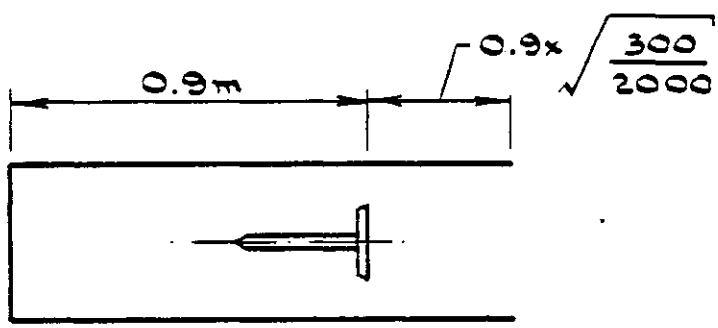

(b) Combustion chamber corrected for increased velocity of sound in hot gases

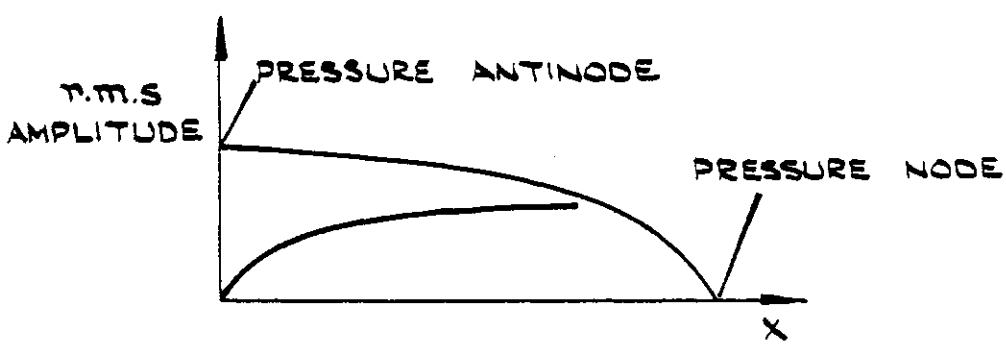

(c) Postulated pressure amplitudes for two acoustic standing quarter-waves

Figure 4.14 Postulated standing pressure waves (quarter-wave tube)

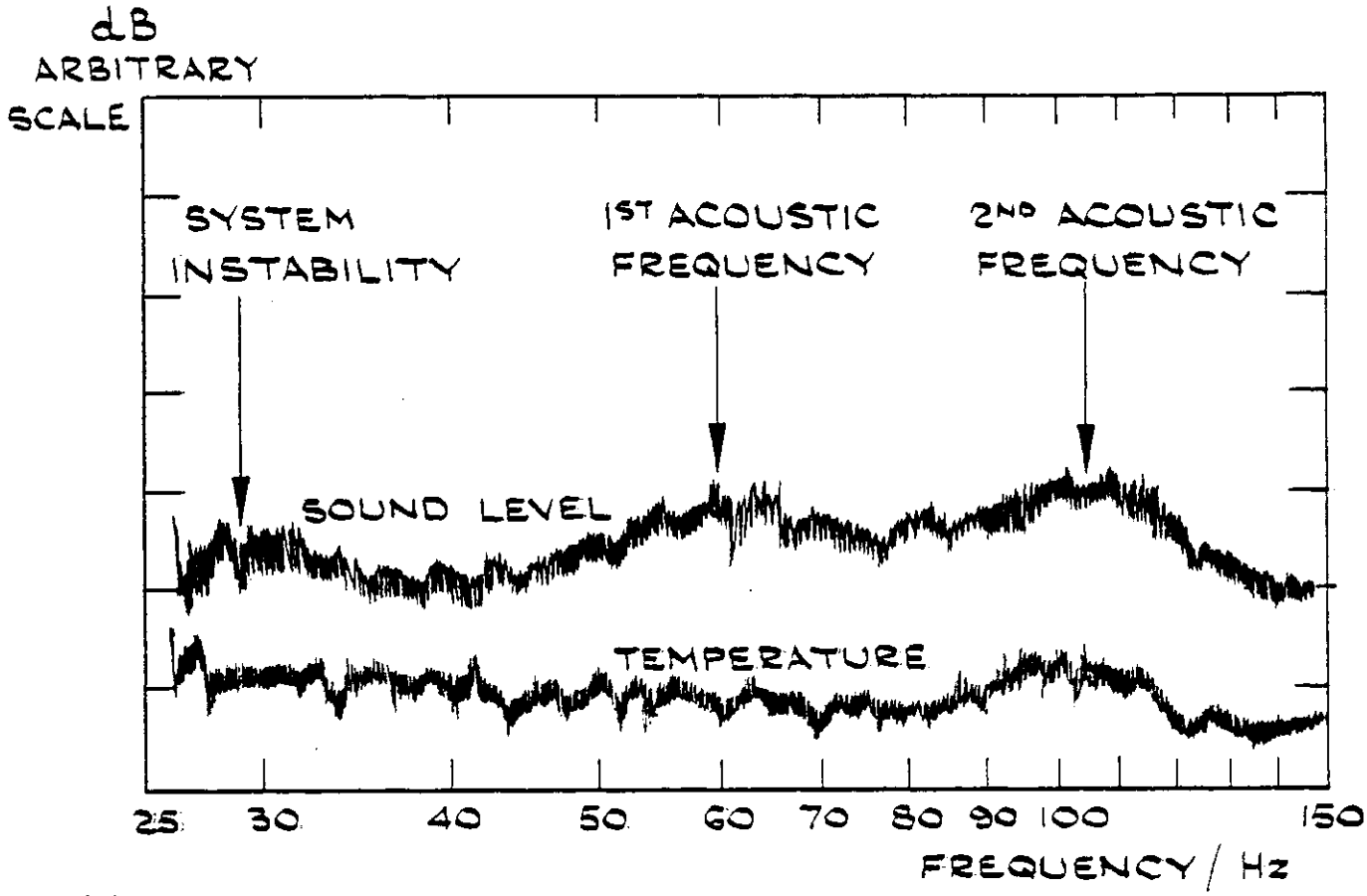

(a) Equivalence ratio is 0.86; U_o = 8.57 m/s

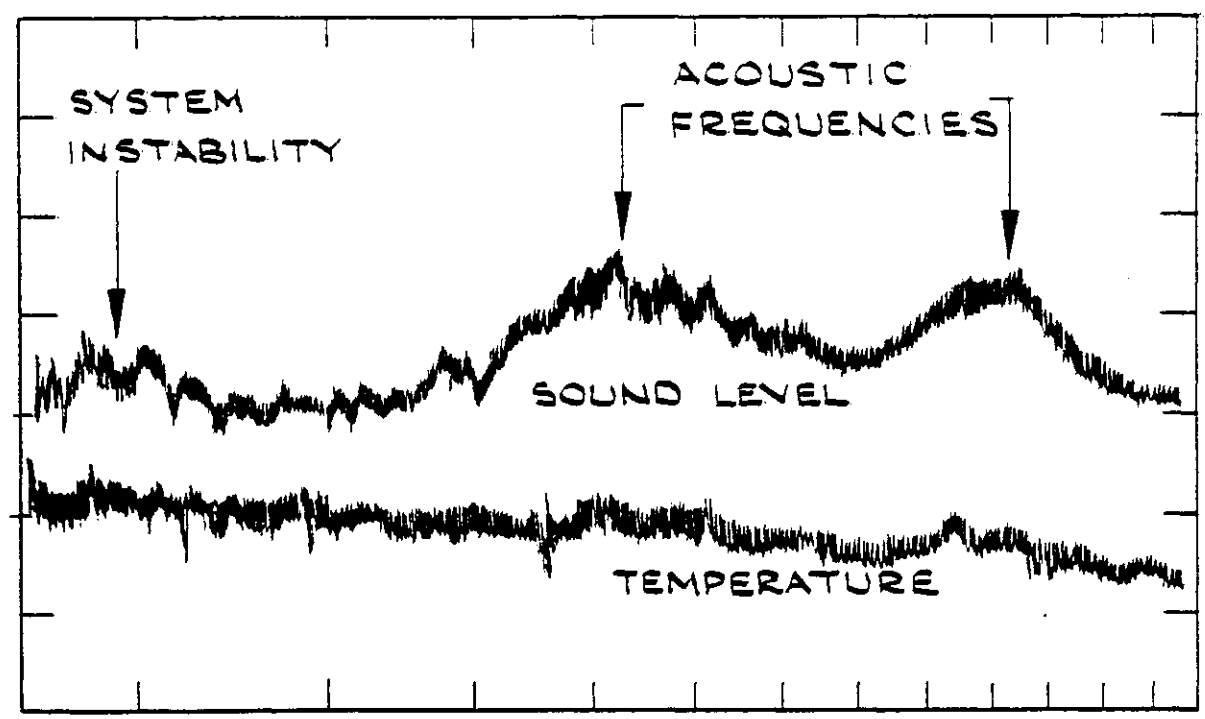

(b) Equivalence ratio is 0.89; U_o = 8.57 m/s

Figure 4.15 Disc, 25% blockage: spectrograms of sound level and temperature fluctuations

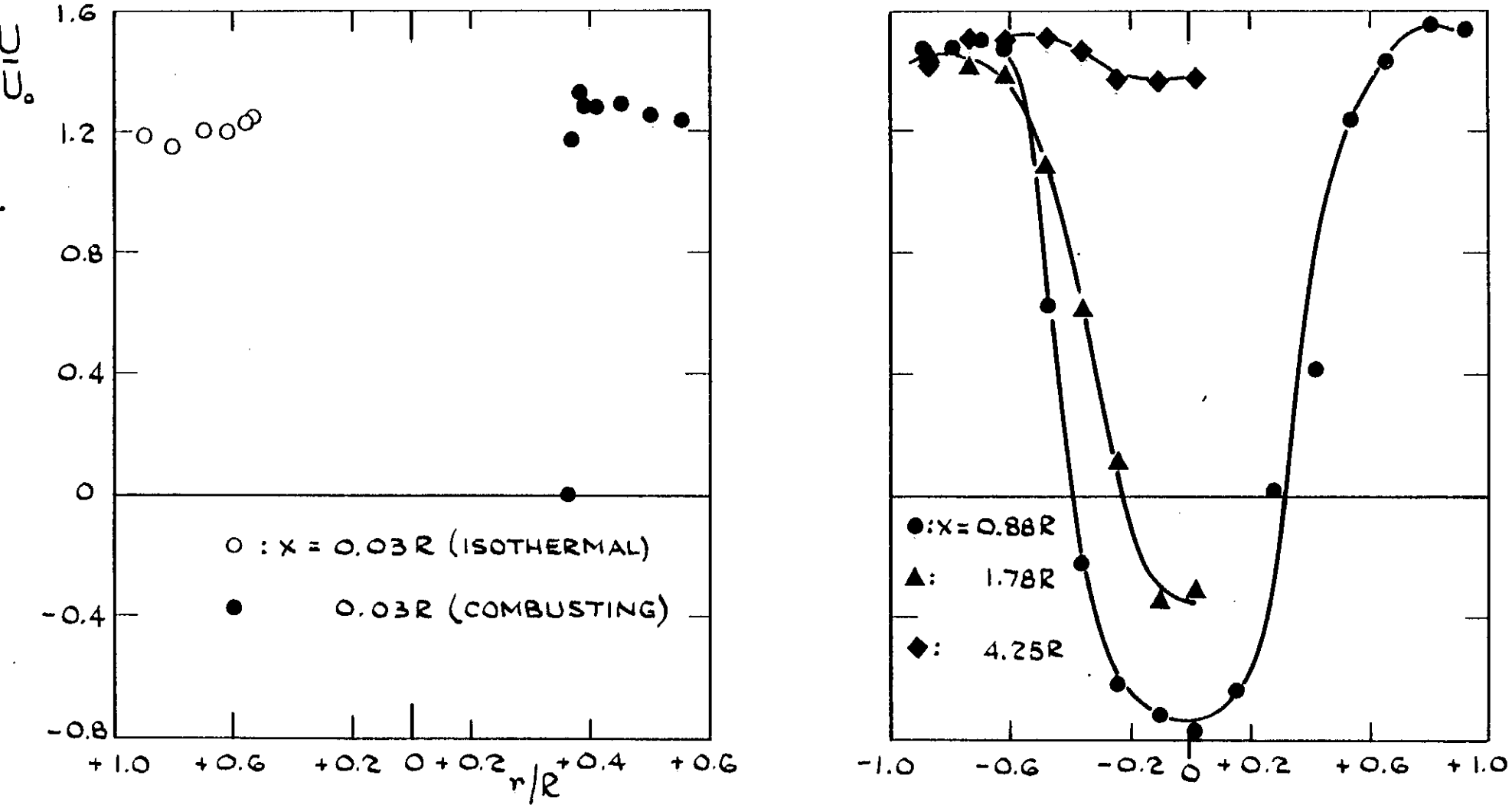

Figure 4.16 Disc, 25% blockage: radial profiles of axial velocity at successive axial stations. Equivalence ratio is 0.69; U_o = 8.7 m/s

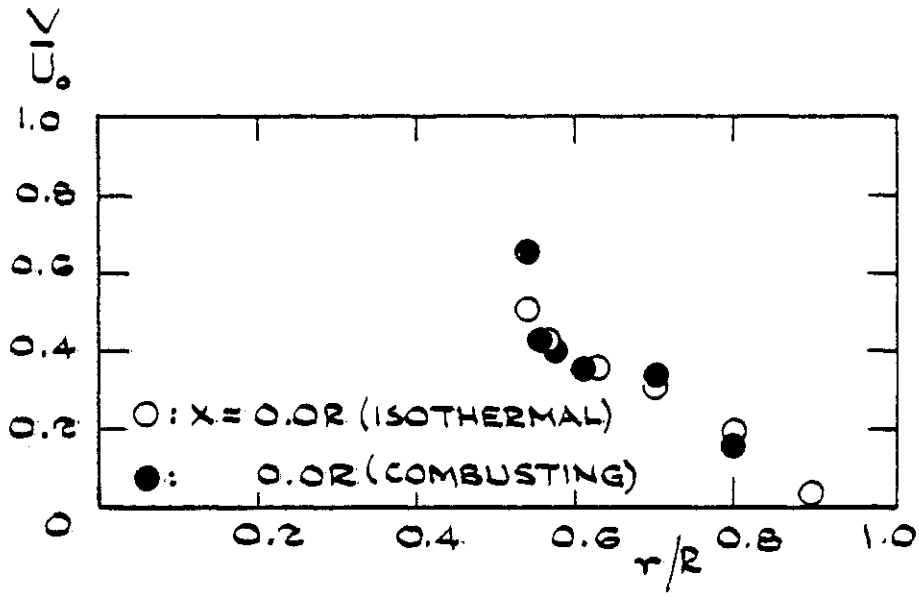

(a) Disc, 25% blockage, U_0 = 8.7 m/s. Equivalence ratio is 0.69

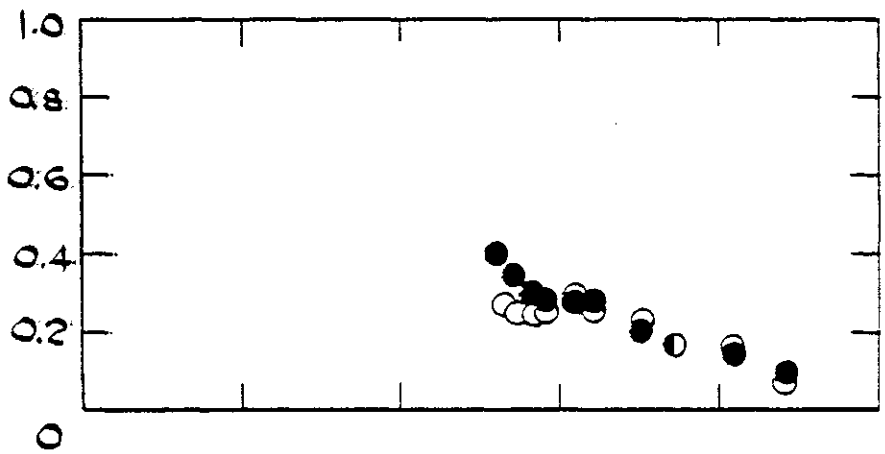

(b) Cone, 25% blockage, U_0 = 8.7 m/s. Equivalence ratio is 0.68

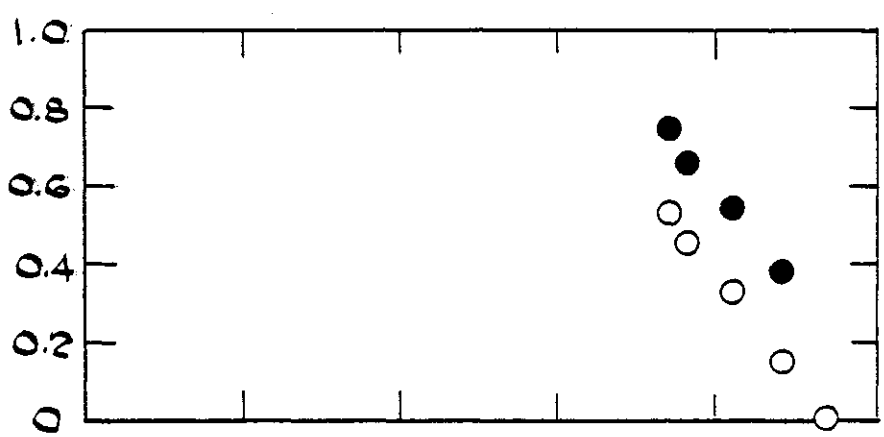

(c) Disc, 50% blockage, U_0 = 12.9 m/s. Equivalence ratio is 0.70

Figure 4.17 Radial profiles of radial velocity at x = 0

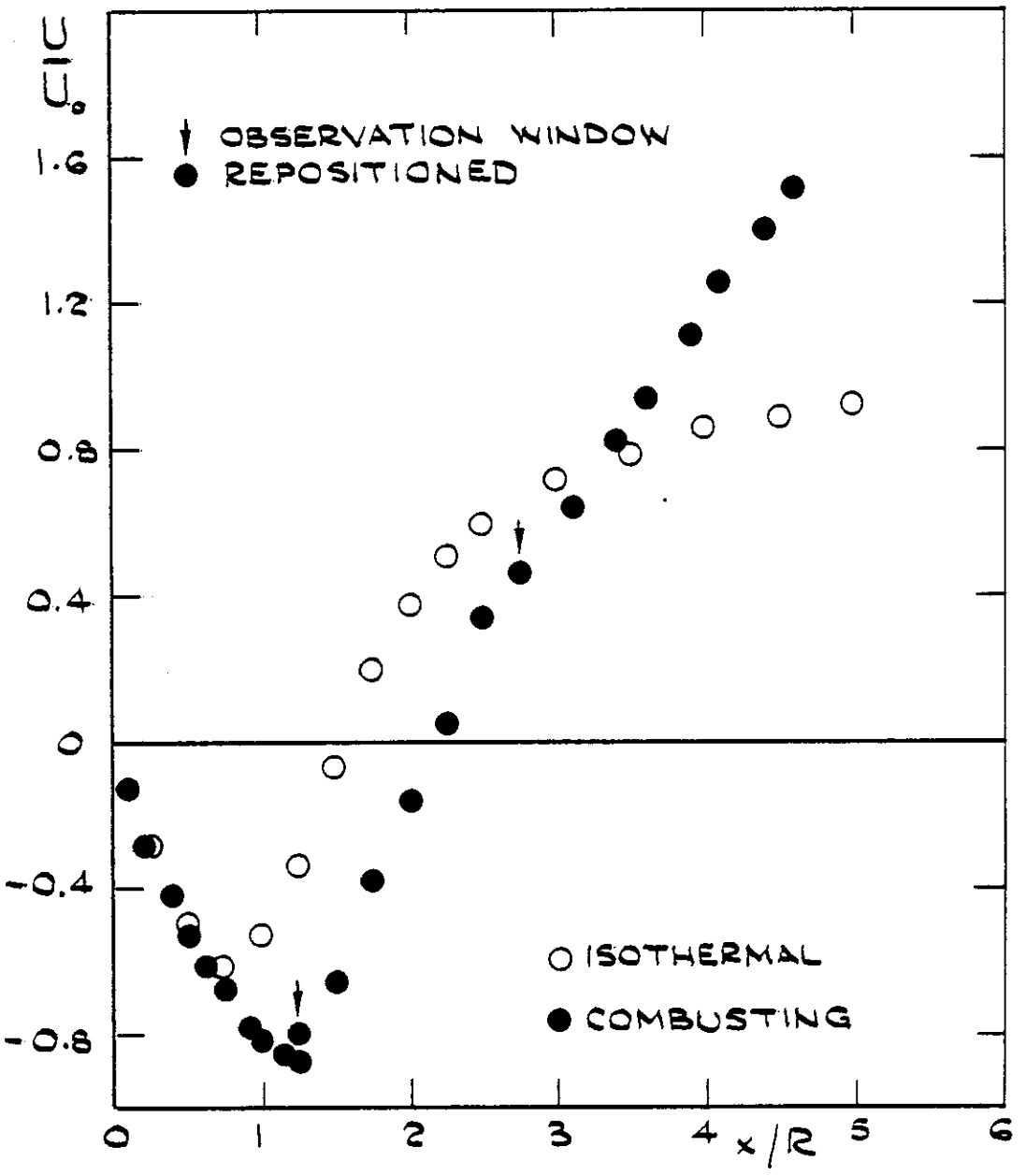

Figure 4.18 Disc, 25% blockage: centreline profile of axial velocity. Equivalence ratio is 0.69.

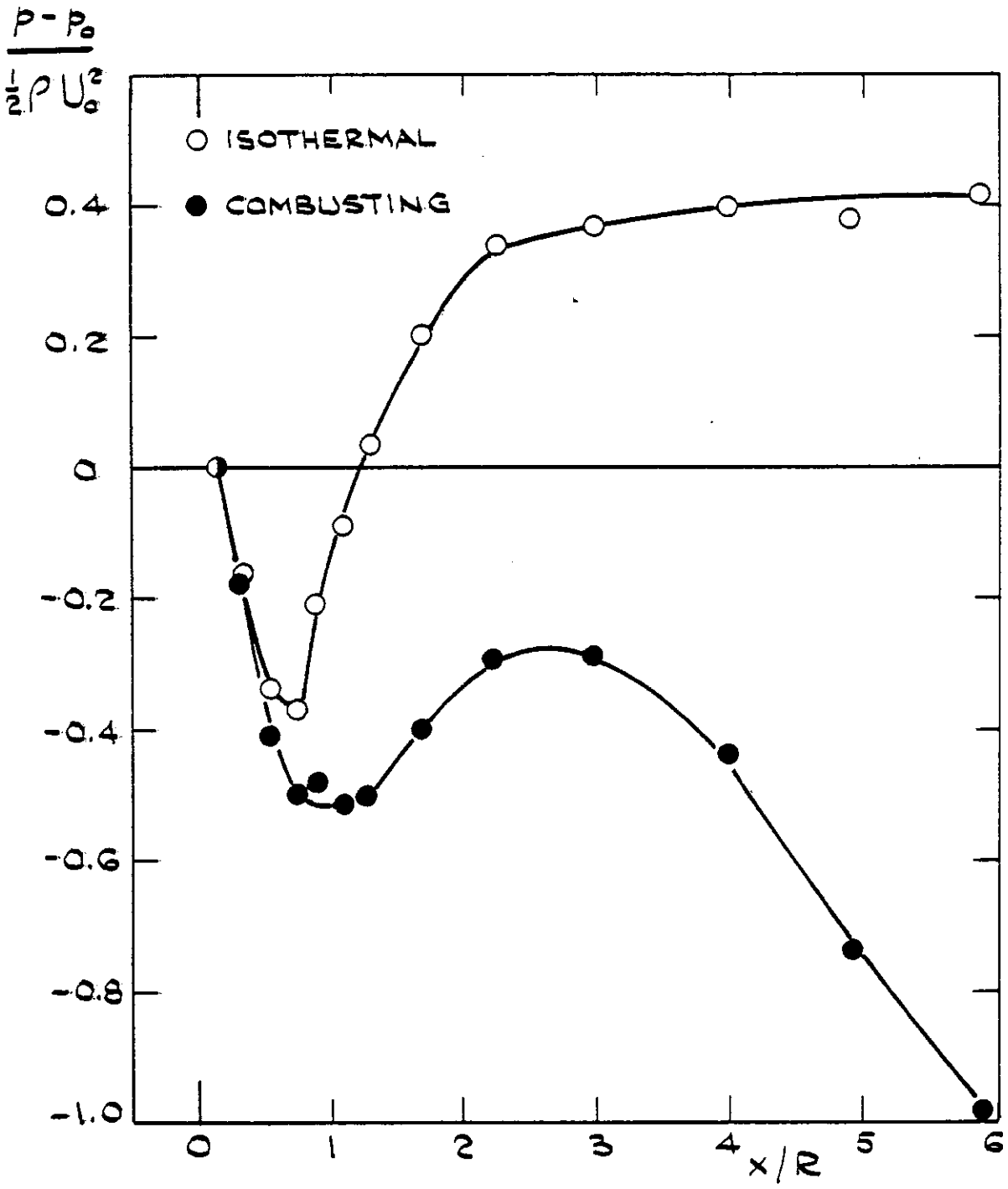

Figure 4.19 Disc, 25% blockage: axial variation of wall pressure coefficient. Equivalence ratio is 0.69.

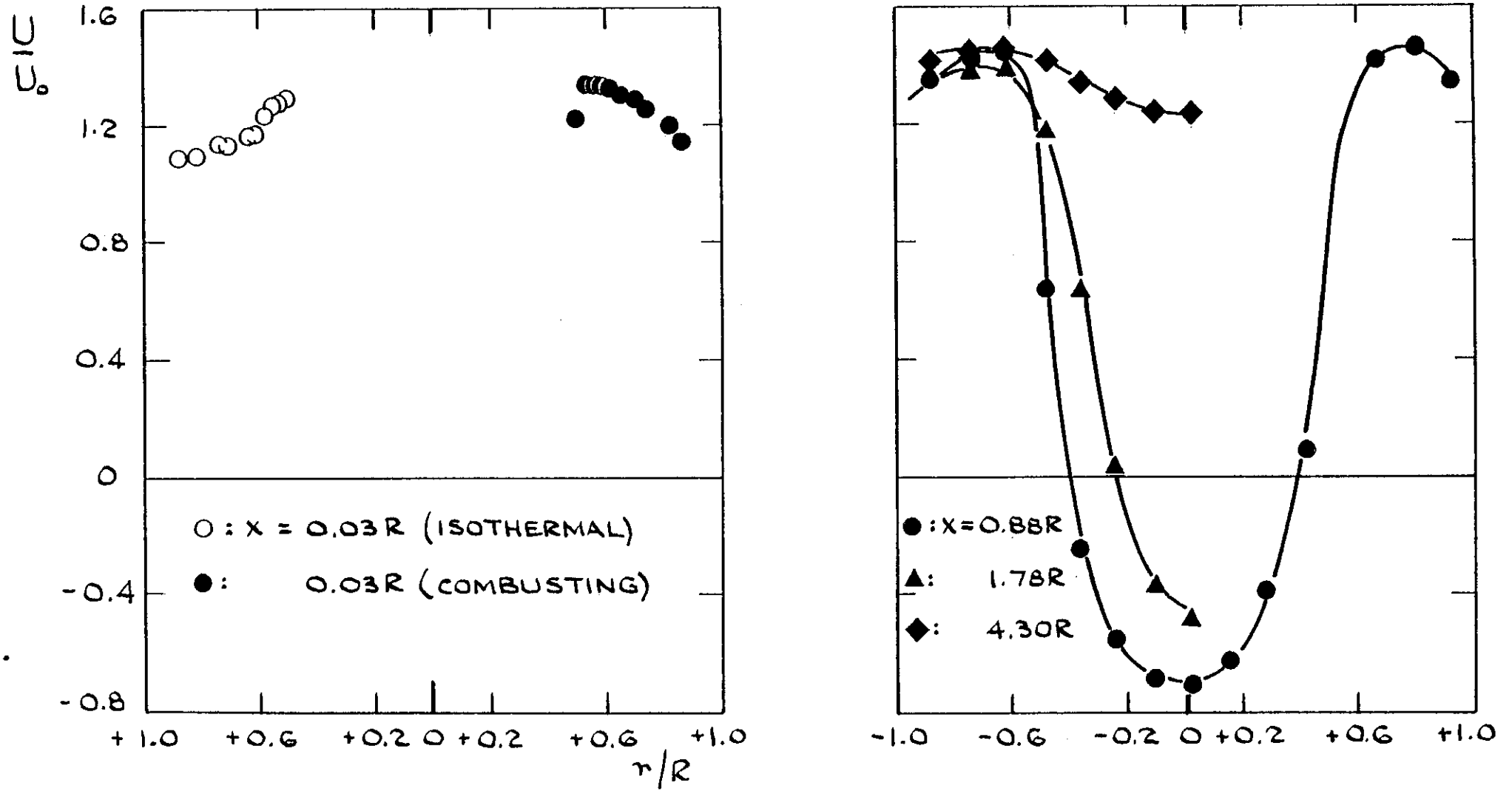

Figure 4.20 Cone, 25% blockage: radial profiles of axial velocity at successive axial stations. Equivalence ratio is 0.69; U_0 = 8.7 m/s

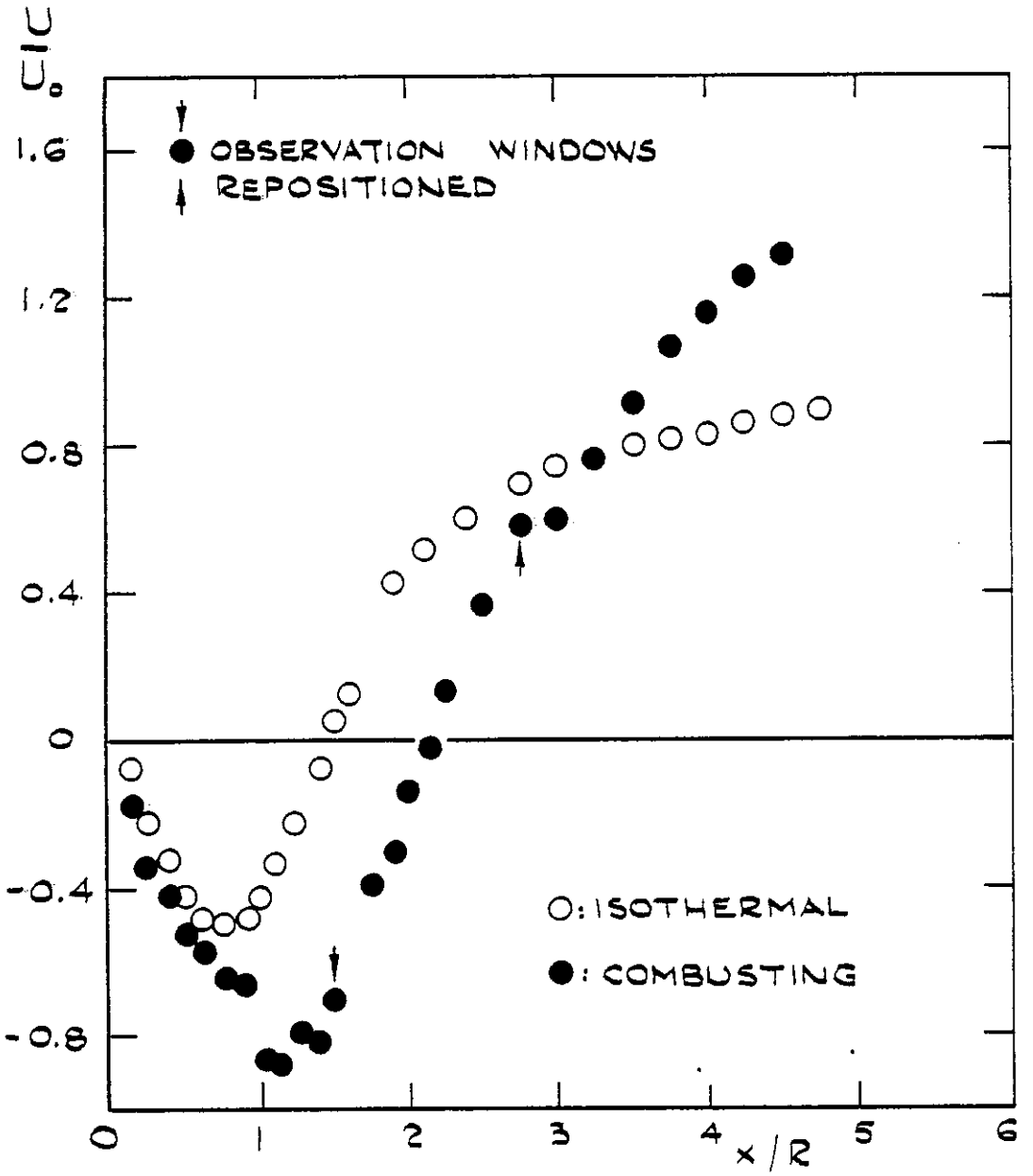

Figure 4.21 Cone 25% blockage: centreline profile of axial velocity. Equivalence ratio is 0.69

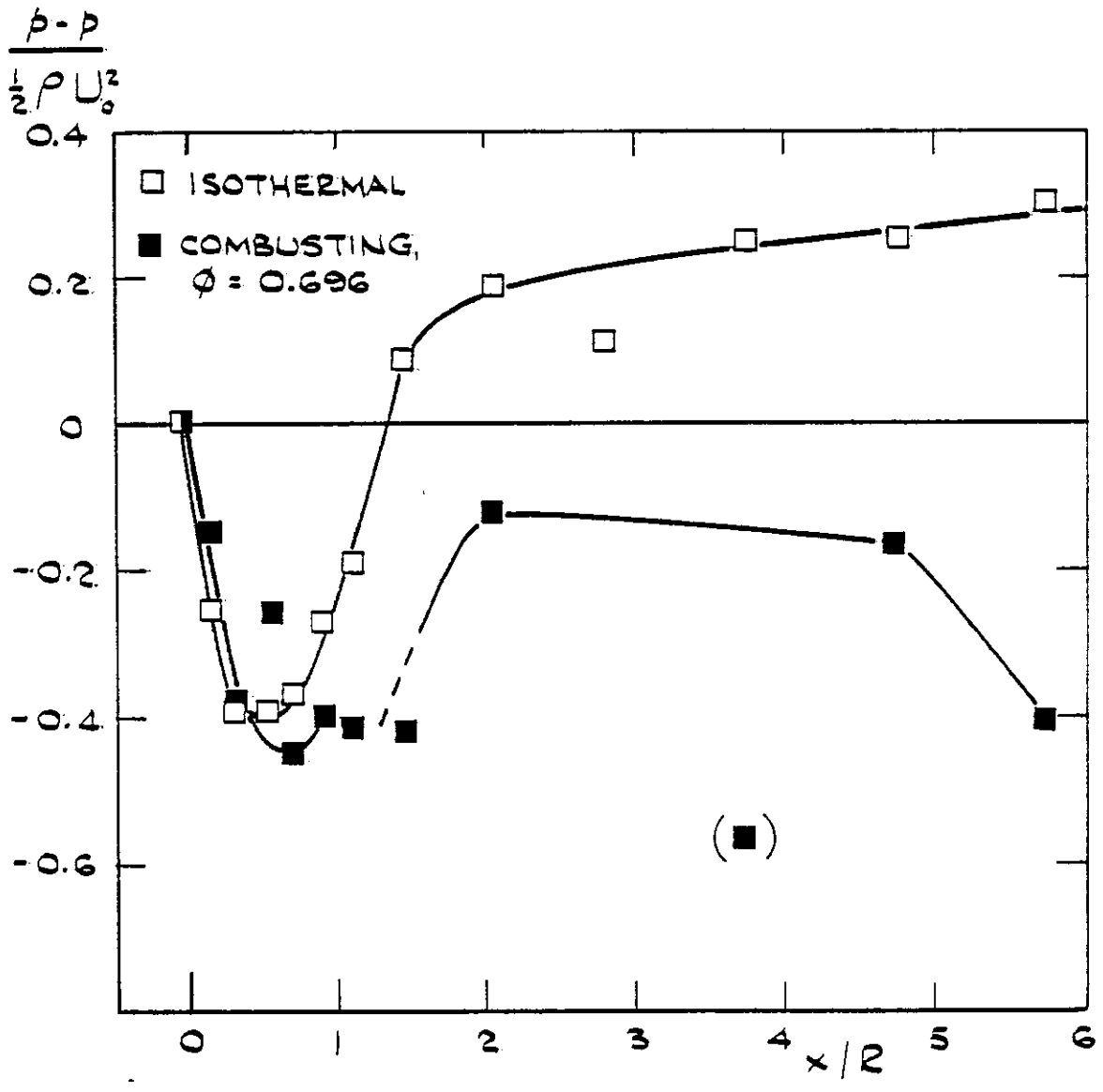

Figure 4.22 Cone, 25% blockage: axial variation of wall pressure coefficient

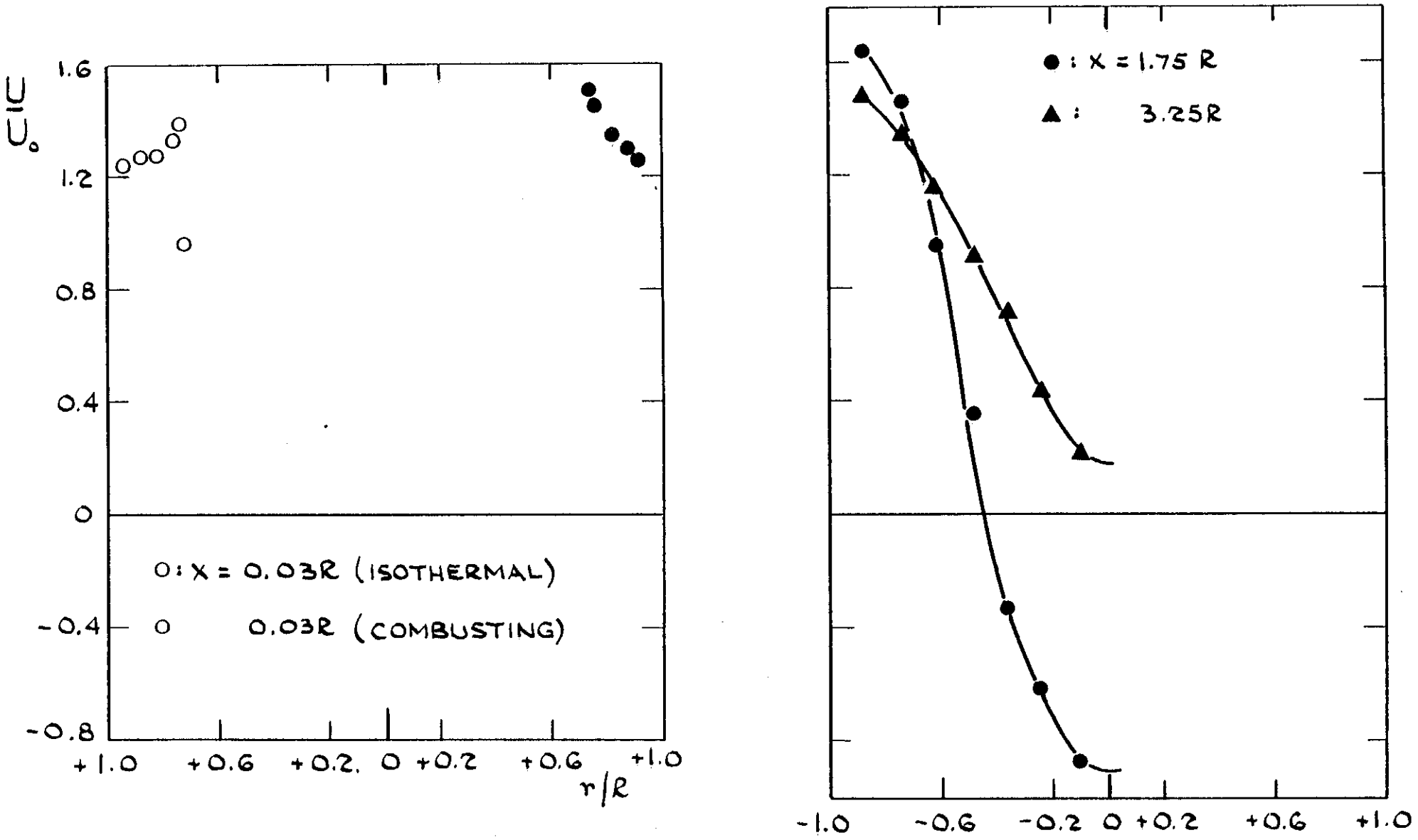

Figure 4.23 Disc, 50% blockage: radial profiles of axial velocity at successive axial stations. Equivalence ratio is 0.70; U_0 = 13.1 m/s

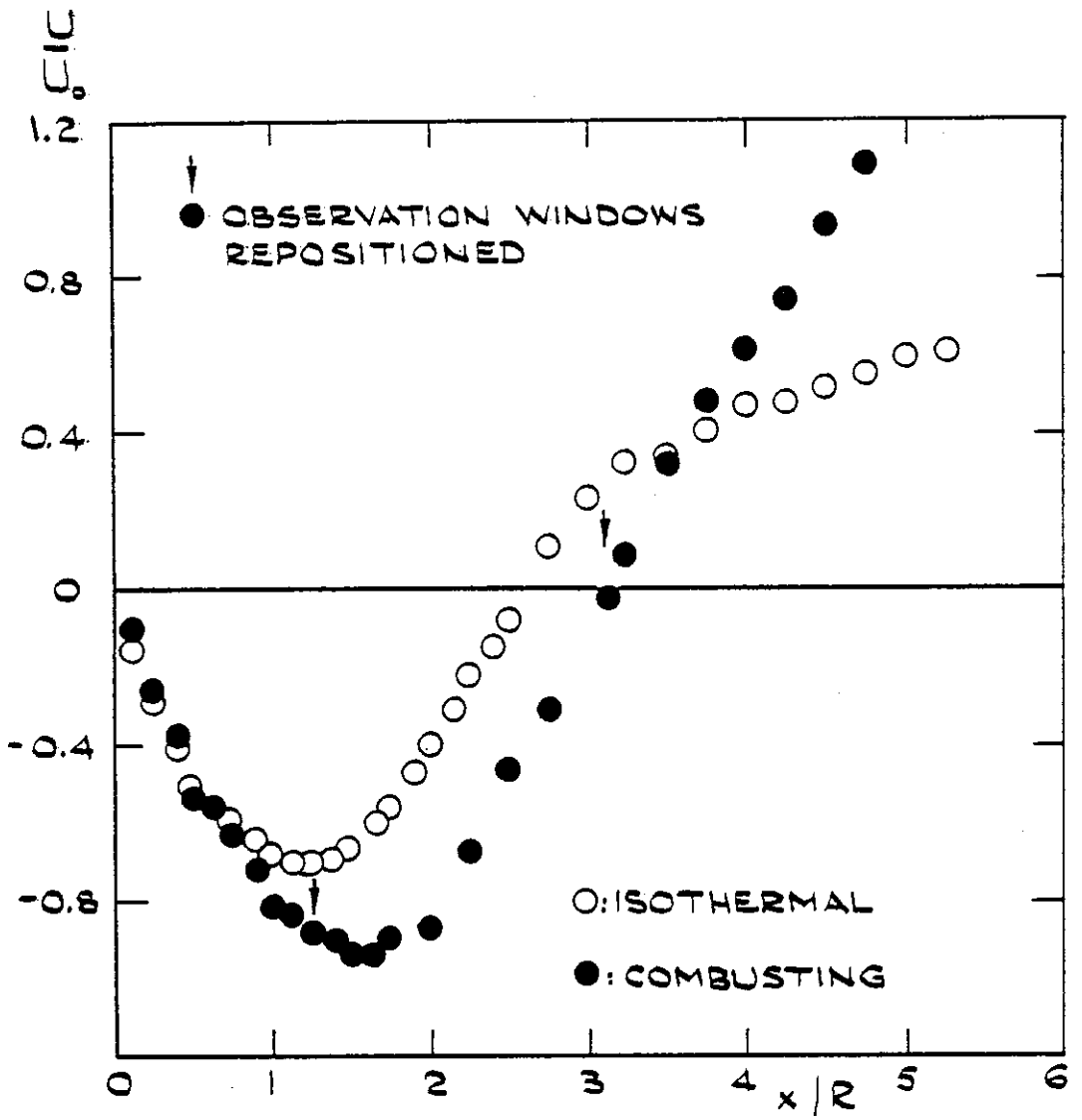

Figure 4.24 Disc, 50% blockage: centreline profile of axial velocity. Equivalence ratio is 0.70.

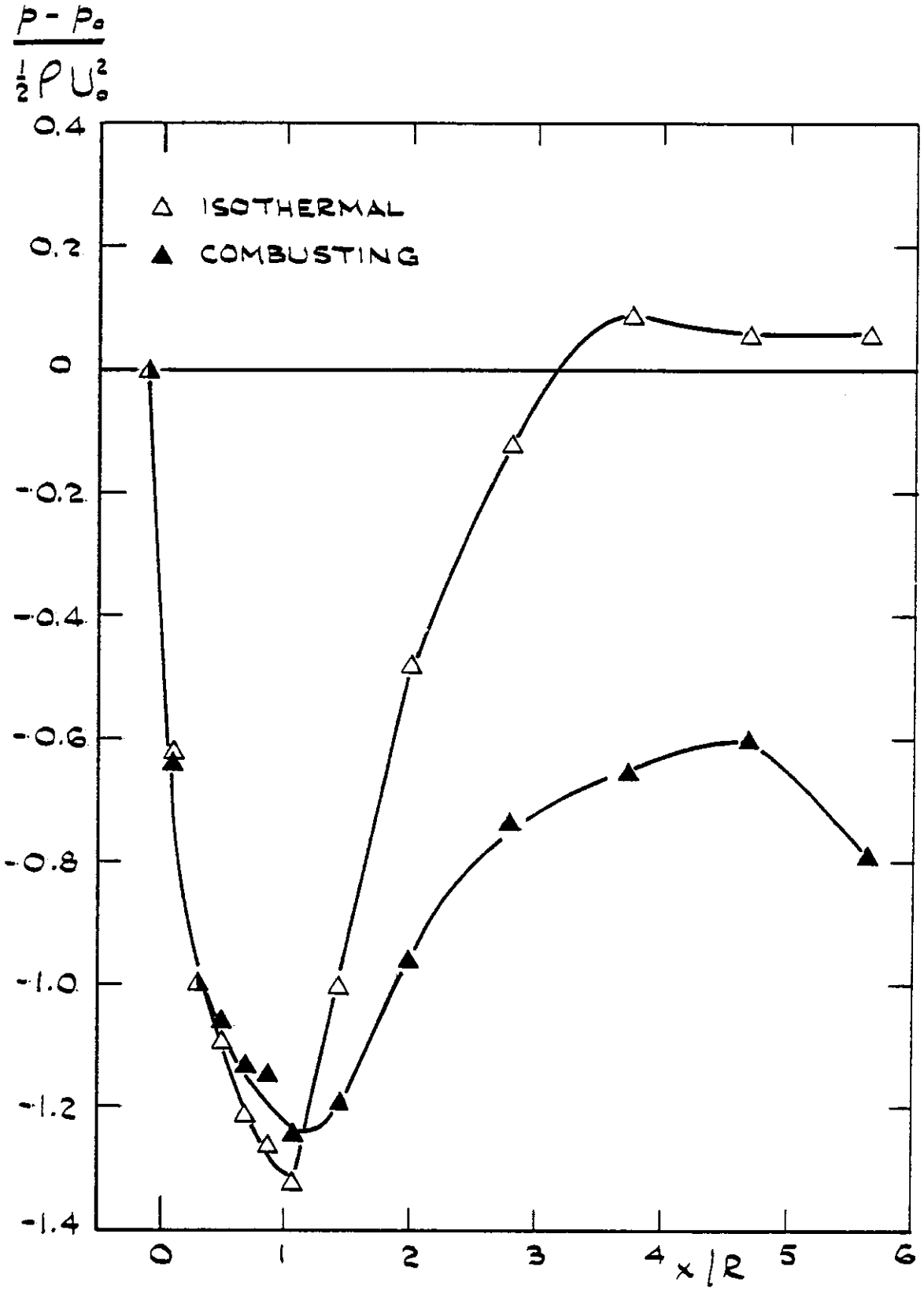

Figure 4.25 Disc, 50% blockage: axial variation of wall pressure coefficient. Equivalence ratio is 0.69.

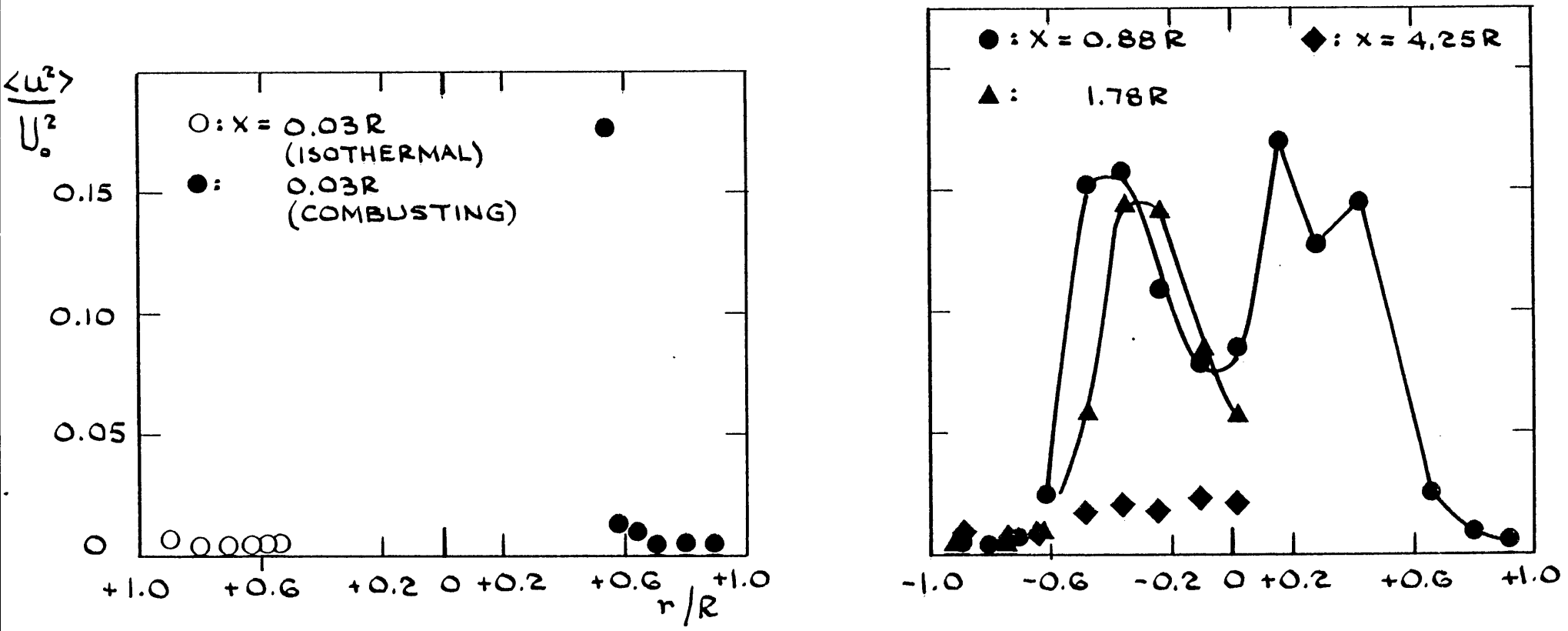

Figure 4.26 Disc, 25% blockage: radial profiles of variance of axial velocity fluctuations at successive axial stations. Equivalence ratio is 0.69; U_o = 8.7 m/s

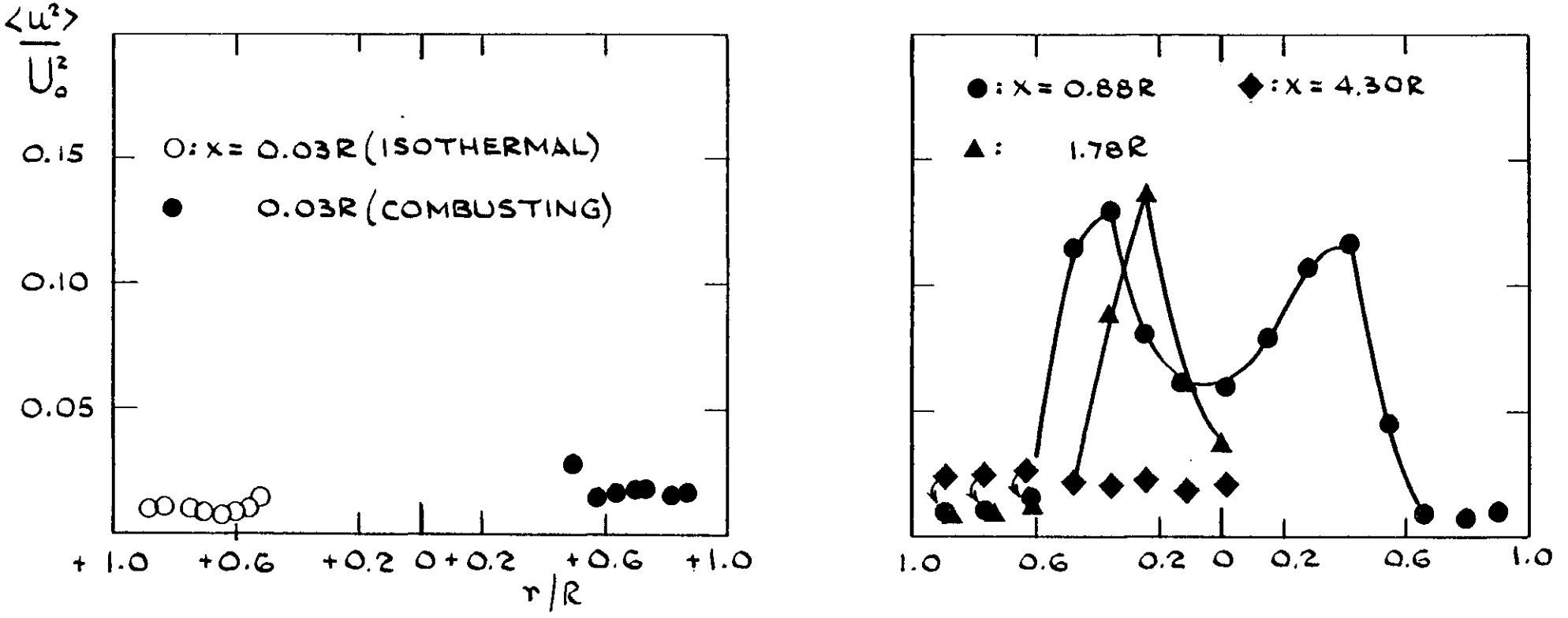

Figure 4.27 Cone, 25% blockage: radial profiles of variance of axial velocity fluctuations at successive axial stations. Equivalence ratio is 0.69; U_o = 8.7 m/s

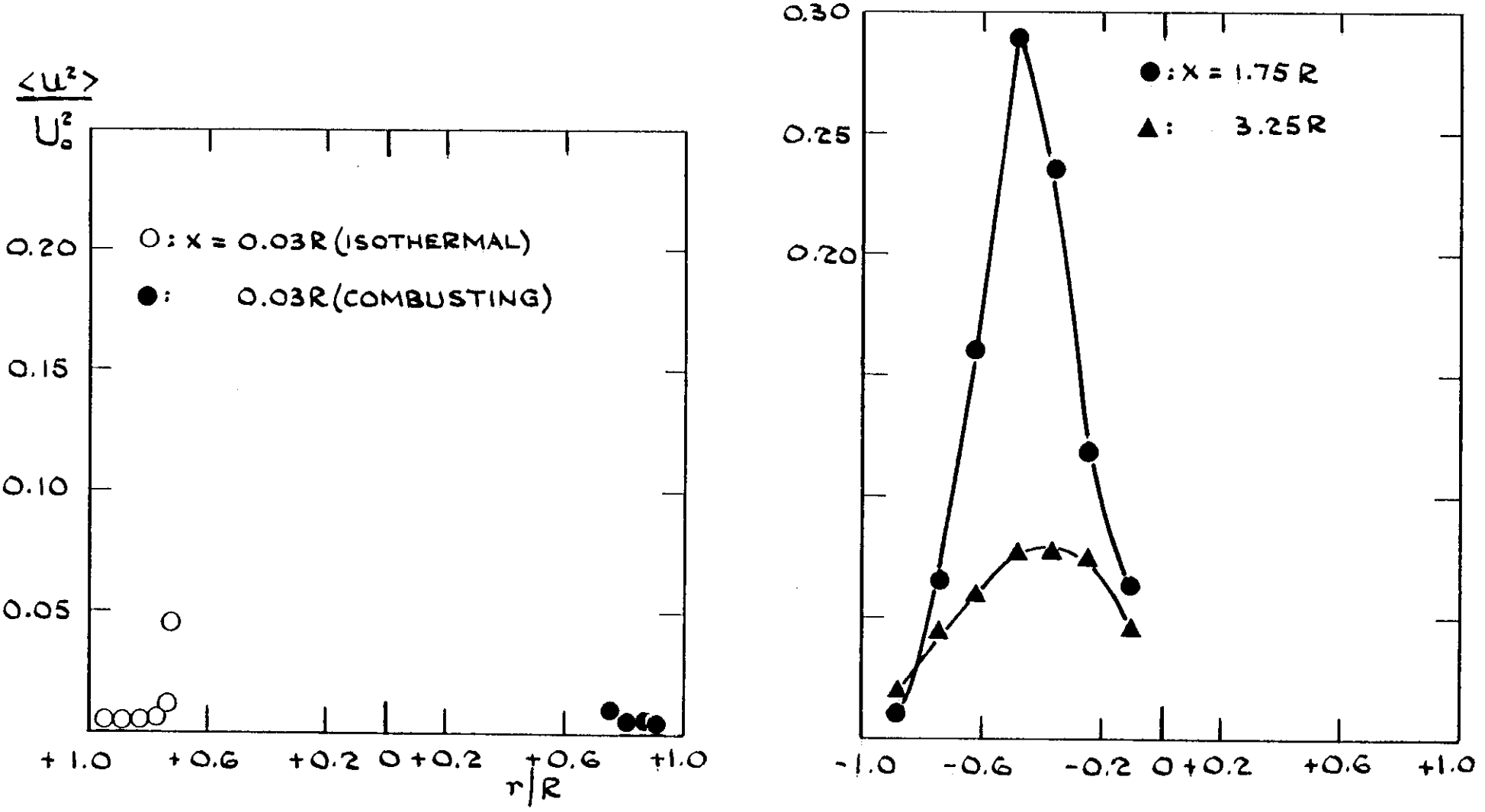

Figure 4.28 Disc, 50% blockage: radial profiles of variance of axial velocity fluctuations at successive axial stations. Equivalence ratio is 0.70; U_o = 13.1 m/s

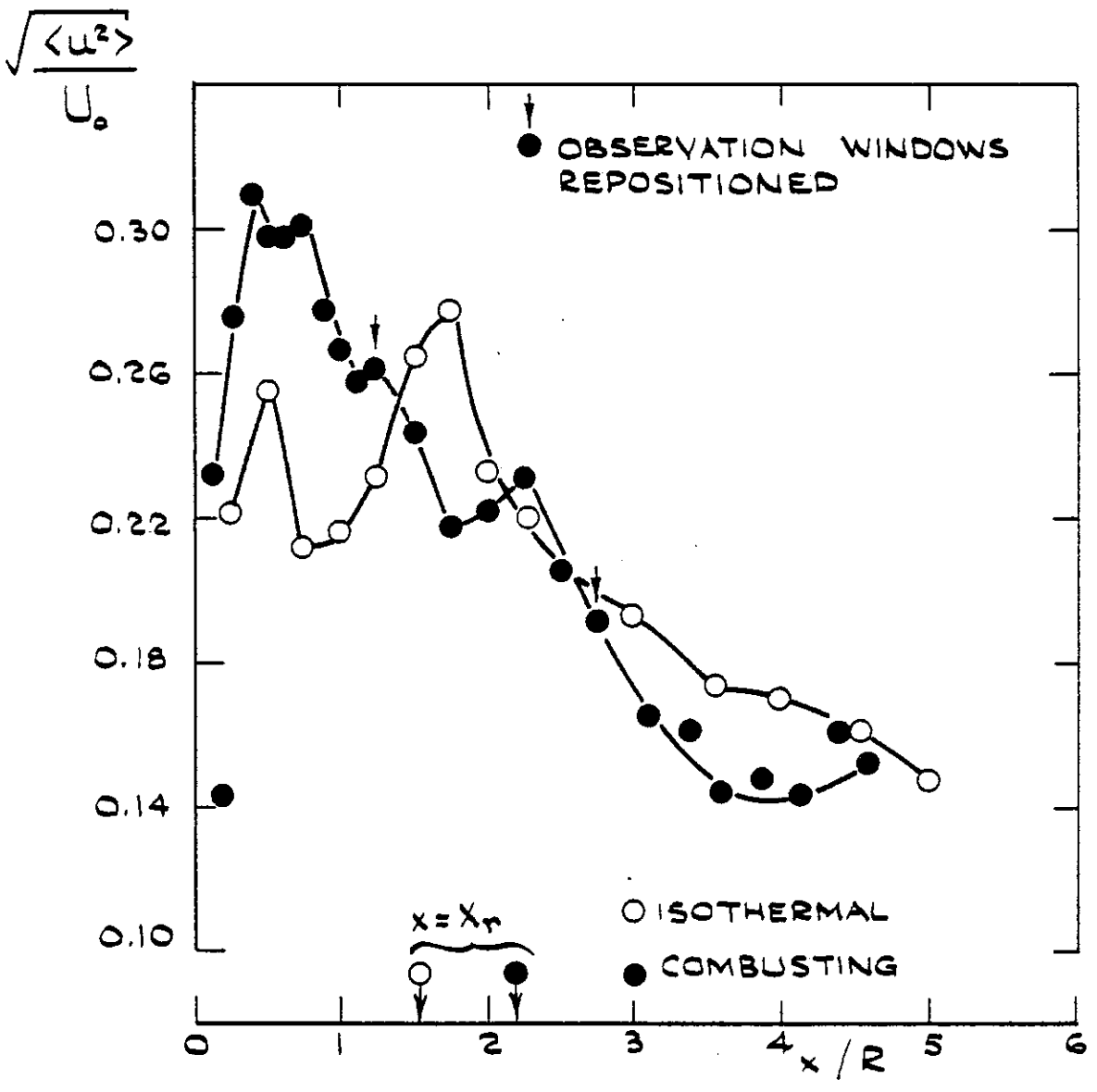

Figure 4.29 Disc, 25% blockage: centreline values of turbulence intensity. Equivalence ratio is 0.69.

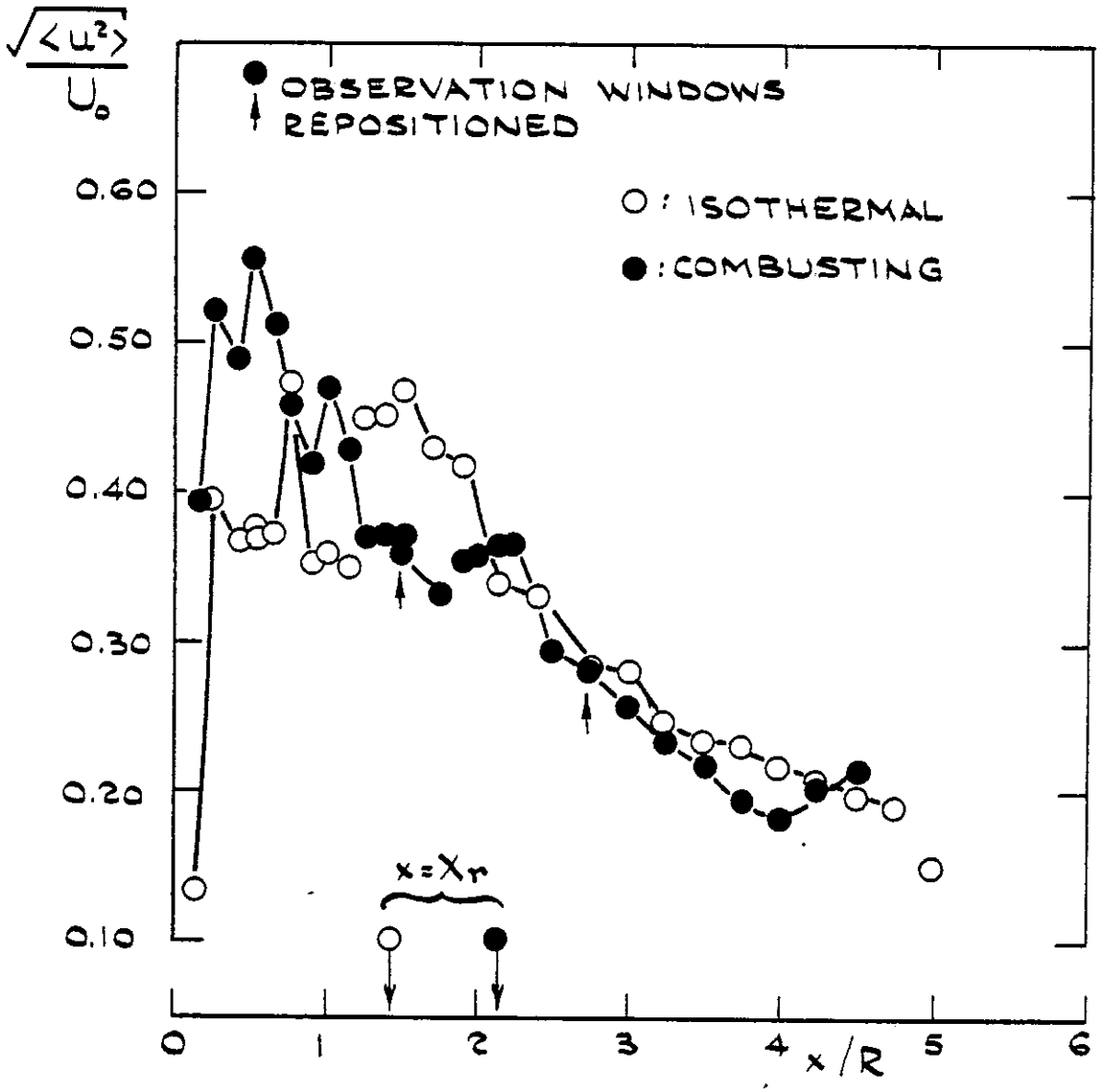

Figure 4.30 Cone, 25% blockage: centreline values of turbulence intensity. Equivalence ratio is 0.69.

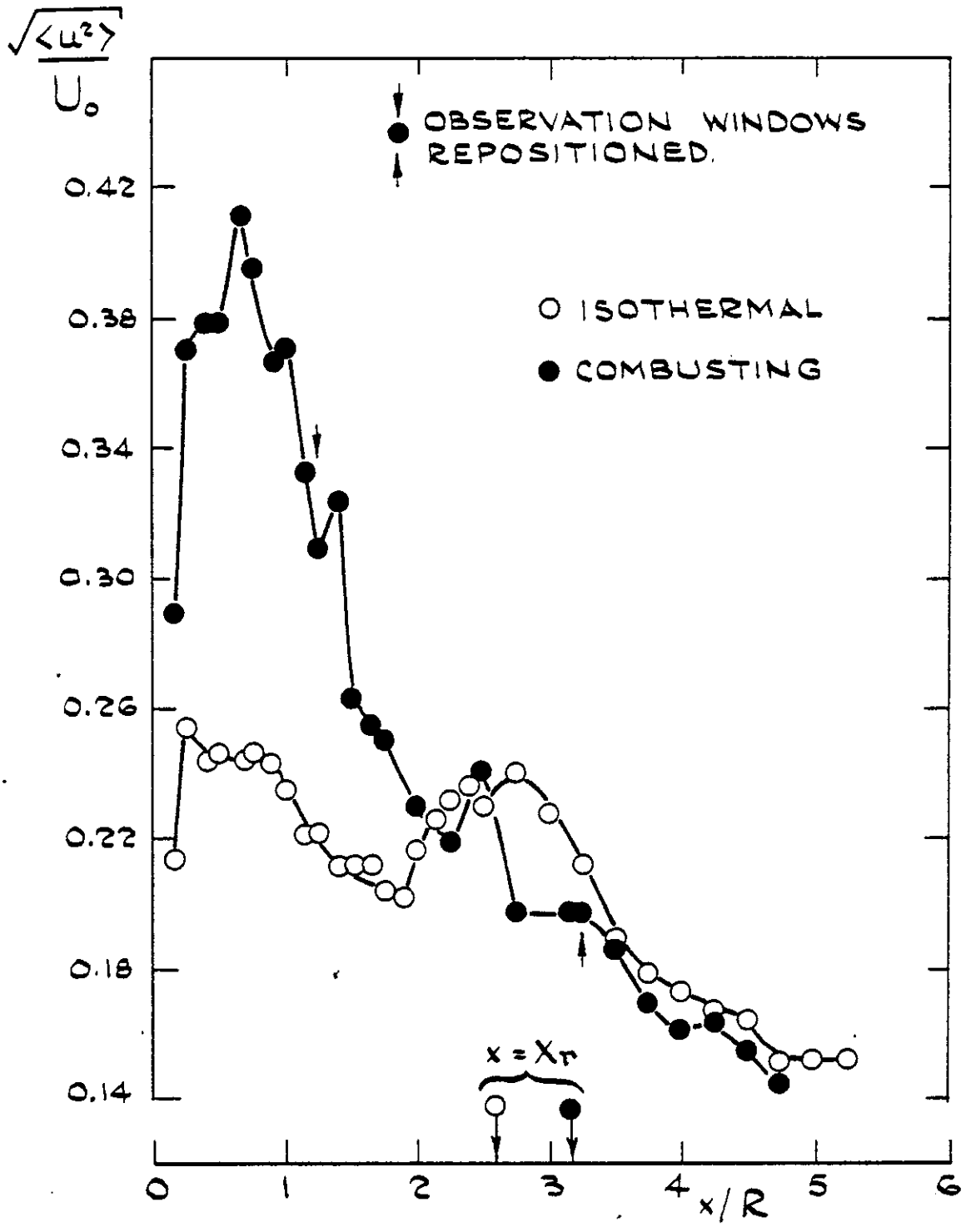

Figure 4.31 Disc, 50% blockage: centreline values of turbulence intensity. Equivalence ratio is 0.70

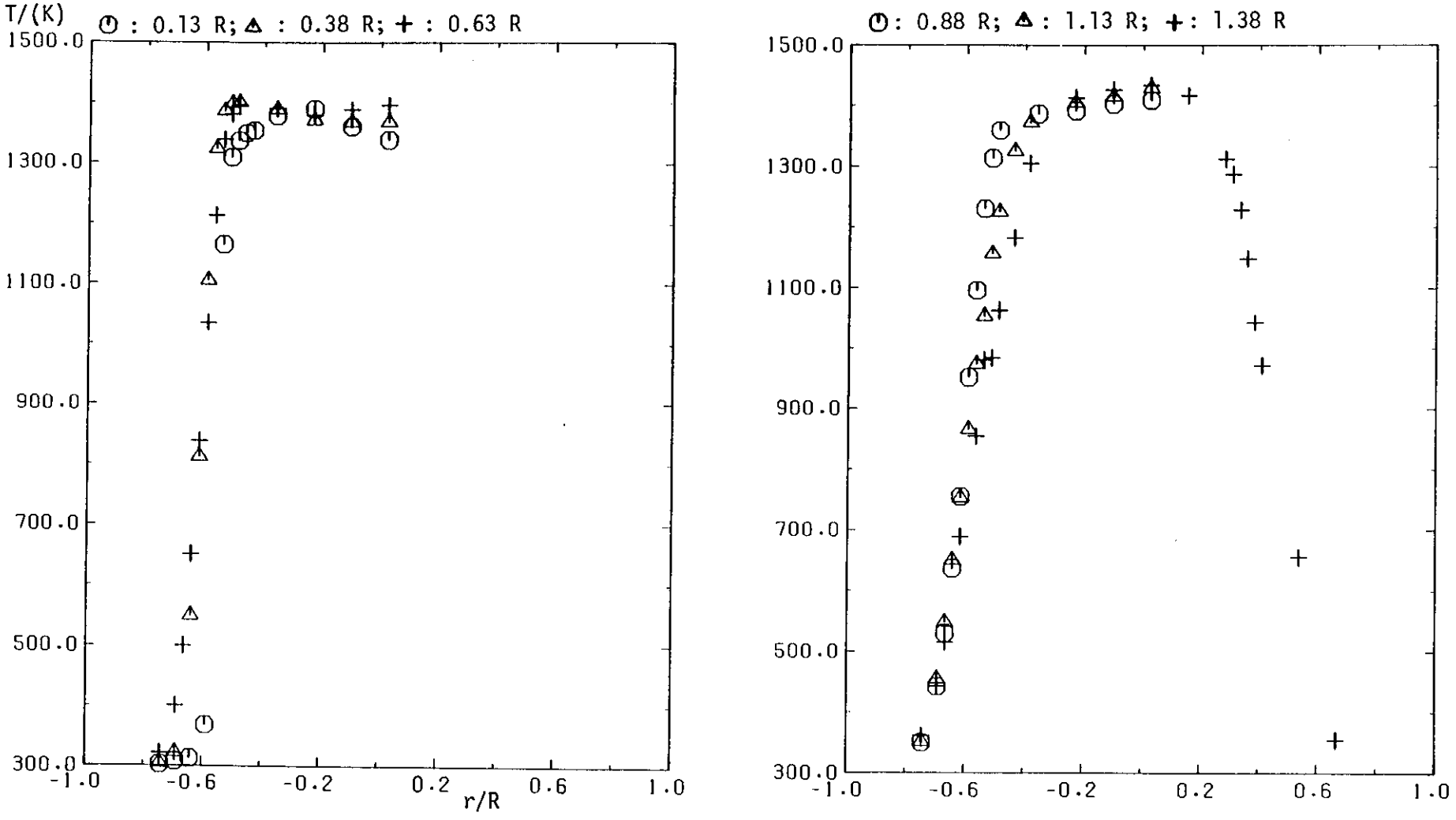

Figure 4.32 Disc, 25% blockage: radial profiles of mean temperature at successive axial stations. Equivalence ratio is 0.69; adiabatic flame temperature = 1820 K

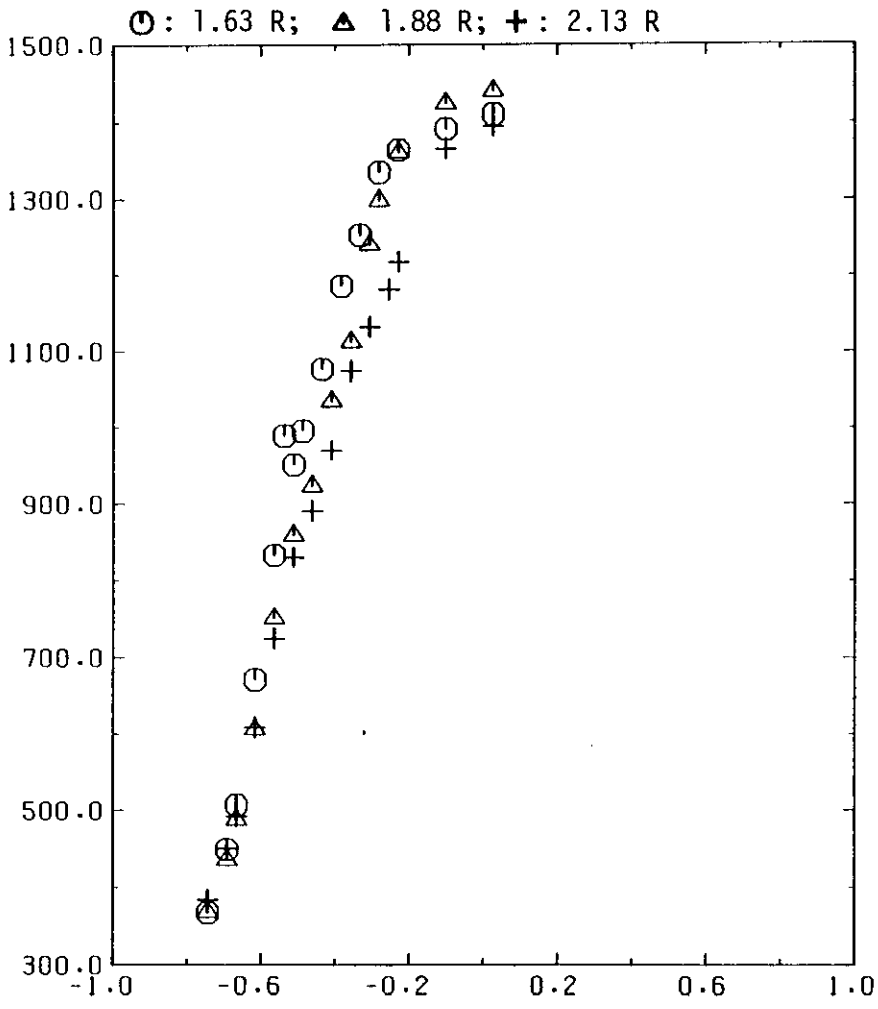

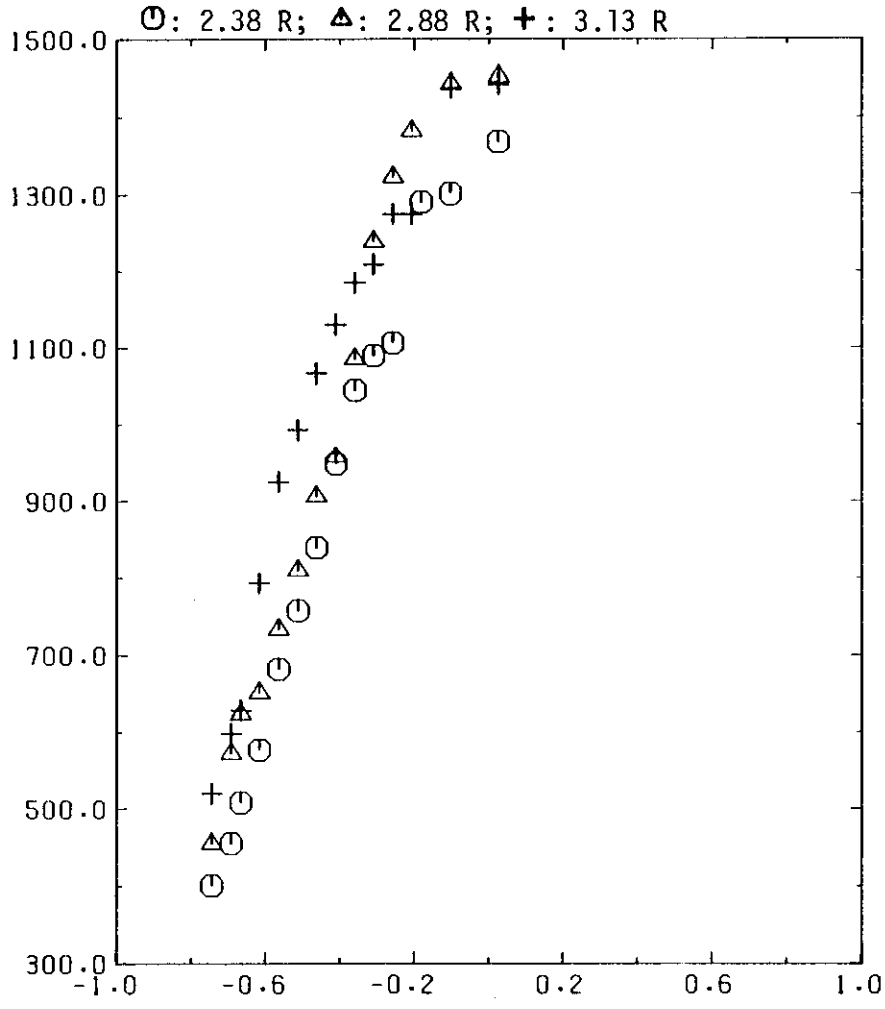

Figure 4.32 Concluded

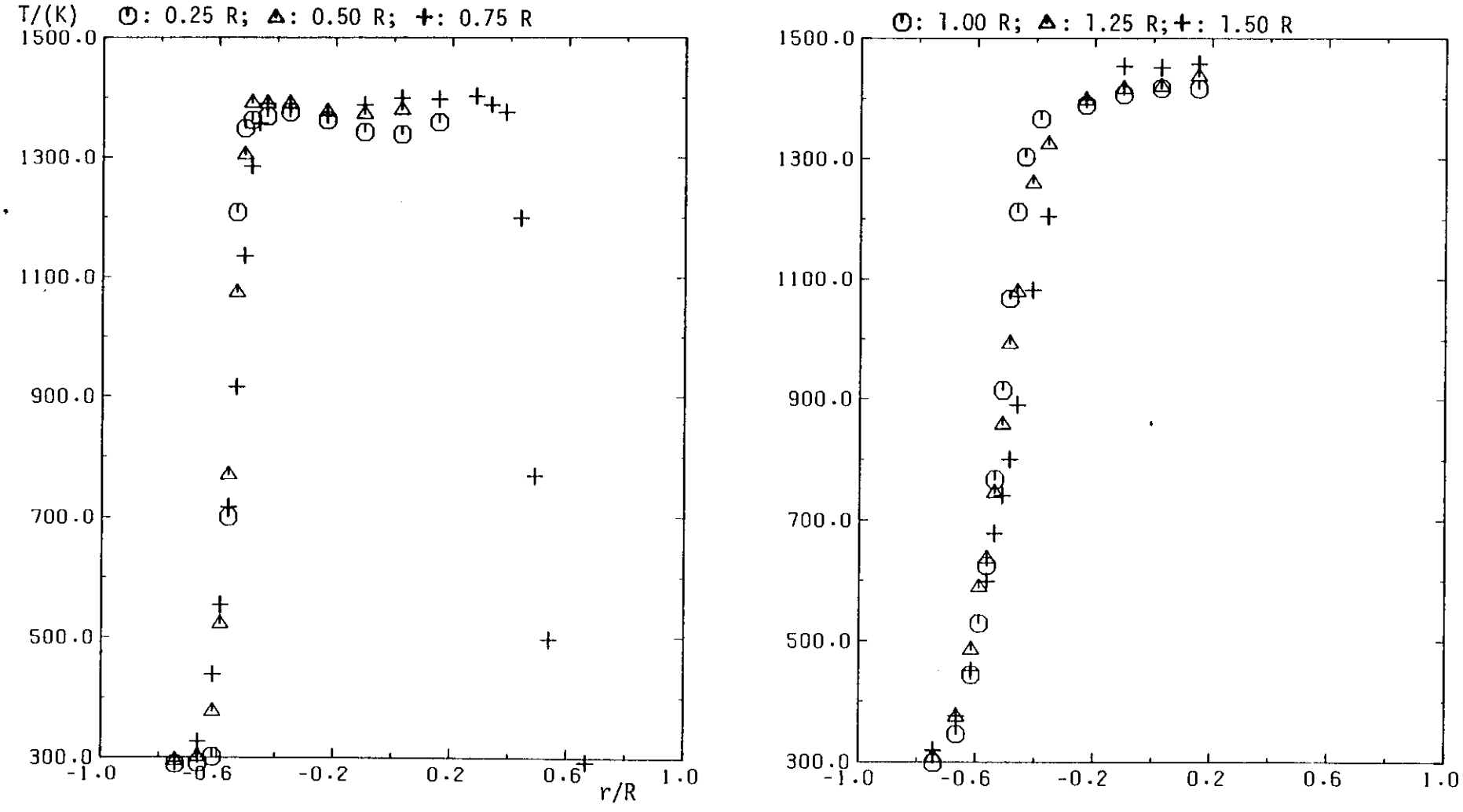

Figure 4.33 Cone, 25% blockage: radial profiles of mean temperature at successive axial stations. Equivalence ratio is 0.69; adiabatic flame temperature = 1820 K

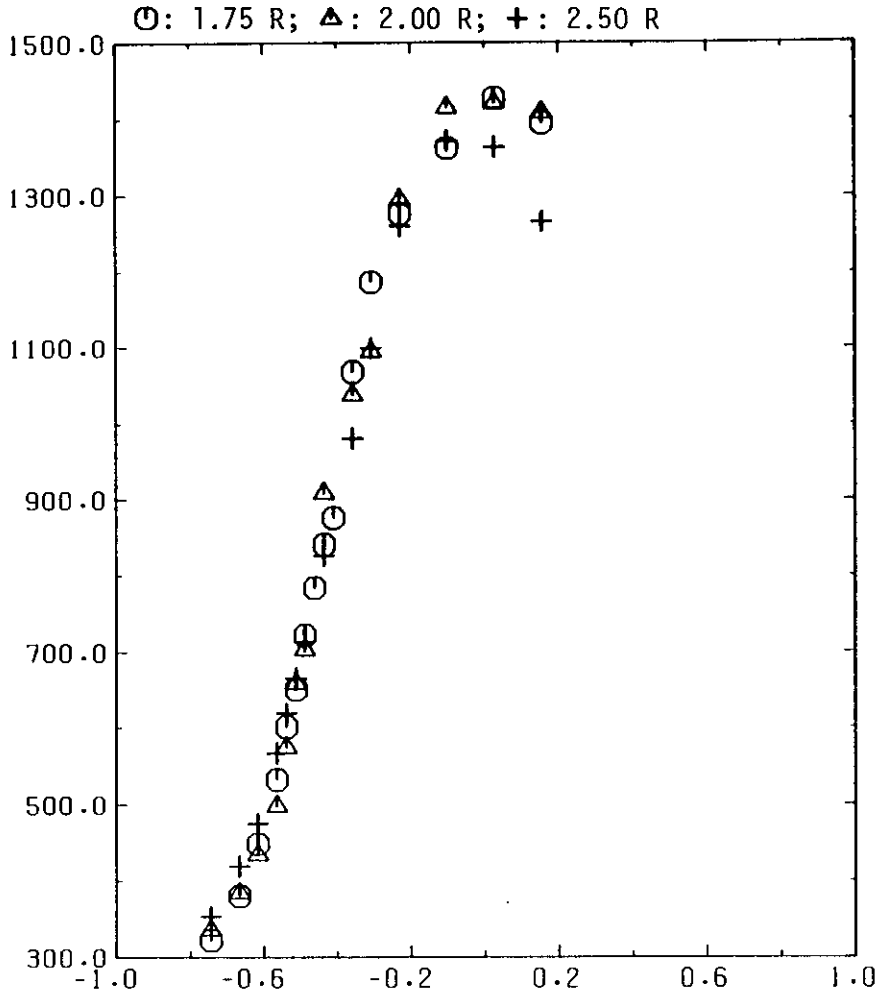

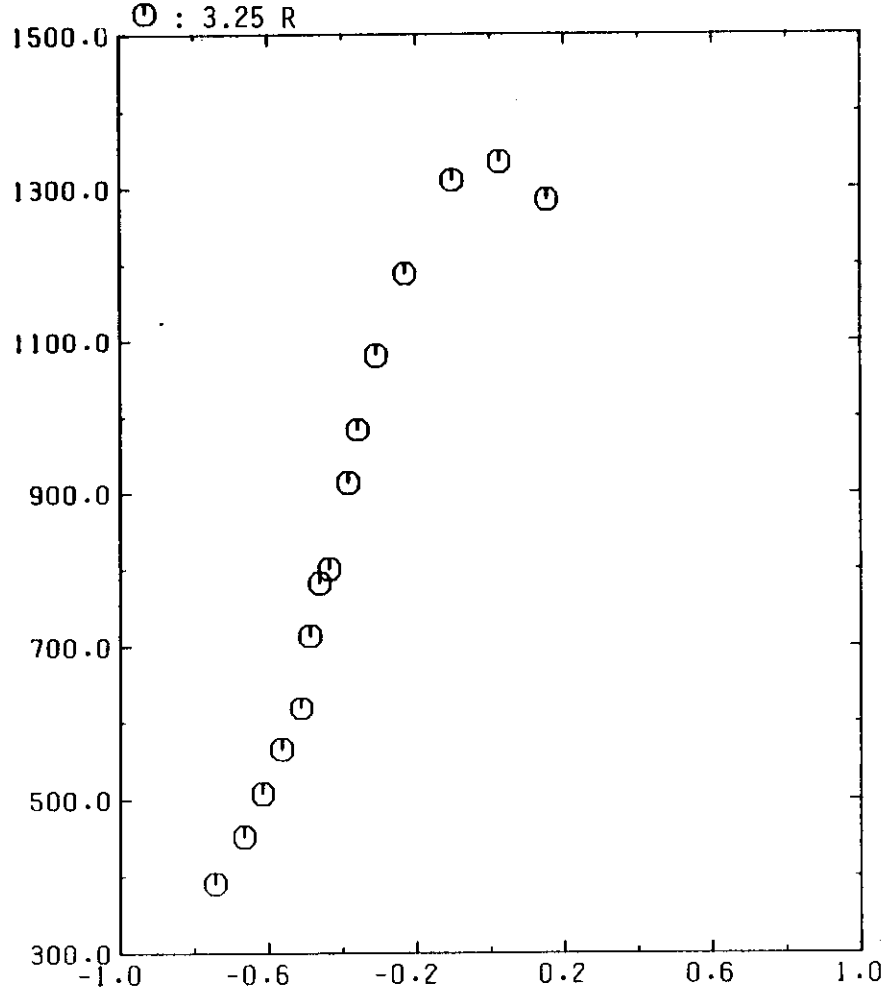

Figure 4.33 Concluded

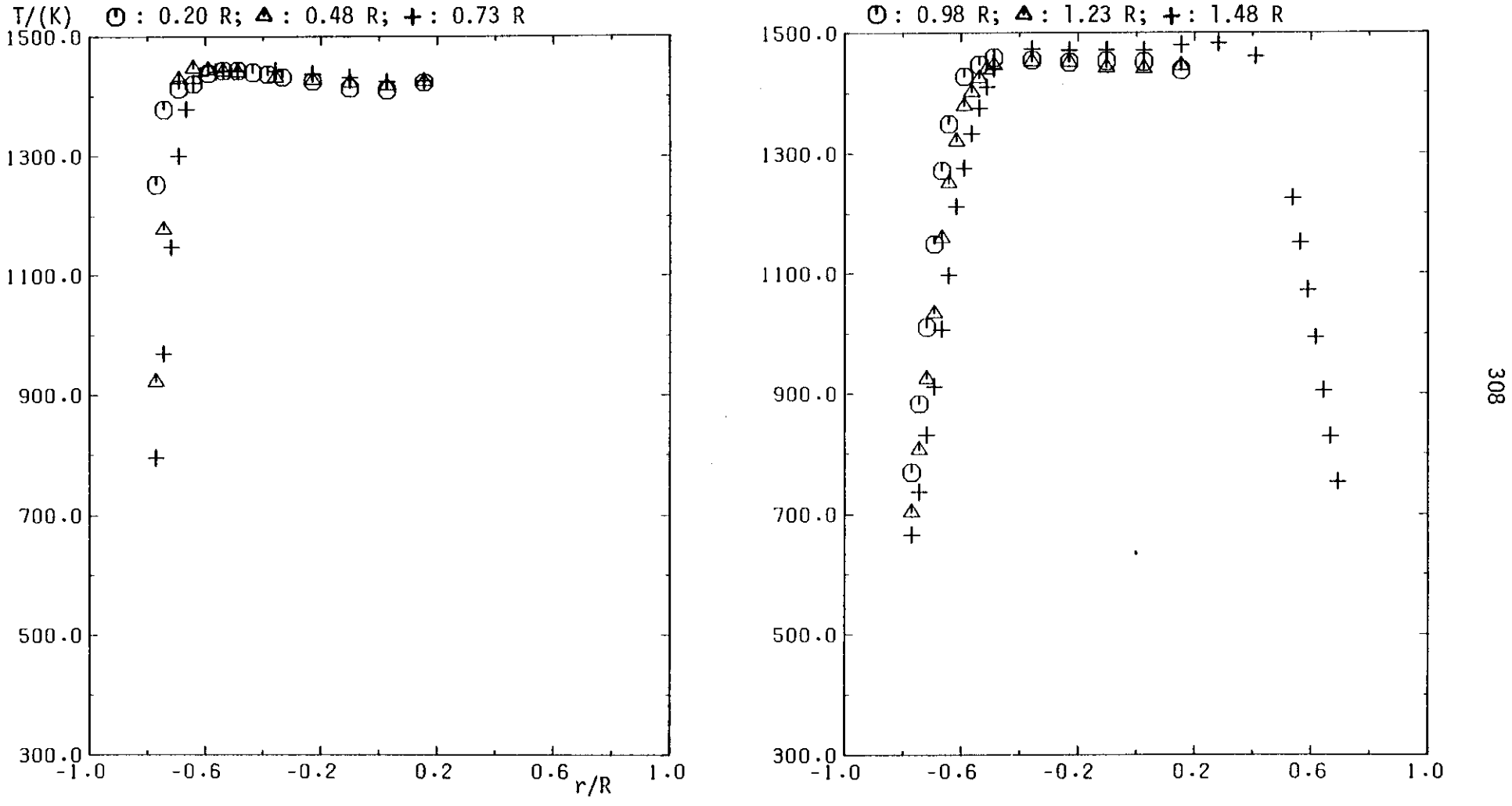

Figure 4.34 Disc, 50% blockage: radial profiles of mean temperature at successive axial stations. Equivalence ratio is 0.70; adiabatic flame temperature = 1830 K

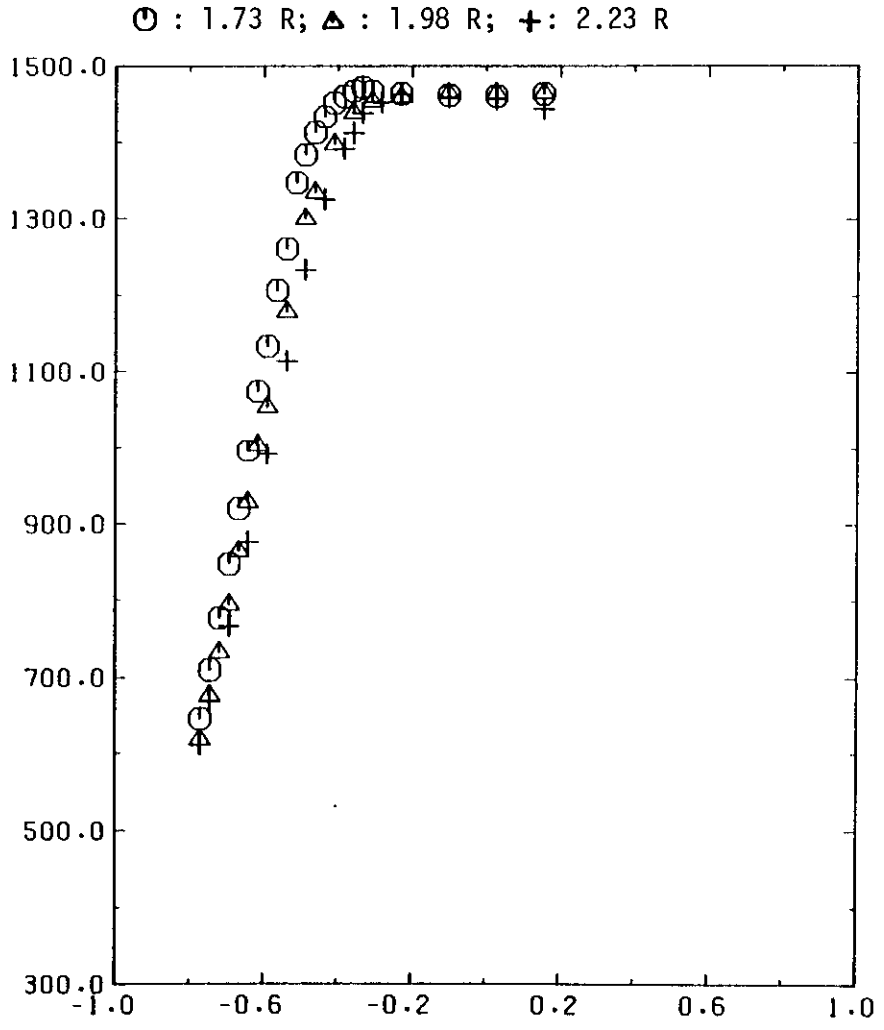

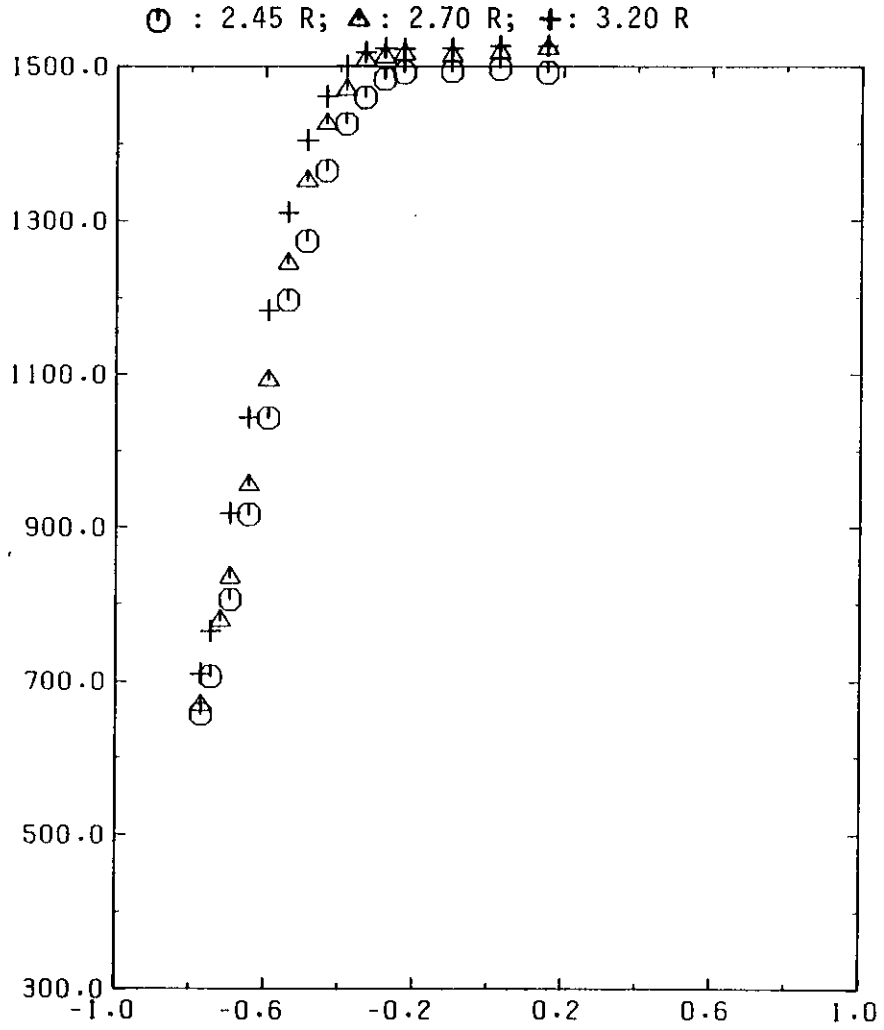

Figure 4.34 Concluded

CHAPTER V

CLOSURE TO THE THESIS

5.1 Achievements and conclusions

The paragraphs which follow give the main original findings of the thesis and thereby indicate the way in which the investigation has advanced the study of confined isothermal and combusting flows behind axisymmetric baffles. The contributions are classified under the categories of isothermal and combusting flow, following the practice of section 1.3. Detailed information concerning the findings and conclusions has been summarised at the end of each chapter and is not repeated here. Section 5.2 puts forward views on the way in which further work should proceed.

5.1.1 Isothermal flow

Measurements were made in the near wake of bluff bodies placed in a long pipe. These bodies were a disc and a cone of 25 per cent area blockage ratio and a disc of 50 per cent blockage: the measurements were primarily of mean and variance of velocity, made by a laser-Doppler velocimeter.

For blockages of 25 per cent, the size of the recirculation zone was slightly larger for the disc than for the cone but the recirculating mass flow rate and the levels of turbulence were substantially higher. On increasing the blockage of the disc to 50 per cent the length of the recirculation bubble, in terms of baffle diameters, increased: this behaviour is the opposite to that which has been found in annular jet flows and is attributed to the influence of the confining wall on the separation streamline. At the higher blockage ratio the maximum value of the turbulent kinetic energy is

no longer found at the rear stagnation point, but rather within the free shear layer surrounding the recirculation zone. This change is associated with the decrease of importance of generation near the centreline through normal stress ∿ normal strain interaction.

In reviewing the contribution of this work to the calculation of turbulent flows behind bluff bodies, it is helpful to recall the conclusions drawn from the literature survey of chapter I. Previous calculations had shown there to be a comparatively large discrepancy between the solutions and experiment in even gross quantities such as the length of the recirculation zone and the rate of spread of the wake downstream. For those calculations which included as a boundary the trailing edge of the baffle, some doubts existed as to the accuracy of the boundary conditions that were specified. However, turbulence models more advanced than the two equation "k-ε" model conferred no improvement and it seemed that the modelled equation for ε was responsible.

For the calculations of this dissertation, measurements of the flow conditions at the trailing edge of the baffle were available and thus removed one impediment to accurate solutions. The other impediment is the question of numerical accuracy ("numerical diffusion") which has been examined carefully, using the method of McGuirk and Rodi (1978). Calculations are presented which are free of numerical diffusion and, using the standard "k-ε" model, the recirculation length is found to be only one tenth too small whereas Pope and Whitelaw (1976) reported a discrepancy of one third.

The greatest demonstrable weakness of this model is its inability to represent the influence of streamline curvature on the turbulent field and, in particular, on shear stress. Previous work in simpler flows has established that the Reynolds stress turbulence

model is better able to represent this influence than is the "k-ε" model. Exhaustive reconsideration in this work of previous, published, solutions has shown these to have been tainted by numerical diffusion and, consequently, the potential advantages of the Reynolds stress model have yet to be realised in such flows. These conclusions are applicable to recirculating, turbulent flows in general and not just to those downstream of bluff bodies.

5.1.2 Combusting flow

The experiments in combusting flow have been carried out in apparatus which is, as nearly as possible, the same as that of isothermal flow. The parameters of interest are not only the forebody shape and blockage of the baffle but also the fuel-to-air ratio of the premixed reactants. In addition to aerodynamic quantities, extensive measurements of the mean temperature have also been made.

Within the flame extinction limits, the fuel-to-air ratio is found to be important in determining whether or not combustion occurs upstream of the trailing edge of the baffle (stable combustion). For a wide range of ratios around the stoichiometric, combustion is 'unstable' and, as compared with the stable kind, is accompanied by large increases in the sound output and the variance of velocity and a decrease in the recirculation zone's length. Up to four preferred pressure-fluctuation frequencies were identified as existing during combustion, but it is likely that only one of these is involved in the transition from stable to 'unstable' operation.

Field measurements of the mean and variance of axial velocity were taken during stable combustion for three different baffles. In each case the recirculation lengths are longer and the variance of velocity larger than for the corresponding isothermal

flow. The increase in the variance is due to shear generated turbulence which is larger because of the greater rate of strain present during combustion. If a thin flame model is assumed, then the mean temperature field suggests that, even during nominally stable combustion, reaction is absent at the mean free stagnation point for something approaching one fifth of the time. This result suggests large intermittancy in the flow between reactants and products within the recirculation zone.

5.2 Suggestions for further work

The focus of this thesis has been the aero- (or hydro-) dynamics of the near wake and further work should be directed towards experimental investigations of the basic turbulent processes in this region: by the phrase basic processes is meant the turbulent transport of momentum, heat and mass. Such investigations, in non-reacting flows, have application beyond the narrow objective of simulating bluff body stabilised flames: an example is the transport of chemical substances, dissolved gases and suspended material between the main flow of a river and groynes on its banks.

Although confined axisymmetric water flows are convenient for experiments, the measurement of the cross-correlation $\langle uv \rangle$, which is responsible for momentum transport, is not feasible (see chapter II) and is a shortcoming of importance. An effort, beyond that which has already been made, is necessary to find a liquid with a refractive index close to that of Perspex, with a kinematic viscosity sufficiently low so that turbulent flows can be easily established but which is not a solvent or, say, highly flammable. The liquid will make feasible measurements of both second- and third-order correlations and with the latter it becomes possible to construct approximations for the

balance of turbulent kinetic energy and shear stress. The behaviour of turbulent length scales, such as the integral correlation length, the Taylor microscale and the mixing length, should be investigated in the vicinity of the free stagnation point to examine the suggestion (Bradshaw and Wong, 1972) that there is a pronounced decrease in the eddy length scale in this region.

Work should extend to the comparable study of plane, two-dimensional baffles which introduces the added complexity of strong vortex shedding. The plane geometry and vortex shedding suggest the use of conditional sampling techniques to investigate the turbulent structure. A number of conditioning criteria are available but, as pointed out by Buchhave, George and Lumley (1979), seeding the flow on only one side of the plane of symmetry is a particularly attractive method.

In the discussion of chapter III it was argued that the Reynolds stress model of turbulence should be used in future calculations of the flows of chapter II and the existing experimental results will be useful in assessing whether any improvements exist. Although it is economical to include the trailing edge of the baffle as a boundary for the solution, it is unlikely that in any practical problem the boundary conditions will be known at this station. Calculations should be made in which this boundary lies far upstream of the baffle so as to evaluate the solution accuracy and the increase in the computational effort. It is likely, however, that the finite difference grids will be large and the potential of higher-order differencing schemes in providing better accuracy, at modest grid sizes, than the hybrid differencing scheme should be examined closely.

Turning to combusting flow, the results of chapter IV can usefully, and comparatively easily, be complemented by measurements

of $\langle w^2 \rangle$ and the concentrations of major and minor species (recommendations for work concerned with combustion-induced oscillations have already been given in this chapter). These results can form the basis for evaluating the performance of current calculation procedures in combusting flows. Because of its importance to some models of turbulent combustion, the probability density function of temperature should also be measured, possibly by a frequency-compensated thermocouple but preferably by an optical technique such as Rayleigh scattering. This method is preferable because there is no fragile probe in the flow and because of the high frequency response (0 - 15 kHz) of which it is capable (Dibble and Hollenbach, 1980).

An important question which remains unanswered is whether gradient transport hypotheses, of the kind common in isothermal turbulence models, are applicable in combusting flows (Libby and Williams, 1981). For experimental work to proceed it is necessary to be able to measure instantaneous values of density and velocity fluctuation, particularly shear stress. Density fluctuations may be measured by Rayleigh scattering and although measurements of shear stress are difficult in confined axisymmetric flows these are possible in unconfined or plane, two-dimensional flows.

The suggestions for further work, and indeed the rationale behind the work of this thesis, involve carefully co-ordinated programmes of experiments and calculations in comparatively simple configurations. This reflects the opinion that such co-ordination represents a fruitful way to achieve an engineering understanding of turbulent flows.

REFERENCES CITED

ALVERMANN, W. and STOTTMANN, P. (1964)
Temperatur-messungen mit Thermoelementen in Verbrennungsgasen.
DLR-Forschungsbericht, 64-18.

ANON., (1972)
Frequency analysis and power spectral density measurements.
Brüel & Kjaer, Nærum, Denmark.

ARCOUMANIS, C. (1980)
Water analog of the opposed-jet combustor: velocity field measurements and flow visualization.
M.S. Thesis, University of California, U.S.A.

ASALOR, J. O. and WHITELAW, J. H. (1974)
The design and performance of a cross-flow particle generator for use in laser-Doppler anemometry.
Dept. of Mech. Eng. Report HTS/74/25, Imperial College, London.

ASALOR, J. O. and WHITELAW, J. H. (1975)
The influence of combustion-induced particle concentration variations in laser-Doppler anemometry.
Proceedings LDA-Symposium Copenhagen, PO Box 70, DK-2740 Skovlunde, Denmark.

ATTYA, A. M. (1980)
Temperature and species concentration measurements in unconfined kerosene spray flames.
Fluids Section Report FS/80/15, Dept. of Mech. Eng., Imperial College, London.

BAKER, R. J. (1974)
The influence of particle seeding on laser anemometry measurements.
Report AERE-M2644, Chemical Engineering Division, AERE Harwell, Oxon.

BALLAL, D. R. and LEFEBVRE, A. H. (1975)
The structure and propagation of turbulent flames.
Proc. R. Soc. Lond. A. 344, 217.

BARNETT, D. O. and BENTLEY, H. T. (1974)
Statistical bias of individual realization laser velocimeters.
Proceedings of the Second International Workshop on Laser Velocimetry, Vol. 1, Purdue University, Lafayette, Indiana (Engineering Experiment Station Bulletin No. 144).

BARRÈRE, M. and MESTRE, A. (1954)
Stabilisation des flammes par des obstacles.
Selected Combustion Problems, Butterworths Scientific Publications, London.

BARRÈRE, M. and WILLIAMS, F. A. (1969)
Comparison of combustion instabilities found in various types of combustion chambers.
Twelfth Symposium (International) on Combustion, The Combustion Institute, Pittsburgh, Pa.

BEER, J. M. and CHIGIER, N. A. (1974)
Combustion Aerodynamics.
Applied Science Publishers Ltd., London.

BENDAT, J. S. and PIERSOL, A. G. (1971)
Random Data: analysis and measurement procedures.
Wiley-Interscience, New York.

BESPALOV, I. V. (1967)
IN Physical principles of the working process in combustion chambers of jet engines (Raushenbakh et al).
(Translated from Russian, Clearinghouse for Federal, Scientific and Technical Information, U.S.A. AD 658 372).

BILGER, R. W. (1977)
Probe measurements in turbulent combustion.
Experimental diagnostics in gas phase combustion systems. Progress in Aeronautics and Astronautics, Vol. 53 (Eds. Zinn, B. T. et al).

BILGER, R. W. (1980)
IN Turbulent reacting flows. (Eds. Libby, P. A. and Williams, F. A.)
Springer-Verlag, Berlin.

BLACKSHEAR, P. L. (1956)
The Growth of disturbances in a flame-generated shear region.
Sixth Symposium (International) on Combustion, Reinhold Publishing Corp., New York.

BORGHI, R. (1975)
Turbulent mixing in non reactive and reactive flows. (Ed. S. N. B. Murthy).
Plenum Press, New York.

BORGHI, R. and DUTOYA, D. (1978)
On the scales of the fluctuations in turbulent combustion.
17th Symposium (International) on Combustion. Combustion Institute, Pittsburgh, Pa.

BORGHI, R., MOREAU, P. and BOUTIER, C. (1978)
Theoretical predictions of a high velocity, premixed, turbulent flame (in French).
Rech. Aerosp. 3, May - June, 1978.

BOVINA, T. A. (1958)
Studies of exchange between re-circulation zone behind the flame-holder and outer flow.
7th Symposium (International) on Combustion. Butterworths Scientific Publications, London. For the Combustion Institute.

BRADBURY, L. J. S. (1976)
Measurements with a pulsed-wire and a hot-wire anemometer in the highly turbulent wake of a normal flat plate.
J. Fluid Mech. (1976), 77, 3.

BRADSHAW, P. (1971)
An introduction to turbulence and its measurement.
Pergamon Press, Oxford.

BRADSHAW, P. (1973)
Effects of streamline curvature on turbulent flow.
AGARDograph 169.

BRADSHAW, P. (1976)
Turbulence. (Ed. P. Bradshaw).
Springer-Verlag, Berlin.

BRADSHAW, P. (1980)
Introduction to the section on "Coherent Structures" in Turbulent shear flows 2. (Eds. Bradbury, L. J. S. et al).
Springer-Verlag, Berlin.

BRADSHAW, P. and WONG, F. Y. F. (1972)
The reattachment and relaxation of a turbulent shear layer.
J. Fluid Mech. (1972), 52, 1.

BRAGG, S. L. (1963)
Combustion noise.
J. Inst. Fuel, 36, 12.

BRAY, K. N. C. (1980)
IN Turbulent reacting flows. (Eds. Libby, P. A. and Williams, F. A.).
Springer-Verlag, Berlin.

BRAY, K. N. C. and MOSS, J. B. (1974)
A unified statistical model of the premixed turbulent flame.
Dept. of Aeronautics and Astronautics, AASU report no. 335, University of Southampton. See also Acta Astronautica, 4 (1977).

BUCHHAVE, P. (1975)
Biasing errors in individual particle measurements with the LDA-counter signal processor.
Proceedings LDA-Symposium, Copenhagen, PO Box 70, DK-2740 Skovlunde, Denmark.

BUCHHAVE, P., GEORGE, W. K. and LUMLEY, J. L. (1979)
The measurement of turbulence with the laser-Doppler anemometer.
Annual review of fluid mechanics, 11, pp. 443-503.

CALVERT, J. R. (1967)
Experiments on the low-speed flow past cones.
J. Fluid Mech. (1967), 27, 2.

CARMODY, T. (1964)
Establishment of the wake behind a disc.
Trans. ASME, Journal of Basic Engineering, December, 1964.

CASTRO, I. P. (1978)
The numerical prediction of recirculating flows.
Proc. 1st International Conference on Numerical Methods in Laminar and Turbulent Flow. (Eds. C. Taylor et al), Pentech, Press, London.

CASTRO, I. P. (1979)
Numerical difficulties in the calculation of complex turbulent flows.
Turbulent shear flows 1. (Eds. F. Durst et al), Springer-Verlag, Berlin.

CASTRO, I. P. and ROBINS, A. G. (1977)
The flow around a surface-mounted cube in uniform and turbulent streams.
J. Fluid Mech. (1977), 79, 2.

CEBECI, T. and BRADSHAW, P. (1977)
Momentum transfer in boundary layers.
Hemisphere Publishing Corp., Washington.

CHAMPAGNE, F. H., HARRIS, V. G. and CORRSIN, S. (1970)
Experiments on nearly homogeneous turbulent shear flow.
J. Fluid Mech. (1970), 41, 1.

CHIGIER, N. A. and GILBERT, J. L. (1968)
Recirculation eddies in the wake of flameholders.
J. of the Institute of Fuel, 41, March, 1968.

CLARE, H., DURÃO, D. F. G., MELLING, A. and WHITELAW, J. H. (1976)
Investigation of a V-gutter stabilized flame by laser anemometry and schlieren photography.
Applications of non-intrusive instrumentation in fluid flow research.
AGARD-CP-193, 1976, Paper No. 26.

CRABB, D., DURÃO, D. F. G. and WHITELAW, J. H. (1978)
Velocity characteristics in the vicinity of a two-dimensional rib.
Fluids Section Report No. FS/78/34, Dept. of Mech. Eng., Imperial College, London.

DAVIES, T. W. and BEÉR, J. M. (1971)
Flow in the wake of bluff-body flame stabilisers.
13th Symposium (International) on Combustion, Combustion Institute, Pittsburgh, Pa.

DE VAHL DAVIS, G. and MALLINSON, G. D. (1976)
False diffusion in numerical fluid mechanics.
Computers and Fluids, 4.

DeZUBAY, E. A. (1950)
Characteristics of disk-controlled flame.
Aero. Digest, July, 1950.

DIBBLE, R. W. and HOLLENBACH, R. E. (1980)
Laser-Rayleigh thermometry in turbulent flames.
18th Symp. (International) on Combustion. (To be published).

DIMOTAKIS, P. (1976)
Single scattering particle laser Doppler measurements of turbulence.
Applications of non-intrusive instrumentation in fluid flow research.
AGARD-CP-193, Paper No. 10.

DURÃO, D. F. G. (1976)
The application of laser anemometry to free jets and flames with and without recirculation.
Ph.D. Thesis, University of London.

DURÃO, D. F. G., FOUNTI, M. and WHITELAW, J. H. (1979)
Velocity characteristics of three-dimensional disc-stabilised diffusion flames.
Letters in Heat and Mass Transfer, 6, 1979.

DURÃO, D. F. G., LAKER, J. and WHITELAW, J. H. (1978)
A micro-processor controlled frequency analyser for laser-Doppler anemometry.
Fluids Section Report FS/78/21, Dept. of Mech. Eng., Imperial College, London.

DURÃO, D. F. G. and WHITELAW, J. H. (1974)
Performance characteristics of two frequency-tracking demodulators and a counting system: measurements in an air jet.
Heat Transfer Section Report HTS/74/12, Dept. of Mech. Eng., Imperial College.

DURÃO, D. F. G. and WHITELAW, J. H. (1974)
Measurements in a region of recirculating flow with a Bragg-cell optical system and a counter.
Proceedings of the second international workshop on laser velocimetry, Vol. 1. (Engineering experiment station, Bulletin 144), Purdue University, Indiana.

DURÃO, D. F. G. and WHITELAW, J. H. (1975)
The influence of sampling procedures on the velocity bias in turbulent flows.
Proceedings LDA-Symposium, Copenhagen, PO Box 70, DK-2740 Skovlunde, Denmark.

DURÃO, D. F. G. and WHITELAW, J. H. (1977)
Velocity characteristics of disk-stabilised diffusion and premixed flames.
Experimental diagnostics in gas phase combustion systems. Progress in aeronautics and astronautics, Vol. 53. (Eds. Zinn, B. T. et al).

DURÃO, D. F. G. and WHITELAW, J. H. (1978)
Velocity characteristics of the flow in the near wake of a disc.
J. Fluid Mech. (1978), 85, 2.

DURÃO, D. F. G. and WHITELAW, J. H. (1979)
Relationship between velocity and signal quality in laser Doppler anemometry.
J. Phys. E: Sci. Instrum., 12.

DURÃO, D. F. G., LAKER, J. and WHITELAW, J. H. (1980)
Bias effects in laser Doppler anemometry.
J. Phys. E: Sci. Instrum., 13.

DURRANI, T. S., GREATED, C. and WILMSHURST, T. H. (1972)
An analysis of simulators and tracking systems for laser Doppler velocimeters.
Electro-Optic Systems in flow measurement. (Eds. Durrani, T. S. and Greated, C). University of Southampton.

DURST, F. and KLEINE, R. (1973)
Velocity measurements in turbulent premixed flames by means of laser-Doppler anemometers.
Report SFB/EM/3, Sonderforschungsbereich 80, University of Karlsruhe.

DURST, F., MELLING, A. and WHITELAW, J. H. (1976)
Principles and practice of laser-Doppler anemometry.
Academic Press, New York.

DURST, F. and RASTOGI, A. K. (1979)
Theoretical and experimental investigations of turbulent flow with separation.
Turbulent shear flows 1. (Eds. F. Durst et al). Springer-Verlag, Berlin.

DURST, F. and ZARÉ, M. (1974)
Removal of pedestals and directional ambiguity of optical anemometer signals.
Applied Optics, 13, 11.

EL BANHAWY, Y., MELLING, A. and WHITELAW, J. H. (1978)
Combustion-driven oscillations in a small tube.
Combustion and Flame, 33, 281.

EL BANHAWY, Y. and WHITELAW, J. H. (1979)
Assessment of an approach to the calculation of the flow properties in spray flames.
Combustor Modelling. AGARD-CP-275, 1979, Paper No. 12.

ELLIMAN, D. G., FUSSEY, D. E. and HAY, N. (1978)
Predictions and measurements of a turbulent, axisymmetric ducted diffusion flame.
Int. J. Heat Mass Transfer, 21.

ERDMAN, J. C. and GELLERT, R. I. (1976)
Particle arrival statistics in laser anemometry of turbulent flow.
Appl. Phys. Lett., 29, 408.

ETHERIDGE, D. W. and KEMP, P. H. (1978)
Measurements of turbulent flow downstream of a rearward-facing step.
J. Fluid Mech. (1978), 86, 3.

FAIL, R., LAWFORD, J. A. and EYRE, R. C. W. (1957)
Low speed experiments on the wake characteristics of flat plates normal to an air stream.
Ministry of Supply, Reports and Memoranda No. 3120, R.A.E. Report Aero. 25160.

FAVRE, A., KOVASNAY, L. S. G., DUMAS, R., GAVIGLIO, J. and COANTIC, M. (1976)
"La turbulence en mécanique des fluides".
Gauthier Villars, Paris.

FERRI, A. (1973)
Reduction of NO formations by premixing.
AGARD Conference Proceedings No. 125.

FREEMAN, A. R. (1975)
Laser anemometer measurements in the recirculating region downstream of a sudden pipe expansion.
Proceeding LDA-Symposium Copenhagen, PO Box 70, DK-2740 Skovlunde, Denmark.

FUJII, S., GOMI, M. and EGUCHI, K. (1978)
Cold flow tests of a bluff-body flame stabilizer.
Trans. ASME: Journal of Fluids Eng., 100, 3.

GANJI, A. R. and SAWYER, R. F. (1979)
An experimental study of the flow field and pollutant formation in a two-dimensional premixed, turbulent flame.
AIAA 17th Aerospace Sciences Meeting, New Orleans, Louisiana, January 15 - 17, 1979, Paper 79-0017.

GANJI, A. R. and SAWYER, R. F. (1980)
Experimental study of the flowfield of a two-dimensional premixed turbulent flame.
AIAA Journal, 18, 7, 817.

GEORGE, W. K. (1975)
Limitations to measuring accuracy inherent in the laser Doppler signal.
Proceedings LDA-Symposium, Copenhagen, PO Box 70, DK-2740 Skovlunde, Denmark.

GEORGE, W. K. and LUMLEY, J. L. (1973)
The laser-Doppler velocimeter and its application to the measurement of turbulence.
J. Fluid Mech., 60, 321.

GIBSON, M. M. and RODI, W. (1981)
A Reynolds-stress closure model of turbulence applied to the calculation of a highly curved mixing layer.
J. Fluid Mech. (1981), 103.

GOKALP, I. (1980)
On the correlation of turbulent burning velocities.
Comb. Sci. & Tech., 23, 137.

GOSMAN, A. D., JOHNS, R. J. R. and WATKINS, A. P. (1979)
Assessment of a prediction method for in-cylinder processes in reciprocating engines.
Fluids Section Report FS/79/42, Dept. of Mech. Eng., Imperial College, London.

GOSMAN, A. D., LOCKWOOD, F. C. and SALOOJA, A. P. (1978)
The prediction of cylindrical furnaces gaseous fuelled with premixed and diffusion burners.
Fluids Section Report FS/78/36, Dept. of Mech. Eng., Imperial College, London.

GOSMAN, A. D. and PUN, W. M. (1973)
Lecture notes for course entitled Calculation of Recirculating Flows.
Heat Transfer Section Report HTS/74/2, Dept. of Mech. Eng., Imperial College, London.

GOSMAN, A. D., PUN, W. M., RUNCHAL, A. K., SPALDING, D. B. and WOLFSHTEIN, M. (1969)
Heat and mass transfer in recirculating flows.
Academic Press, London.

HABIB, M. A. and WHITELAW, J. H. (1978)
Velocity characteristics of a confined coaxial jet.
Fluids Section Report No. FS/78/6, Dept. of Mech. Eng., Imperial College, London.

HANJALIĆ, K. and LAUNDER, B. E. (1972)
A Reynolds stress model of turbulence and its application to thin shear flows.
J. Fluid Mech. (1972), 52, 4.

HANJALIĆ, K. and LAUNDER, B. E. (1979)
Preferential spectral transport by irrotational straining.
Paper presented at the Joint ASME/CSME Appl. Mech., Fluids Eng. and Bioeng. Conf., Niagara Falls, NY, June 18 - 20.

HANJALIĆ, K., LAUNDER, B. E. and SCHIESTEL, R. (1980)
Multiple-time-scale concepts in turbulent transport modelling.
Turbulent shear flows 2. (Eds. L. J. S. Bradbury et al), Springer-Verlag, Berlin.

HANSEN, S. (1973)
Broadening of the measured frequency spectrum in a differential anemometer due to interference plane gradients.
J. Phys. D: Appl. Phys., 6.

HOWE, N. M., Jr., SHIPMAN, C. W. and VRANOS, A. (1963)
Turbulent mass transfer and rates of combustion in confined turbulent flames.
9th Symposium (International) on Combustion. Organized by the Combustion Institute, Academic Press, New York.

HOWLAND, A. H. and SIMMONDS, W. A. (1953)
Combustion inside refractory tubes.
Fourth Symposium (International) on Combustion, Williams & Wilkins, Baltimore.

HUMPHRIES, W. and VINCENT, J. H. (1976)
Experiments to investigate transport processes in the near wakes of disks in turbulent air flow.
J. Fluid Mech. (1976), 75, 4.

HUMPHRIES, W. and VINCENT, J. H. (1976)
Near wake properties of axisymmetric bluff body flows.
Appl. Sci. Res. 32, December, 1976.

HUSSAIN, A. K. M. F. and ZAMAN, K. B. M. Q. (1978)
The free shear layer tone phenomenon and probe interference.
J. of Fluid Mech., 87, 349.

IRWIN, H. P. A. H. and ARNÔT SMITH, P. (1975)
Prediction of the effect of streamline curvature on turbulence.
The Physics of Fluids, 18, 6.

JOHNS, R. J. (1979)
Air motion in internal combustion engines.
Ph.D. Thesis, London University.

JOHNSTON, J. P. (1976)
IN Turbulence (Ed. P. Bradshaw).
Springer-Verlag, Berlin.

JONES, W. P. and LAUNDER, B. E. (1972)
The prediction of laminarization with a two-equation model of turbulence.
International Journal of Heat & Mass Transfer, 15.

JONES, W. P. and WHITELAW, J. H. (1978)
Coupling of turbulence and chemical reaction.
Fluids Section Report No. FS/78/13, Dept. of Mech. Eng., Imperial College, London.

KARPUK, M. E. and TIEDERMAN, W. G. (1976)
Effect of finite-size probe volume upon laser-Doppler anemometer measurements.
AIAA J., 14, 1099.

KENT, J. H. and BILGER, R. W. (1973)
Turbulent diffusion flames.
Fourteenth Symposium (International) on Combustion, The Combustion Institute, Pittsburgh, Pa.

KILHAM, J. K., JACKSON, E. G. and SMITH, T. J. B. (1961)
An investigation of tunnel burner noise.
Institution of Gas Engineers Journal, 1.

KILHAM, J. K., JACKSON, E. G. and SMITH, T. J. B. (1965)
Oscillatory combustion in tunnel burners.
Tenth Symposium (International) on Combustion, The Combustion Institute, Pittsburgh, Pa.

KIRMSE, R. (1974)
Optische Probleme bei der Anwendung des Laser-Doppler-Anemometers zu Messung von Stroemungsgeschwindigkeiten in Fluessigkeiten.
Archiv fuer technisches Messen, Blatt V, 1246-1, 1974.

KOGELNIK, H. and LI, T. (1966)
Laser beams and resonators.
Proc. IEEE, 54, 1312.

LAUNDER, B. E., REECE, G. J. and RODI, W. (1975)
Progress in the development of a Reynolds-stress turbulence closure.
J. Fluid Mech. (1975), 68, 3.

LAUNDER, B. E. and SPALDING, D. B. (1972)
Lectures in mathematical models of turbulence.
Academic Press, London.

LAUNDER, B. E. and SPALDING, D. B. (1974)
The numerical computation of turbulent flows.
Computer Methods in Applied Mechanics and Engineering, 3, 269.

LEFEBVRE, A. H. and REID, R. (1966)
The influence of turbulence on the structure and propagation of enclosed flames.
Comb. Flame, 10, 355.

LENZ, W. and GUENTHER, R. (1980)
Measurements of fluctuating temperature in a free-jet diffusion flame.
Comb. Flame, 37, 63.

LEONARD, B. P., LESCHZINER, M. A. and McGUIRK, J. (1978)
Third order finite-difference method for steady two-dimensional convection.
Proc. 1st International Conference on Numerical Methods in Laminar and Turbulent Flow. (Eds. C. Taylor et al), Pentech Press, London.

LESCHZINER, M. A.
Practical evaluation of three finite-difference schemes for the computation of steady-state recirculating flows.
(To be published in Computer Methods in Applied Mechanics and Engineering).

LESCHZINER, M. A. and RODI, W. (1980)
Calculation of annular and twin parallel jets using various discretization schemes and turbulence model variants.
Report SFB80/T/159, Sonderforschungsbereich 80, Universität Karlsruhe.

LEWIS, K. J. and MOSS, J. B. (1978)
Time-resolved scalar measurements in a confined turbulent premixed flame.
17th Symposium (International) on Combustion. Combustion Institute, Pittsburgh, Pa.

LIBBY, P. A. and BRAY, K. N. C. (1977)
Variable density effects in premixed turbulent flames.
AIAA Journal, 15, 8, 1186.

LIBBY, P. A. and BRAY, K. N. C. (1980)
Counter-gradient diffusion in premixed turbulent flames.
AIAA 18th Aerospace Sciences Meeting, Pasadena, California, 1980.

LIBBY, P. A. and WILLIAMS, F. A. (1981)
Some implications of recent theoretical studies in turbulent combustion.
AIAA Journal, 19, 3, 261.

LONGWELL, J. P., CHENEVEY, J. E., CLARK, W. W. and FROST, E. E. (1949)
Flame stabilisation by baffles in a high velocity gas stream.
3rd Symposium on Combustion and Flame and Explosion Phenomena. The Williams & Wilkins Co., Baltimore, Ma.

LUMLEY, J. L. (1978)
Computational modelling of turbulent flows.
Advances in Applied Mechanics, Vol. 18.

MARBLE, F. E. and CANDEL, S. M. (1979)
An analytical study of the non-steady behaviour of large combustors.
Seventeenth Symposium (International) on Combustion. Combustion Institute, Pittsburgh, Pa.

MARBLE, F. E., SUBBAIAH, M. V. and CANDEL, S. M. (1979)
Analysis of low-frequency disturbances in afterburners.
Combustor Modelling, AGARD-CP-275, Paper No. 12.

MASON, H. B. and SPALDING, D. B. (1973)
Prediction of reaction rates in turbulent premixed boundary layer flows.
Heat Transfer Section Report HTS/73/11, Dept. of Mech. Eng., Imperial College, London.

McGUIRK, J. J. and RODI, W. (1978)
A depth-averaged mathematical model for the near field of side discharges into open-channel flow.
J. Fluid Mech. (1978), 86, 4.

McLAUGHLIN, D. K. and TIEDERMAN, W. G. (1973)
Biasing correction for individual realization of laser anemometer measurements in turbulent flows.
Physics of Fluids, 16, 12, 2082.

MELLING, A. (1975)
Investigation of flow in non-circular ducts and other configurations.
Ph.D. Thesis, London University.

MONEIB, H. A. (1980)
Experimental study of the fluctuating temperature in inert and reacting turbulent jets.
Ph.D. Thesis, University of London.

MOREAU, P. and BOUTIER, A. (1977)
Laser velocimeter measurements in a turbulent flame.
Sixteenth Symposium (International) on Combustion. Combustion Institute, Pittsburgh, Pa.

MORSE, A. and LAUNDER, B. E. (1979)
Numerical prediction of axisymmetric free shear flows with a Reynolds stress closure.
Turbulent shear flows I. (Eds. F. Durst et al), Springer-Verlag, Berlin.

MORSE, A. P., WHITELAW, J. H. and YIANNESKIS, M. (1978)
Turbulent flow measurements by laser-Doppler anemometry in a motored reciprocating engine.
Fluids Section Report No. FS/78/24, Dept. of Mech. Eng., Imperial College, London.

MOSS, W. D., BAKER, S. and BRADBURY, L. J. S. (1979)
Measurements of mean velocity and Reynolds stresses in some regions of recirculating flow.
Turbulent shear flows I. (Eds. F. Durst et al), Springer-Verlag, Berlin.

NIELSEN, P. V., RESTIVO, A. and WHITELAW, J. H. (1978)
The velocity characteristics of ventilated rooms.
Trans. ASME J. of Fluids Engineering, September, 1978, 100.

OLDENGARM, J., van KRIEKEN, A. H. and RATERNIK, H. J. (1976)
Development of a rotating grating and its use in laser velocimetry.
Bericht R117/76, ISL, St. Louis, France. Proceedings of the ISL/AGARD workshop on laser anemometry, May 5 - 7, 1976.

OWEN, J. M. and ROGERS, R. H. (1975)
Velocity biasing in laser Doppler velocimeters.
Proceedings LDA-Symposium, Copenhagen, PO Box 70, DK-2740 Skovlunde, Denmark.

PATANKAR, S. V. (1980)
Numerical heat transfer and fluid flow.
Hemisphere Publishing Corp., Washington.

PATANKAR, S. V. and SPALDING, D. B. (1972)
A calculation procedure for heat, mass and momentum transfer in three-dimensional parabolic flows.
Int. J. Heat Mass Transfer, 15, p. 1787.

PECK, R. E. and SAMUELSEN, G. S. (1976)
Eddy viscosity modelling in the prediction of turbulent, backmixed combustion performance.
Sixteenth Symposium (International) on Combustion. Combustion Institute, Pittsburgh, Pa.

PEIN, R., PESCHEL, H. and FETTING, F. (1970)
Recirculation zone concentrations and temperatures of bluff-body stabilised turbulent flames.
Combustion Science & Technology, 1, 327.

PITZ, R. W. and DAILY, J. W. (1979)
Experimental studies of combustion in a two-dimensional free shear layer.
Paper presented at the second symposium on turbulent shear flows, July 2 - 4, 1979, Imperial College, London.

POPE, S. B. (1976)
The calculation of the flow behind bluff bodies with and without combustion.
Ph.D. Thesis, University of London.

POPE, S. B. (1978)
An explanation of the turbulent round-jet/plane-jet anomaly.
AIAA 16, 3, p. 279.

POPE, S. B. and WHITELAW, J. H. (1976)
The calculation of near-wake flows.
J. Fluid Mech. (1976), 73, 1.

PUTNAM, A. A. (1971)
Combustion-driven oscillations in industry.
American Elsevier Publishing Co. Inc., New York.

PUTNAM, A. A. and DENNIS, W. R. (1955)
Low frequency oscillations in a flame-filled tube.
ASME Paper 55-SA-48.

QUIGLEY, M. S. and TIEDERMAN, W. G. (1977)
Experimental evaluation of sampling bias in individual realization laser anemometry.
AIAA J. 15, 266.

RAITHBY, G. D. (1976)
Skew upwind differencing schemes for problems involving fluid flow.
Computer methods in Appl. Mech. and Eng., 9, p. 153.

REYNOLDS, W. C. (1976)
Computation of turbulent flows.
Annual Review of Fluid Mechanics, 8, 1976.

ROACHE, P. J. (1976)
Computational fluid dynamics.
Revised printing. Hermosa Publishers, Albuquerque, N.M.

ROSHKO, A. (1976)
Structure of turbulent shear flows: a new look.
AIAA Journal, 14, 10, 1349.

RODI, W. (1970)
Basic equations for turbulent flow in cartesian and cylindrical co-ordinates.
Report BL/TN/A/36, Dept. of Mech. Eng., Imperial College, London.

RODI, W. (1975)
A note on the empirical constant in the Kolmogorov-Prandtl eddy-viscosity expression.
Trans. ASME, J. of Fluids Engineering, 97, p. 387.

SCHEFER, R. W. and SAWYER, R. F. (1976)
Lean premixed recirculating flow combustion for control of oxides of nitrogen.
16th Symposium on Combustion. Combustion Institute, Pittsburgh, Pa.

SCHOFIELD, W. H. and KEEBLE, T. S. (1975)
Measurements of mean velocity and mass exchange in a separated recirculating flow.
Transactions of the ASME, J. of Fluids Engineering, 97, 334.

SCHUMANN, U. (1977)
Realizability of Reynolds stress turbulence models.
Phys. Fluids, 20, 721-725.

SMITH, G. D. (1978)
Numerical solution of partial differential equations: finite difference methods.
2nd Edition, Clarendon Press, Oxford.

SMITH, D. M. and MEADOWS, D. M. (1974)
Power spectra from random-time samples for turbulence measurements with a laser velocimeter.
Proceedings of the second international workshop on laser velocimetry, Vol. 1, Purdue University, Lafayette, Indiana (Engineering Experiment Station, Bulletin No. 144).

SMYTH, R. (1979)
Turbulent flow over a disk normal to a wall.
Trans. ASME J. of Fluids Engineering, December, 1979, 101.

SPALDING, D. B. (1971)
Mixing and chemical reaction in steady confined turbulent flames.
13th Symposium (International) on Combustion. Combustion Institute, Pittsburgh, Pa.

SPALDING, D. B. (1972)
A novel finite difference formulation for differential expressions involving both first and second derivatives.
International J. for Numerical Methods in Engineering, 4, 551-559.

SPALDING, D. B. (1976)
Development of the eddy-break-up model of turbulent combustion.
16th Symposium (International) on Combustion. Combustion Institute, Pittsburgh, Pa.

SPALDING, D. B. (1979)
Combustion and mass transfer.
Pergamon Press, Oxford.

SULLEREY, R. K., GUPTA, A. K. and MOORTHY, C. S. (1975)
Similarity in the turbulent near wake of bluff bodies.
AIAA Journal, 13, 11.

TAYLOR, A. M. K. P. and WHITELAW, J. H. (1980)
Velocity and temperature measurements in a premixed flame within an axisymmetric combustor.
Testing and measurement techniques in hear transfer and combustion, AGARD-CP-281, Paper No. 14.

TENNEKES, H. and LUMLEY, J. L. (1972)
A first course in turbulence.
The MIT Press, Cambridge, Ma.

THRING, M. W. (1969)
Combustion oscillations in industrial combustion chambers.
Twelfth Symposium (International) on Combustion. Combustion Institute, Pittsburgh, Pa.

TIEDERMAN, W. G. (1977)
Interpretation of laser velocimeter measurements in turbulent boundary layers and regions of separation.
Paper presented at 5th Biennial Symp. on Turbulence, October, 1977, University of Missouri, Rolla.

TOWNSEND, A. A. (1980)
The structure of turbulent shear flow.
2nd Edition, Cambridge University Press, Cambridge.

VLACHOS, N. S. (1977)
Computer aided plotting of flow computational results (the computer program KRONOS).
Fluid Section Report FS/77/31, Dept. of Mech. Eng., Imperial College, London.

VINICKIER, J. and van TIGGELEN, A. (1968)
Structure and burning velocity of turbulent premixed flames.
Comb. Flame, 12, 6, 561.

WEINBERG, F. J. (1974)
The first half-million years of combustion research and today's burning problems.
15th Symposium (International) on Combustion. Combustion Institute, Pittsburgh, Pa.

WESTENBERG, A. A. and RICE, J. L. (1959)
Further measurements of turbulence intensity in flame zones.
Comb. Flame, 3, 459.

WILLIAMS, G. C., HOTTEL, H. C. and SCURLOCK, A. C. (1949)
Flame stabilisation and propagation in high velocity gas streams.
3rd Symposium on Combustion and Flame and Explosion Phenomena. The Williams & Wilkins Co., Baltimore, Ma.

WINTERFELD, G. (1965)
On processes of turbulent exchange behind flame holders.
Tenth Symposium (International) on Combustion. Combustion Institute, Pittsburgh, Pa.

WOLFSHTEIN, M. (1968)
Numerical smearing in one-sided difference approximations to the equations of non-viscous flow.
Report EF/TN/A/3, Dept. of Mech. Eng., Imperial College, London.

WRIGHT, F. H. (1959)
Bluff-body flame stabilisation: blockage effects.
Combustion & Flame, 3, 319.

WRIGHT, F. H. and ZUKOSKI, E. E. (1962)
Flame spreading from bluff-body flameholders.
8th Symposium (International) on Combustion. Baillière, Tindall & Cox, London.

WYGNANSKI, I. and FIELDER, H. E. (1970)
The two-dimensional mixing region.
J. Fluid Mech., 74, 2.

YOSHIDA, A. and GUENTHER, R. (1980)
Experimental investigation of thermal structure of turbulent premixed flames.
Comb. Flame, 38, 249.

YANTA, W. J. (1973)
Turbulence measurements with a laser-Doppler velocimeter.
Naval ordnance laboratory report NOLTR 73-94, White Oak, Silver Spring, Ma.